The effect of the build orientation and heat treatment on the fatigue and fracture properties of a directed energy deposited nickel-based superalloy (Inconel 718)

Prepared by Mikyle Paul

Supervised by Dr. Sarah George

This dissertation is submitted for the degree of Master of Science in Mechanical Engineering

University of Cape Town

March 2020

Plagiarism declaration

I know the meaning of plagiarism and declare that all the work in the document, save for that which is properly acknowledged, is my own. This thesis/dissertation has been submitted to the Turnitin module and I confirm that my supervisor has seen my report and any concerns revealed by such have been resolved with my supervisor.

This plagiarism declaration was signed by Mikyle Paul, (student number – PLXMIK001), on the 31/03/2020 for the submission of a dissertation for the degree of Master of Science in Mechanical Engineering, at the University of Cape Town.

Signed by candidate

Abstract

This project focused on determining the effect of build orientation and heat treatment on the fatigue crack growth rate and fracture toughness properties of the nickel-based superalloy, Inconel 718 that has been manufactured by additive manufacturing technique, directed energy deposition (DED). Three different build orientations namely XY, XZ and ZX, in both the as-built and heat-treated conditions were tested through a combination of comparative fatigue crack growth rate (FCGR) and fracture toughness (FT) tests.

A heat treatment protocol was applied to the material to relieve residual stress from the building process to homogenise the microstructure and to introduce precipitation hardening to the material for strengthening. This heat treatment protocol consisted of a solution treatment at 1200 °C for 2 hours followed by a water quench. Thereafter an ageing procedure was conducted at 650 °C for 16 hours followed by air cooling.

The Paris equation for each build orientation and material condition was determined with the aid of a crack measurement technique that was developed in this project. This technique was designed to significantly improve the measurement accuracy of the fatigue crack during testing. The developed crack measurement system consisted of a digital camera and stereomicroscope that were mounted to the ESH servo-hydraulic testing machine with a rig that was designed and manufactured during this project.

The FCGR and FT tests were conducted on compact tension (CT) specimens and the ASTM E647 and ASTM E1820 test standards were used as guidelines to test the specimens respectively. FCGR tests were conducted at a load range of 7.2 kN and a stress ratio of 0.1. The results indicated that there was a significant variation in the fatigue performance with respect to the material's build orientation. The fatigue crack path encountered several deviations during testing, resulting in inconsistent Paris data. FT tests were conducted at a cross-head speed of 2 mm/min (in the range of 0.8 to 2.0 MPa√m/s). The material exhibited an elastic-plastic behaviour and therefore, a J-integral fracture toughness analysis was undertaken. J_{max} values (the value of J at the maximum load) were obtained for each build orientation and material condition, and compared. It was seen that the average J_{max} values for each build orientation differed, indicating that the build orientation affected the fracture toughness properties of the material.

The applied heat treatment protocol homogenised the microstructure of the material and induced precipitation hardening. This was confirmed with the aid of light microscopy and scanning electron microscopy with energy dispersive X-ray spectroscopy, where a high concentration of niobium-rich Laves phase was almost completely eliminated by the heat treatment. The positive effects of the heat treatment on the material were noticed during the FCGR tests as the fatigue crack growth resistance and fatigue life of the material increased. The gradient of the Paris curve, m, was seen to increase from approximately 5 to approximately 8. This effect was also noticed during the FT tests where a uniform increase in J_{max} of approximately 50 kJ/m^2 was recorded for each build orientation.

It was concluded that a post manufacture heat treatment is essential for residual stress relief and homogenisation to occur in IN718 manufactured by DED. The material's response to fatigue is not uniform when in the as-built state for all build orientations due to the presence of the niobium-rich Laves phase. The material displays superior mechanical properties after the heat treatment protocol in terms of fatigue crack growth resistance and fracture toughness when compared to the as-built condition. Furthermore, it was also seen that the build parameters such as scanning width and hatch spacing affected both the fatigue and fracture properties of the material and must therefore also be taken into consideration when producing the material. A successful crack measurement technique

and apparatus was also developed that greatly increases the accuracy of Paris data obtained. The XZ orientation was seen to possess the most uniform fatigue and fracture properties amongst the three orientations tested in this project in both the as-built and heat-treated conditions.

Acknowledgments

I would like to take this opportunity to give thanks to those individuals who have assisted me during the course of my enrolment for the degree, with special thanks to the following:

- To my supervisor, Dr Sarah George. Her guidance, support and approachability throughout the duration of the project was extremely helpful and highly appreciated especially during the numerous challenging circumstances that were experienced during this project. Her vast knowledge of materials science and her quick thinking ability to address issues in a methodical manner is admirable and made the experience even more enjoyable.
- To my family, with special thanks to my parents, Michel and Sheryl Paul. Their constant support both emotionally and financially to achieve my goals is highly appreciated and I am forever grateful and indebted for their support.
- To my immediate group of friends and my colleagues. The constant support and companionship over the course of this degree played a vital role in its completion. Having a group of people to support you at all hours of the day is truly special and irreplaceable.
- To Professor Robert Tait. His expansive knowledge and experience in the field of fracture mechanics was immensely helpful during the testing phase of this project. Without his help, guidance and ideas, the completion of this project would not be possible.
- To the staff at the Centre for Materials Engineering at UCT with special thanks to Dr. Richard Curry, Penny Louw and Soraya Von Willingh. Their assistance in the laboratory with the testing equipment and their knowledge that pertained to various aspects of my project was highly appreciated. A special thanks to Nasheeta Hanief from the Electron Microscope Unit for her assistance with the scanning electron microscope.
- To the UCT workshop staff. Their hard work in the workshop to machine the parts necessary for my rig and for my test specimens was highly appreciated.
- To the CSIR for providing the DED produced material with special thanks to Nana Arthur for liaising with me and providing me with all the material production information that was required.
- To the University of Cape Town, EBE faculty and the Centre for Materials Engineering for providing me with the necessary tools and platform to complete this project, as well as providing the funding to support me financially during the course of my degree.

Table of Contents

List of figures

List of tables

1. Introduction

A gas turbine engine is composed of several parts which work together to convert chemical potential energy from a hydrocarbon-based fuel into useful mechanical energy in the form of thrust and rotation. One of these critical components is the turbine which comprises several individual turbine blades. The turbine blades are responsible for converting the high temperature and high energy combustion gasses from the combustor into work. As a result, the blades must be manufactured from highly resilient materials in terms of high temperature strength and fatigue and creep resistance. These materials are known as superalloys.

Micro gas turbine engines function on the same principle as full-sized gas turbine engines but on a smaller scale. These turbines experience extremely high rotational speeds and therefore the turbine blades and the rotor disk which is mounted to a common shaft is incorporated into a single unit known as the blisk. The use of a blisk minimises the number of working components in the engine and is usually manufactured through investment casting. The Council for Scientific and Industrial Research (CSIR) has attempted to manufacture a new blisk design using investment casting however, it is proving difficult to manufacture. As a result, additive manufacturing (AM) was considered as a possible manufacturing technique. AM is a manufacturing process whereby parts are produced in a layer by layer additive technique and is commonly known as 3D printing. The additive manufacturing technique of interest here is directed energy deposition (DED), more specifically the laser engineered net shaping process (LENS), due to the ability to produce metallic components with a high geometric accuracy. The main concern with using this manufacturing technique is the effect of the build orientation on the mechanical properties of the finished product. Since the material is designed to be highly resistant to creep and fatigue crack initiation at a wide range of temperatures, it is questionable whether the build orientation will alter this critical material property for each of the blades within the blisk.

The material under investigation for this project is the nickel-based superalloy, Inconel 718 (IN718) and will be supplied by the CSIR. Test samples will be manufactured at the National Laser Centre in Pretoria.

1.1. Aims and objectives

This project aims to determine the effect of the build orientation and heat treatment on the fatigue and fracture properties of a directed energy deposited (DED) nickel-based superalloy (Inconel 718) at room temperature.

In order to achieve this aim, the following objectives must be met:

- The design, manufacture and set-up of a crack monitoring procedure with high linear accuracy in order to determine the crack length for the development of the Paris equation.
- Determine heat treatment parameters for the DED IN718 material in order to stress relieve, homogenise and introduce precipitation hardening.
- Investigate the microstructure of the DED IN718 samples in the various build orientations and determine the effect of the heat treatment on the as-built material.
- Perform FCGR tests and develop the Paris equation for all build orientations (XY, XZ and ZX) and conditions (as-built and heat treated) in order to investigate the effect of build orientation and the effectiveness of the heat treatment.

- Determine the fracture toughness properties for all build orientations (XY, XZ and ZX) and conditions (as-built and heat treated) in order to investigate the effect of build orientation and the effectiveness of the heat treatment.

1.2. Scope and limitations

This project focuses primarily on a combination of fatigue crack growth rate (FCGR) and fracture toughness (FT) testing of the nickel-based superalloy IN718 produced by the directed energy deposition (DED) additive manufacturing technique in three varying build orientations. FCGR and FT tests were performed with reference to the ASTM E647, ASTM E1820 and BS 7448: Part 1 test standards respectively and were performed on compact tension (CT) test specimens. In addition to these tests, tensile tests, density tests and Vickers hardness tests were conducted according to ASTM E8, ASTM B311 and ASTM E92 respectively. All testing was performed at room temperature according to the relevant ASTM test standards for each test. Dummy specimens manufactured from stainless steel were also tested to predict the behaviour of the nickel-based superalloy specimens during the FCGR and FT tests.

Some specimens were heat treated before testing to determine homogenisation and precipitation hardening effects. The behaviour of the heat-treated material was compared to identical as-built material through the FCGR, FT, tensile, density and Vickers hardness tests. Light microscopy and scanning electron microscopy (SEM) were used to look at the microstructure of as-built and heat-treated material and to determine the differences between these two material conditions. Energy dispersive X-ray spectroscopy (EDS) was also used to determine the chemical composition of the material and to identify features seen within the microstructure, most notably any segregation as a result of the build process. Fractographs of the fracture surfaces of each material condition and build orientation were also examined using SEM.

This project also involves a design aspect in terms of the testing methodology and crack measurement technique used during the fatigue crack growth rate testing. It was necessary to improve the in-situ crack length measurement technique in order to obtain accurate fatigue data. This involved the design and build of a bolt-on camera system for crack length evaluation and measurement.

The project was limited by the low number of compact tension test specimens and the variation in the build parameters used to manufacture them. The sample material was built by the National Laser Centre which forms part of the Council for Scientific and Industrial Research (CSIR) in South Africa. The author did not dictate the build parameters. The tensile tests were limited by the size of the test specimens that were harvested from unusable CT specimens.

2. Background and literature review

In this section, a review of the relevant background information and literature pertaining to the use of nickel-based superalloys for high temperature gas turbine applications will be presented as well as the use of these materials in the directed energy deposition additive manufacturing method. An introduction to the mechanical properties being researched in this study will also be provided.

2.1. Gas turbines

A gas turbine engine is a type of engine that utilises continuous combustion to generate power. The gas turbine is fuelled by hydrocarbon-based fuels and the energy is extracted from the combustion process to perform work. This engine functions according to the Brayton cycle during which intake, compression, combustion and expansion of the hot gasses occur. Expansion occurs through the turbine, which in turn drives the compressor that is mounted on the same shaft. The power generated from the combustion process can be extracted from the shaft and converted into useful electrical energy via an electric generator. The exhaust gasses that pass through the turbine can also be used to generate thrust, which can propel an object forward as shown in Figure 2.1.

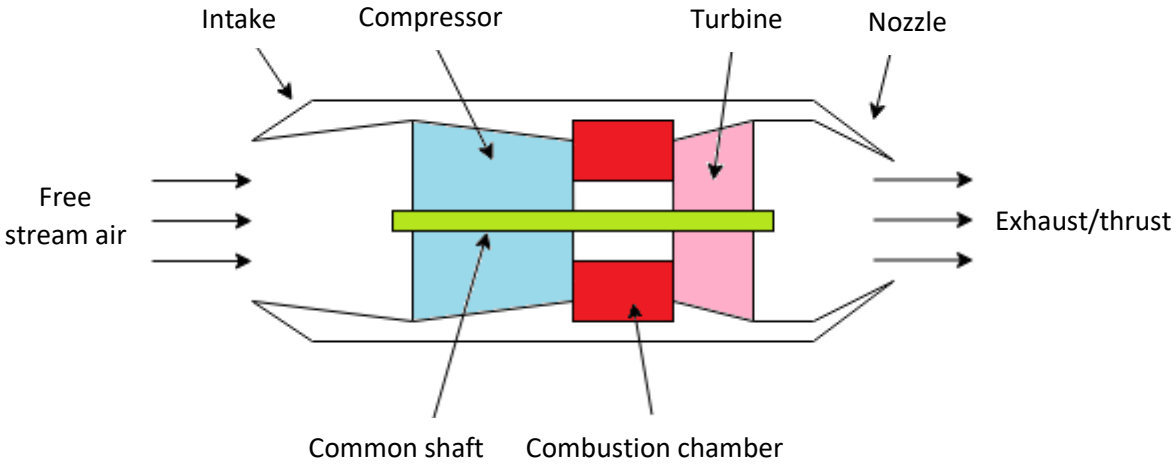

Figure 2.1: Schematic of gas turbine engine

The figure above displays a simplified schematic of a gas turbine engine and its working components including the intake, compressor, combustor, turbine, shaft and nozzle. For aviation propulsion purposes, the nozzle is designed such that the exhaust gasses can be converted into useful thrust and minimising the energy lost from the combustion process as well as to compensate for the energy used to drive the compressor. Figure 2.2 below displays a schematic of the Brayton cycle and all key components. This process comprises constant pressure heat addition between points 2 and 3 and constant pressure heat rejection between points 4 and 1. The thermodynamic process of the gas turbine engine will not be looked at further in this report.

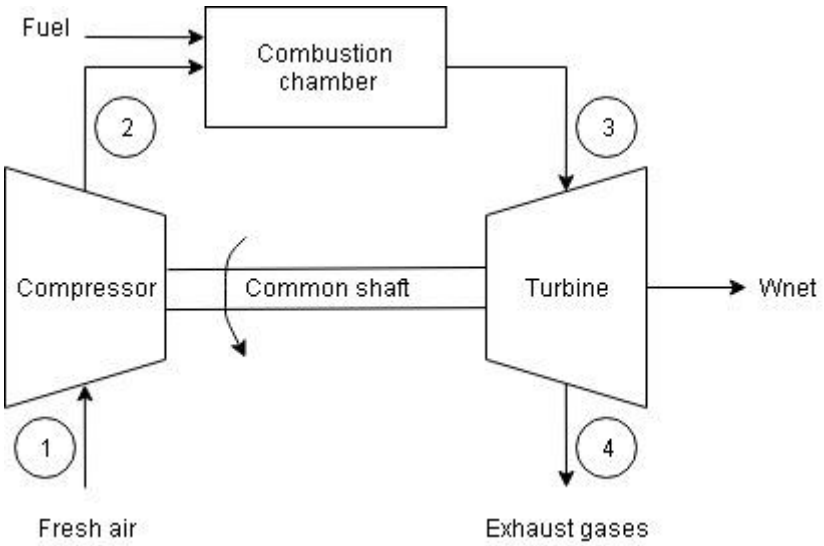

Figure 2.2: Schematic of Brayton cycle

Similarly, with an internal combustion engine that utilises four main steps for power production namely intake, compression, combustion and exhaust, a gas turbine engine also uses these steps however, these steps occur in different locations in the engine unlike the internal combustion engine where all processes occur in the combustion chamber (cylinder head). These four steps all occur at the same time but in different locations namely the inlet section, the compressor section, the combustion section and the turbine and exhaust section.

Intake and compression of the air, as well as fuel injection, are considered the cold section of the engine. The cold section is not susceptible to the effects of thermal degradation but can fall prey to foreign object damage (FOD) and hence is manufactured from lightweight and strong materials. Combustion and expansion are considered the hot section of the engine. The ignition of the air-fuel mixture occurs in the combustion chamber in a continuous process and expansion of these gasses occurs over the turbine and out the rear of the engine as exhaust gasses that can also produce thrust in the case of propulsion. Unlike the cold section of the engine, the hot section cannot be manufactured from arbitrary materials since the temperatures experienced during the combustion process are very high, in excess of 1000 $^{\circ}$C. Therefore, the material used to manufacture the turbine has to be a high-temperature material, which can maintain constant mechanical properties at elevated temperatures. As a result, the turbine material limits the maximum operating temperature of the engine. If a material able to withstand extremely high temperatures can be used, then the total power output of the engine and its efficiency can be increased.

2.2. Micro gas turbines

Micro gas turbines are essentially regular gas turbines on a smaller scale. These turbines are used in commercial aviation, power generation and by hobby enthusiasts. Micro gas turbines are small and compact and can generate a large amount of power for their size (high power to weight ratio). Other benefits of micro gas turbines include a smaller number of moving parts as compared to a fully sized gas turbine as well as simpler assemblies. Figure 2.3 shows a schematic of a micro gas turbine engine.

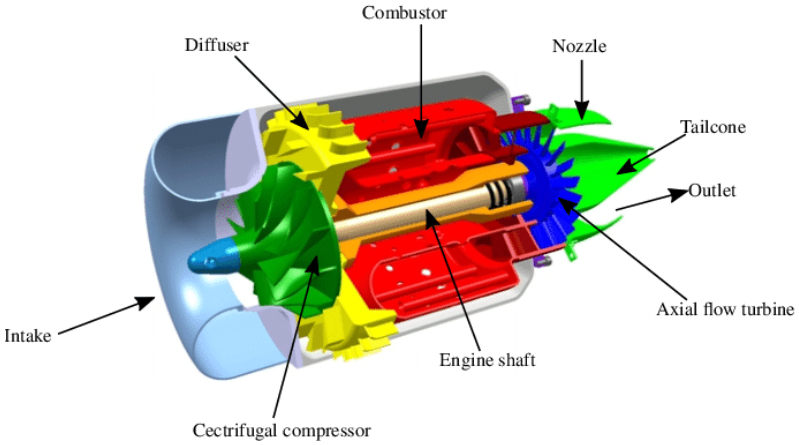

Figure 2.3: Micro gas turbine engine [1]

Due to the compact nature of micro gas turbine engines, it is possible for extremely high rotational speeds to be achieved by the shaft, compressor and turbine. This high rotational speed is encouraged by a low mass moment of inertia of the rotating parts due to the small size. These rotational speeds are often limited by the material from which the components are manufactured. Once high enough speeds are reached, the material will reach its operating limit and eventually fail. These failure mechanisms will be outlined in greater detail in the coming sections. This is more prevalent in micro gas turbines since the rotational speed is much higher than that of regular gas turbines by a factor of about 10 in some cases. Fully sized gas turbine engines that are used for aviation applications often experience a rotational turbine speed of approximately 10 000 revolutions per minute (rpm). Micro gas turbines however, can often have speeds that exceed 100 000 rpm. Cape Aerospace Technologies produces three micro gas turbine engines with the smallest having a diameter of 108 mm. This engine has a maximum operating speed of 125 000 rpm and an exhaust gas temperature (EGT) of 750 °C [a].

2.3. Turbine blades

A turbine is comprised of many turbine blades as shown in Figure 2.4. Each blade is responsible for converting the heat energy from the combustion process into useful rotational energy as well as thrust in the case of propulsion.

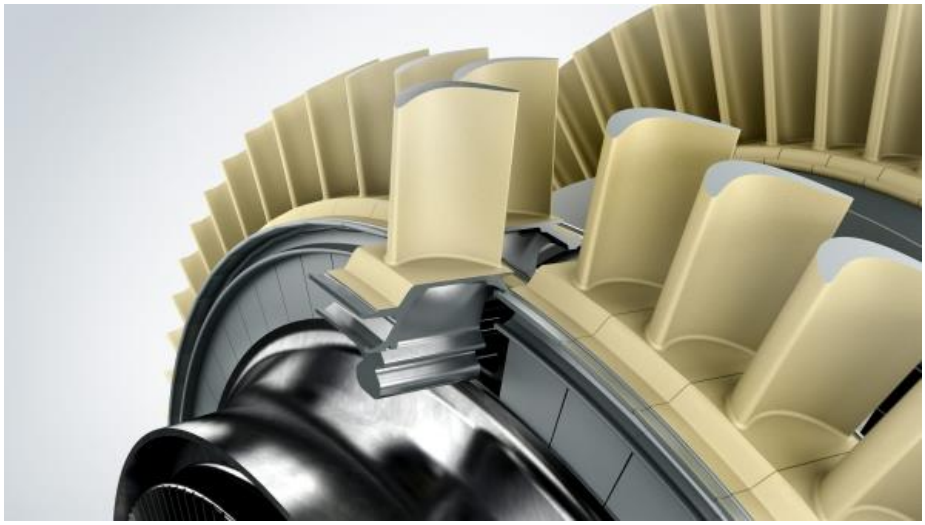

Figure 2.4: Turbine blades on rotor [b]

The flow of hot expanding gasses over each blade causes the turbine to rotate. This rotation drives the compressor as mentioned in Section 2.1. The blades are exposed to extremely harsh environments

due to the high temperatures achieved during the combustion process as well as the high rotational speed of the turbine itself. Turbines often fall prey to failure caused by fatigue and creep. These failure mechanisms will be explained later in the coming sections.

For high speed micro gas turbines, the turbine blades and the rotor disk are incorporated into a single unit and is known as a blisk. An example of blisk designs can be seen in Figure 2.5 below.

Figure 2.5: Examples of various blisks [c]

The advantages of using a blisk rather than having multiple blades attached to a rotor disk with individual screws or bolts is that the number of components in the turbine assembly will be drastically decreased as well as allowing for a smooth surface over which hot expanding gases can flow resulting in an increase in efficiency. Conventional manufacturing methods of the blisk include investment casting, which is typically used to manufacture small parts containing complex geometries. Similarly, with full size gas turbine engines, micro gas turbines are exposed to harsh operating environments in terms of heat and rotational speed and are therefore susceptible to fatigue and creep of the blade or blisk material. Therefore, there is a need to use superalloys in order prevent premature failure. An attempt was made by the CSIR to manufacture a micro gas turbine blisk from IN713LC using investment casting and is pictured in Figure 2.6.

Figure 2.6: Attempt at investment casted blisk

It can be seen in the figure above that the production of the blisk design in this investigation was unsuccessful since the surface finish and geometrical accuracy of the casting is not sufficient. It is also not possible for a working fluid to flow over the blades of this blisk since the poorly cast material obstructs the flow.

2.4. High temperature materials and superalloys

The major requirements for the selection of gas turbine materials include a high melting point, good oxidation and corrosion resistance properties, high temperature performance, microstructural stability at a wide range of temperature especially at high temperatures, low density due to weight concerns, high stiffness, reasonable cost and most importantly, reliable performance. High temperature materials are used to manufacture the blades as well as other materials that offer resistant to creep and fatigue and are robust enough to withstand the harsh environment in terms of oxidation and corrosion at high temperatures. Common materials used for this application are superalloys since they fit the above criteria perfectly.

Superalloys display superior mechanical strength and creep resistance at elevated temperatures as high as *0.8 Tm* (melting temperature), a good surface stability and are resistant to corrosion and oxidation. The crystal structure of such materials is generally face-centred cubic and consisting of a base metal such as nickel, cobalt or nickel-iron [d]. Figure 2.7 below shows the face centred cubic structure that consists of an atom on the centre of each face of the cubic structure.

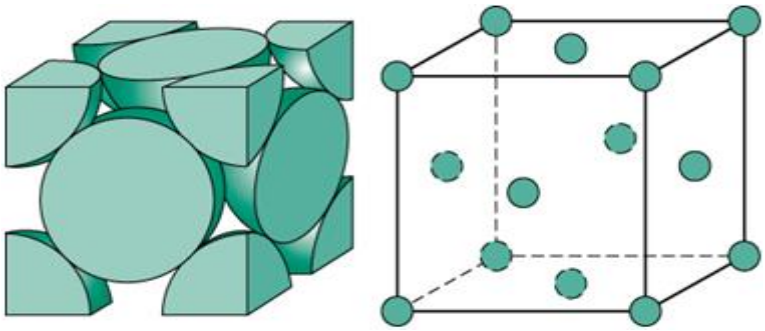

Figure 2.7: Face centred cubic structure [e]

Superalloys can withstand harsh environments due to atoms in solid solution as well as the presence of stable secondary phase precipitates. The precipitates impede dislocation movement, which is a fundamental characteristic of a high strength material, as well as enabling a material to be resistant to creep even at elevated temperatures. In addition to the strengthening mechanisms mentioned above, superalloys can sometimes contain carbides on the grain boundaries to prevent grain boundary sliding as well as Boron and Zirconium for a similar purpose. Generating larger grains, columnar grains or single crystals within the microstructure of the alloy can prevent boundary shear resulting in further strengthening [2]. Furthermore, superalloys display something known as a yield strength anomaly, which occurs when the yield strength of a material increases with an increase in temperature, and is usually a characteristic of precipitation hardening materials [3].

2.5. Common materials used for high temperature applications

There are a wide variety of superalloy compositions that are used for high temperature applications. The turbine disk for aircraft gas turbine engines is commonly manufactured using alloy 718. This alloy is usually produced through conventional ingot metallurgy. In terms of powder metallurgy, the production of nickel-based superalloys is more common than other superalloys such as nickel-iron and cobalt based superalloys. Superalloys such as IN100 and Rene95 can be manufactured using powder metallurgy since they are difficult to produce with conventional methods [9]. Cobalt based superalloys do have the potential to perform better at high temperature applications and efforts are being made to develop these alloys due to the oxidation and wear resistance properties of cobalt superalloys. The cobalt based superalloys however, are not as commonly used as the nickel-based superalloys due to the lack of γ’ phase strengthening at high temperatures. Since cobalt also has a higher melting point

than nickel, there is potential for cobalt based superalloys to be used for gas turbine applications, which operate more efficiently at higher temperatures.

This study will focus on nickel-based superalloys, more specifically Inconel 718, which is a common material used to manufacture turbine blades due to its high temperature creep resistance properties.

2.6. Inconel 718

Inconel refers to a group of metallic alloys that are primarily nickel-based. These alloys also fall under the category of superalloys and are therefore used for high temperature applications due to their high oxidation resistance and high temperature strength. Inconels are used widely in the aerospace industry which takes advantage of these properties to produce high performance gas turbine engines. IN718 is a class of Inconel and will be detailed below.

2.6.1. Chemical composition

The chemical composition for IN718 varies slightly for different suppliers of the alloy but the basic composition and proportion of the alloying elements remains relatively consistent. According to AZO Materials, the chemical composition of IN718 is shown in Table 2.1 below [f].

Table 2.1: Chemical composition of IN718

Element	Percentage
Carbon (C)	0.08 max
Manganese (Mn)	0.35 max
Phosphorus (P)	0.015 max
Sulphur (S)	0.015 max
Silicon (Si)	0.35 max
Chromium (Cr)	17.0-21.0
Nickel (Ni)	50.0-55.0
Molybdenum (Mo)	2.80-3.30
Niobium (Nb)	4.75-5.50
Titanium (Ti)	0.65-1.15
Aluminium (Al)	0.2-0.8
Cobalt (Co)	1.00 max
Boron (B)	0.006 max
Copper (Cu)	0.3 max
Tantalum (Ta)	0.05 max
Iron (Fe)	Balance

The main alloying elements are iron, chromium and niobium. Chromium is present to provide corrosion resistant properties to the material where niobium forms γ'' precipitates that are used for strengthening the material and will be outlined in the next section.

The alloy also has a melting range of 1370 – 1430 °C and a density of 8220 kg/m^3 in the solution treated and aged condition [2]. The material in the wrought condition is 200 GPa [2].

2.6.2. Material strengthening mechanism

As mentioned in Section 2.4, superalloys, such as IN718, undergo a process known as solid solution strengthening and precipitation hardening. Nickel is the main constituent of the γ matrix. By adding the alloying elements such as Co, Cr, Nb and Mo, the γ phase is super saturated, hardening the material. There is also a formation of carbides in the material. The γ' phase has a stoichiometry of Ni_3 (Al, Ti) and forms a part of the strengthening phase of the alloy. This phase forms a fine cuboidal

structure and is characterised by a face centred cubic lattice which hardens the alloys. Furthermore, the Cr element in this alloy enables the formation of a protective Cr_2O_3 layer which aids in corrosion resistance. The material is also strengthened by a γ'' phase with Niobium which forms body centred tetragonal Ni_3Nb. This phase is more prevalent in the alloy than the γ' phase as there is higher percentage of Nb in the alloy than Ti and Al. IN718 generally contains about 3% γ' and about 20% γ''. Alloys that are strengthened with the γ'' phase sometimes have limitations to their maximum operating temperatures since the γ'' begins to decompose as temperatures exceed around 650 °C. This decomposition results in a thermodynamically stable δ phase with a loss in strength [5].

Figure 2.8 below displays the various phases mentioned above that occur in IN718.

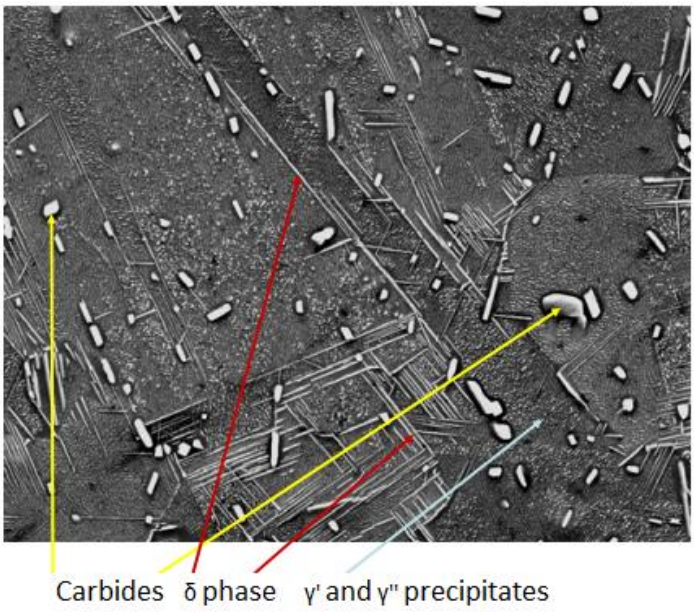

Figure 2.8: Phases present in IN718

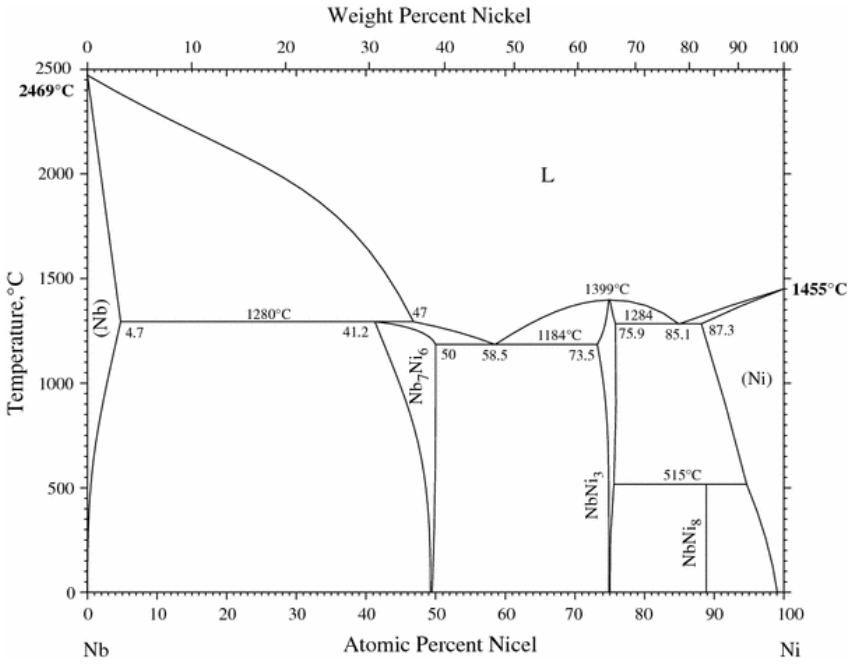

Figure 2.9: Nickel-Niobium phase diagram [6]

The phase diagram in Figure 2.9 shows that the Ni_3Nb phase falls within the region of 50-55 percentage composition of Nickel in the alloy. In this region, the formation of Ni_3Nb is promoted at a temperature below 1184 °C.

The γ + γ’ phase accounts for the some of the solid solution strengthening mechanism of the alloy. A nickel-based superalloy such as IN713 uses γ’ as its primary strengthening mechanism. IN713 has a similar chemical composition as IN718 however, IN713 possesses a greater Aluminium content and a lower Niobium and Molybdenum content therefore, the γ’ phase is the primary strengthening phases in IN713. The γ + γ’ phase can be seen in the Nickel-Aluminium phase diagram below.

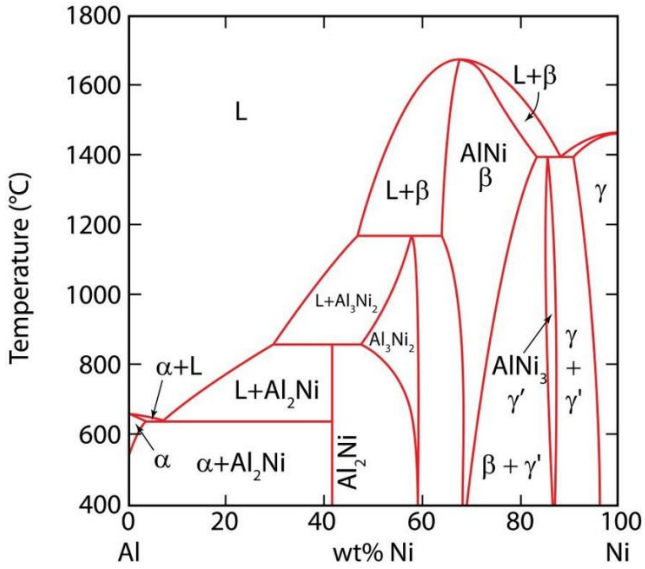

Figure 2.10: Nickel-Aluminium phase diagram [7]

The microstructure of IN713 in the casted state is shown in Figure 2.11 below.

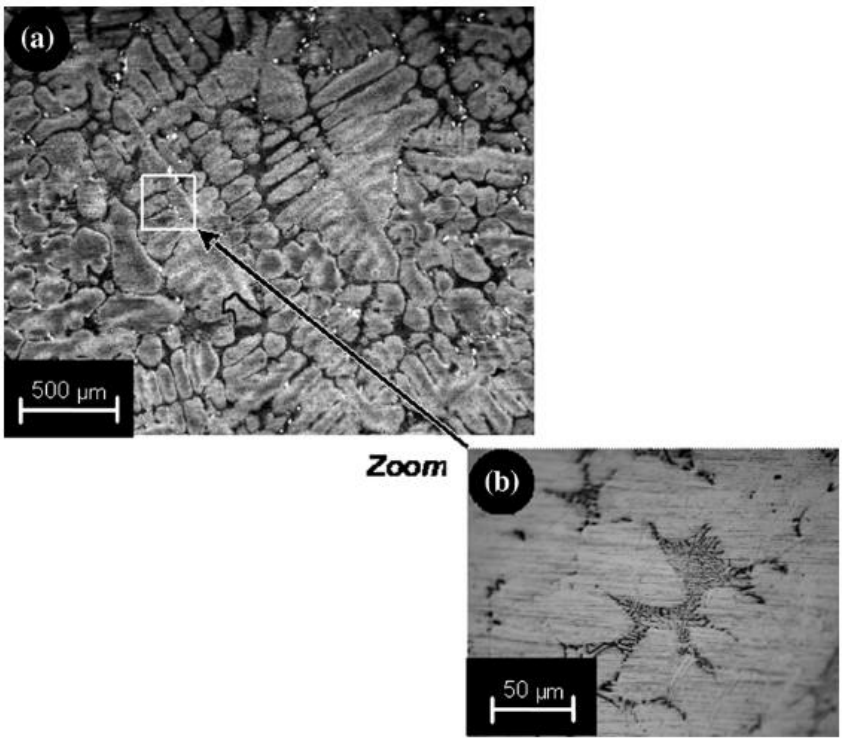

Figure 2.11: Microstructure of IN713 in as-cast state [8]

Figure 2.11 displays the microstructure of IN713 using optical microscopy and chemical etching [8]. This microstructure is characteristic of IN713 which is comprised of a dendritic structure resulting from primary solidification as seen in (a) with interdendritic precipitates shown in lighter contrast. Looking at a greater magnification in (b), the microstructure shows the eutectic γ/γ' phases which can be predicted by the aluminium-nickel phase diagram shown in Figure 2.10.

The effect of temperature on the short-term mechanical properties of wrought IN718 is shown in Table 2.2 below.

Table 2.2: Effect of short-term mechanical properties of IN718 [2]

	Ultimate tensile strength (MPa)			**0.2 % yield strength (MPa)**			**Tensile elongation %**		
	21 °C	**540 °C**	**760 °C**	**21 °C**	**540 °C**	**760 °C**	**21 °C**	**540 °C**	**760 °C**
IN718	1435	1275	950	1185	1065	740	21	18	25

From the information presented in Table 2.2 above, this alloy displays an increase in yield strength as the temperature increases which is a key characteristic that is required for gas turbine applications. Furthermore, the tensile elongation decreases which shows that the ductility of the material is in fact decreasing as the temperature increases.

AM nickel-based superalloys could behave in different ways to that of conventionally manufactured material as a result of the building parameters and the microstructure evolution throughout the manufacturing process. This will be outlined further in Section 2.8.

2.7. Failure of gas turbines

Failure of the casted turbine blades occurs due to three mechanisms; fatigue, stress corrosion cracking and ductile creep, where fatigue was seen due to striations on the fracture surface on both the trailing and leading edges of the turbine blade, also known as fatigue streaks, and the centre of the blade was associated with transgranular stress corrosion cracking due to ductile dimpled rupture [8]. These results indicate that turbine blades fail as a result of the variation in thermal and mechanical stresses experienced during service.

These three damaging mechanisms are in agreement with the work presented by Tim J Carter on common failures in gas turbines [9]. Direct mechanical damage, such as foreign object damage (FOD), does not affect the turbine blades in the combustion chamber since the foreign objects that may pass through the compressor are completely shredded and later incinerated during the combustion process. High strength stainless steel is often used for the first row of compressor blades especially in military applications in order to protect the rest of the engine from foreign bodies that may enter the intake.

Due to the high temperatures and stresses that occur in the turbine, creep is likely to occur in the blades and therefore limits the life of the turbine. The blades stretch over time and eventually rub against the housing of the engine. This is known as tip rub and is shown in Figure 2.12.

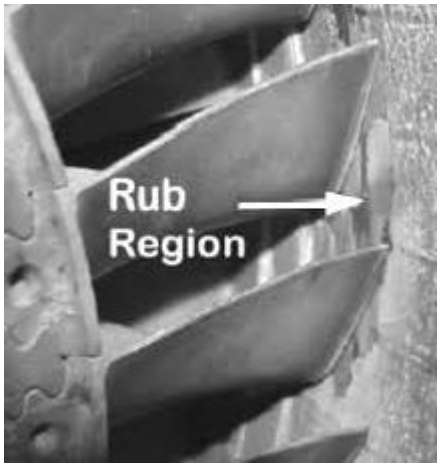

Figure 2.12: Region of tip rub [10]

According to Carter [9], high cycle fatigue failures are not very common in the rotating parts of gas turbines and tend to occur when some sort of external initiating factor influences the performance of the blades, such as foreign object damage. Microstructure defects that arise from imperfections in the manufacturing procedure of the blades can also play a role in fatigue failure of the blades. In modern day gas turbine engines, fatigue failure has been considered during the design phase of the engine and hence it is unlikely to occur during the lifetime of the engine however, it is of key interest to know the fatigue properties of the material when designing the turbine. Low cycle fatigue is also to be considered since the stresses imposed on the turbine during starting and stopping of the engine are large. Thermal stresses may be induced as a result of frequent start up and shut down of the engine. Therefore, aircrafts for example that fly shorter but more frequent trips have an engine lifespan far less than another flying longer distance trips due to reduction of the thermal gradient experienced by the engine.

Corrosion of the blades during service occur primarily due to ingested air from the atmosphere. The air can contain contaminants depending on where the turbine is operating, such as near a marine environment, a highly polluted environment such as an industrial area and even volcanic ash which may be located in the atmosphere at high altitude. Oxidation can occur on the turbine blades due to combustion process and its high operating temperature. Elements such as sulphur from the atmosphere and the fuel can corrode the blades of the turbine at elevated temperatures. As mentioned above, a protective layer is sometimes introduced to the blades by the addition of certain alloying elements such as chromium which forms a Cr_2O_3 protective layer.

2.8. Additive manufacturing

Additive manufacturing (AM) methods are most commonly referred to as 3D printing. These processes work by converting a 3D CAD model into a working part by means of a layer by layer additive technique. AM can be used for a variety of different materials, including polymers and metals. A CAD model is sliced into thin layers of a specified thickness within the limits of the machine. The machine then replicates each layer according to the current slice and this process repeats itself until the part has been completed. The scope for additive manufacturing has increased drastically in recent years as processes have become more refined and easier to replicate. Although mass production of AM produced parts has not been fully optimised yet, the flexibility and diversity associated with the industry is extremely promising. AM has the potential to replace conventional production processes such as casting, forging and machining due to the high accuracy achieved by the process and the ability

to produce complex shapes that are not achievable conventional machining processes. These advantages will be explained in Section 2.9.

2.8.1. Directed energy deposition

Directed energy deposition, also known as laser metal deposition (LMD) or direct metal deposition (DMD), is a metallic AM technique that converts a three-dimensional computer aided design into a near net shape and fully functional part by melting a metallic powder.

This method allows for complex geometries to be achieved whilst using one tool whereas with other manufacturing procedures, special tooling may be required for a specific shape or design.

The process of building the 3D model is as follows. The 3D computer aided drawing (CAD) model is broken down into individual layers and this information is then sent to the deposition machine. The feeder nozzle will then propel the metallic powders into the high energy density laser beam, and this causes localised melting of the powders. Fusion of metallic powders occurs as a result of the melting. The material is deposited on to a substrate, which is used to support the first layer of the build. Thereafter, the remaining layers are deposited in an additive manner until finally, a high-density part is produced. Either the support platform or the nozzle can be moved depending on the application and the geometry of the part. The LENS process in particular is carefully controlled in an argon filled non-reactive atmosphere, keeping oxygen and moisture levels to below 10 parts per million. This prevents corrosion and oxidation of the material and keeps the part clean. The energy system utilises an IPG fibre laser with a power output of 1 kW. A schematic of the process is shown in Figure 2.13 below.

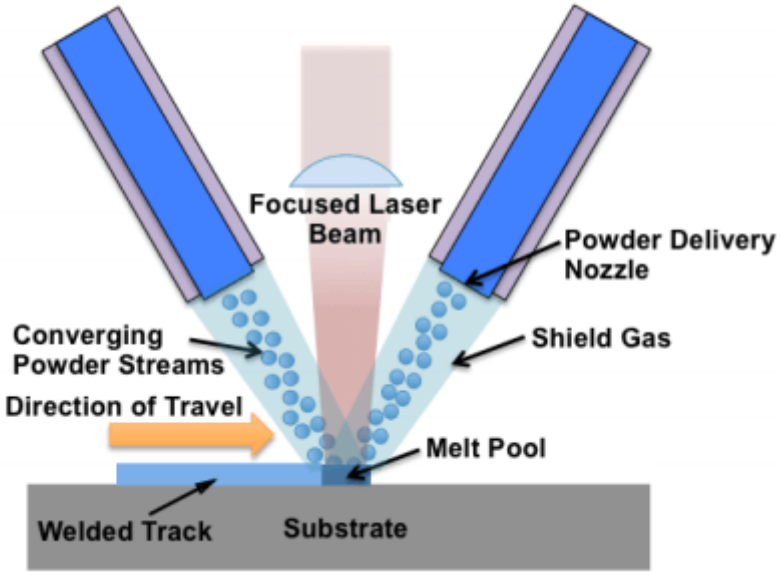

Figure 2.13: Schematic of LENS process [g]

This process is similar to other metallic AM techniques that all produce three-dimensional metallic parts, such as selective laser melting (SLM) and direct metal laser sintering (DMLS) however, SLM and DMLS are powder bed fusion (PBF) techniques that require material to be deposited on a substrate first and melted by the laser thereafter. These techniques require the surrounding and unused metallic powders to support the part being made whereas for DED, little to no wastage or recycling of the material is required as most of the powder delivered is melted and deposited to the part [h]. DED is also beneficial in that it can be used to build larger scale parts in a shorter period of time as compared

to PBF processes as the layer thickness and width is greater in DED than in PBF processes [i]. PBF requires material to be deposited after each layer is melted and this process takes time whereas DED deposits material when needed. The LENS process can be used to manufacture superalloy materials from start to finish and repair them if parts fail during service. One of the major benefits of the LENS process is the ability to repair existing superalloys components since a pre-deposition of metallic powder is not required as in PBF processes. Since superalloys are difficult to weld, the LENS process can be used to repair damaged components with a wide range of sizes [11]. There is limited literature available on nickel-based superalloys manufactured by DED, however research has been conducted on other AM procedures such as SLM on nickel-based superalloys as well as other high-performance alloys. This work can be used as a general benchmark to predict the behaviour of Inconel that has been manufactured by DED, more specifically, the LENS process as this project entails. A schematic of the SLM process is shown in Figure 2.14 below.

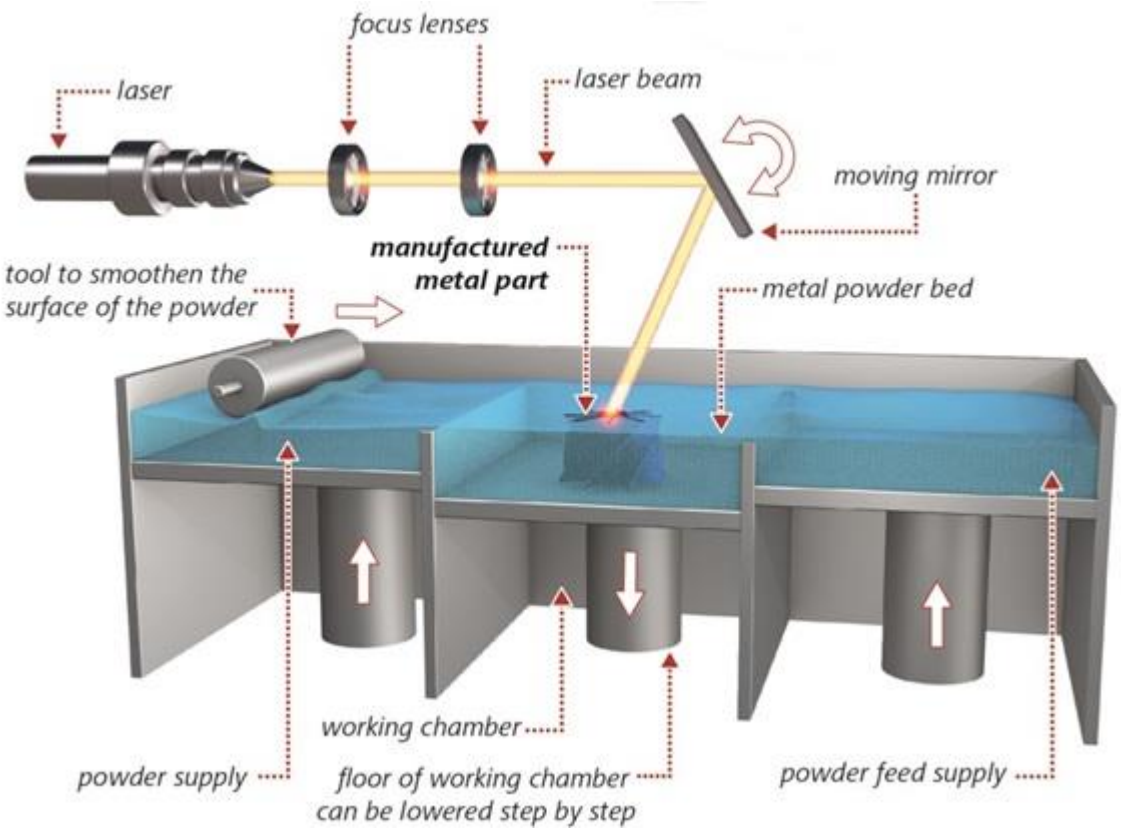

Figure 2.14: Selective laser melting process (SLM) [j]

Additive manufacturing methods are beneficial as they allow for near net shape products to be formed resulting in a reduction of raw material consumption. In some cases, no post processing is required before the component can be used, meaning a highly efficient output of parts. Furthermore, the manufacturing costs per part as well as carbon emissions can be reduced when compared to traditional processing methods.

2.8.2. Scanning techniques

Scanning refers to the line that the laser follows as it melts the metallic powders. Various scanning strategies can be used to develop one single part. This could result in differences in the final product in terms of microstructure and material properties. As presented in a study of the effect of scanning methods in SLM of 316L/TiC nanocomposites by Almangour *et al.* [12], the method of scanning influences the final product in terms of the degree of densification, microstructure and hardness. It

was found that each sample displayed a fine grain size as a result of rapid cooling which is expected as the laser melts a very small area at a time and hence the heat is dispersed quickly throughout the rest of the material. The major differences were seen between double and single scanning. Passing the laser over the same path twice is known as double scanning and this allows for the solidified layer to re-melt. This in turn causes the dendrites to become even finer than what is achieved in single scanning. The second pass results in less energy being absorbed by the material since the material is already in the solidified form and not in powdered form. Furthermore, the number of pore defects are eliminated by this process and the density of the final product was seen to increase. A double scanning procedure could also potentially result in a reduction of residual stresses in the material after the SLM process since the double pass of the laser anneals the solidified material on the second pass. Residual stress will be outlined in the coming sections.

In DED, the variation of the laser power, speed and the feed rate of the powder can be altered in such a way to produce a desired layer thickness. This would also result in the ability to produce certain patterns on the surface and control the melt pool size. The size of the melt pool is important as it can affect the microstructure of the material as well as the mechanical properties of the material such as hardness, tensile and fatigue properties [13]. The macroscopic features of AM techniques include a "V" shaped structure in the direction of scanning which is similar to that of welding. A cross sectional view of the material shows a scale-like structure in which the individual melts can be seen. This is characteristic of the SLM process as the melt pool width is generally larger than the spot size of the laser. The "V" shaped and scale structures can be seen in Figure 2.15 below.

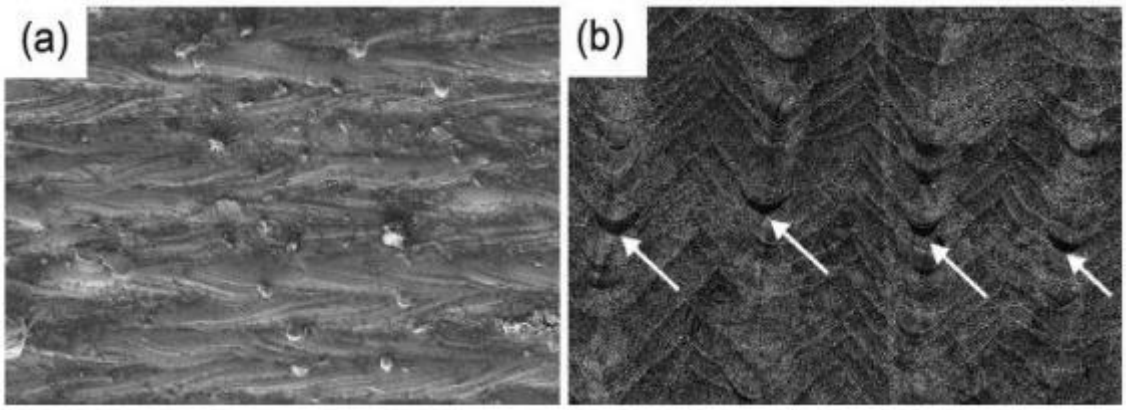

Figure 2.15: V-shaped (a) and scale-like (b) structures [14]

2.8.3. Build orientation

The build orientation of a product manufactured using additive manufacturing refers to the direction in which the layers of the part are deposited and melted on the previous layer when the part is being formed. Since DED, more specifically the LENS process, uses a procedure where the platform is lowered or the nozzle is raised for each subsequent layer, the orientation of the part is rotated in order to change the build direction of the part. This orientation is in terms of the X, Y and Z coordinate system. The convention used to label the build orientations is derived from ASTM E399 which is the standard test method for plane-strain fracture toughness of metallic materials [15] and is shown in Figure 2.16.

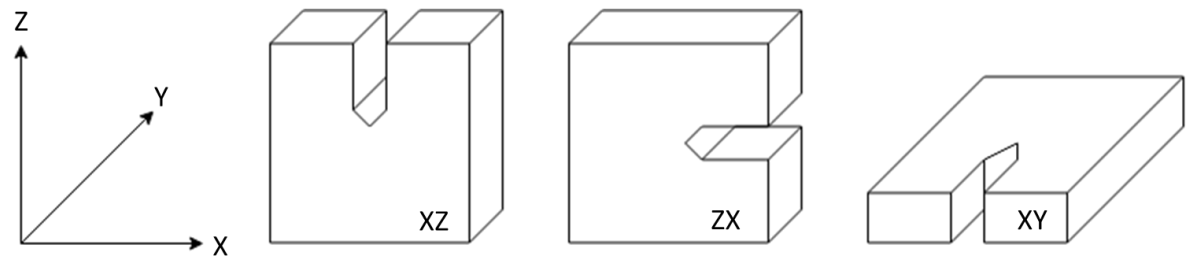

Figure 2.16: Two-letter code for identifying build orientation

The two-letter code is used to describe the building orientation in terms of the X, Y and Z axes. The schematic is also based on the geometry of a compact tension test specimen which is a specimen used for fatigue crack growth rate and fracture toughness testing. The first letter refers to the direction that is normal to the crack plane and the second letter refers to the direction in which the crack is expected to propagate.

The build orientation also affects the part accuracy to a certain extent especially in the case of circular cross-sections as can be seen in the figure below. For a cylinder that is formed with its axis in the Z direction (vertical direction), each slice will be in the form of a circular disk and therefore the cylinder will have a smooth surface finish on the outside. A cylinder in which the axis is perpendicular to the Z axis will have to consist of rectangular slices each with a length of the total cylinder length but with varying widths. This will result in a staggered surface finish and possibly a flat spot on the curved surface of the cylinder on which the first layer is formed. This is exaggerated in Figure 2.17 below where the left cylinder shows the axis is parallel to the Z direction and the right cylinder shows the axis perpendicular to the Z direction. Rectangular cross sections would be less affected by this phenomenon.

Figure 2.17: Cylinders built with different orientations [k]

In a study performed by M. Simonelli *et al.* [16] regarding the effect of build orientation on the mechanical properties and fracture modes of selective laser melted Ti-6Al-4V it was seen that the build direction of the specimens did have an effect on the tensile properties of the material. The orientations used in this study were the XZ, ZX and XY directions. The XZ specimens displayed the best tensile properties as well as the greatest elongation at fracture. This data is of some significance as it

gives an indication that the build orientation cannot be overlooked when manufacturing parts using additive manufacturing techniques. In addition, another study by Cain *et al.* [17] on the crack propagation and fracture toughness of Ti-6Al-4V alloy by SLM was conducted. This study showed that the build orientation does have an effect on the fracture toughness and fatigue crack growth rate.

2.8.4. Residual stresses

In metallic materials, residual stresses can be induced from plastic deformation or thermal factors. In terms of plastic deformation, residual stresses usually occur when the material is constrained in some way that prevents certain parts of the material from expanding, contracting or releasing elastic strain [l]. Additively manufactured components will usually possess high amounts of thermal residual stresses. These stresses occur due to extremely high temperature gradients during the solidification process after the powders are melted. Since a small amount of powders are melted at once, the material cools rapidly. This may cause residual stress to form during phase change as well. During cooling of material, the outer portion near the surface will cool much quicker than the inner portion. This will cause the surface to contract and induce a compressive stress on the inner portion. The inner portion will then begin to cool but the outer portion will resist further contraction and therefore, the inner portion will be in tension. Residual tensile and compressive stresses are therefore induced in the material. This is shown in Figure 2.18 below, for a bulk sample.

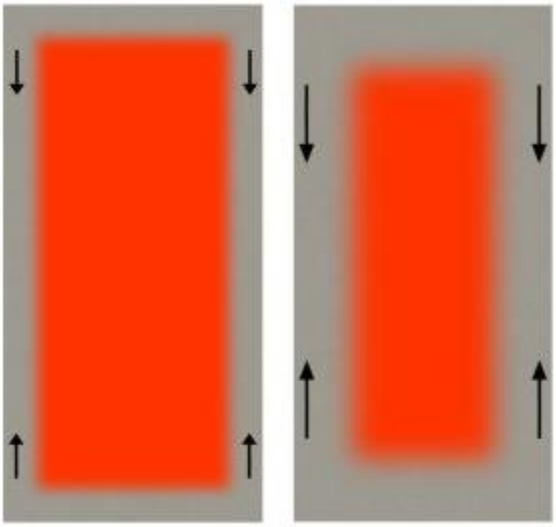

Figure 2.18: Residual stress causing induced compression and tension respectively [l]

Additively manufactured components do not solidify in the same manner as shown in Figure 2.18 above, as the material is melted in layers. The temperature gradient mechanism is responsible for the induction of residual stresses in parts. The laser rapidly heats the upper surface of the material locally and therefore, the strength of the material will decrease due to the increase in temperature. The underlying material layers remain cool due to the local heating of the upper layer and therefore, the expansion of the top layer is restricted by the lower layer and elastic compressive strains are induced. The stress will increase until the yield strength is reached, and the top layer will be plastically compressed. When the material begins to cool, the upper layer will shrink and bend towards the laser. This is illustrated in Figure 2.19 below.

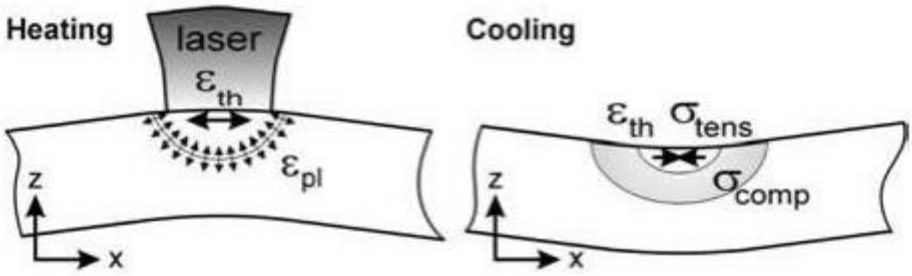

Figure 2.19: Distribution of stresses in AM produced metallic parts [18]

The geometry of a part can be affected significantly if the residual stress induced is large enough. Figure 2.20 below depicts the scenario shown in Figure 2.19 above.

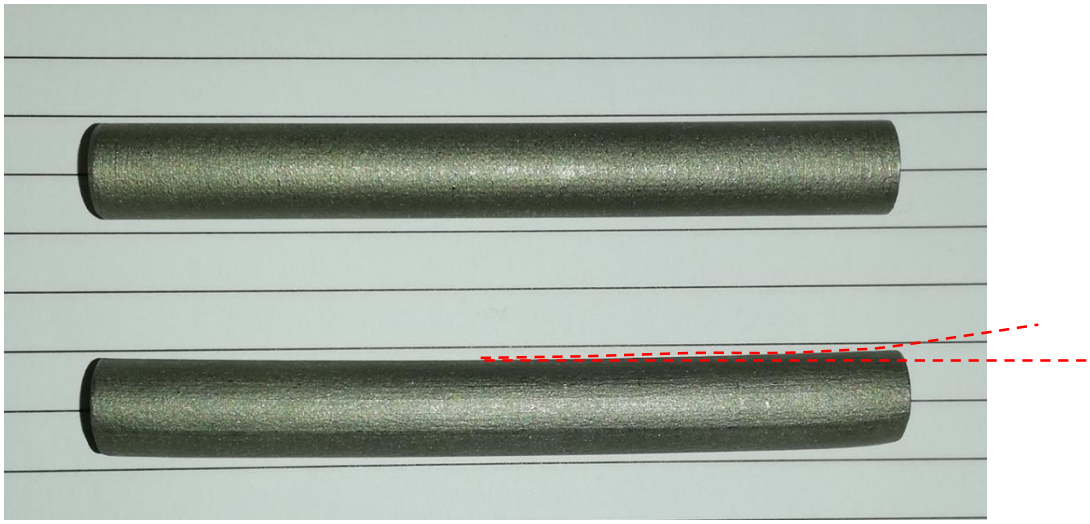

Figure 2.20: Effect of residual stress on SLM IN718 part geometry

Figure 2.20 above shows two IN718 cylindrical rods that have been produced by SLM. They were built to have an identical geometry but as it is seen in the picture, the bottom rod is slightly warped and is illustrated by the dotted lines. This is due to residual stresses that were induced during the building process as these rods were built in two different build orientations. Therefore, the build orientation with respect to the part geometry is not to be ignored when building a geometrically critical part since the temperature gradient during melting and solidification are contributing factors to part accuracy.

The magnitude of the residual stress of an AM part is highly dependent upon the build parameters of the part, which include the type of AM process, the scanning rate and strategy and the build orientation. To reduce or eliminate residual stresses, it is usually encouraged to expose AM components to a stress relief heat treatment. The yield strength of metals decreases as the temperature increases since the material becomes more ductile. Stress relief can occur if the material is heated to a temperature where the yield strength and residual stress are similar. Thermal stress relief on titanium alloys has been shown to be more effective than on nickel and aluminium alloys without hindering strength properties as a result of the thermal treatment [m]. Heat treatments will be outlined further in Section 2.10.

2.8.5. Microstructure of AM parts

A description of the microstructure of nickel-based superalloys has been illustrated in Figure 2.8 and discussed in Section 2.6. The microstructure shown in Figure 2.11 can be expected for cast nickel-

based superalloys. AM nickel-based superalloys possess microstructures that can differ from their wrought counterparts. The AM microstructure is dependent upon the processing parameters of the part, such as laser parameters, building conditions and post manufacture heat treatments.

The microstructure of SLM produced IN718 is shown in Figure 2.21 below.

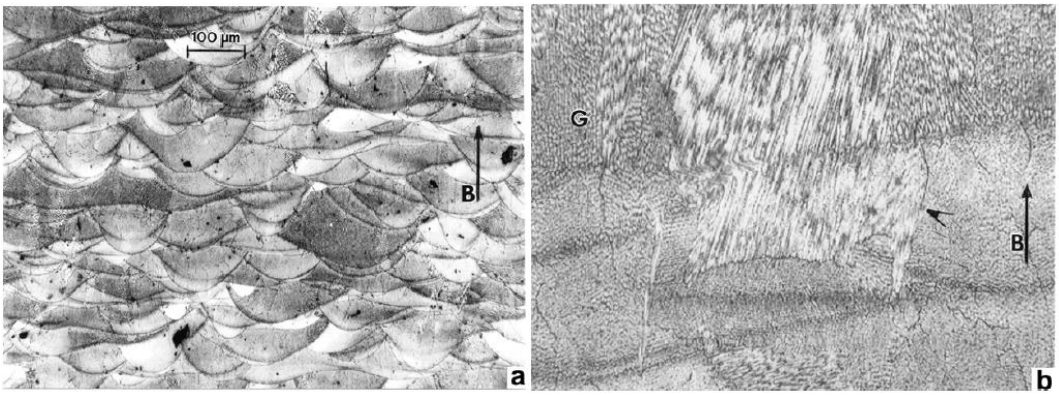

Figure 2.21: Microstructure of SLM produced IN718 [19]

Figure 2.21 above shows a cross section of SLM produced IN718. Here, the individual layers and lines of solidification as well as the melt pool overlap can be seen clearly in (a), with respect to the build orientation indicated with the arrow. Picture (b) shows a higher magnification of picture (a).

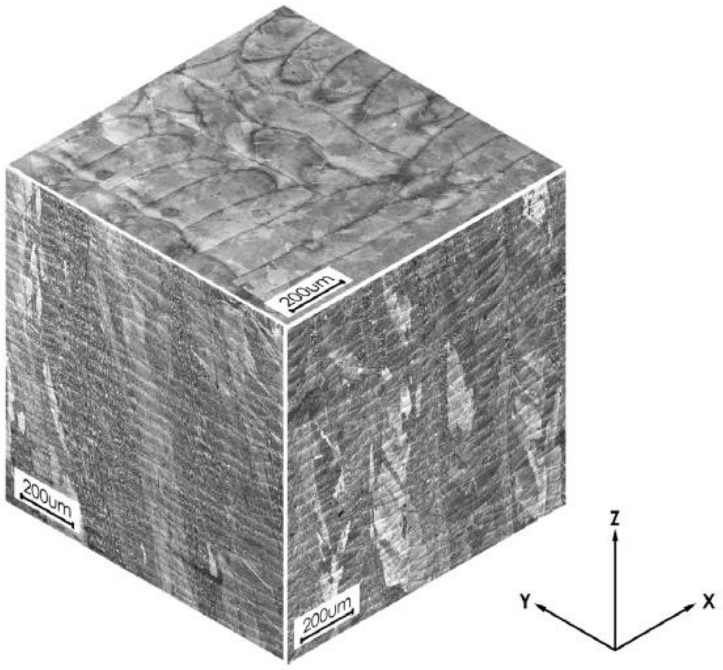

Figure 2.22: 3-Dimensional structure of SLM produced IN718 [52]

In Figure 2.22 a three-dimensional view of the microstructure is shown with respect to the X, Y and Z coordinates. The build direction is in the positive z direction. On the top surface of the cube (XY plane), the individual laser scans and scanning tracks can be seen clearly. Looking at both the YZ and XZ planes on either side of the cube, a similar structure to that shown in Figure 2.21 above can be seen. Columnar architecture and laminar material structure are clearly visible. The columns are created by grains of solid solution γ which have been elongated in the direction of growth.

The microstructure of as-built IN718 was also investigated by S. Raghavan *et al.* [20]. The following images are taken at a higher magnification than in the figure above and hence, the individual layers and scanning tracks cannot be seen.

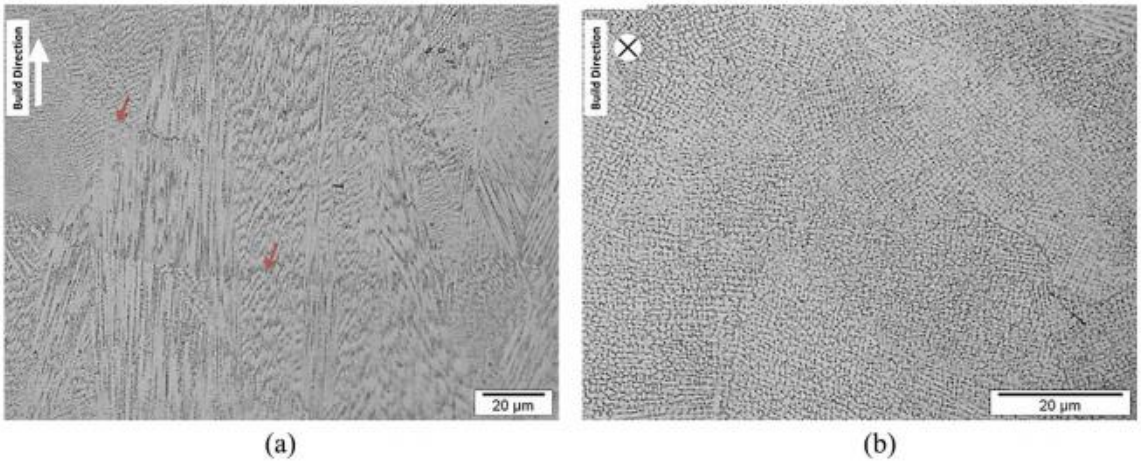

Figure 2.23: Microstructure of IN718 at a higher magnification [20]

Figure 2.23 above shows the microstructure of SLM produced IN718 in two different orientations where, in (a), fine dendritic structures can be seen in the building orientation and in (b), the cores of the dendrites can be seen perpendicular to build direction.

AM procedures are well known to produce columnar grain structures that stretch in the Z direction as shown in the figures above. This is due to the directional cooling of the material as the building process is performed. The microstructure displays anisotropy as a result. As the material is deposited to form the next layer, the existing layer is not melted. Therefore, there will be a temperature gradient that flows from the molten layer that is being deposited, to the existing layer that was deposited previously and columnar grains in the building direction will grow [14].

AM processes do not result in an effective precipitation of the γ' and γ'' phases due to the temperature gradients and anisotropy that results during rapid solidification. Fine dendritic grain structures can be expected however, and a heat treatment is required to homogenise the segregation and to precipitate the γ' and γ'' strengthening phases [21].

A common occurrence in the additive manufacturing of IN718 is the formation of Laves phase. This usually results during the rapid solidification of the alloy during the AM process which can be desirable due to grain refinement and fine microstructure development, but niobium diffuses quickly at the liquid-solid interface during rapid solidification. Segregation of niobium will therefore occur, leading to the formation of the brittle intermetallic Laves phase. This phase is unwanted in IN718 as it significantly reduces the niobium content available for the formation of precipitation hardening γ'' phase. Properties such as tensile ductility, fatigue life and fracture toughness have also been seen to deteriorate as a result of Laves phase formation [22]. Figure 2.24 shows the form of Laves phase in SLM produced IN718.

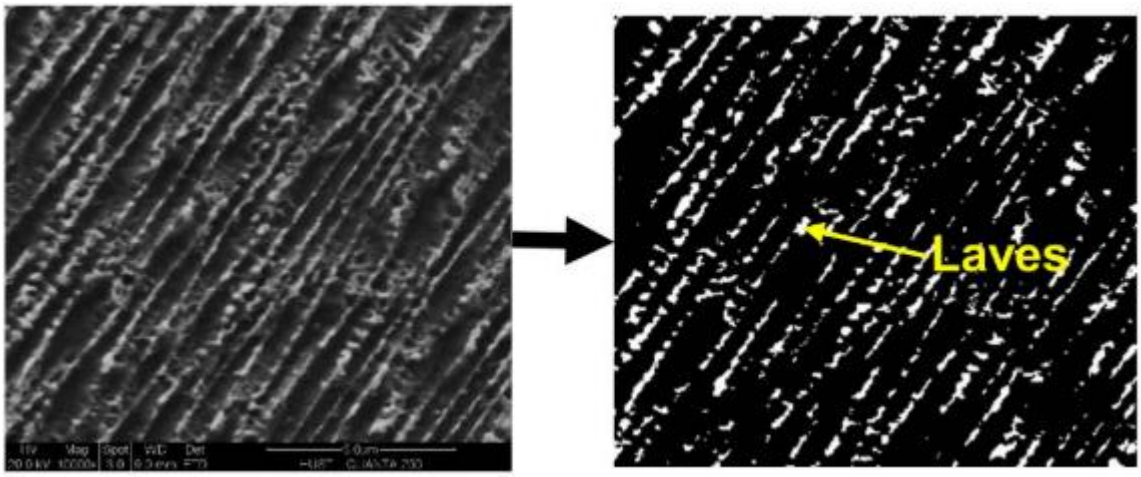

Figure 2.24: Laves phases in SLM produced IN718 [23]

2.8.6. Density of AM parts

The density of parts produced by AM are generally high with densities near or equal to 100%. This is only achieved if the processing parameters, such as the laser power and scanning speed, are at the optimum value for the material of interest. Failure to use the correct processing parameters can result in a lower density of the finished product. Defects in the part usually result due to internal voids, partially melted powders and internal cracks due to residual stresses from the large temperature gradients [24]. Incomplete melting of the powders can also result in cavities and pores in the material once the material has cooled. Some of the factors that contribute towards porosity include the size of the powder particles, the temperature of the build chamber and the speed and temperature of the laser [n].

A simple technique used to calculate the density of parts manufactured by AM is the Archimedes method. Archimedes principle states that a body completely or partially submerged in a fluid at rest is acted on by a buoyant force which has a magnitude equal to the weight of the fluid that is displaced by the body [o]. This principle can be used to determine the density of an object by measuring the mass of the object before and while it is submerged in water. The ASTM B311-17 test standard is used to measure the density of powder metallurgy materials and will be used to measure the density of the DED produced IN718 material. The density of cast IN718 as mentioned in Section 2.6.1 is known to be 8220 kg/m^3 [4]. This value can be used as a reference to determine the difference in density between cast and DED produced IN718.

2.9. Comparison between AM and investment casting

AM is advantageous over conventional manufacturing methods since it allows for high geometrical freedom and personalisation of parts, manufacturing cycle time is reduced as post processing requirements are minimal and AM requires one process to manufacture a full component. Materials that are difficult to conventionally process can be made using AM. In conjunction with geometrical freedom, AM can produce parts with complex cooling channels specifically for high temperature applications [25]. Figure 2.25 displays gas turbine blades manufactured from a nickel-based superalloy using SLM.

Figure 2.25: Turbine blades manufactured by SLM [p]

Static and dynamic material properties must be adequate to adhere to loadings and operational requirements during service, which can be an issue with using AM. Since DED and SLM involve a concentrated high energy density laser beam, the temperature gradients experienced during the formation of the part can vary significantly and rapid solidification can occur resulting in the formation of non-equilibrium microstructures, as well as high levels of residual. Therefore, even though these AM procedures can produce parts with the abovementioned advantages, the mechanical properties also need to match their conventionally produced counterparts.

The part accuracy can also be affected by the build orientation of an AM part whereas investment casting can produce an even surface finish and is dependent on the quality of the mould. Furthermore, for an accuracy dependent application such as a gas turbine, the surface finish of the part is critical. AM is able to produce a smooth surface finish as shown in the Figure 2.25 but the build orientation may also play a role in this, as shown in Figure 2.17 in Section 2.8.3.

AM does not require moulds and special tooling and as a result, the start-up cost is reduced significantly since the part to be manufactured can simply be uploaded on to a computer and the part will be formed as per the AM process. In the case of investment casting, the mould has to be prepared, which is a lengthy process involving the creation of wax patterns that are then dipped in a slurry and hardened. The wax is then melted out and the mould remains. This process is time consuming and restricts the freedom of altering the design of the parts. As the parts become bigger in size, investment casting tends to be more favourable as using AM to manufacture a large part will take a long period of time to complete. Furthermore, the size of the AM machine will have to be increased to form bigger parts.

Casting processes also consist of the liquefaction of the entire metal or alloy which is then poured into the desired mould. A phenomenon that can occur during this process is known as segregation which is the occurrence of a variation in the composition in alloy castings. This can affect the properties of casted materials negatively [26]. During the solidification process, there is relative movement of segregated liquid and solid phases. Most of the alloying elements display lower solubility in the solid phase than the liquid phase. As a result, during solidification the solute atoms are rejected by the solid phase into the liquid phase continually which leads to an enrichment of liquid phase and hence, the solid phase has a lower concentration of solutes. This ultimately results in the uneven composition of

the material when solidified and is difficult to rectify unless the part is re-melted. An uneven composition is not ideal for a high-performance part such as a turbine. AM however, melts each layer of the powdered material to construct the part. Therefore, segregation is not an issue since the melt pool of the AM process is very small. It may be possible for local segregation to occur within the melt pool as the powders are melted, however solidification occurs so rapidly that the segregation effect will be significantly less.

Investment casting is a carefully controlled process in terms of the rate and type of solidification. As mentioned above, segregation can occur during the solidification process of casted alloys. Alloys that are casted and left to cool naturally with no special heat control produce polycrystalline microstructures which consist of many grains throughout the solidified alloy. Another technique used during the solidification process is known as directional solidification. This process is completed by cooling the casted material evenly from one end of the casting to the other to achieve single grain or columnar grain structures. This flexibility in solidification practice gives a great amount of freedom to the design of turbine blades since the microstructure can be tailored in different ways depending on the application. In the case of AM, the rate of cooling cannot be controlled as freely when compared to casting. Parameters such as the scanning speed of the laser can partially affect the rate of solidification but not to the extent of temperature control during the solidification of castings [27]. This lack of solidification control ultimately leads to a set microstructure with high levels of residual stress, as mentioned in Section 2.8.4 and can affect the mechanical properties of the alloy. The fine grain microstructure however, can be beneficial in AM parts since the higher number of grain boundaries present in the material can obstruct crack propagation [28]. AM produced materials also develop columnar grains, as shown in Figure 2.22 and Figure 2.23 since the cooling occurs in a directional sense from the bottom upwards, but the amount of cooling control is less than that of conventionally casted materials.

Quantity, time and part accuracy are key factors in determining which manufacturing procedure is more suitable for the application of micro gas turbines. As shown in Figure 2.6, investment casting is not able to meet the dimensional accuracy and surface finish requirements of such a critical component of the gas turbine. Therefore, AM is considered since it is able to produce the part with the required accuracy. In 2017, Siemens successfully performed a full load test on additively manufactured gas turbine blades [q]. The blades were attached to a 13 MW SGT-400-type industrial gas turbine and tested at full load for one hour. An image of the manufactured blade is shown in the figure below.

Figure 2.26: AM produced blade by Siemens [q]

The overall time period associated with the design to production was reduced significantly from two years to two months.

2.10. Heat treatments

In the case of additive manufacturing, the parts have not been cast and formed into their net shape as per conventional manufacturing procedures. These parts have transformed from an atomized powder to the near net shape by means of a concentrated laser beam. Therefore, it is questionable whether a homogeneous distribution of precipitates can be achieved during the AM process in order to deliver effective creep resistance at the elevated that will be experienced in a gas turbine. In this context, homogenisation refers to the uniformity of the microstructure where there is an even distribution of all alloying elements and precipitates within the material and a reduction or complete elimination of Laves phase. Solidification of the melt pool occurs rapidly, and this can result in high levels of residual stress to be present in the finished product due to a large thermal gradient in the solidified material. The residual stress can be removed by means of a heat treatment as mentioned above in conjunction with homogenisation. The general procedure involved in precipitation hardening for nickel-based superalloys involves a solution treatment in which the alloy is heated within the range of 1050 – 1200 °C (depending on the alloy) to achieve a single-phase region. This aids in the removal of dislocations and homogenises any solute segregation that may have occurred. Thereafter the alloy is quenched or cooled in air to form a supersaturated solid solution. Quenching results in a high vacancy concentration as well as super saturation, which acts as a driving force for the nucleation and growth of second phase particles upon the addition of further heat treatment in the form of ageing. An aging process then follows during which the supersaturated solid solution is decomposed into two phases to form fine precipitates and occurs within the temperature range of 850 – 1050 °C. Depending on the superalloy and its composition, a second ageing procedure can be performed at a lower temperature than the first. The initial solution treatment allows for the existing γ’ and carbides to dissolve. The first ageing process then allows the γ’ phase that was formed during quenching or cooling to coarsen and to precipitate more γ’. If a second ageing process is performed, then finer γ’ phase will precipitate.

Thöne *et al.* [29] showed that Ti-6Al-4V produced by SLM possesses a fine laminar structure with internal stresses in the as-built state. Heat treatments applied to Ti-6Al-4V produced via SLM resulted in a reduction in the existing internal stresses that occur due to the fluctuating temperatures during the manufacturing procedure, and an increase in the laminar structure size is achieved. It was also shown that the microstructure of the material was changed with the use of higher temperatures and a longer annealing time [29]. This study shows that, with the application of a post-production heat treatment, it is possible to change the microstructure of parts produced by SLM to gain more favourable characteristics that can aid during service of the part. Heat treatment has also been seen to effectively reduce the effect of build orientation on Ti-6Al-4V manufactured by DED by homogenising the directional porosity and microstructure of the material as determined by Bian *et al.* [13].

S. Raghavan *et al.* [20] conducted a study on the effect of heat treatment on the microstructure and mechanical properties of IN718 manufactured by SLM, which is similar to the purpose of this project. It was seen that exposing the as-built specimens to the same solutionising temperature (1040 °C) results in the same grain structure and segregation levels. Increasing the solutionising temperature (1100 °C and 1200 °C) increases the homogenisation of elements and the level of segregation dropped however, the grains remain columnar and coarsen with the increase in temperature. As-built specimens displayed greater ductility than that of the heat-treated specimens since the heat treatments allowed for precipitation of the secondary phase and hence the material was strengthened. Further increase of temperature resulted in a reduction of the volume fraction of secondary phases as these phases were dissolved into the matrix again. This results in a strength

reduction but an increase in ductility. These heat treatments could potentially be applied to this project as the effect could be similar between the as-built and heat-treated specimens.

According to Huang *et al.* [23], the greater the solutionising temperature for SLM produced IN718, the more likely it is for complete recrystallisation to occur as well as coarsening of the grains. This is shown in Figure 2.27 below.

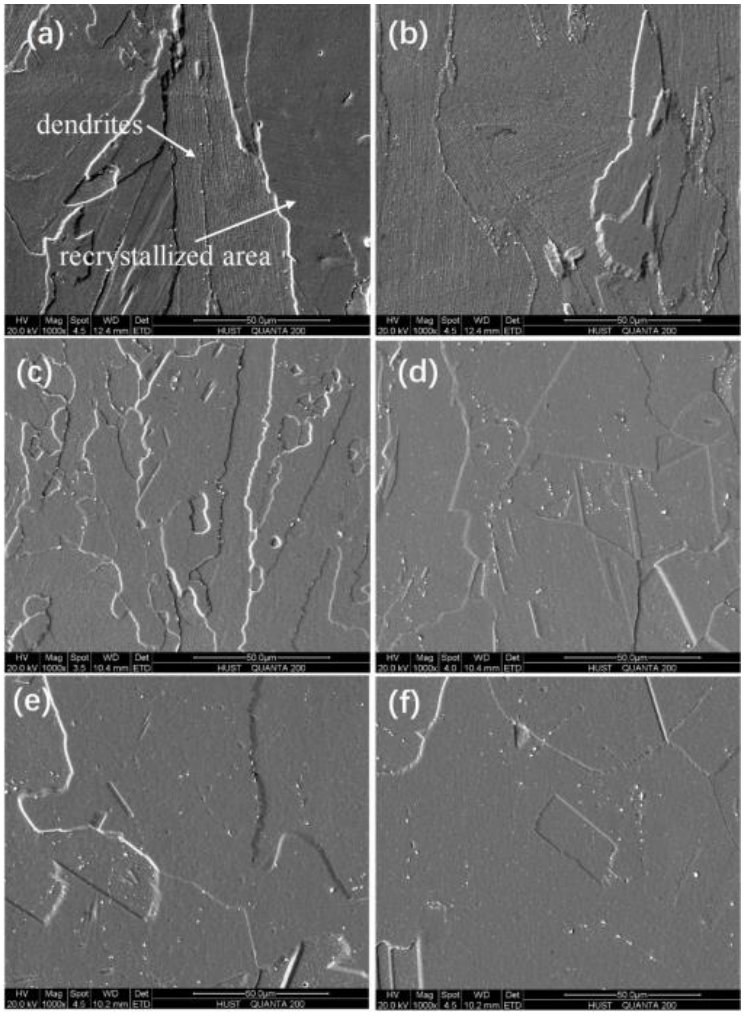

Figure 2.27: Microstructure of IN718 as a result of increasing solutionising temperature [23]

In Figure 2.27 above, the images (a) to (f) are in order of increasing solutionising temperature. The difference in grain structure can be seen in these images where dendrites are more visible in (a) and (b), and in the remaining images, the microstructure becomes more homogeneous. This type of microstructure is expected in SLM produced IN718 and can also be expanded to other AM procedures such as DED.

The microstructures of additively manufactured nickel-based superalloys are highly dependent upon the thermal history of the material. As compared to their wrought counterparts, the AM alloys undergo rapid temperature fluctuations during the building process. Standard heat treatments that were developed for wrought materials can be applied to AM materials and the effects of the heat treatments can be seen within minutes. This is due to the relief of residual stress after the building process when the temperature is increased. For IN718, the Vickers hardness values differ between as-built, solutionised, and aged [30]. Figure 2.28 displays the effects of various heat treatments on the hardness of IN718.

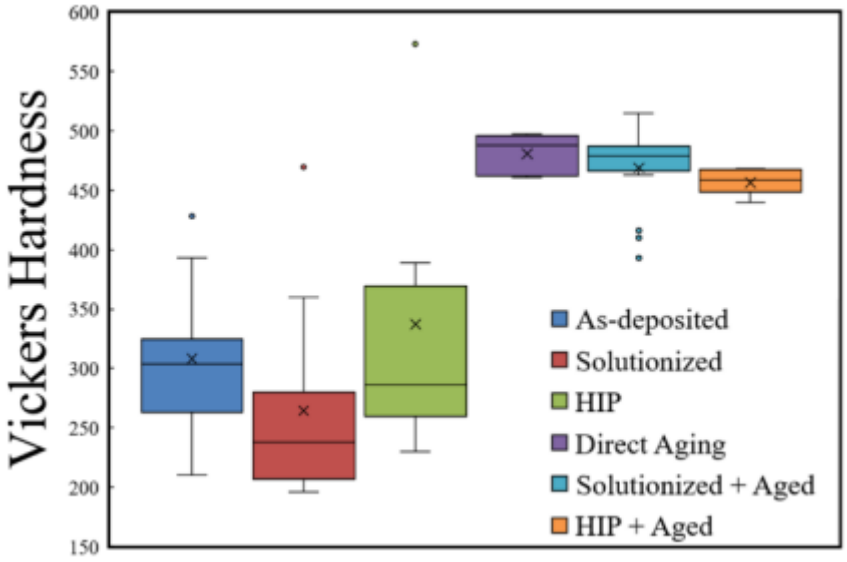

Figure 2.28: Variation in Vickers hardness of AM produced IN718 as a result of material condition [30]

The as-built hardness of IN718 is higher than that of solutionised IN718 at 980 °C for 1 hr as the solutonising treatment restores some ductility to the material. A solutionising and aging procedure is seen to significantly increase the hardness of the material due to the nucleation and growth of γ' and γ'' precipitates. This is a double aging procedure at 720 °C for 8 hours followed by 620 °C for 8 hours [30].

A hot isostatic pressing (HIP) procedure has also been proven to enhance the properties of casted IN713LC. Chang [31] proved that a HIP process at 1180 °C, 175 MPa for 2 hours allowed for a decrease in porosity, increased in density, increase in hardness and improvement in the tensile strength, 0.2 % yield strength and elongation, as compared to the as-casted and standard heat treated IN713LC material. The HIP process allows for these superior properties to be developed as finer γ' was precipitated during this process which promotes further strengthening. The HIP process will not be further investigated in this project.

The tensile properties of IN718 manufactured by AM processes differ from that of the wrought material in the as-built condition, but this difference is reduced significantly after a heat-treatment process as seen by Wang *et al.* [32]. The UTS of SLM produced IN718 was seen to be in the range of 1137-1148 MPa in the as-built condition, whereas in the heat-treated condition, the UTS was seen to be in the range of 1280-1358 MPa. The wrought material was seen to have a UTS in the range of 1275-1400 MPa. From this study, it can be seen that the gain in UTS after the heat-treatment was approximately 200 MPa and the heat-treated material displays comparable tensile properties to the wrought material. The heat-treatment protocol used for this study a solution treatment (980 °C for 1 hour, air cooling), followed by double ageing (720 °C for 8 hours, furnace cooling and 620 °C for 8 hours, air cooling).

2.11. Fracture mechanics

Fracture mechanics provides a quantifiable understanding of the manner in which a crack will propagate in a material as a result of an existing flaw in the material itself. These flaws will magnify the stress in the region of the crack, and this results in accelerated failure of the material when exposed to loading. Fracture mechanics is based on the stress intensity factor (SIF), which is a function of the applied stress and the crack size and geometry, which will be outlined in Section 2.11.1. There are two approaches to fracture mechanics that are dependent in the type of material. These

approaches are the linear elastic fracture mechanics (LEFM) approach and the elastic plastic fracture mechanics approach (EPFM) approach. These two approaches will be outlined below.

2.11.1. Stress intensity factor

The stress intensity factor is important in fracture mechanics as it describes the stress state at the tip of a crack [r]. This stress state is based on the applied load and the geometrical conditions. In parts or components that contain stress concentrations, the stress intensity factor at these stress concentrations is greater. This is shown in the figure below in terms of load-flow lines [33]. The concentration of load lines in the area of the notch is increased significantly. This concentration of load lines can be otherwise referred to as a stress concentration which is why sharp corners are generally avoided in mechanical design. This is illustrated in Figure 2.29 below.

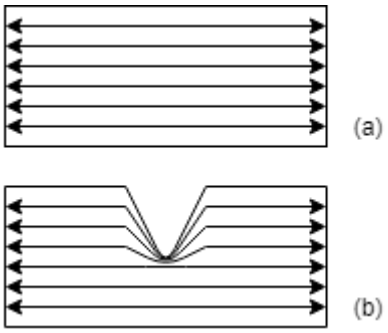

Figure 2.29: Load flow lines highlighting stress concentrations

The sharper the tip of the notch, the lower the radius of the tip and the greater the stress gradient experienced at the tip. Theoretically, if the tip were to have a radius of zero, the stress at the tip would approach infinity but since every corner has a finite radius, this is not the case. Therefore, the stress concentration is intensified by the geometry of the tip and this is known as the stress intensity factor, K. The stress intensity factor can be calculated by use of Equation 2.1 below.

$$K = Y\sigma\sqrt{\pi a}$$

Equation 2.1: Stress intensity factor

In Equation 2.1 above, σ is the applied stress, Y is a geometrical modification factor and a is the crack length. This is most commonly measured in $MPa\sqrt{m}$.

A stress analysis on a compact tension specimen performed in Solidworks is shown in Figure 2.30. This illustrates the stress distribution and stress intensity at a sharp notch. The compact tension specimen will be elaborated on in the next section.

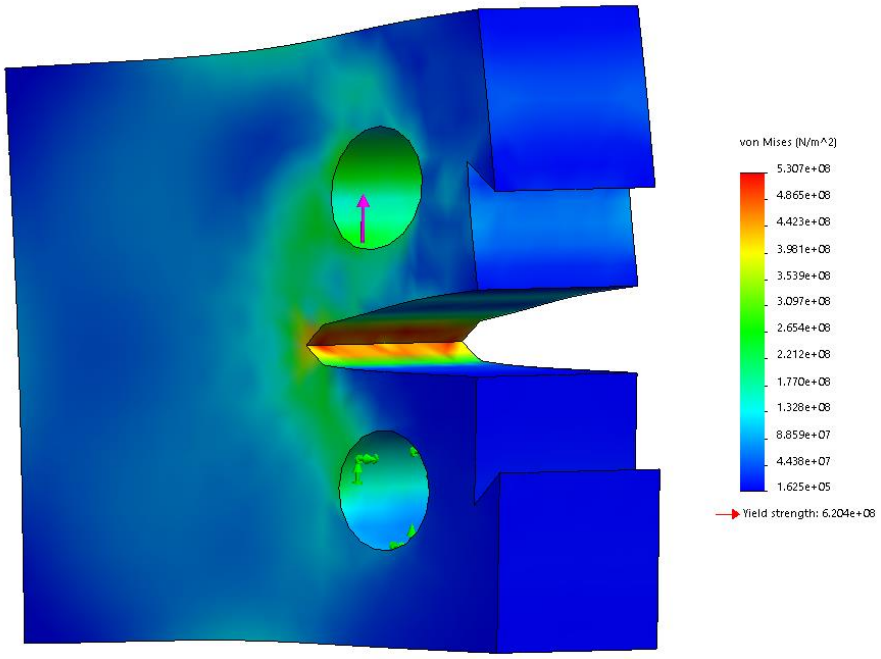

Figure 2.30: Solidworks stress distribution simulation

In Figure 2.30 above, the stress distribution of a compact tension specimen subjected to a tensile load can be seen. The red region represents the area of highest stress which is expected since the notch tip is an area of high stress concentration. The deformation seen in the figure is highly exaggerated. This simulation was performed on a stainless-steel alloy with a yield strength of 620 MPa and exposed to a load of 8 kN.

2.11.2. Fracture toughness

Fracture toughness is an important material property when designing mechanical components as it gives an indication of how resistant a material is to crack growth. A material with a high fracture toughness is less likely to undergo brittle fracture. Fracture toughness consists of three different modes which occur under different types of loading. These modes are shown in Figure 2.31.

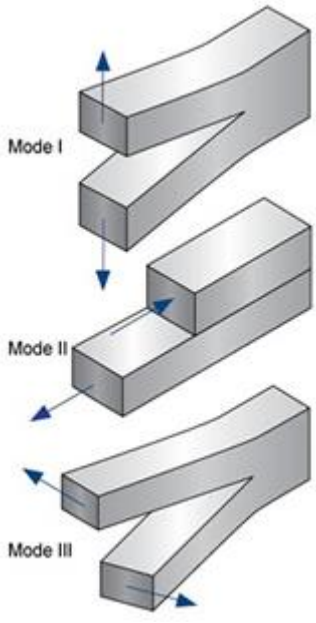

Figure 2.31: Three modes of fracture [s]

Mode I fracture is the most common since the crack plane is normal to the direction of the greatest tensile loading and will be investigated in the current study. The specific details to the different methods of analysis will be shown in the subsections below.

2.11.2.1. Linear elastic fracture mechanics (LEFM)

The LEFM approach is taken when the material behaves in a linear elastic manner. This means that the material exhibits little to no ductility during fracture and where the plasticity of the material is very small in comparison to the size of the crack or flaw. The fracture toughness that is determined using the LEFM approach is known as K_{1C}.

In fracture toughness testing, thicker test specimens give a more accurate representation of the material's true fracture toughness, known as the plain strain fracture toughness. This value is desirable as it is independent of the material thickness. The specimen is valid for plain strain fracture toughness if the thickness, *B*, is greater than or equal to half the width, *W*, of the specimen. Further requirements of the determination of a materials K_{1C} can be found in the ASTM E399 test standard [15]. Figure 2.32 below shows the relationship between thickness and fracture toughness K_C, which is dependent upon thickness.

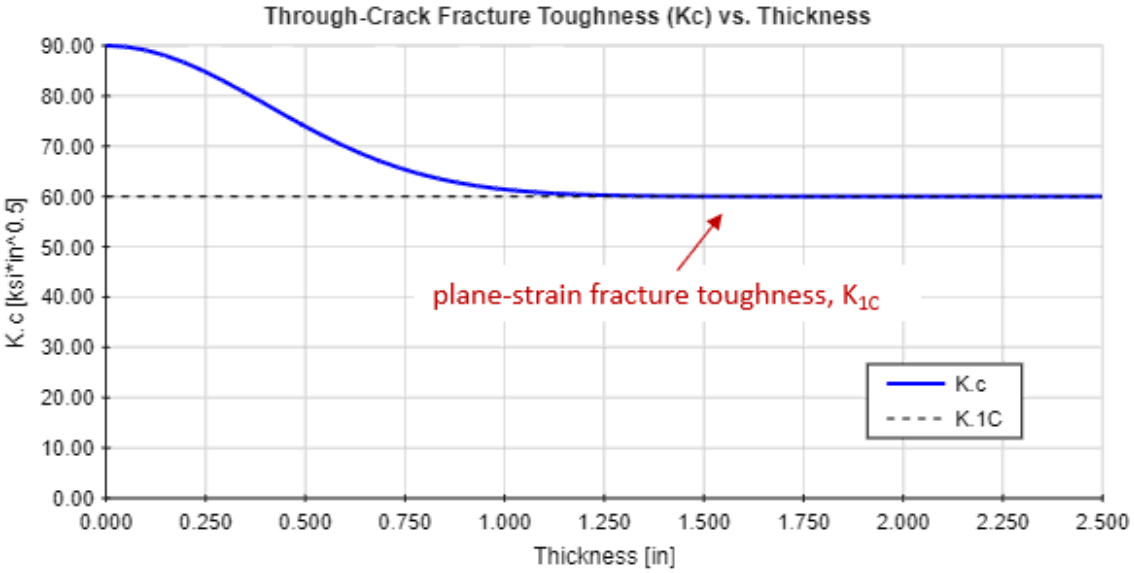

Figure 2.32: Effect of specimen thickness on fracture toughness result [t]

It can be seen in Figure 2.32 above that the fracture toughness K_C is higher for thinner sections and begins to decrease as the section thickness increases until ultimately reaching an asymptote. This asymptotic value is the plain strain fracture toughness and is known as K_{1C}, and is an important value that is used in design and analysis in engineering problems. Thicker sections result in a stress-strain field in the crack tip to transform from the plane stress state to the plain strain state. This means that tension is experienced in three directions at the crack tip and the plastic zone will be limited. Therefore, there is a higher likelihood of brittle fracture occurring rather than ductile fracture and hence the fracture toughness is lower for thicker sections [34].

For gas turbine engine components, a material with a high fracture toughness is generally desired to aid in the resistance of crack initiation and propagation [35]. The plain strain fracture toughness is determined by performing a fracture toughness test according to ASTM E399 test standard.

The fracture toughness of AM parts can significantly differ from their wrought counterparts due to the differences in the manufacturing parameters. High cooling rates of AM produced parts can result in

the material being more brittle and hence having a low fracture toughness. The fracture toughness of SLM produced Ti-6Al-4V was seen to be slightly less than conventional production methods even though the densities were the same, due to the metastable microstructure with a fine martensitic phase which is known to be brittle [28]. Rapid solidification can cause the material to become brittle and therefore have a lower fracture toughness, but the fracture toughness can be increased by preheating the building chamber and platform, as well as by performing a post-manufacture heat treatment to increase ductility.

There is not an abundance of literature pertaining to the K_{1C} fracture toughness of the Inconel family. According to MechaniCalc [u], the K_{1C} of IN718 that has been solution treated and aged was seen to be 87.907 $MPa\sqrt{m}$. There is a similar study that investigates the fracture toughness of SLM produced Ti-6Al-4V that was mentioned in Section 2.8.3 [17]. Fracture toughness values for the Ti-6Al-4V cannot be used directly to gauge the fracture toughness of Inconel however, the way that fracture toughness is influenced by the build orientation can be taken note of. The as-built fracture toughness results showed the most noticeable deviations in K_{1C} value which was a result of the anisotropic residual stress distribution. The as-built XY, XZ and ZX build orientations showed K_{1C} values of 28, 23 and 16 $MPa\sqrt{m}$ respectively.

K_{1C} fracture toughness values for cast aluminium alloys commonly range between 20 and 30 $MPa\sqrt{m}$, whereas steel castings can have a range of K_{1C} fracture toughness values between 40 and 250 $MPa\sqrt{m}$ depending on the percentage composition of the alloying elements, such as carbon [36]. For nickel alloys, K_{1C} fracture toughness values range between 80 and 110 $MPa\sqrt{m}$ [37]. These K_{1C} values are provided for reference.

2.11.2.2. Elastic plastic fracture mechanics (EPFM)

In the case where there is extensive plastic deformation of the material prior to fast fracture, if fast fracture even occurs, then the linear elastic fracture mechanics approach, in terms of K and K_{1C}, is invalidated. The LEFM approach applies primarily to samples with a high yield stress, very thick sections and a small plastic zone. Elastic plastic fracture mechanics (EPFM) is to be applied to materials that do not behave in this regime. To determine a definitive K_{1C} for materials that behave in a ductile manner, large test specimens are required, and this could be a costly process, which is why EPFM is considered. Possible methods for EPFM include the crack tip opening displacement (CTOD) and the J-integral.

2.11.2.2.1. Crack tip opening displacement

The *CTOD* refers to the opening displacement or movement at the original crack tip position. This can be seen in Figure 2.33 below.

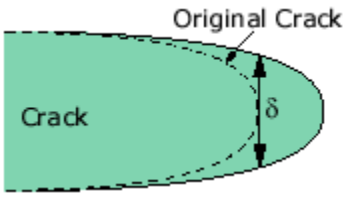

Figure 2.33: Crack tip schematic showing CTOD (δ) [v]

This method provides a characterisation of a material's fracture toughness through the crack tip opening displacement and can be conducted in accordance with ASTM E1290 or BS 7448: Part 1. The test method is identical to K_{1C} determination however, the method of analysis is different. The CTOD result for various test specimens can be compared with each other to determine the differences

between the fracture toughness of materials. According to Yeni *et al.* [38] the CTOD *(δ_m)*, which corresponds to the maximum load experienced during the test, was seen to be 0.89 mm for IN718. The determination of the CTOD requires the yield strength, Young's modulus and Poisson's ratio to be known. Therefore, experiments will have to be performed to determine these properties if they are not available for the material of interest. This test method has been withdrawn by ASTM as of 2013 and therefore, will not be used as a method of analysis in this study.

2.11.2.2.2. J-integral

The J-integral provides an expression of a material's fracture toughness in terms of energy per unit of crack area. The test procedure for J-integral testing is conducted according to ASTM E1820, which is the standard test method for measurement of fracture toughness. This test method is the same as the K_{1C} and *CTOD* test procedure where the fatigue pre-cracked specimen is loaded in tension until it breaks, however, the analysis of test results is different when compared to the K_{1C} and *CTOD tests*. The load line displacement is recorded during the test and the displacement versus load curve is plotted. An example of this can be seen in Figure 2.34 below.

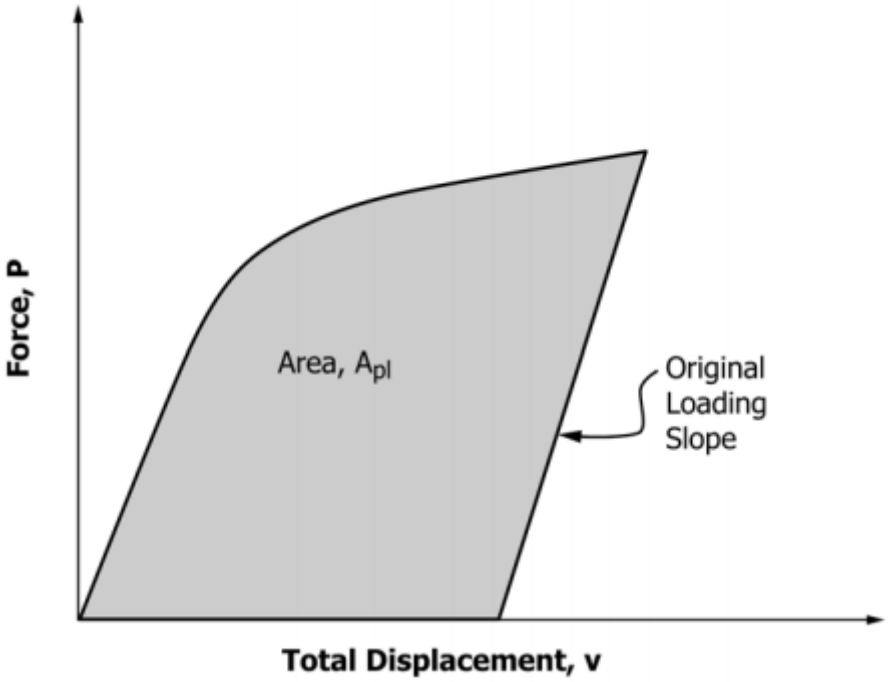

Figure 2.34: J-integral load line displacement vs load graph [39]

Figure 2.34 above is adapted from ASTM E1820. The area under the curve acquired from the test data is determined and is used to calculate the fracture toughness J_m that is the value of *J* that corresponds to the maximum load experienced during the test. This is adapted from BS 7448: Part 1.

Both the *CTOD* and J-integral methods can be used to determine the fracture toughness of the material in terms of different metrics, such as displacement and energy per unit displacement respectively. Both methods are also beneficial for the current study as the current study is a comparative one. Determination of a fracture toughness value such as J_{1C} is not applicable to this study as it requires the determination of a resistance curve (R-curve), which is beyond the scope of this project due to the method's high demand of test specimens. Ganesh *et al.* [40] performed J-integral fracture toughness tests on LRM (laser rapid manufactured) IN625. The J-integral fracture toughness was seen to be 225-255 kJ/m^2 and 196 kJ/m^2 for 12 mm and 25 mm compact tension specimens respectively.

2.12. Fatigue

Fatigue occurs when a material undergoes a prolonged exposure to loading, which in turn can influence the integrity of the material. The fatigue properties of a material are of great interest especially for the application of turbine blades. This is as a result of the constant cyclic loading experienced by the rotating parts of the gas turbine engine which generate stresses that are below the yield stress of the material. The stresses should not result in the failure of material but since fatigue occurs over a long period of time, the time factor cannot be negated. If the fatigue properties of the material are not known, catastrophic failure of the component can occur without warning. Failure due to fatigue generally occurs in sequential process. Micro cracking will usually occur at stress concentrations in the component, areas with sharp corners or material discontinuities due to the manufacturing procedure. The micro crack will then begin to grow if the part continues to experience a fluctuating load. In the case of an oscillatory tensile load, the crack will grow in the direction orthogonal to the applied load. The growing of the crack is known as crack propagation and propagation will continue until the remaining cross-sectional area of the un-cracked part is not able to support the load. Once this critical point is reached, fracture will suddenly occur. Crack formation is shown in Figure 2.35 below.

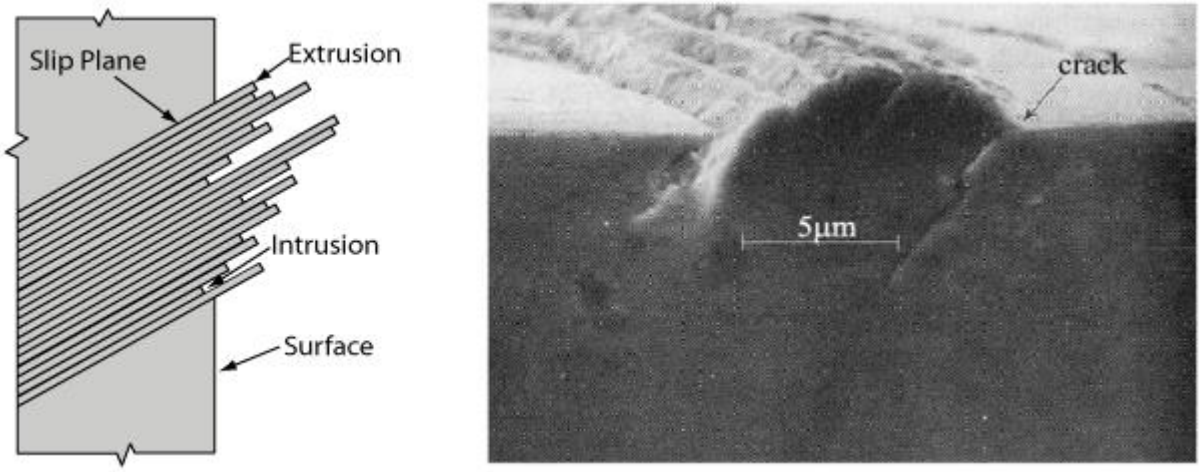

Figure 2.35: Crack formation [w]

Cracks that occur in the material often cannot be seen or noticed without a thorough inspection of the material. When designing a component to be used in some industrial applications, it is necessary to theoretically compute the fatigue properties by performing calculations in order to estimate the number of cycles a part can withstand based on the type and magnitude of the loading.. The fatigue performance of SLM manufactured specimens have been shown by Spierings *et al* [41]. to be significantly lower than that of wrought alloys [41]. In conjunction with this, it was also shown that the porosity of the manufactured part was one of the contributing factors that decreases fatigue life, linked back to the density of the part as well as the processing parameters. Improvement of the surface condition and residual stresses within SLM manufactured parts can result in a better fatigue performance [25]. SLM produced parts do not behave well under fatigue in the as-built condition as a result of voids and production defects connecting during loading, whereas with conventional production processes, the crack propagation usually results due to microstructure changes [42]. This can also be applied to the DED process as similar microstructures develop from both SLM and DED processes.

The fatigue crack growth rate is the rate at which the crack will move through the material when exposed to a fluctuating load. It is crucial to know or at least obtain an estimate of the fatigue crack

growth rate in order to understand how quickly the crack will propagate through the material for a specific loading. This will give an indication of the mechanical properties of the material as well as the type of microstructure that the material possesses. For example, a crack may propagate much more quickly through a material in which the grains are aligned parallel to the direction of the crack growth as compared to grains that are aligned perpendicularly to the direction of crack growth. With this comparison in mind, the same can be applied to parts produced by AM as the build orientation could potentially affect the way in which the crack propagates. Since the laser melted part is comprised of layers, the boundaries between layers could be seen as weaker points and analogous to grain boundaries and the crack could propagate along these lines. This is show graphically in Figure 2.36 below.

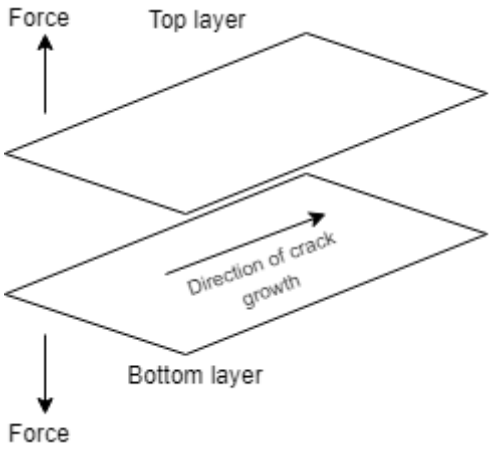

Figure 2.36: Applied load normal to AM layer deposition

Fatigue crack growth rate testing can be performed by using a suitable testing machine capable of producing a fluctuating load at a desired magnitude and frequency. The specimens used for this type of test are known as compact tension specimens. An example of this specimen is shown in Figure 2.37 below.

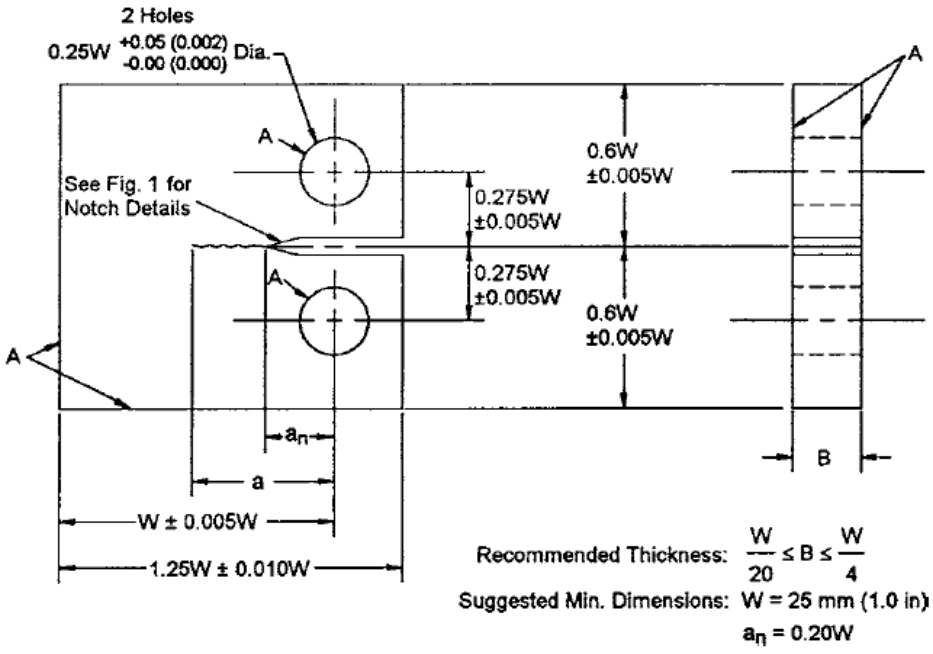

Figure 2.37: FCGR CT specimen geometry constraints [43]

The compact tension specimen consists of a notch that tapers to a well-defined crack tip. The dimensioning of the specimen adheres to ASTM E647, which is the test standard for the measurement of fatigue crack growth rates. Validity requirements of the FCGR test can be found in the test standard (E647).

The crack tip of the specimen acts as a stress concentration and hence crack initiation will occur at that specific point. The crack will then propagate in the direction orthogonal to the applied load. The crack propagation is shown and exaggerated in Figure 2.38 below.

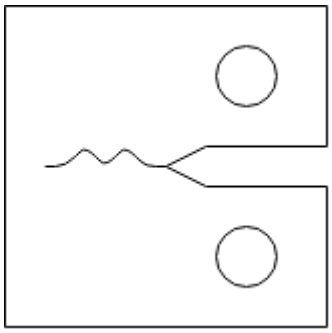

Figure 2.38: Direction of crack growth in CT specimen

The propagation of the crack must be monitored closely in order to observe any deviations in the crack direction as well as to monitor the rate of crack growth. This can be calculated by monitoring the change in crack length and the change in number of cycles. This is shown in Figure 2.39 below.

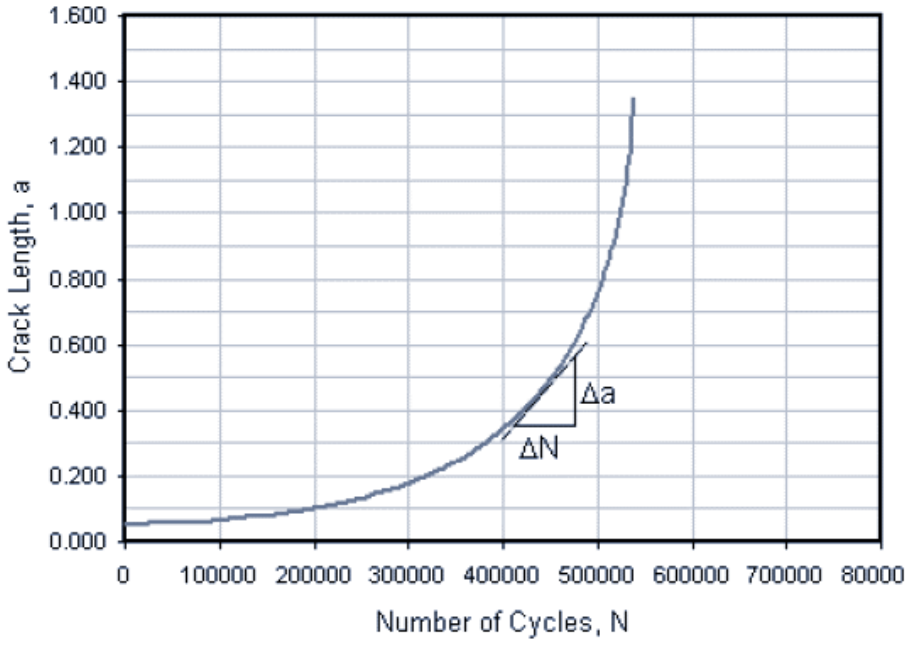

Figure 2.39: Example of number of cycles vs crack length graph

In Figure 2.39 above, the number of cycles has been plotted against the fatigue crack length. The gradient of the resulting curve represents the fatigue crack growth rate, $(\frac{da}{dN})$, as shown on the plot above.

Fatigue crack propagation can be divided into three main stages namely the crack initiation (I), stable crack growth (II) and finally unstable crack growth or fast fracture (III). Figure 2.40 shows these three stages in terms of the Paris curve.

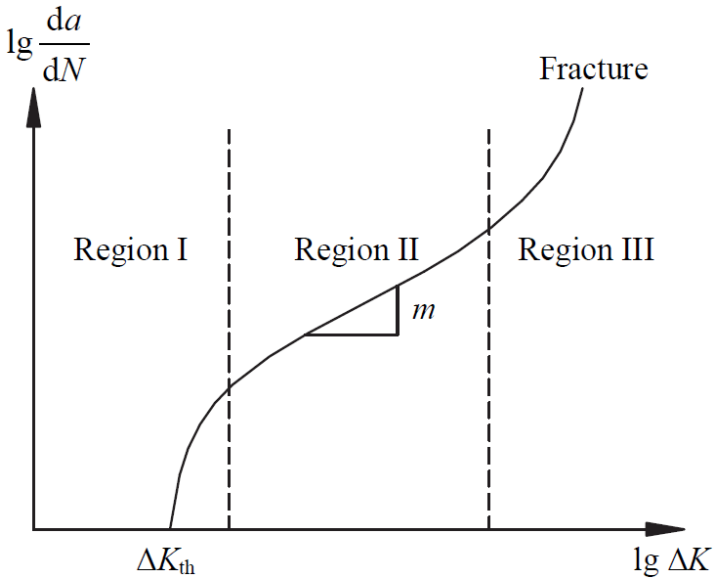

Figure 2.40: Paris curve [44]

The Paris curve is shown above in Figure 2.40 and is placed on a log-log scale. This scale is used because the crack propagation does not display a linear trend. At the beginning of the test, the crack growth rate can be extremely low but as the crack propagates, the crack growth rate can increase dramatically. The Y-axis of this graph is the crack growth rate, ($\frac{da}{dN}$), which is measured in unit of length (usually meters) per cycle. The X-axis is the stress intensity factor range, ΔK, which was explained in Section 2.11.1. The equation for calculating ΔK can be found in the ASTM E647 test standard.

The X-intercept of this curve is the fatigue threshold (ΔK_{th}), which represents the value of stress intensity below which a crack will not grow. Region II refers to the stable growth of the crack and is known as the Paris region. This linear relationship exists on a log-log scale and can be represented by Equation 2.2.

$$\frac{da}{dN} = C(\Delta K)^m$$

Equation 2.2: Paris law

In Equation 2.2, *C* and *m* are parameters relating to the material of interest. *C* can be determined as the Y-intercept of the linear portion of the Paris region and *m* as the gradient of this linear line, as shown in Figure 2.40 above, on a log-log scale. In region III, unstable crack growth occurs and leads to fast fracture. This can be seen by the increasing gradient of the curve. Fracture occurs at a critical value of stress intensity, K_C. This is the value of stress intensity that limits the materials' performance and is known as the fracture toughness. Fracture toughness will be elaborated on more in the next section. The Paris region can be sub-divided into two separate stages namely stage A and stage B. According to the BS 7910:1999 guide on methods for assessing the acceptability of flaws in fusion welded structures, the Paris region can contain two stages of stable crack growth which correspond to different *m* and *C* values [45]. Figure 2.41 illustrates this relationship with stage A and B being the two stage Paris region.

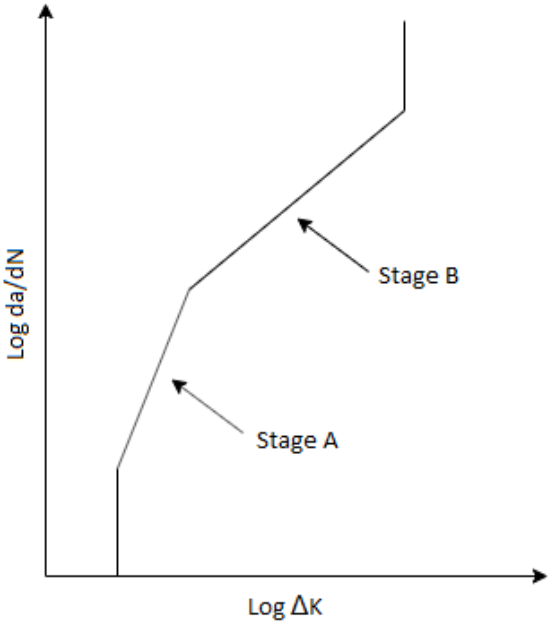

Figure 2.41: Two-stage Paris region

Another important factor to be considered prior to performing a fatigue crack growth rate test is the stress ratio, *R*, which is the ratio between the minimum and maximum stress or load experienced during the test. It is also commonly known as the load ratio. This ratio can define the type of loading conditions experienced during a test. Purely tensile conditions result for stress ratios greater than zero and less than 1. Reversed loading conditions result from stress ratios less than zero while, fully reversed conditions result from a stress ratio of -1. Reversed and fully reversed conditions imply that the specimen will be in compression and full compression at some point in the load cycle respectively. If the stress ratio is higher, then this implies that there is a greater load range (ΔP), which is directly proportional to the stress intensity range (ΔK), as shown in Equation 2.2. This results in a greater starting ΔK and hence the $\frac{da}{dN}$ vs ΔK curve will be shifted to the right and the crack growth rates experienced will be higher as compared to a lower stress ratio. This can be seen in Figure 2.42 below.

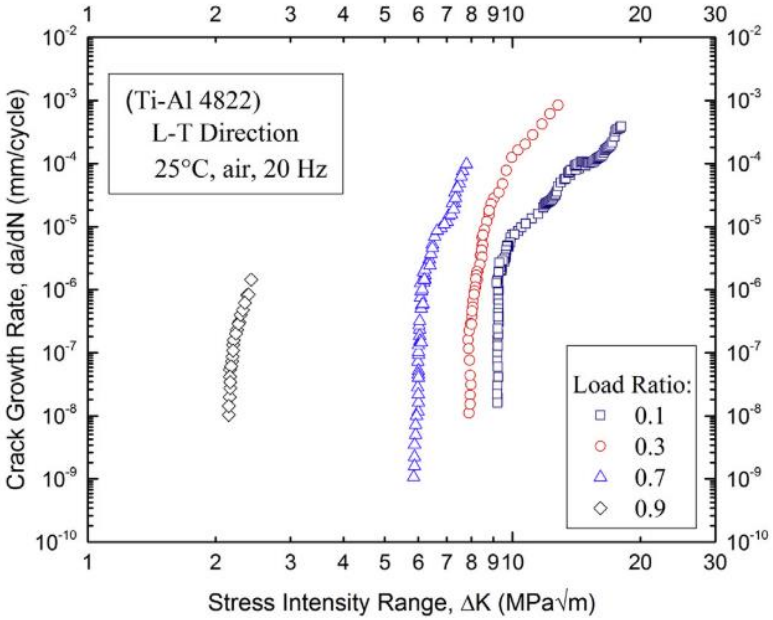

Figure 2.42: Effect of stress ratio on Paris curve [46]

Figure 2.42 is adapted from the work by Dahar *et al.* [46] and illustrates the effect of stress ratio on the fatigue crack growth rate data. This data represents a very brittle material with a low fracture toughness.

The life of a component can also be predicted using the Paris equation and the size of an existing flaw in the component. Equation 2.1 can be substituted into Equation 2.2 to obtain Equation 2.3.

$$N_f = \int_0^{N_f} dN = \int_{a_i}^{a_f} \frac{da}{C(\Delta\sigma Y\sqrt{\pi a})^m}$$

Equation 2.3: Component life

Equation 2.3 above can be integrated between the initial crack length and the critical crack length at failure and the number of cycles to failure can be obtained.

This information is important and beneficial as it provides an estimate of the number of cycles of a component to failure for a particular loading scenario and flaw size. This can allow designers to fabricate maintenance schedules and inspections ahead of time to prevent failure of components during service. It also provides insight to what defects and flaws are allowable in a component and how to manage these flaws throughout the duration of the component's life. The fatigue life of IN718 will not be investigated in this project.

Literature pertaining to the fatigue crack growth rate properties of DED produced IN718 or IN713 is limited, however, there is work on laser rapid manufactured (LRM) IN625 by Ganesh *et al.* [62]. LRM is type of additive manufacturing similar to DED and the LENS process in particular. This alloy is also a nickel-based superalloy but differs in composition to IN718 and IN713 as it contains a higher percentage of chromium and molybdenum and a lower percentage of aluminium. Fatigue crack growth rate tests were performed on this material. It was seen that the empirical constants "*C*" and "*m*" from the Paris equation were consistent under different test conditions implying that the material responded well to fatigue in the as-built state. The test results are shown in Table 2.3 below for reference.

Table 2.3: FCGR test results for LRM IN625 [62]

Material	Test conditions			C	m
	CT specimen thickness (mm)	ΔK range ($MPa\sqrt{m}$)	Stress ratio (R)		
IN625-LRM	25	14.0-25.0	0.3	3.23 E-12	5.21
IN625-LRM	12	21.0-31.1	0.1	1.48 E-12	5.42
IN625-LRM	12	27.6-36.6	0.1	1.95 E-12	5.33

These results show an improvement in the fatigue behaviour of the material, which could be due to the increase in yield strength of the material after the LRM process and the residual stress present in the material after building.

2.13. Fatigue crack measurement techniques

There are several techniques that are used to measure the length and monitor the propagation of the fatigue crack during fatigue testing. These techniques include laser interferometry, the alternating and direct current potential difference methods and optical methods. However, new experimental techniques are constantly being developed and tested, such as phased array ultrasonics for example,

which was used to measure the fatigue crack growth rate [x]. The ASTM E647 test standard recommends the compliance and potential difference method to measure the crack size as well as a visual method, which involves marking the test specimen at regular intervals to track the growth of the crack [43]. Most high precision modern techniques tend to be expensive. Compliance is a common technique used for measuring crack length and is calculated based on the crack opening displacement (COD). The COD is measured with the use of a COD gauge (clip gauge) and this data is captured and converted into a crack length based on the specimen dimensions and the material's elastic modulus.

The visual technique for the measurement of crack length is the simplest since it requires minimal equipment and attention during the fatigue test. The crack growth can be monitored using a stereo-microscope. A graticule is often inserted in front of the eyepiece of the microscope with an appropriate scale relative to the magnification of the lens. This aids in the measurement of the crack to a fraction of a millimetre. There is a limit to the accuracy of these microscopes since the measurement is performed whilst the test specimen is still attached to the test rig. Hence, the magnification is restricted slightly since the microscope needs to be small in order to move in and out of the test area. This introduces uncertainty into the measurement of the crack length at any given point. A proposed method to improve the accuracy of visual crack measurement techniques will be outlined in Section 3.4.

3. Methodology development

Before attempting to perform any tests on the nickel-based superalloy material, preliminary testing was performed on dummy specimens to practice and perfect the test method due to the high cost of the superalloy material. Fatigue crack growth rate and fracture toughness testing were performed during these preliminary tests according to the ASTM E647 and E399 test standards respectively. This portion of the project also aided in the optimisation of the testing procedure as well as allowing for the addressing of any uncertainties in factors, such as the specimen geometry, testing procedure and data collection. The visual crack measurement technique that was developed to obtain accurate crack length measurements will also be shown in this section.

3.1. Preliminary testing

Both fatigue crack growth rate and plain-strain fracture toughness tests were performed on the stainless-steel dummy specimens according to the ASTM E647 and E399 test standards. Testing was performed on the ESH servo hydraulic testing machine. A figure of the machine can be seen in Section 4.5. The preliminary test method and results for the FCGR and FT tests will be shown in this section.

3.1.1. Dummy specimen configuration

The dummy test specimens were machined from M201 stainless steel and were sized according to the ASTM test standards mentioned above. The stainless-steel material had an estimated ultimate tensile strength of approximately 880 MPa (based on the Vickers hardness value that was measured for the material). This allowed for an estimation of the yield strength to be about 750 – 800 MPa for the stainless steel, which is within a similar range to the wrought nickel-based superalloy yield strength in the non-heat-treated condition. As a result, the preliminary tests could provide a reasonable estimate of the behaviour of the nickel-based superalloy tests without having to waste an unnecessary number of superalloy test specimens.

Since this project involves a combination of fatigue crack propagation and fracture toughness testing, the geometry of the specimen is adapted to accommodate both tests in a single specimen. The geometry is shown in Figure 3.1 below.

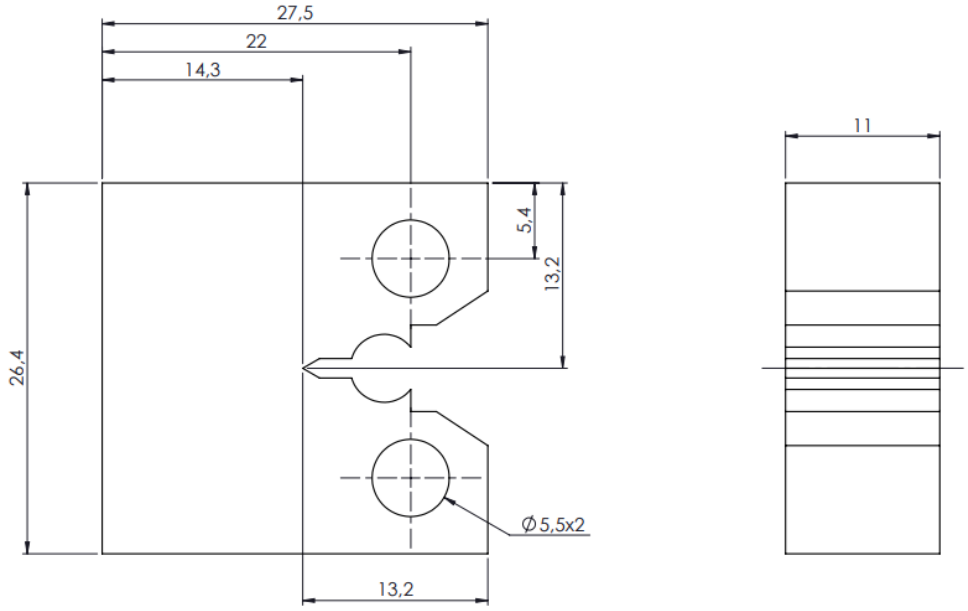

Figure 3.1: CT specimen with modified dimensions (in millimetres)

The details regarding the machining of these specimens are outlined in greater detail in Section 4 of this report. Fifteen dummy specimens were manufactured in the mechanical engineering workshop at the University of Cape Town according to the geometry shown in Figure 3.1 above.

Before testing of the dummy specimens, a surface preparation process is required. Each specimen was polished to a mirror finish to allow for the crack propagation to be clearly seen. The specimens were also marked at regular intervals to be used as reference points for the visual crack measurement process. This process is outlined in greater detail in Section 4.2.2.2 of this report. Sources of error in the accuracy relating to the marking process of the test specimens were identified and will be outlined in Section 3.4.

3.1.2. Fatigue crack growth rate

The dummy specimens were tested for a variety of different load ranges and *K* control procedures. The ASTM E647 test standard provides two different *K* control testing procedures, namely a K-decreasing procedure and a constant force amplitude procedure. For this project, a constant force amplitude procedure was used as it is most useful for crack growth rates above 10^{-8} m/cycle.

The initial tests were performed to provide a benchmark for the behaviour of the material as the fracture toughness was not known. A load range of 7.2 kN was initially used with a stress ratio of 0.1 and a frequency of 7 Hz. Fatigue cracks were grown to a length of 4 mm, which was in the range of 0.45W to 0.55W as specified by ASTM E399. Typically, a fatigue crack growth rate test would run until fracture of the specimen, but this is not possible for the current project as the specimen needs to be tested for fracture toughness as well. According to ASTM E399, a specimen is required to be pre-cracked in fatigue before the fracture toughness test is performed. Therefore, this initial pre-cracking will be used to obtain the necessary fatigue crack growth data for this project while maintaining the integrity of the test specimen for the fracture toughness test. The only issue with not growing the crack until fracture is that it will not be possible to obtain the full range of data. The results obtained during the preliminary FCGR tests will be shown below.

The first three specimens were used to obtain a consistent testing load range as well as to practice the crack growth procedure and to analyse and measure the crack growth rate during the test. This was performed by using a maximum load of 8 kN with a stress ratio of 0.1. The crack growth rate was maintained at approximately 1×10^{-4} mm/cycle. This was made possible by incrementally decreasing the load after a certain amount of crack growth and monitoring the stress intensity range during the test. The test data for specimen seven (SS7) is shown below in terms of a “number of cycles vs crack length” graph.

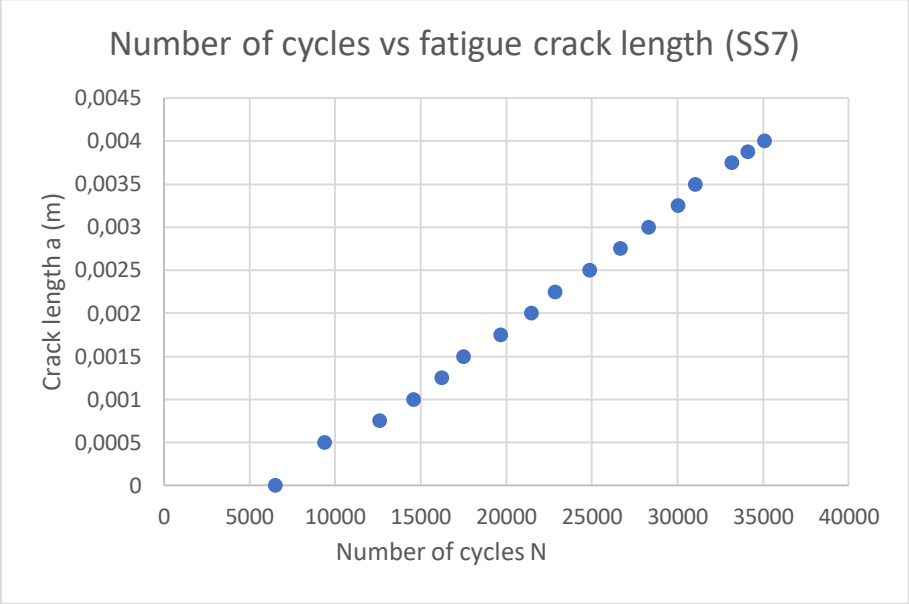

Figure 3.2: Number of cycles vs crack length for SS7

This graph is not characteristic of a general number of cycles vs crack length graph but this is expected in this case because the load range was changed as the crack growth rate increased. Therefore, the curve resembles a more linear trend as the gradient, wh2ch is the crack growth rate, is kept as constant as possible. It can also be seen that the curve can be broken up into smaller characteristic "*N vs a*" curves for their respective loading ranges as exaggerated in Figure 3.3 below.

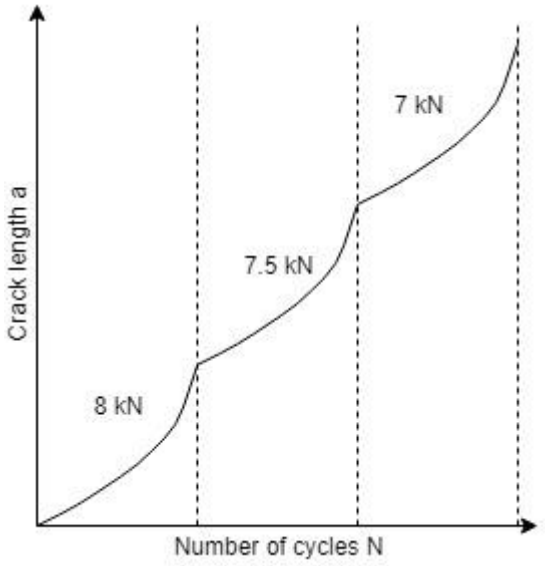

Figure 3.3: Schematic showing the effect of decreasing load on the FCGR test

The fatigue crack growth rate vs the stress intensity factor range was also plotted to obtain the required Paris data and is shown in Figure 3.4 below on a log – log scale.

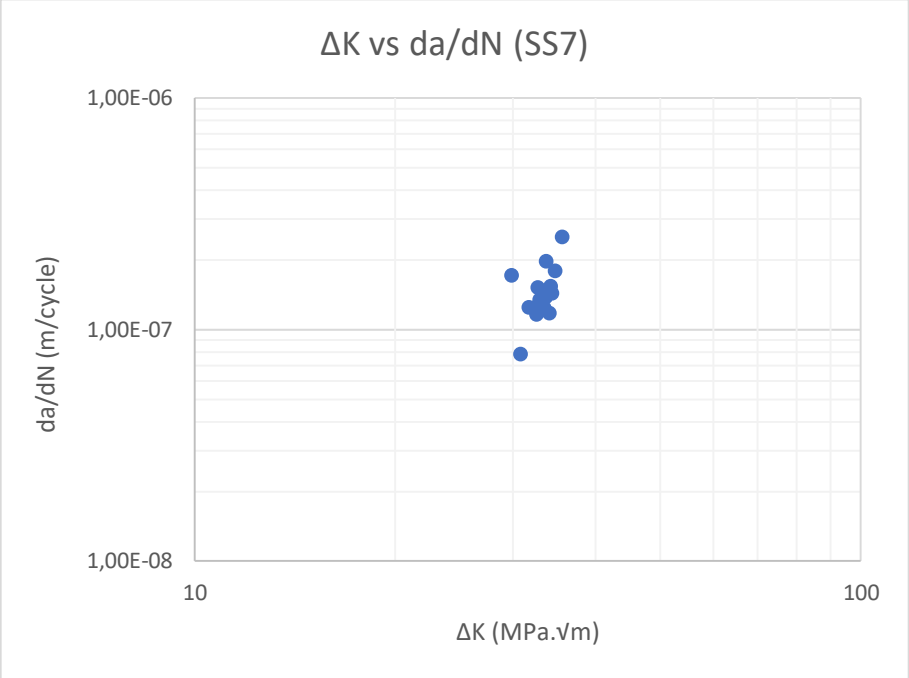

Figure 3.4: Paris curve for SS7

The graph above is not characteristic of the standard $\frac{da}{dN}$ vs ΔK data and this is due to the maintenance of the fatigue crack growth rate during the test. Since the load is lowered regularly, the corresponding fatigue crack growth rate would be different than if the load was kept constant and therefore, the Paris curve obtained is not a genuine Paris curve despite the similar resemblance.

Further testing of the M201 stainless steel dummy specimens was conducted under constant load conditions. This would give an indication of the data and trends to be expected during the testing of the superalloy material. Specimen nine (SS9) was tested at a maximum load of 6 kN with a stress ratio of 0.1. This resulted in a ΔP of 5.4 kN. The fatigue crack was grown to a length of 3 mm and crack growth rate and ΔK data were recorded. The *N* vs *a* curve is shown in Figure 3.5 below.

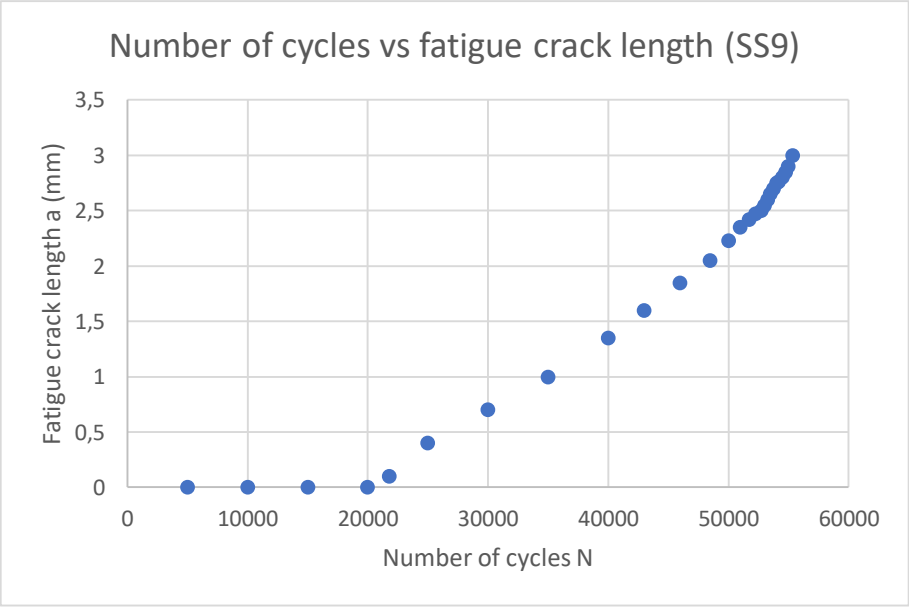

Figure 3.5: Number of cycles vs crack length for SS9

The curve above shows a more characteristic representation of the N vs a curve however, there it is difficult to obtain crack measurements in the early stages of crack initiation which is why the data lies on the X-axis for the first 20 000 cycles. Towards the top end of the graph, the data is recorded more frequently as the crack growth rate is higher and hence it takes a lower number of cycles to extend the crack further. Growth of the crack was terminated until the crack length was 3 mm in length which is within the ASTM E399 standard for fatigue pre-crack length. Figure 3.6 below displays the $\frac{da}{dN}$ vs ΔK data for the SS9 test on a log – log scale.

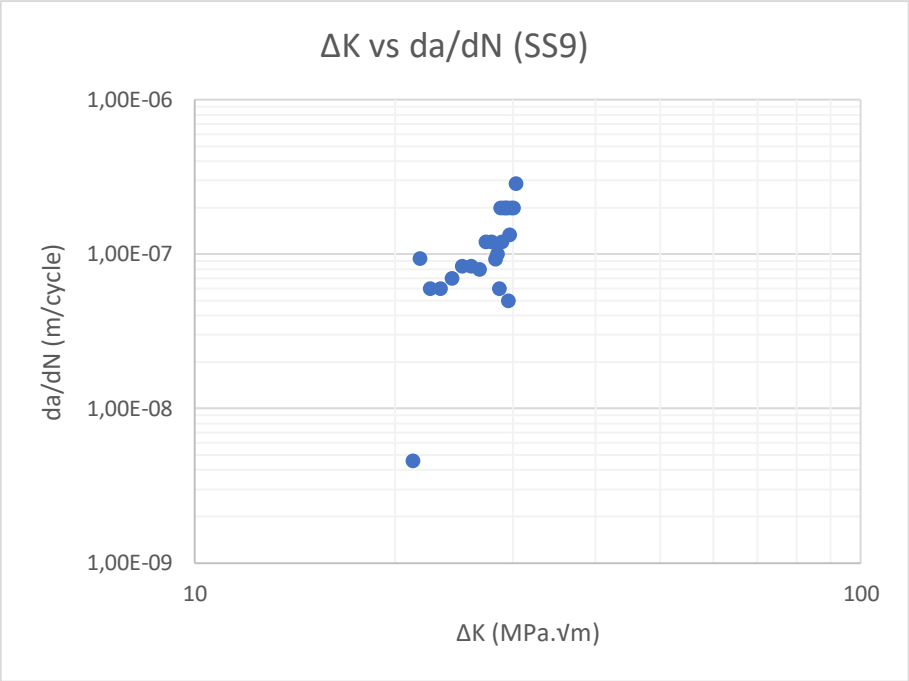

Figure 3.6: Paris curve for SS9

In Figure 3.6 above, it can be seen that there is a high level of scatter in the data points. This is as a result of the inaccuracies involved with measuring the crack length during the fatigue crack growth rate test. Since the crack growth rate is sensitive to change in crack length at a micron level, it is neither easy nor accurate to estimate the length of the crack using a stereomicroscope without a graticule or some sort of accurate measuring device. Accurate Paris data cannot be obtained from these results.

The specimens each had to pass the validity test for the results to be regarded as valid data. The validity check is governed by Equation 3.1.

$$(W - a) \geq \left(\frac{4}{\pi}\right)\left(\frac{K_{max}}{\sigma_{ys}}\right)^2$$

Equation 3.1: Validity check for FCGR test

In Equation 3.1, $(W - a)$ is the length of the uncracked ligament of the specimen, K_{max} is the maximum stress intensity factor and σ_{ys} is the yield strength of the material. It was seen that all fatigue tests conducted were valid based on a yield strength of 700 MPa, which was estimated from a Vickers hardness test.

The specimens were all tested in the mid-life regime as the total number of cycles was in the region of 10^3 to 10^5 cycles. This regime was carried through to the testing of the nickel-based superalloy specimens.

3.1.3. Fracture toughness

The fracture toughness test made use of the fatigue pre-cracked stainless-steel specimens. The basic principle of the test is to load the CT specimen in tension at a desired loading rate until fast fracture occurs. The existing pre-crack acts as a stress concentration and promotes stable tearing of the material as the stress intensity factor increases until the material fracture toughness is reached. Thereafter, the material undergoes fast fracture and the specimen fails. The specimen is then broken into two pieces in order to take measurements of the pre-crack for calculation purposes.

These tests are performed according to ASTM E399, which is the testing standard for plain strain fracture toughness of metallic materials. According to the test standard for CT specimens, the specimen is to be loaded in tension such that the rate of increase of stress intensity factor is within the range of 0.55 and 2.75 $MPa\sqrt{m}/s$. The ESH testing machine and the Instron software used for this testing does not have this type of load control and therefore a constant cross head speed was set. This increased the stress intensity factor accordingly. A variety of cross-head speeds were used for the testing of the dummy specimens to determine the validity of the tests according to the test standard (ASTM E399). These cross-head speeds were 0.25, 0.5 and 0.75 mm/min which equate approximately to 0.31, 0.62 and 0.87 $MPa\sqrt{m}/s$. These approximations were based on the time taken to complete each test as well as the value of K_Q as calculated using equation A4.1 from ASTM E399.

Before the test, the clip gage is mounted on to the knife edges, which are integral on the specimen. The clip gauge measures the crack opening displacement as the specimen is pulled apart. The force applied, cross-head displacement, time and the clip gauge displacement were recorded during testing. These results were then exported to Microsoft Excel and analysed for validity and to calculate conditional *K* values for fracture toughness. The M201 stainless steel dummy specimens that had been pre-cracked in fatigue were used for these tests and the test data is shown below for the three different loading rates mentioned above.

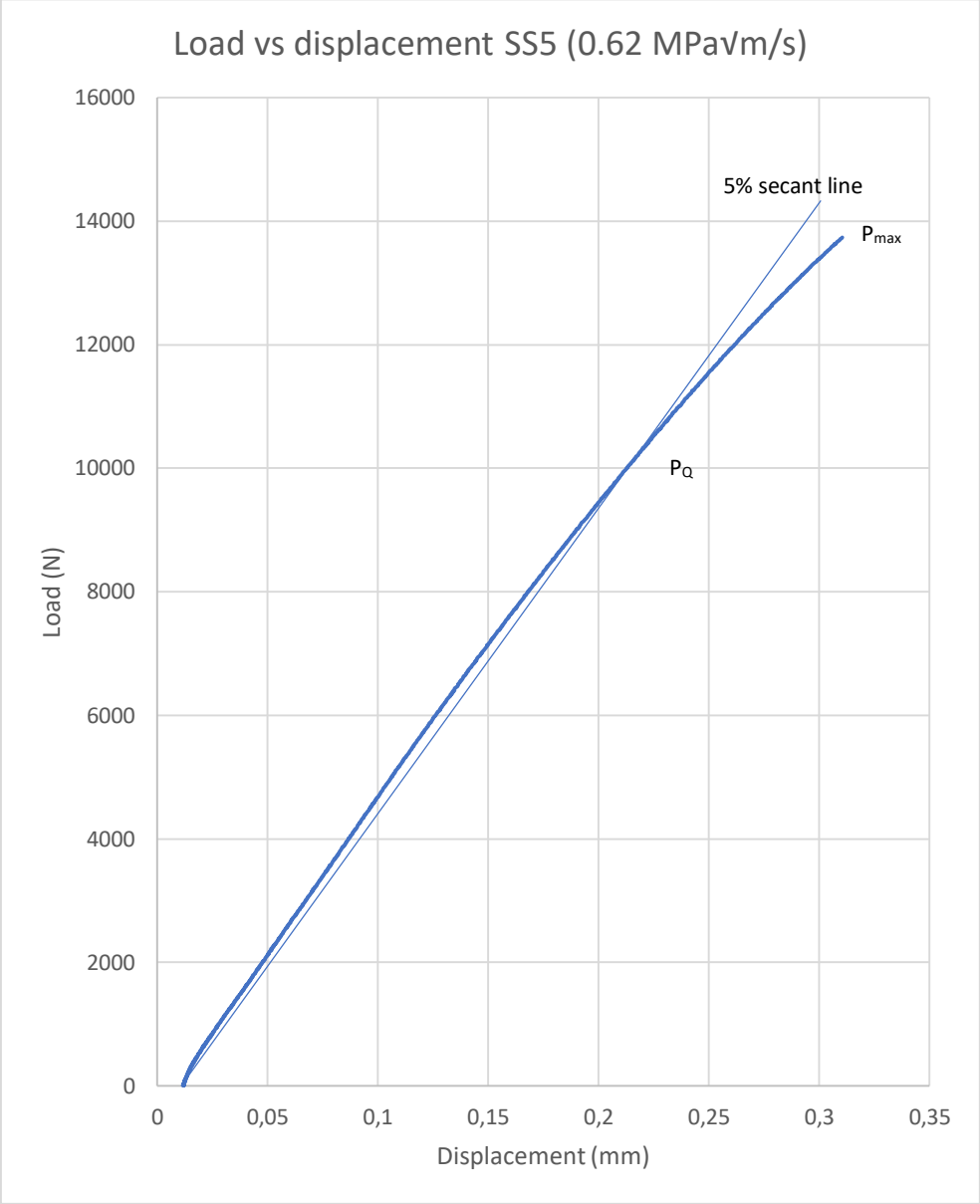

Figure 3.7: Load vs load line displacement SS5

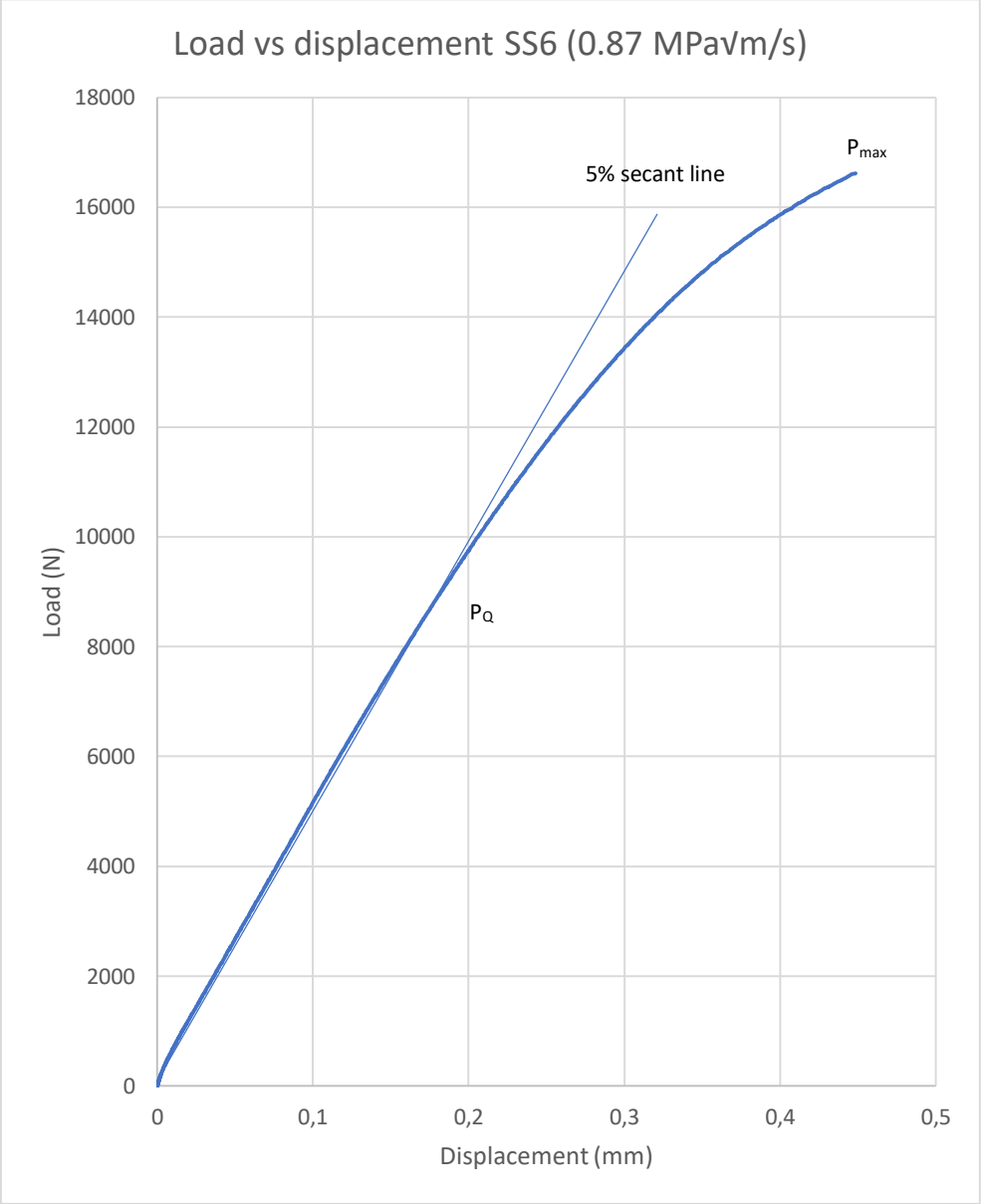

Figure 3.8: Load vs load line displacement SS6

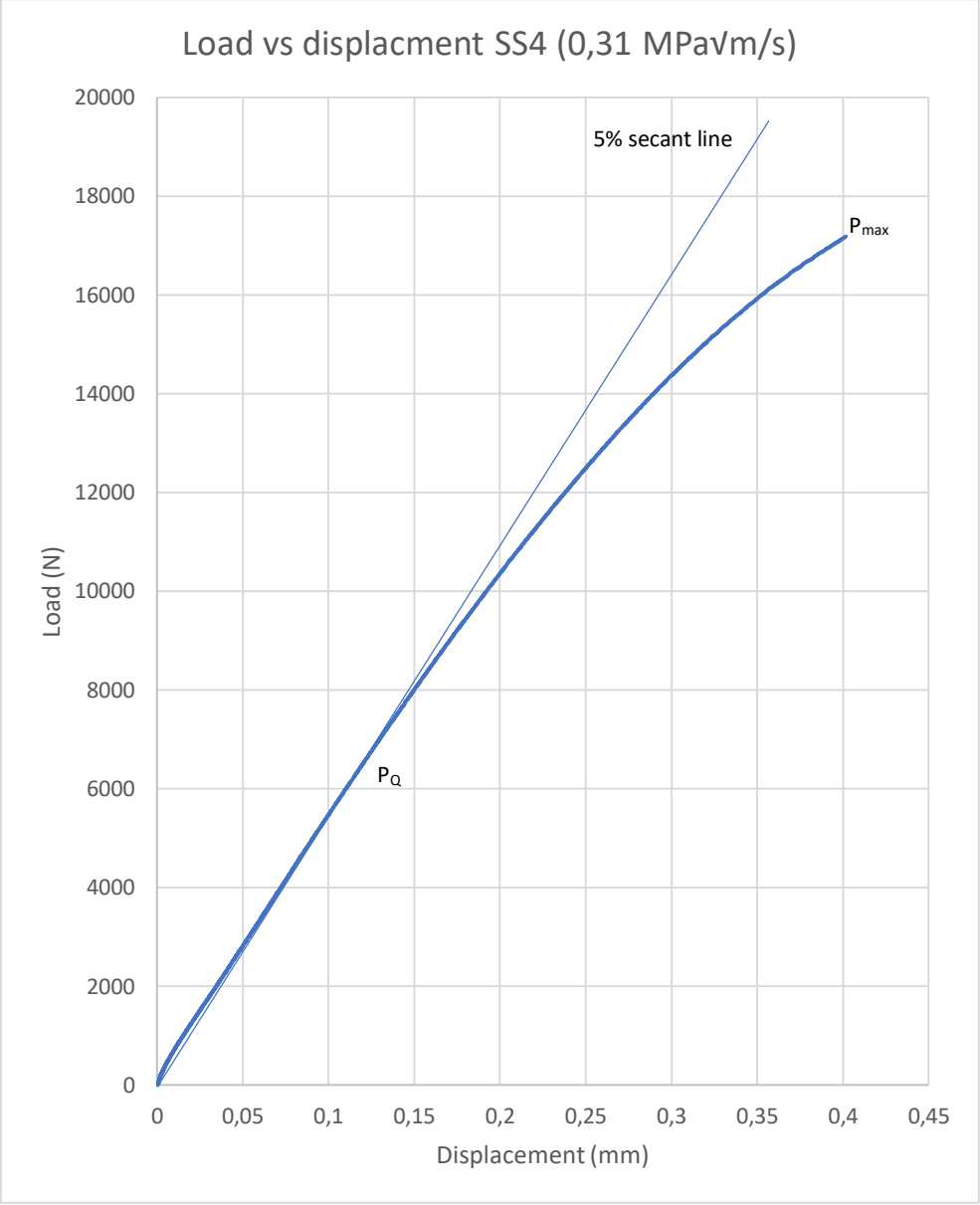

Figure 3.9: Load vs load line displacement SS4

Figures 3.7 to 3.9 shown above display the data obtained from testing three stainless steel dummy specimens at different loading rates. After solving the fracture toughness validity equations with the test data obtained for each test, it was noticed that the data fell slightly out of the validity range to provide a true fracture toughness value. The condition that needed to be satisfied was $\frac{P_{max}}{P_Q} \leq 1.10$ where P_{max} is the maximum load experienced and P_Q is the load corresponding to the 5% secant line. The calculations for this are detailed in ASTM E399. The data was suspected to have been invalid due to the small sizing of the specimen therefore, a thicker specimen would potentially solve this issue. Since the data was invalid for a K_{1C} test, it was decided that the data still be used as comparative data as a specimen redesign was not an option. Further testing of dummy specimens was conducted with some of the tests being valid at a cross-head speed of 0.5 mm/min (0.58 MPa√m/s). The result for SS7 is shown in Figure 3.10.

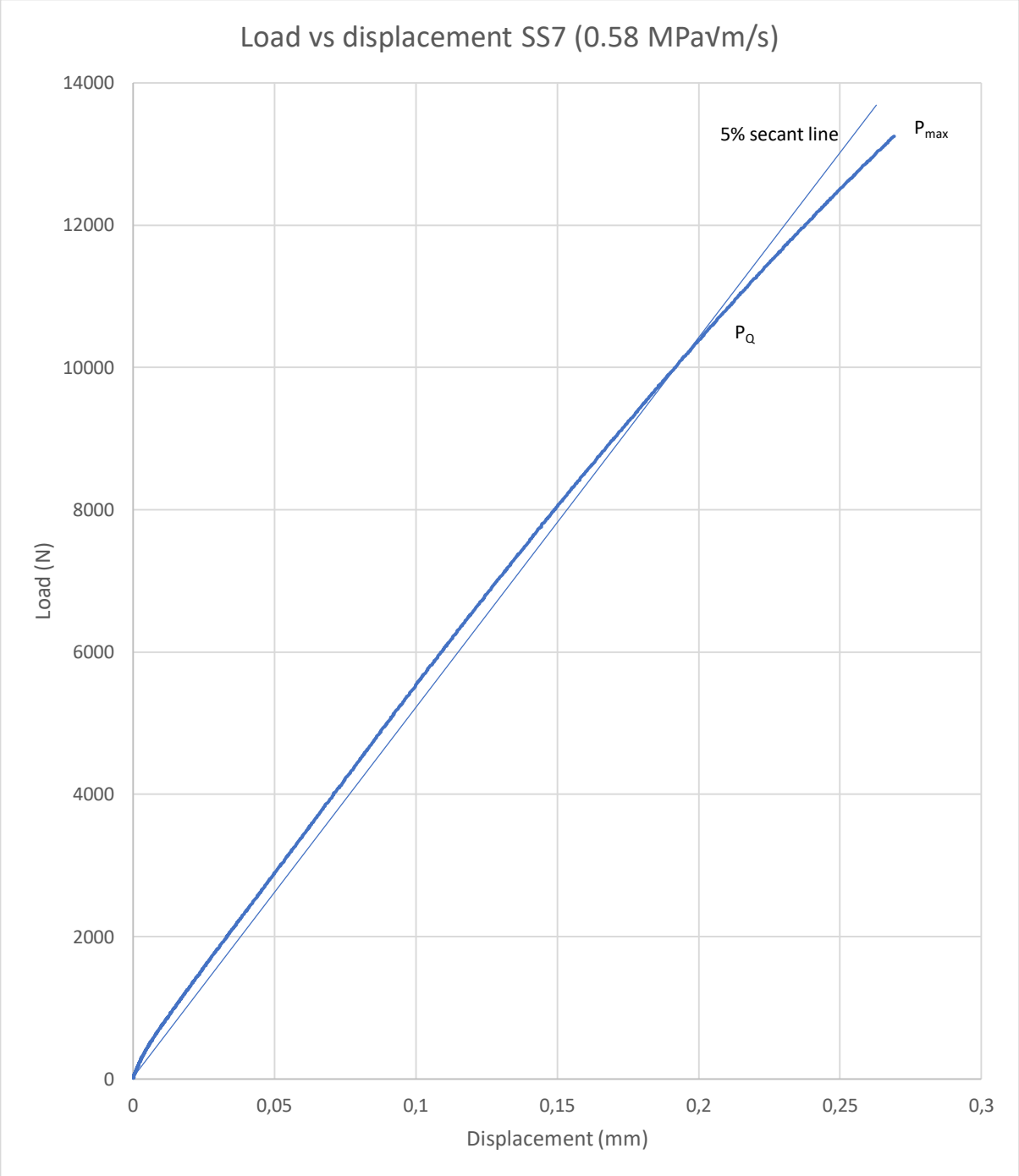

Figure 3.10: Load vs load line displacement SS7

In the test of SS7 at 0.5 mm/min (0.58 MPa√m/s), it was seen that the P_Q value was much closer to the P_{max} value and specimen displayed a more elastic response to the loading. This is expected for this type of test. The load ratio calculated for this test was seen to be 1.06, making this test valid. A conditional fracture toughness value K_Q for this specimen was calculated to be 87.9 $MPa\sqrt{m}$. The validity of this value to be regarded as a K_{1C} value is governed by Equation 3.2.

$$(W - a) \geq 2.5\left(\frac{K_{IC}}{\sigma_{ys}}\right)^2$$

Equation 3.2: Validity check for FT test

In this case, the specimen did not pass the validity requirement with an estimated yield strength of 700 MPa. This was probably due to the small size of the specimen and the length of the uncracked ligament *(W – a)*. To rectify this issue, the length of the crack could be reduced but this would mean less fatigue data would be obtained. A new specimen could have been designed to have a shallow machined notch to increase the length of the uncracked ligament, but this may not have been enough because the properties of the nickel-based superalloy were not entirely known at the time of preliminary testing. Resizing of the specimen to be larger than intended would have been the best option however, this was not possible due to cost constraints. The fracture toughness tests were therefore assumed to not provide a set K_{1C} value but used as comparative data to determine the difference in conditional K_Q values between the various build orientations to be tested. A cross-head speed of 0.5 mm/min was seen to be the optimum testing speed.

3.2. Test configuration issues

As expected throughout the preliminary testing phase of this project, multiple issues were encountered. These issues were welcomed as the data obtained and the experience gained would be used to perfect the testing procedure for the superalloy specimens as planned.

3.2.1. Fatigue crack growth rate test accuracy

The fatigue crack growth rate portion of the preliminary testing proved to be slightly less trivial than expected. It was seen that the measurement of the fatigue crack was inaccurate. The crack measurement technique used at the time was a visual technique during which, lines were scribed on to the polished surface of the test specimen and the crack propagation was observed through a microscope during the test. Achieving equal spacing on such a small scale is extremely difficult by hand and therefore the fatigue data obtained for these preliminary tests were not satisfactory. Therefore, a revised technique was envisioned. This method involved using a camera through a stereomicroscope to take a picture of the fatigue crack during stoppage of the machine. On this picture, a line can be drawn on the camera software to measure the crack to micron accuracy provided the camera is correctly calibrated. This technique required a stable mounting device to the ESH testing machine and therefore a rig was designed to mount the camera and microscope to the machine. The rig design process is outlined in Section 3.4.

3.2.2. Notch geometry

In terms of the fracture toughness testing and accuracy of the data obtained, it was seen that the original specimen geometry shown in Figure 3.1 was flawed slightly. For the fracture toughness testing, a clip gauge is used to determine the crack opening displacement from compliance. The current clip gauge at the Centre for Materials Engineering is designed for a gauge length of 10 mm with a 4 mm travel. The original drawing was made with a gauge length of 3 mm which is significantly less than the rated gauge length of the clip gauge. As a result, there were minor complications in obtaining accurate displacement data during the test.

3.3. Optimised heat treatment protocol for IN718

As mentioned in Section 1, this project deals with the application of heat treatments to the as-built LENS manufactured IN718 material. The fatigue performance and fracture toughness of the as-built and heat-treated specimens will be compared to determine the potential improvement after homogenisation and precipitation hardening of the as-built microstructure. Various sources of literature provide heat treatment protocols for cast or investment cast or wrought IN718, but there is no set procedure of IN718 manufactured by AM processes. Therefore, different heat treatment protocols were performed on small IN718 samples in order to investigate the effects of heat treatment on the material hardness. The protocols used for this project were that of cast IN718 and generally

consists of a high temperature solution treatment, water quench to room temperature, followed by a lower temperature ageing. Offcuts of the AM produced IN718 material were heat treated according to the heat treatment protocols that will be detailed below.

The high temperature solution treatment was performed using a Gallenkamp furnace. The solution treatment was conducted at a temperature of 1200 °C for 2 hours followed by water quenching to room temperature thereafter. This solution treatment is performed to homogenise the microstructure of the material and to remove any residual stress after the AM process. This in turn is expected to soften the material significantly. The samples were slow heated at a rate of 100 °C/hour to the target temperature of 1200 °C to prevent the material from cracking due to assumed rapid residual stress relief. Samples that were placed directly into the hot furnace at 1200 °C were seen to possess significant surface cracks upon removal after the solution treatment therefore, it was decided that the samples be heated gradually to prevent cracks from forming. This is assumed to not be characteristic of Inconel alloys however, the slow heating was seen to prevent these cracks from forming and was therefore carried through all heat treatment protocols.

After the high temperature solution treatment, an ageing process was required. According to literature, some ageing protocols were conducted at a temperature of approximately 900 °C for a period of 16 hours. To gauge whether 16 hours was the ideal ageing time, a number of samples were cut from the IN718 material and were firstly solution treated at 1200 °C. Thereafter, the samples were aged at 930 °C for durations ranging from 2 hours to 25 hours in a muffle furnace. Hardness profiles were plotted and the results were inconclusive within the 25 hour range.

A lower ageing temperature ageing procedure of 650 °C was conducted. This temperature was used by Chang [31] and improvements in the material hardness were seen. A similar test matrix was used for this process with a high temperature solution treatment at 1200 °C for 2 hours. Samples were then aged for a duration between 4 and 24 hours and Vickers hardness tests were conducted thereafter. The results obtained for this experiment are shown in Figure 3.11 below.

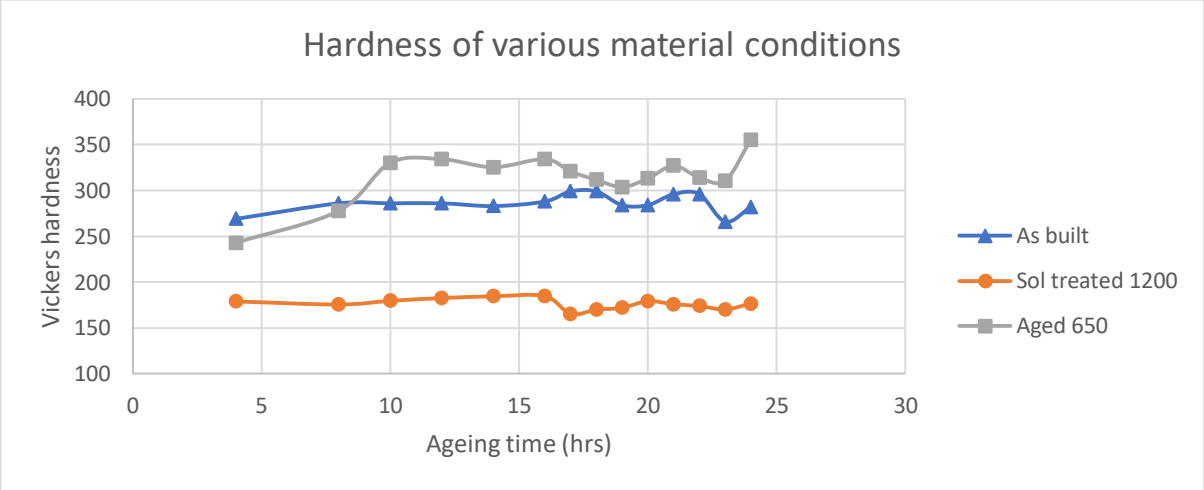

Figure 3.11: Corrected Vickers hardness of various material conditions after 650 °C ageing

As shown in the graph above, it can be seen that the hardness values after ageing are very similar from hours 10 to 23 indicating that the precipitation hardening effects tend to reach a plateau after 10 hours. The hardness gained from the ageing process after the solution treatment ranges between 136 and 155 HV. After 24 hours, it can also be seen that there is a great spike in the hardness level. This could either be an anomaly or it could mean that there is some secondary hardening mechanism in the material beyond 24 hours of ageing. No samples were aged beyond 24 hours since it is not within

the scope of this project and therefore, it was inconclusive whether the material hardens further after 24 hours.

From the results shown above, it was seen that an ageing period of 16 hours as specified by various sources of literature was best suited for this material. Quenching of the material after solution treating was required in order to promote precipitation hardening. Smaller samples were representative of quenching since the cooling rates were high. The data showed that the hardening effects were consistent from 10 to 23 hours of ageing, but it was decided that an ageing period of 16 be used as it was tested with water quenching.

3.4. Microscope and camera support rig design

In this section, the process followed throughout the design of the microscope and camera support rig will be outlined in detail. This will include a motivation for the rig, the concept designs and various iterations, ease of use of the rig and finally adaption of the camera to the rig.

3.4.1. Motivation for rig

During preliminary fatigue testing of the stainless-steel dummy specimens, it was noticed that the crack measurement technique displayed some inaccuracies when the data obtained was analysed and converted into useful fatigue data. The crack length versus number of cycles and the fatigue crack growth rate $\left(\frac{da}{dN}\right)$ versus ΔK curves for various stainless-steel specimens were not as uniform as was expected for a stainless-steel alloy, especially in the crack initiation region of the test. Effective tracking and measurement of the crack during crack initiation as well as crack propagation was not possible with the measurement technique employed at the time. This technique involved estimating the crack length with reference to marked intervals across the surface of the specimen as described in Section 3.1.1. The marking process (scoring of gradations onto the polished surface of the sample) introduced many uncertainties into the fatigue test as the markings appear to be uniformly distributed at the set interval of 0.5 mm when looked at with the naked eye however, when the specimen was looked at through the existing microscope, it was seen that the markings were not as equidistant as intended. There was a noticeable variation between the markings and hence it proved difficult to obtain accurate fatigue crack length measurements. This showed in the fatigue data as mentioned above.

As a result of this inaccuracy, alternative techniques were brainstormed and conceptualised for the crack measurement. An initial solution to the problem was to obtain and place a graticule on the existing microscope in order to have set increments where the lengths are known with reference to the magnification factor of the lens. This would be the easiest and quickest solution to the problem however, it was later realised that even with a graticule that possessed markings every 0.5 mm or so, it would still not enable accurate measurement of the crack. The accuracy would certainly be improved as compared to the manual marking method with the Vernier calliper but when the image is enlarged, the 0.5 mm increments become much bigger than anticipated and the crack length would have to be estimated between each of the lines on the graticule once again. Therefore, this idea was deemed unsuitable for the required task.

Another method that was conceptualised was a method of etching markings into the surface of the sample using a computer guided laser. This would potentially improve the accuracy of the spacing between each of the markings since there will be less variation and inconsistencies in the marking process. This marking process is similar to using a graticule through the microscope in the sense that it there will be set markings at a set interval however this method will mark lines on the actual surface of the specimen and therefore a graticule would not be necessary. The issue found with this method

is parallel to the issue in the previous concept. On a magnified level, it will not be possible to determine exactly how far the crack has progressed between the spaced lines and hence the length must be estimated which is not suitable for this test. There is a limit to the accuracy of the laser and the tolerance to which it can etch the surface of the material. The costs and efforts of outsourcing a laser capable of performing the task was also an unwanted step in the testing process. Therefore, this method was not viable.

It was seen that in each of the methods developed previously, the problem occurred in the physical markings and how accurately the distance between the markings could be measured. Furthermore, there is a limit to the number of markings that can be scribed on the surface of the specimen and the accuracy to which the crack propagation between the markings can be estimated. Physical markings and estimations of the crack length are therefore not ideal when attempting to obtain useful fatigue results. A method that can measure the instantaneous crack length at any given point throughout the test was required. A possible method will be described below.

A digital image capturing system was conceptualised to enable effective and accurate measurement of the crack propagation and growth throughout the test. By mounting a camera to a stereomicroscope, an image of the test area can be obtained with a desired magnification. The camera will be fixed in position and not moved during the test and it will be calibrated according to its position. For instance, 1 mm of crack growth will be equal to a set number of pixels that can be determined from the captured image and the calibration parameters. This method seemed to be more promising than the other concept ideas since this method does not require physical marking of the specimens and hence, the uncertainty of measurement is significantly reduced. Using an image capturing technique could potentially result in obtaining extremely accurate results.

The existing microscope associated with the ESH in the Centre for Materials Engineering was the Leica 60A which is a stereomicroscope. This microscope is mounted to a multiaxial arm that enables a wide range of motion which allows for the test area to be examined during the test. A picture of the existing microscope and mounting mechanism is shown in Figure 3.12 below.

Figure 3.12: Existing Leica 60A stereomicroscope

The digital image capturing technique cannot be applied to the Leica 60A as the stability of the supporting rig is not sufficient for the accuracy required by the measurement technique. During preliminary testing of compact tension specimens on the ESH, it was seen that the microscope tends to vibrate and move significantly during the test. This is due to the mounting mechanism of the microscope, which is a simple G-clamp that is attached to the base of an adjacent desk. As a result, the mounting mechanism for the proposed system needed to be modified or reengineered to provide the stability and accuracy that was required for this system. The design and development of the proposed microscope mounting rig will be explained in detail in the coming sections.

3.4.2. Specifications and constraints

The design of the supporting rig was developed based on certain geometric and financial constraints. The specifications and constraints pertaining to the development and design of the rig will be mentioned below.

Since the image capturing technique requires a high stability, the supporting rig is required to be as rigid as possible, while being lightweight as well. Mounting of the microscope and camera should be on the support structure of the ESH testing rig itself due to the stability that the machine offers as compared to the current microscope mount mentioned previously. Furthermore, the supporting rig for the microscope should be smoothly integrated with the ESH testing machine in order to ease assembly of components and to ensure that the microscope position can be adjusted for various testing configurations beyond this project. The microscope must be able to lock into the final position in order to begin the calibration process for the image capturing system. The microscope must be able to move linearly to and from the test area in order to aid focusing of the lens as well as to generate space for removing the specimen after testing has occurred. In conjunction with the abovementioned specifications and constraints, the components comprising the microscope supporting rig should be inexpensive since there are alternative methods that can fulfil the purpose of crack measurement

however, they are costly. This solution should be designed to be a cheap yet effective option that can be manufactured and assembled easily.

3.4.3. Design phase

During the concept design phase of the supporting rig, the various components were looked at from a modular point of view. This allows for parts to be easily interchangeable if modifications are required during the implementation phase of the process. There are three main mechanisms comprising the supporting rig namely the clamping mechanism, the linear motion mechanism and the microscope mount. The design of each of these mechanisms will be outlined in the coming sections along with the concept design leading to the final design.

3.4.3.1. Linear motion mechanism

The linear motion mechanism is required to aid the one-dimensional horizontal motion of the microscope. The current system in place with the Leica 60A microscope is a multiaxial arm, as mentioned above. The multiaxial arm allows motion in the X, Y and Z orientations and is versatile enough to position the microscope wherever it is needed. Since the testing methodology is to be refined for fatigue and fracture toughness tests, this multiaxial motion is not necessary as it introduces instabilities to the system, such as vibrations. Narrowing down the motion of the microscope to one direction only will enable a more stable field of view for the microscope during testing.

There are several methods that can be used to achieve one dimensional linear motion in a single horizontal plane. A sliding mechanism can be used in which the various components slide on top of one another using friction to fix the components in place. A telescopic mechanism could also be used, which is similar to a sliding mechanism but could potentially be more compact than the sliding mechanism. Finally, a roller mechanism can be used, which utilises rails and multiple rollers to smoothly roll the microscope to and from the testing region. A suitable braking system would be required to lock the microscope in place since rolling friction is significantly less than static friction.

From the abovementioned mechanisms, the rolling mechanism was chosen to be the most suitable for a number of reasons. Rollers enable smooth motion of the microscope when required as compared to a sliding and telescopic mechanism since rolling is easier to accomplish than sliding owing to friction. A telescopic mechanism could be more compact than using rollers, however, the design and manufacture of the mechanism could be more complex and possibly result in the development of some inaccuracies with the motion of the rig. A sliding mechanism is a simple design however, friction and location of all moving parts could prove to be problematic.

Since the requirements of the design is to be inexpensive, simplified and accurate, the rolling mechanism was chosen as the design can be based of that of modern 3D printers. The 3D printer parts and technology considered for this design will be outlined in Section 3.4.3.4.

3.4.3.2. Clamping mechanism

As mentioned above, the supporting rig should preferably be mounted on a stable platform for the image capturing technique to be effective. As a result, the rig would require a suitable clamping mechanism that will securely clamp it to the ESH frame. Several designs were considered for the clamping mechanism once the linear motion mechanism was finalised. Mounting of the rig was considered on various locations of the ESH testing rig frame. The ESH is shown in Figure 3.13 below.

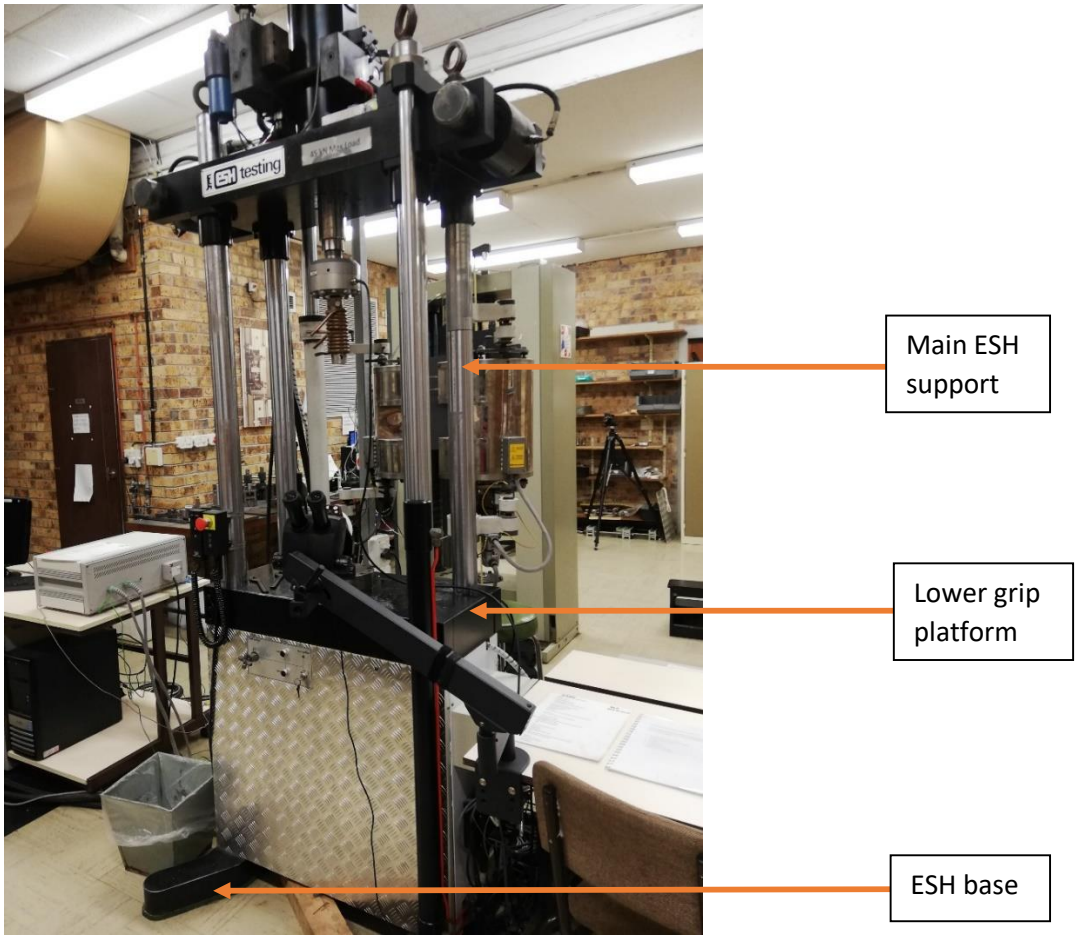

Figure 3.13: ESH servo-hydraulic testing machine

The locations considered included the main supports, the base of the ESH near the floor and the platform where the lower grip is located which are identified by the orange arrows in Figure 3.13. The main supports of the ESH, were seen to be the most convenient location for the clamping mechanism since it was in close proximity to the test area and also would not require much effort to develop the clamp. Other clamping and mounting mechanisms that would potentially be attached to other parts of the ESH rig itself would require far more components and supporting members and also require the panels or sections of machine to be removed for installation. Various iterations of the clamping mechanism were designed and will be outlined in the coming sections.

3.4.3.3. Microscope mount

The microscope mounting mechanism is the portion of the setup that attaches the microscope to the supporting rig. The microscope to be used is a Nikon SMZ-10, which was originally mounted on a vertical stand. The design of this microscope and its components are such that the microscope itself can be easily disassembled. By using the existing holder for the microscope as depicted in Figure 3.14 below, an adaptor must be designed that allows the existing holder to fit seamlessly with the supporting rig. A shaft and bracket can be used to attach the existing holder of the microscope to the proposed supporting rig. This design will be outlined further in the coming sections.

Figure 3.14: Existing Nikon SMZ-10 stereomicroscope and holder

3.4.3.4. 3D printer technology

As mentioned in 3.4.3.1, the design of this rig can be derived from the working mechanisms that currently exist in 3D printers. This allows for accurate, smooth and stable linear motion of the rig. Another benefit from using 3D printer parts is that they are readily available and easy to source at a reasonable price and therefore, they are a suitable choice for this design. They are also manufactured from lightweight materials, which is another benefit. Several 3D printer components will be used and mentioned in the concept design in Section 3.4.3.5. Therefore, the components will be shown below to clearly illustrate the geometry and function of the respective component. The components used in this rig were sourced from the 3Dprintingstore.co.za.

3.4.3.4.1. V-slot rail

The V-slot is a common type of rail used in 3D printers. These rails generally form the frame and structure of the 3D printer rig. They are typically aluminium extrusions with a complex geometry for improved stiffness and possess grooves along the length of the rail that allow wheels to roll along the length of the rail. The V-slot rail is shown in Figure 3.15 below.

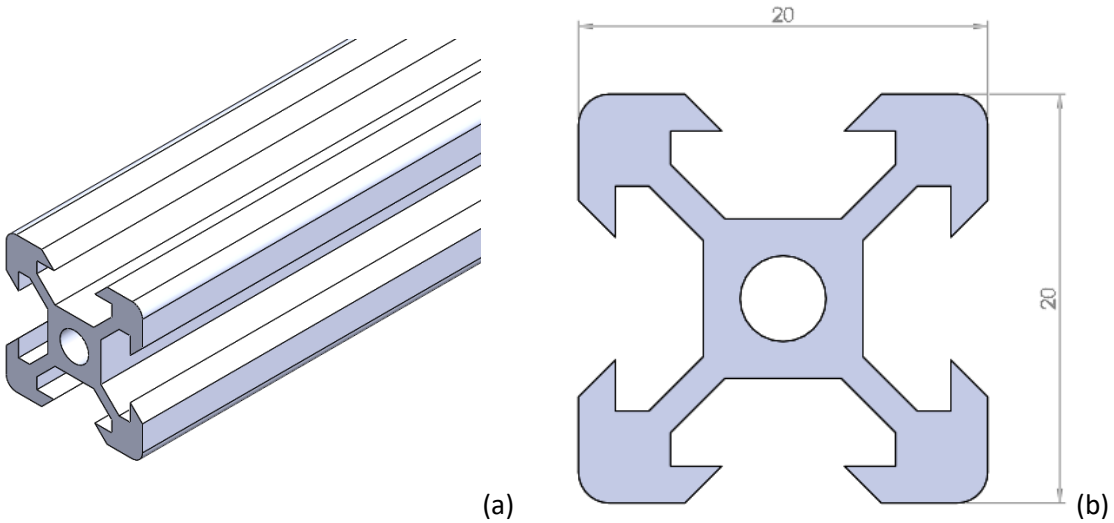

Figure 3.15: V-slot rail isometric view (a), profile view (b)

The figures above were modelled in Solidworks and illustrate an isometric view of a portion of the V-slot rail as well as a cross sectional view of the rail. The major cross-sectional dimensions of the rail are shown in Figure 3.15b. This component was designed to allow for linear motion of devices and is

therefore more than suitable for this application since it is based off existing technology. As mentioned above, the geometry of the rail is such that the stiffness is adequate for supporting a wide range of loads and to accommodate the various components that will attach to the rail such as the V-slot wheels and the T-nuts which will be shown in the next sections.

3.4.3.4.2. V-slot wheel

The V-slot wheel is provided in a kit that comprises a delrin (polyoxymethylene) wheel, two ball bearings, spacer, lock nut and bolt. Figure 3.16 below shows the components in the wheel kit.

Figure 3.16: Exploded assembly of V-slot wheel [y]

The V-slot wheel is chamfered at 45° on each of its sides which allows it to run smoothly along the groove in the V-slot rail, which is chamfered at the same angle and to compensate for any geometrical inaccuracies between opposing wheels. The V-slot rail has provisions for the wheels to roll on all four sides of the rail and this expands the flexibility of the design and possibilities. An M5 bolt and locknut are used to attach the wheel to other parts of the assembly as needed.

3.4.3.4.3. Slide and turn T-nut

There are two types of fasteners generally used in 3D printers which allow the various parts to be attached to one another at a range of different locations. This allows flexibility of the assembly process and eases assembly. The types of T-nuts used for this application are called slide T-nuts and turn T-nuts. The figures below show an isometric view of each T-nut.

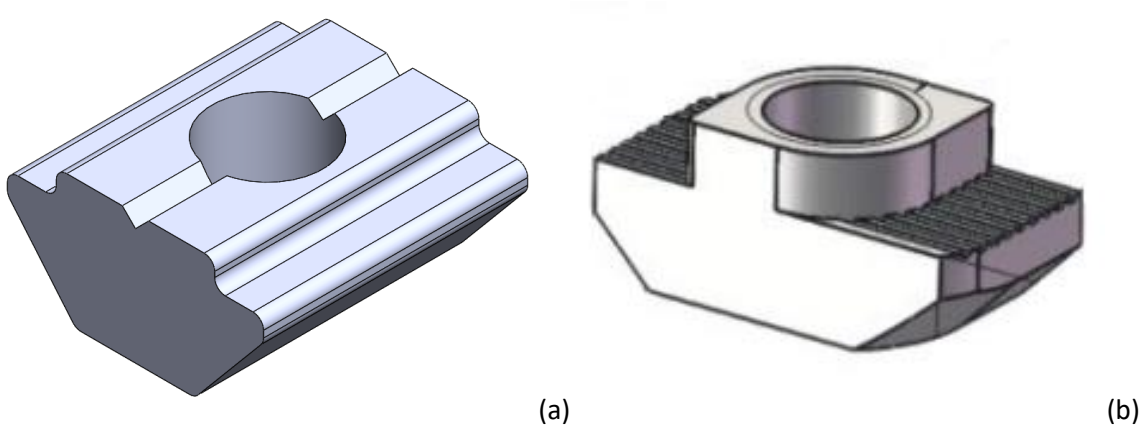

(a) (b)

Figure 3.17: Slide T-nut (a), Turn T-nut (b)

Each of these T-nuts serves a similar purpose of allowing brackets or other fittings to be clamped to the V-slot rails but possess slight differences in their geometry and ease of assembly. These T-nuts have a cross section that resembles the slot profile in the V-slot rail in order to fit into the rail and perform their function of clamping. The T-nuts are threaded and therefore when clamping is required, a bolt will be used to provide the required clamping force with respect to the component that needs

to be clamped. The slide T-nut is introduced to the slot in the rail from either end of the rail and must therefore be inserted at the beginning of the assembly in the event that the ends of the rail become inaccessible towards the end of the assembly process. Figure 3.18 below displays the assembly of the V-slot rail and slide T-nut.

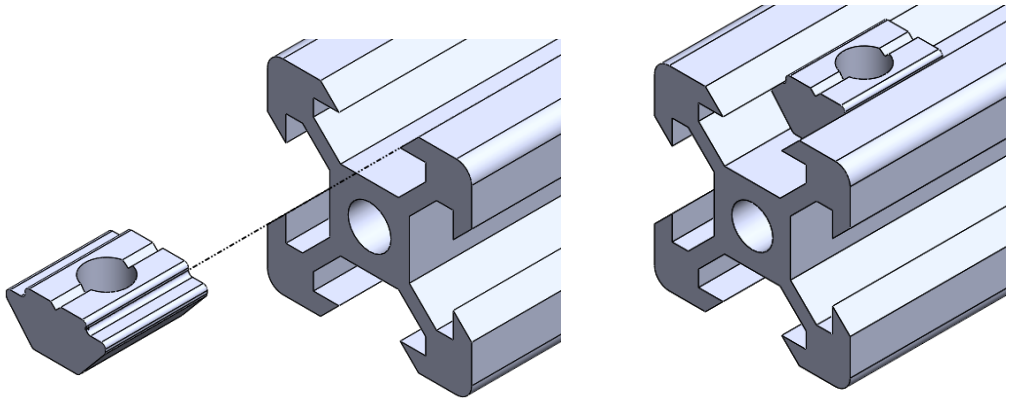

Figure 3.18: Exploded isometric assembly of slide T-nut and V-slot rail

The turn T-nut is useful when the ends of the rail are not accessible during assembly and when a slide T-nut cannot be used as a result. The turn T-nut can be inserted directly into the rail at any position in the slot and is then turned to lock the nut in place. A bolt is then used to fasten the component to be attached in a similar fashion as the slide T-nut. Figure 3.19 below illustrates how the turn T-nut and V-slot rail are assembled.

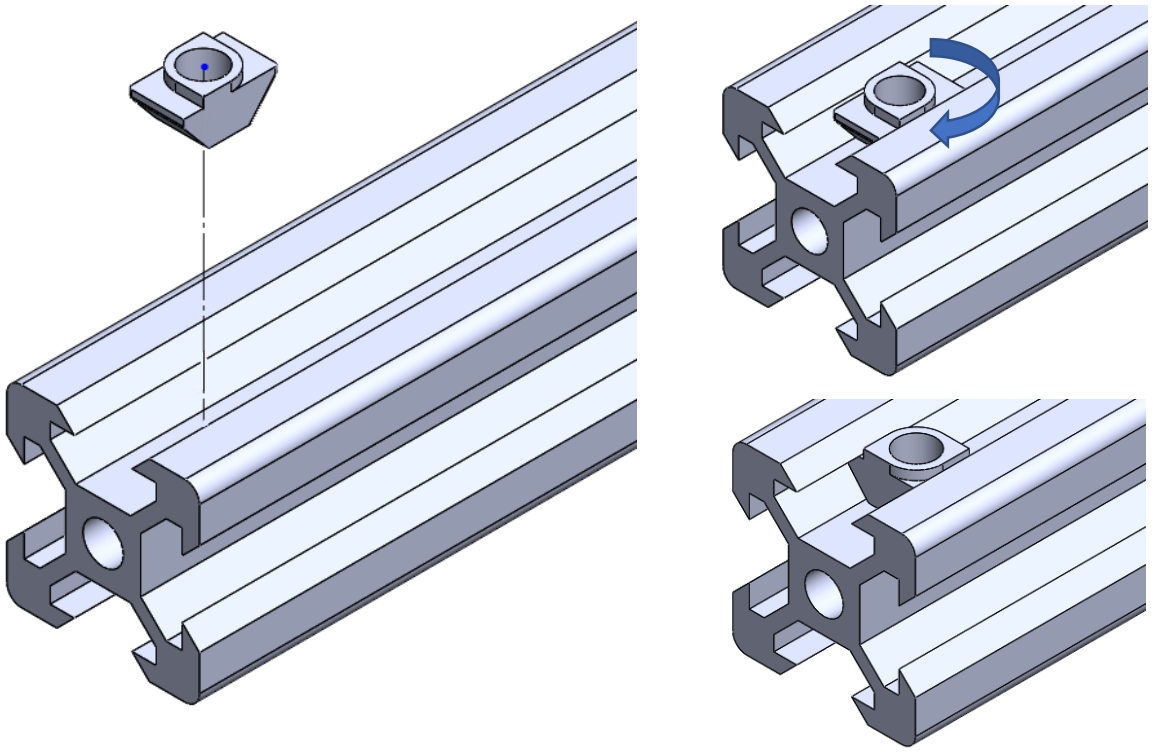

Figure 3.19: Exploded isometric assembly of turn T-nut and V-slot rail

3.4.3.4.4. Corner bracket

The corner bracket is used to connect components on a V-slot rail at 90° to each other. This allows for a 90° join between parts that is rigid and secure. It is clamped to the V-slot rail with the use of two T-

nuts and a bolt between the respective components. The most common application for using the corner bracket is to join two V-slot rails at 90° to one another. Figure 3.20 below shows an isometric view of the corner bracket.

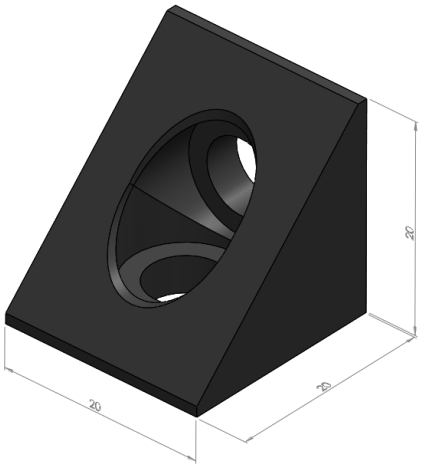

Figure 3.20: Corner bracket

3.4.3.5. Concept design

The development of the concept design encompasses all the elements mentioned in the previous sections, taking into consideration the specifications and constraints and design criteria associated with the function of the finished product. The initial design of the rig required a smooth combination of the various elements mentioned above such as the linear motion mechanism, the clamping mechanism and the microscope mounting mechanism. A Solidworks model of the design was generated and is shown in Figure 3.21 below.

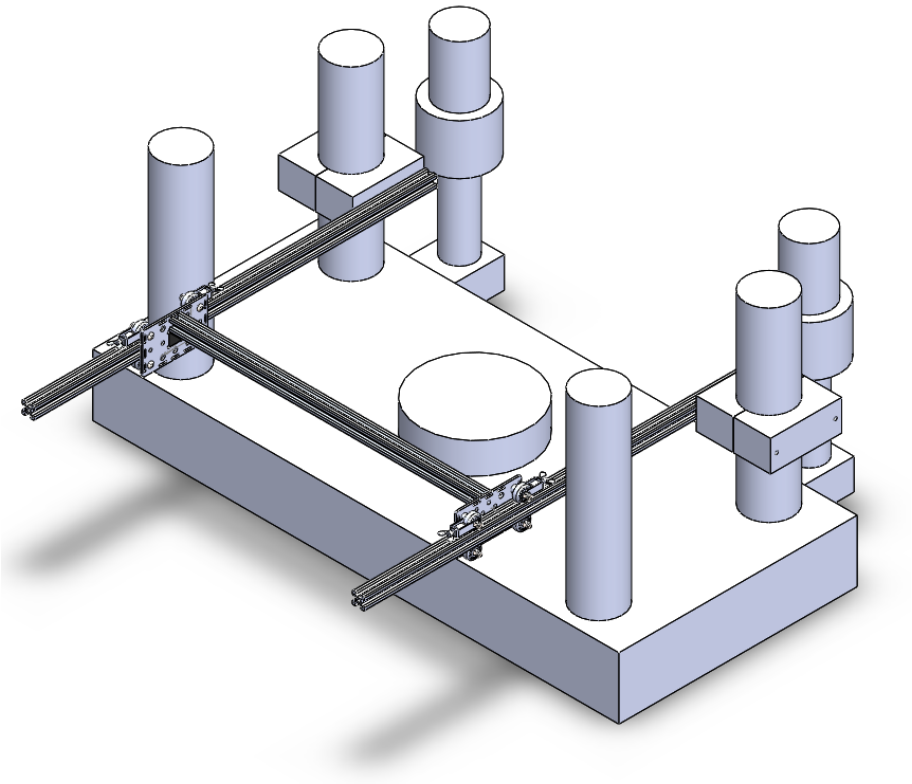

Figure 3.21: Concept rig design

This design was developed during the preliminary stages of the rig development. As a result, a general understanding of where the individual components would fit was obtained and not much thought was devoted to developing the intricacies of each sub-system. The ESH base and supporting uprights are depicted in the model to gain an understanding of how the rig fits into the testing area and how it coincides with the existing structure. In the figure above, the clamping mechanism is attached to the rear upright supports of the ESH by means of a two-part block clamp. This clamp was not designed to be fully functional but used as a concept to develop further designs. The linear motion mechanism is then attached to the clamp by means of a long bolt and a slide T-nut which will be positioned in the V-slot rail. This then allows for a clamping force to be induced and hence the rail will remain horizontal.

The rolling mechanism is then comprised of a gantry plate and 4 rollers on each rail, which is depicted in Figure 3.22.

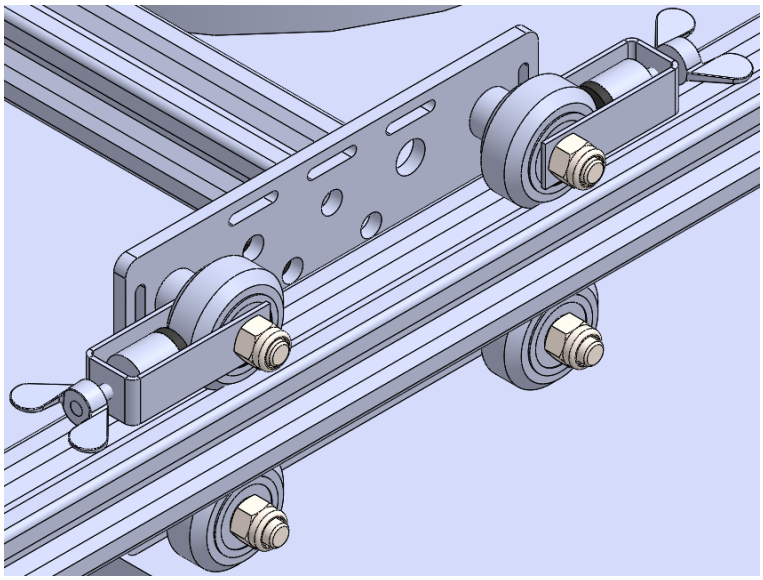

Figure 3.22: Rolling mechanism of concept design

This design allows for smooth and stable linear translation of the microscope when movement is required. In order to lock the rig in place, a locking mechanism was required. This locking mechanism can be seen in the figure above on the top two rollers. It is a simple design comprising a wing nut, a threaded stud, a drilled disk and a polymer pad (shown in black). When locking is required, the wing nut will be turned until the polymer pad contacts the surface of the roller and tightened until motion is restricted completely.

The microscope mounting mechanism was preliminarily designed in order to provide a platform on which to place the microscope but was not designed fully in this initial draft. Figure 3.23 below illustrates the connection of the mount to the rolling mechanism.

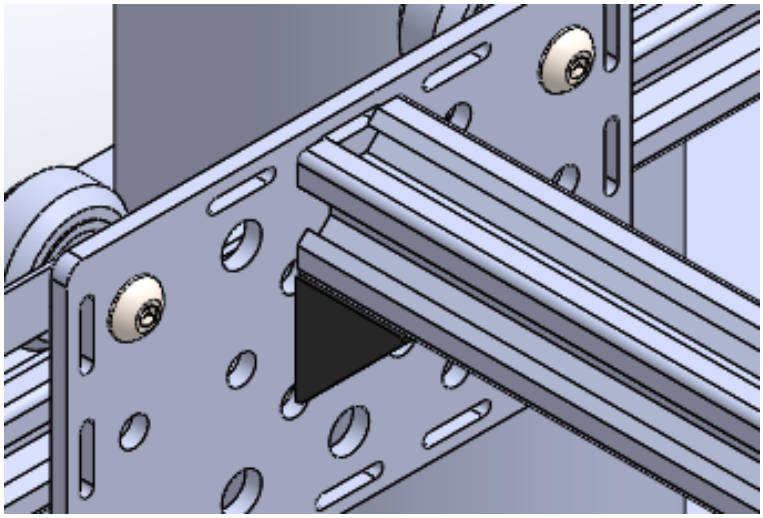

Figure 3.23: Rail to support the microscope mounting mechanism

The microscope will be mounted on a cross member that connects each of the rolling assemblies via the two gantry plates. These will be connected to the plates with the use of the corner brackets and the slide T-nuts mentioned in section 3.4.3.4.3.

The design shown in this section is the concept upon which the final design was based. The iterations following this design address the lack of detail in this design and respond to intricacies that required attention. Since the design process consists of regular evaluation and redesigning of certain components, the concept design underwent many subtle changes and revisions in order to produce a system that worked effectively and efficiently. Each design iteration will not be included in the main body of this report but can be found in Appendix 11.1. The following sections show the major improvements and changes to the design during the designing and implementation phase.

3.4.3.6. Development of concept design

The concept design was developed to create a more functional system that could work in reality. This involved the development of the clamping mechanism and the microscope mounting mechanism which can be seen in Figure 3.24 below.

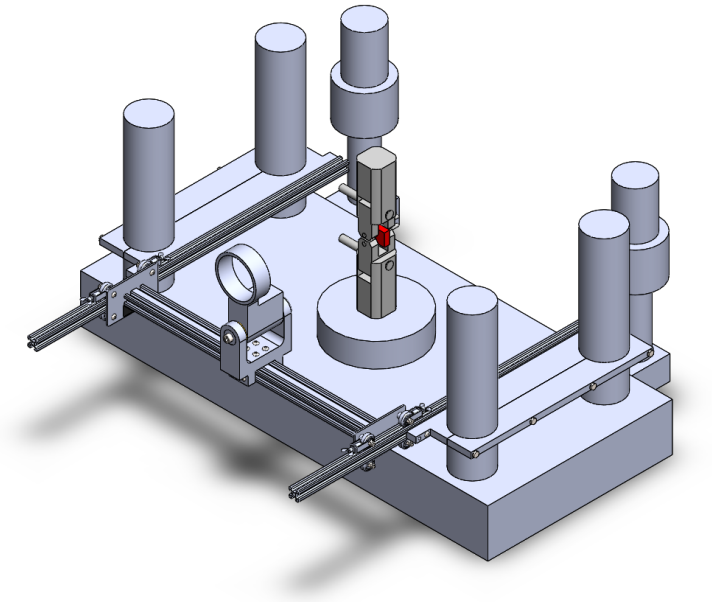

Figure 3.24: Development of concept design

From Figure 3.24 above it can be seen that the clamping mechanism was developed from a block clamp to a plate clamp. The plate would provide stability and use less material than the block. The block was initially used as the foundation for further designs to be developed such as the plate. This mechanism works by having two plates fastened together by a bolt to induce a clamping force on the upright supports of the ESH. These plates will then act as a shelf on which the V-slot rails will be mounted on. The V-slot rails will be fastened to the shelf by means of several slide T-nuts along the length of the shelf. This provides secure location and stability of the rails without having the cantilever effect which was seen in the concept design. The mass of the microscope was measured to be 2.2 kg. With the addition of other supporting components in the microscope mounting sub-assembly the total mass was conservatively assumed to be 5 kg. Calculations were performed to theoretically determine the bending stresses induced in each of the rails as well as the deflection at a distance away from the machine. These calculations can be found in Appendix 11.2. Simplifications were introduced into the calculations. The load was assumed to act as a point load on each of the rails. The maximum bending stress in the rail at a distance of 0.2 m from the front support pillar was calculated to be 7.3 MPa which is very low considering that the yield strength of 6063 T5 aluminium is 145 MPa [z]. This distance was used as a worst-case scenario distance. The maximum deflection at the same distance was calculated to be 2.2 mm, which is small and will not be the actual deflection when the microscope is in use since the distance will be significantly less from the front support pillar.

The microscope mounting mechanism was designed in this development stage and is shown more clearly in Figure 3.25 below.

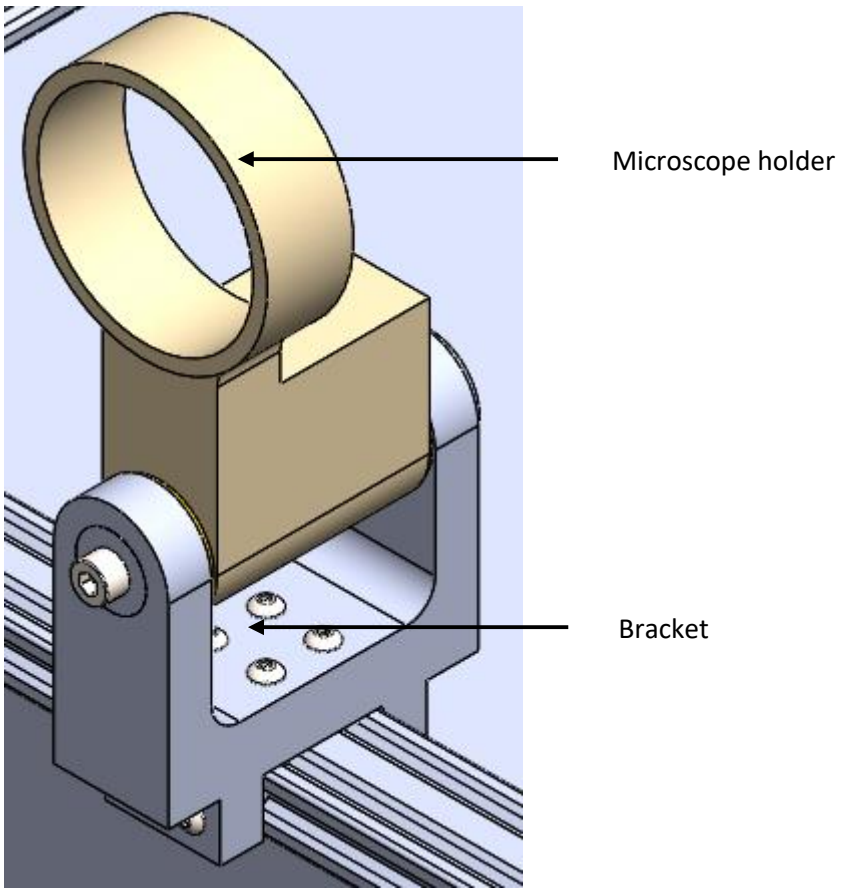

Figure 3.25: Microscope holder and mounting mechanism

The mounting rig for the microscope is mounted to the 20x40 V-slot cross member that joins the two gantry plates. The original holder for the microscope is shown in brown in the figure above and is

joined to the cross member using the bracket shown in the figure above. The bracket is fixed to the rail by means of several turn T-nuts and bolts in order to increase the stability of the microscope during operation. This bracket was designed based on the original stereomicroscope bracket but was modified in order to accommodate adaptation for this rig. The microscope will then fit through the circular portion of the holder as it was designed for and will allow for the lens to focus directly on the specimen during the fatigue test.

This design iteration was eventually chosen to be manufactured as the first prototype to assess the functionality of the overall design.

3.4.3.7. Final design

The final design was obtained after performing many design iterations on the developed design that was shown in the previous section. These iterations can be found in Appendix 11.1. The final design that was manufactured and used for the fatigue crack growth rate tests can be seen in Figure 3.26 below.

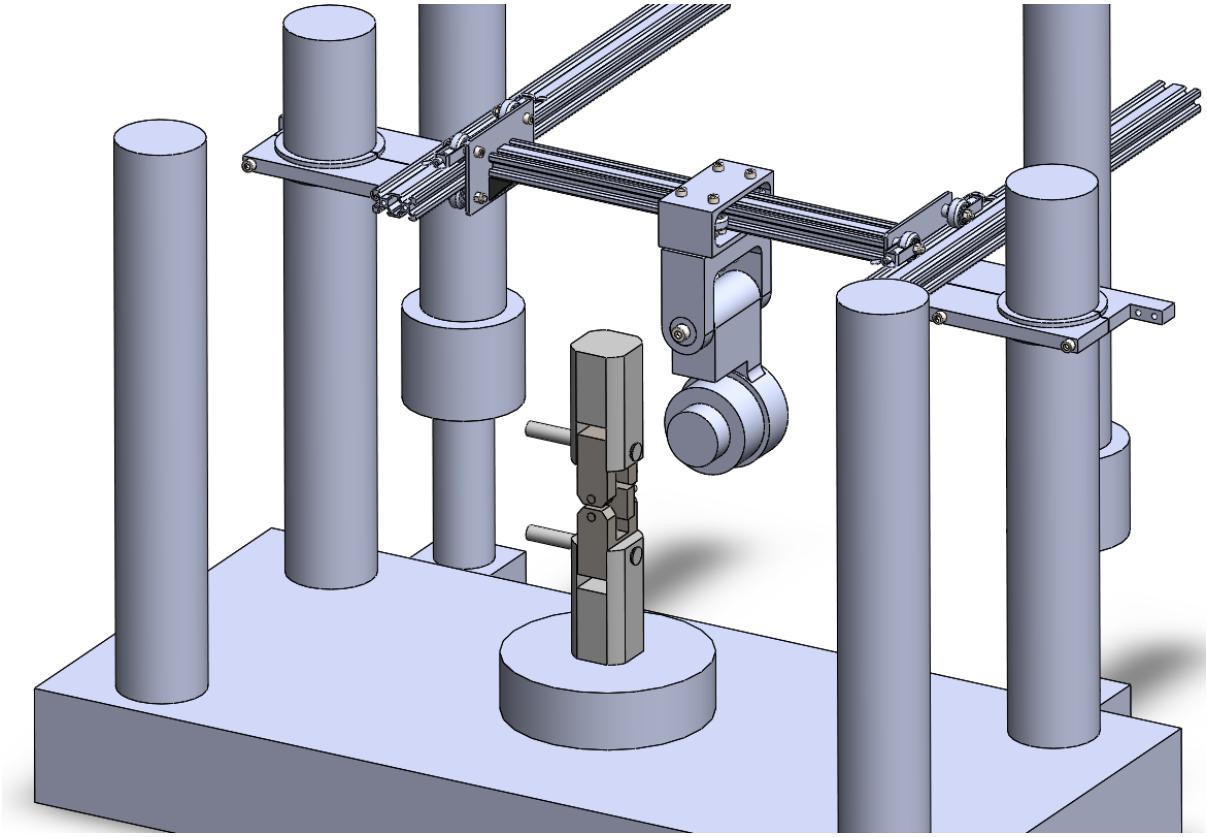

Figure 3.26: Final rig design

From Figure 3.26 above, it can be seen that many changes were made to the developed design from the previous section. These changes addressed issues that were encountered during the implementation phase of the design process when the rig was assembled and tested. The most noticeable change was the removal of the plate clamp that spanned both uprights. Upon assembly of the developed design, it was seen that the shelves were not fitting around the upright supports as intended. This was due to the change in distance between the upright supports as the cross head of the machine moves up and down, which was not taken into consideration. The long plate was therefore shortened to fit on one of the uprights which addressed this issue. This also made the overall assembly lighter and easier to assemble. The 20x20 V-slot rails were also mounted closer to each other after the plates were cut and this allows for a greater clearance between the rails and the ESH furnace.

The contact area between the plate clamp and the ESH upright was protected by means of a nylon bushing. This bushing was manufactured to prevent the ESH upright from being damaged by any compressive forces from tightening the clamps. The nylon provided a smooth and increased surface area for clamping. The clamp and the nylon bushing can be seen in Figure 3.27 below.

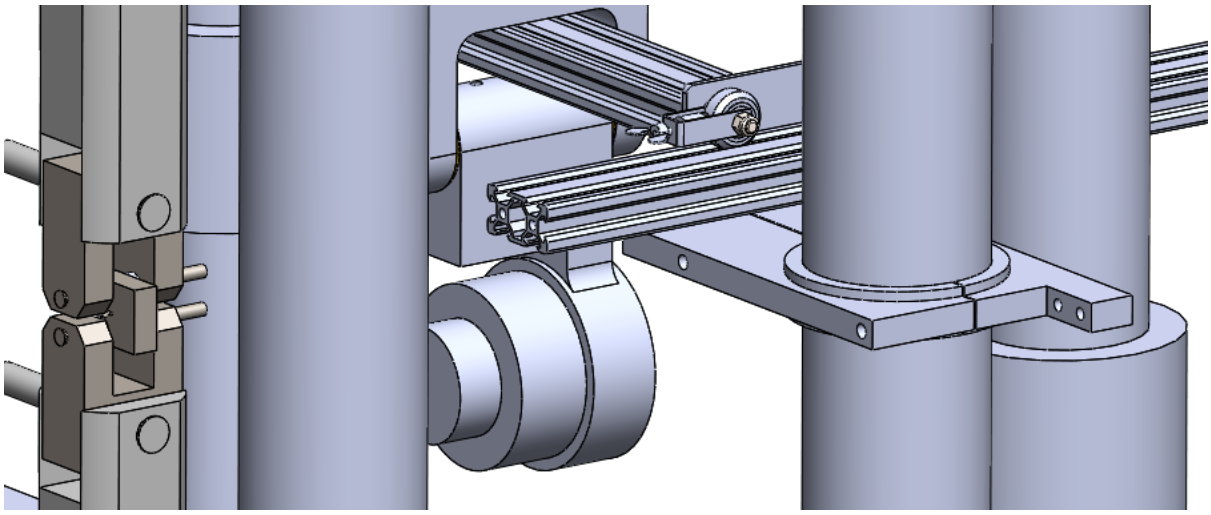

Figure 3.27: View of the clamping mechanism with rear mounted microscope

The final design included a rear mounted microscope that was mounted underneath the cross-member rather than on top of it, which can be seen in Figure 3.27 above. The desire for a rear mounted system was to prevent crowding of the test area and to provide easy access to the test specimen during FCGR testing when changing test specimens or working around the test area. It was also intended for the system to be an integral part of the machine. Mounting the microscope underneath the cross-member was also desired since it provided a lower centre of gravity and hence, no toppling moment, which significantly increased the stability of the rig. Easier movement of the microscope was promoted with the use of a horizontal roller system along the cross member. Since the magnification is so high, extremely fine adjustments are required in terms of position control of the microscope. The roller system enabled small and precise movements that the initial T-nuts did not have. The bearings in the rollers are also able to support axial loads in conjunction with radial loads. These developments are shown in Figure 3.28 below.

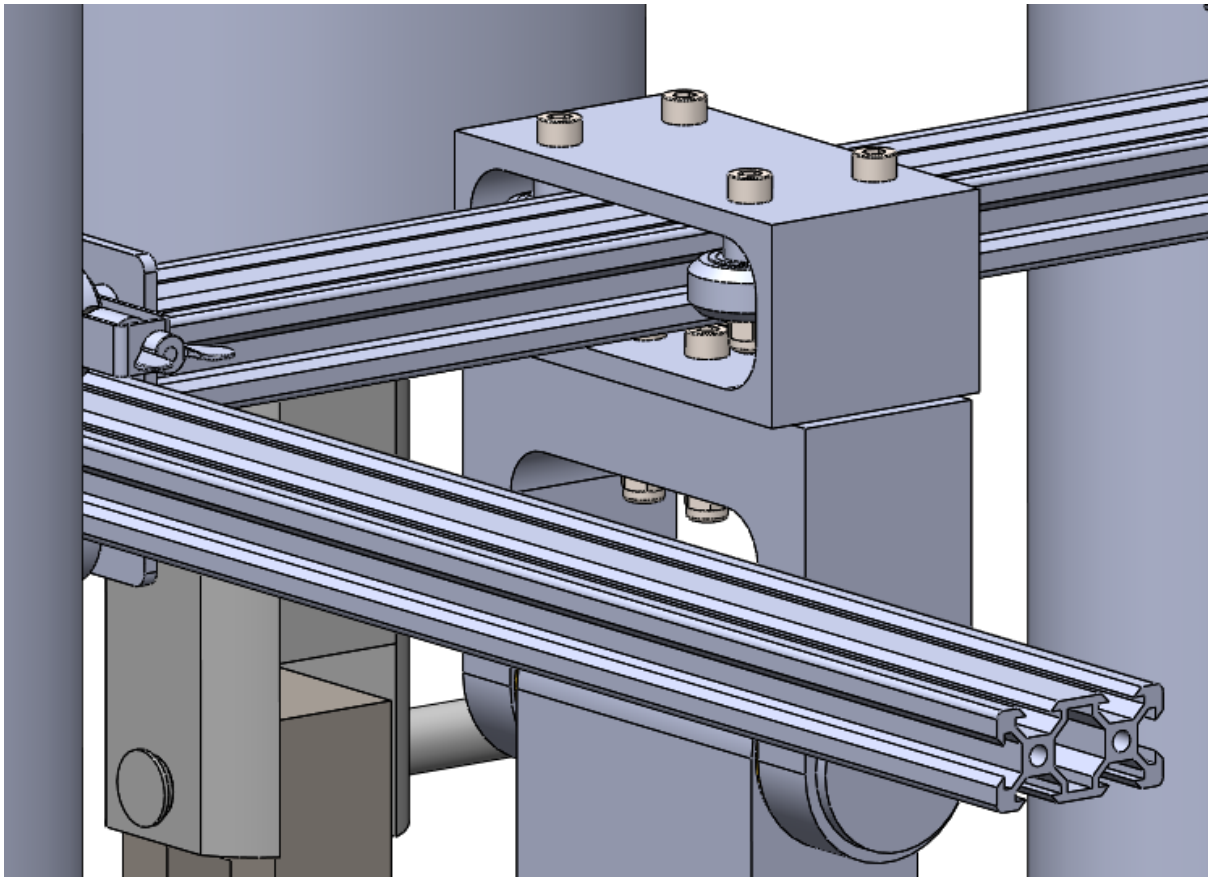

Figure 3.28: Improved microscope mount and lateral motion control

The linear motion mechanism can also be seen to be mounted on top of the plate clamp. This provided increased stability as compared to the previous designs where the rail was mounted on the side of the plate. This would put too much stress on the M5 bolts and T-nuts which would be required to support the entire mass of the system. This required the use of a 20x40 V-slot rail for added support stability. The improved design can be seen in Figure 3.29 below.

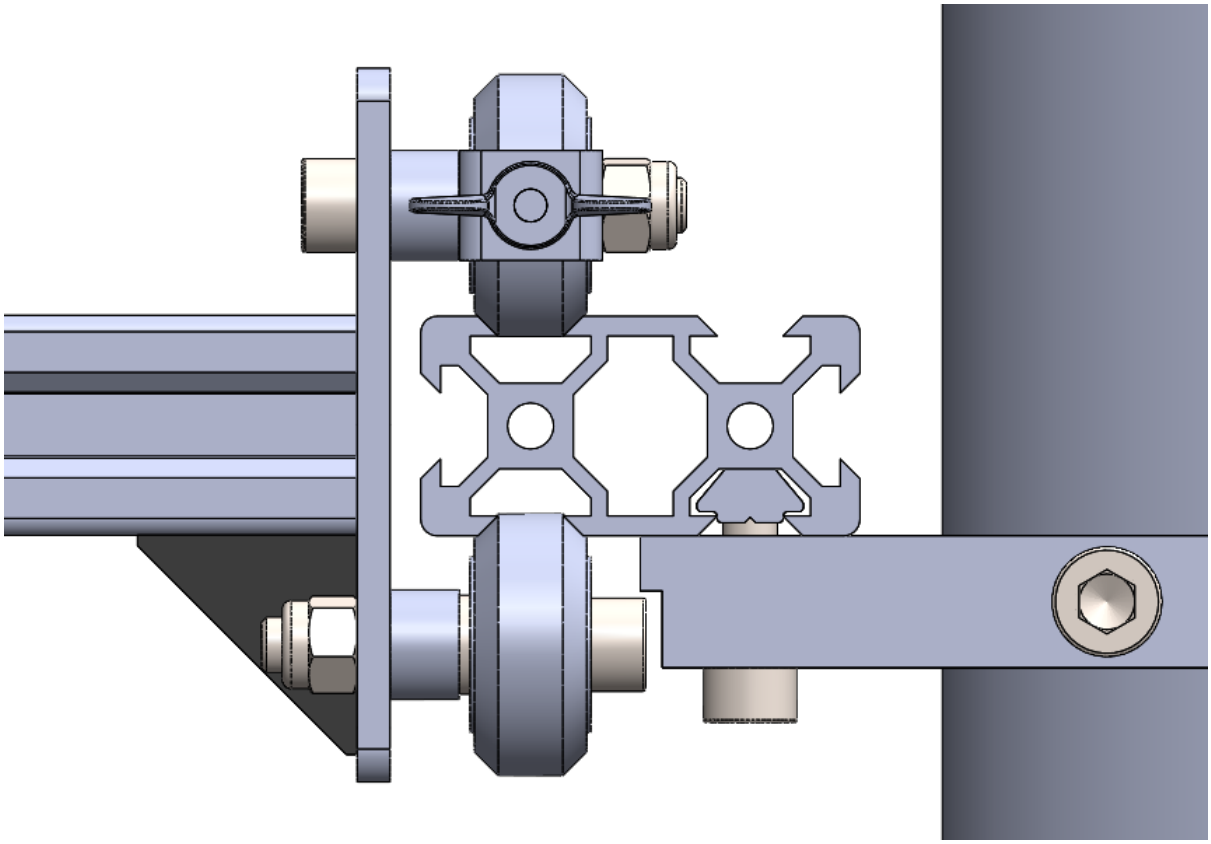

Figure 3.29: Improved support and stability of V-slot rails

It can be seen in Figure 3.29 above that the runner overhangs the shelf and the bottom roller is allowed to move past the shelf without any interference. The bolt head fastening the roller to the gantry does interfere with the shelf and therefore, a small recess has been cut out from the shelf to allow for enough clearance.

Pictures of the assembled rig on the ESH can be seen in the next section.

3.4.4. Parts sourcing and manufacture of the rig

As mentioned previously, some aspects of the rig design involve the use of 3D printer parts. These parts were ordered online from the 3Dprintingstore.co.za. The remaining components of the rig were manufactured in the mechanical engineering workshop at UCT according to the drawings attached in Appendix 11.3. Parts were also sourced from Netram technologies.

3.4.5. Rig assembly

Once the required parts for the rig were acquired, the final rig was assembled. The design of the rig was such that the assembly process was simple and not time consuming. Since the rig would be used for a high volume of fatigue and fracture toughness tests, it does not need to be removed frequently and therefore some leeway was given towards the total time to assemble. The figures below illustrate the final assembly of the completed microscope support rig.

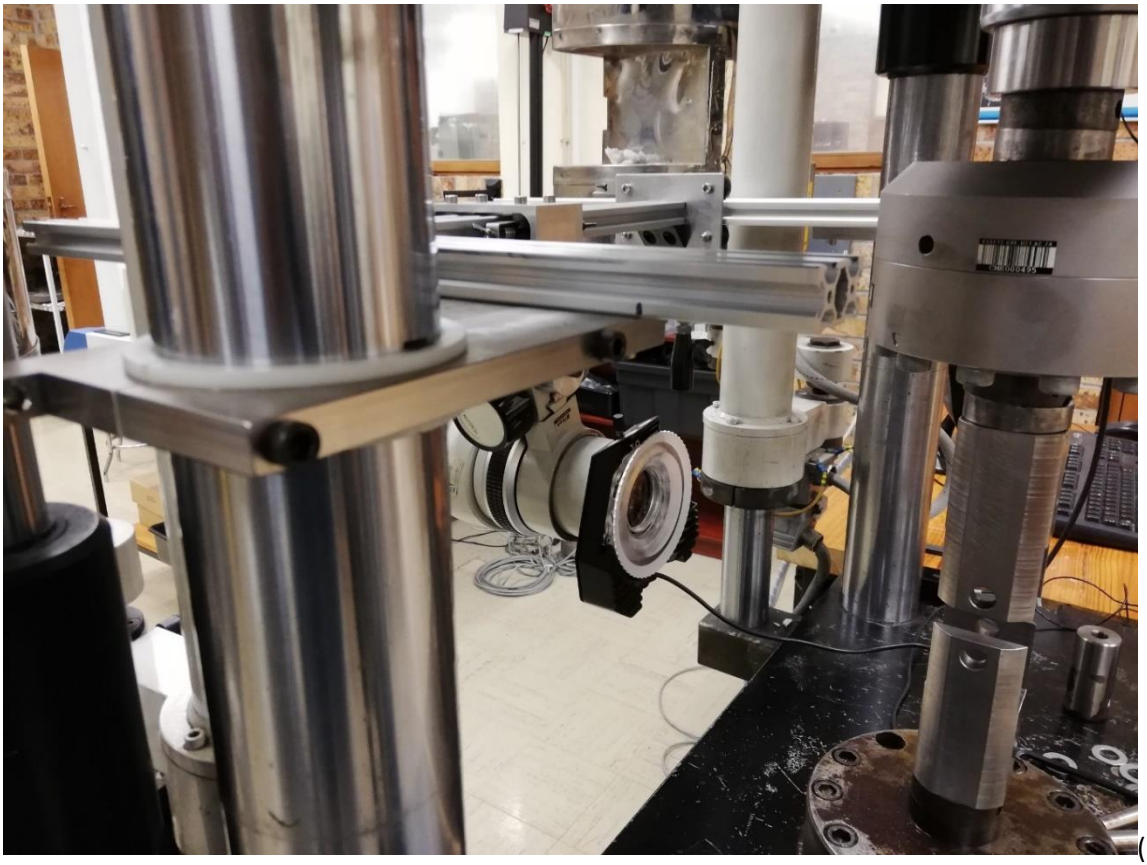

(a)

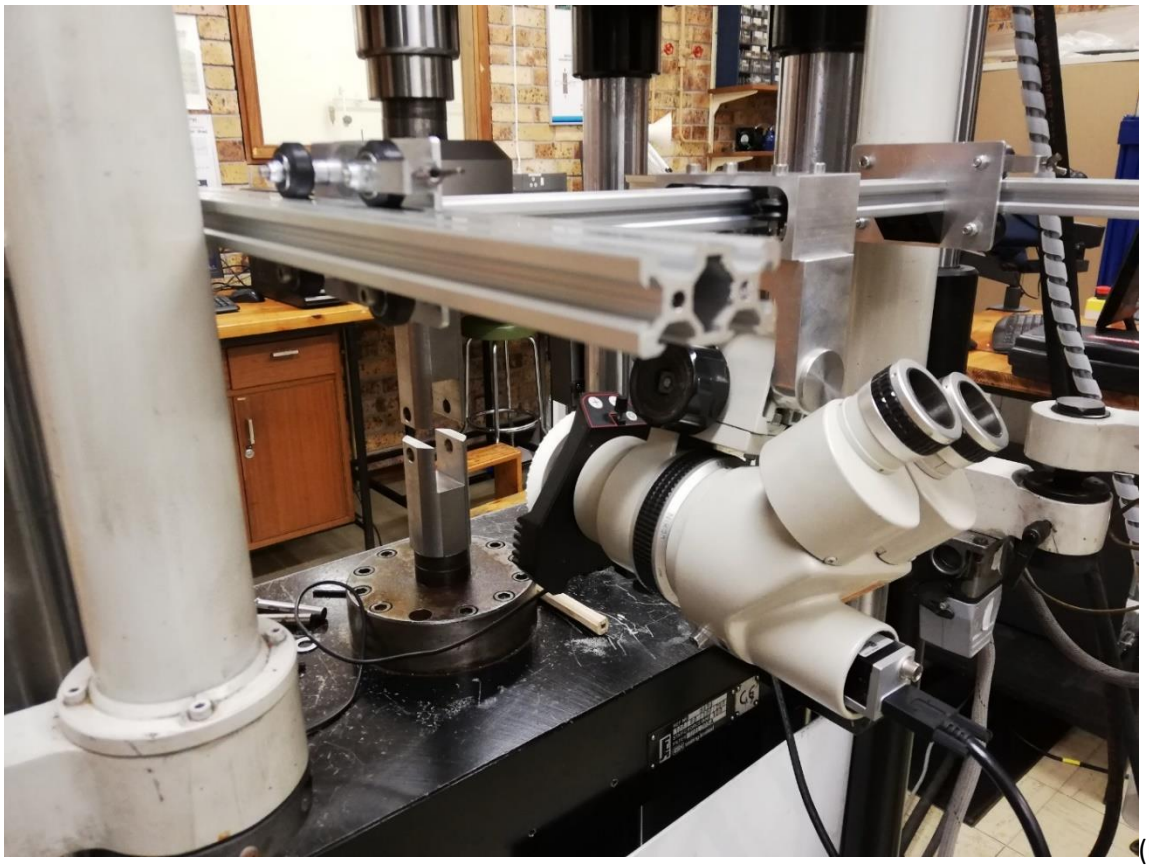

(b)

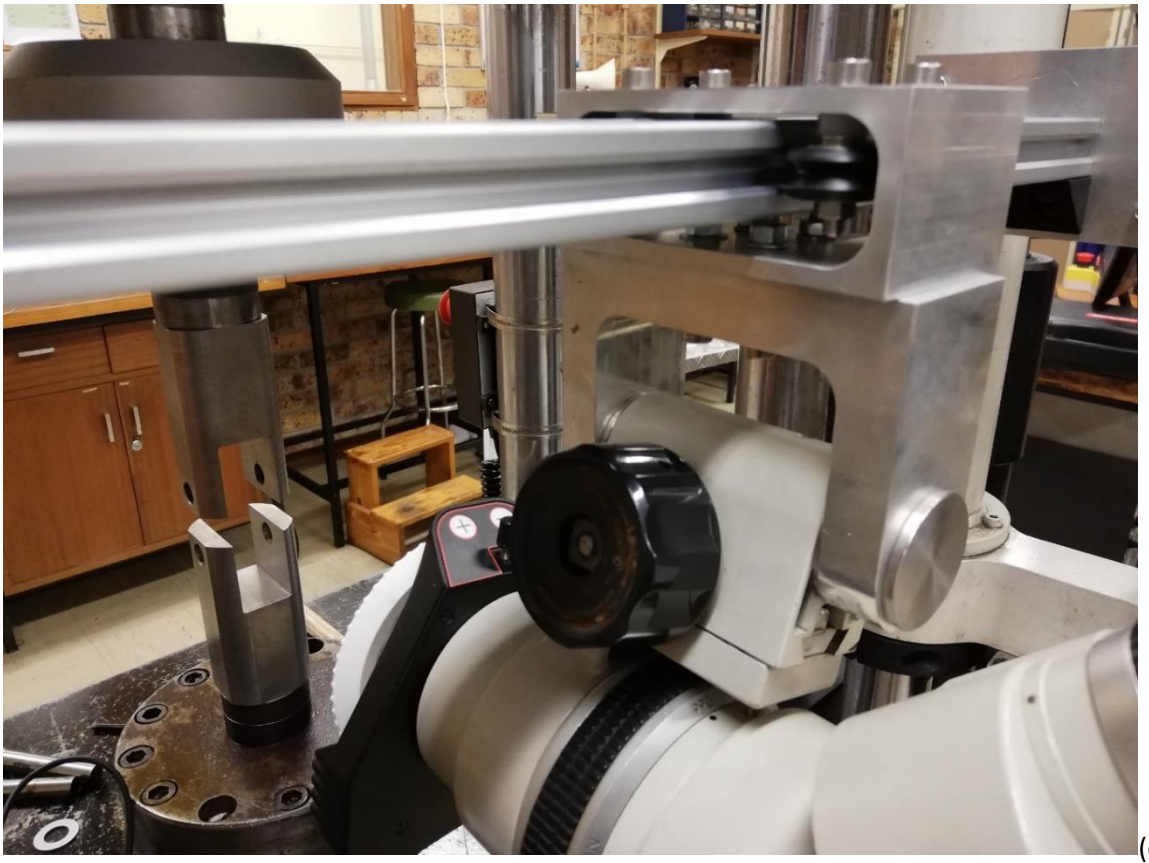
(c)

Figure 3.30: Fully manufactured and assembled rig. Clamping mechanism and front view (a); Rolling mechanism and rear view (b); Microscope mount and microscope in holder (c)

3.4.6. Functionality and ease of use

After assembly and installation of the rig, the stability and ease of use of the working parts was evaluated by adjusting the position of the microscope to and from the test area as well as testing the braking mechanism and other features such as height adjustability. The table below lists some characteristics that can be used to evaluate the overall functionality and ease of use of the rig during assembly and operation.

Table 3.1: Functionality review of rig

Metric	Satisfactory	Adequate	Needs improvement
Rolling resistance	X		
Response to vibration	X		
Stability	X		
Braking mechanism	X		
Height adjustability			X
Integration into ESH		X	
Rigidity	X		
Cost effectiveness	X		

For future developments of the rig, the height adjustability of the rig requires the most improvement in the event that various test specimens are tested.

3.4.7. Camera adaption

Once the rig was fully developed, the adaption of the camera to the microscope was required. The focal point of the original microscope was required in order to find out how far away from the lens the microscope was to be attached. After an iterative process of trying different camera positions, it was discovered that the focal point was within the housing of the microscope. Therefore, the camera needed to sit within the tube as shown in Figure 3.31.

Figure 3.31: Basler camera mounted in the tube of the microscope

The choice of camera for this application was the Basler ace acA2500-14gm due to its small size and ability to fit within the tube of the microscope as well as its availability since the camera was already owned by the Mechanical Engineering department at UCT.

3.4.7.1. Camera mounting

The Basler camera comes standard with a C-mount. The C-mount is a standard thread for mounting these types of cameras and lenses however, the microscope does not have a matching thread within the tube. Therefore, a new tube was machined from aluminium with a matching C-mount thread. The camera is then screwed on to the tube. This also prevents any unwanted light from behind the camera from striking the lens, resulting in a clearer image. The aluminium C-mount adapter and the camera attached to the adapter is shown in Figure 3.32.

(a)

(b)

Figure 3.32: C-mount adapter for camera (a); Camera attached to adapter (b)

3.4.7.2. Camera software

The Basler camera requires specific software provided by Basler to run. This software provides a variety of options for configuring the camera in terms of frame rate, resolution and exposure. An in-depth working knowledge of the overall capabilities of this camera was not necessary. The camera is able to take still images, record a video or provide a live image. It does not provide colour images, which is not a problem as colour is not needed for this application.

Still images will be the most useful function for this project. The crack measurement can then be performed on the image taken at any point during the testing. The Basler software does not allow for annotations or calibration of scales on images taken, therefore the image processing cannot be performed by this software. Micro-Manager is a free software that can be used for this function. It is able to run the camera and adjust various camera options and also provide live and still imaging. Images taken from the camera can be opened in ImageJ, which is integrated with Micro-Manager, and annotations can be drawn and measured using the software. Furthermore, scales can be calibrated using a reference image with a known scale. The Micro-Manager User interface is shown in Figure 3.33 below.

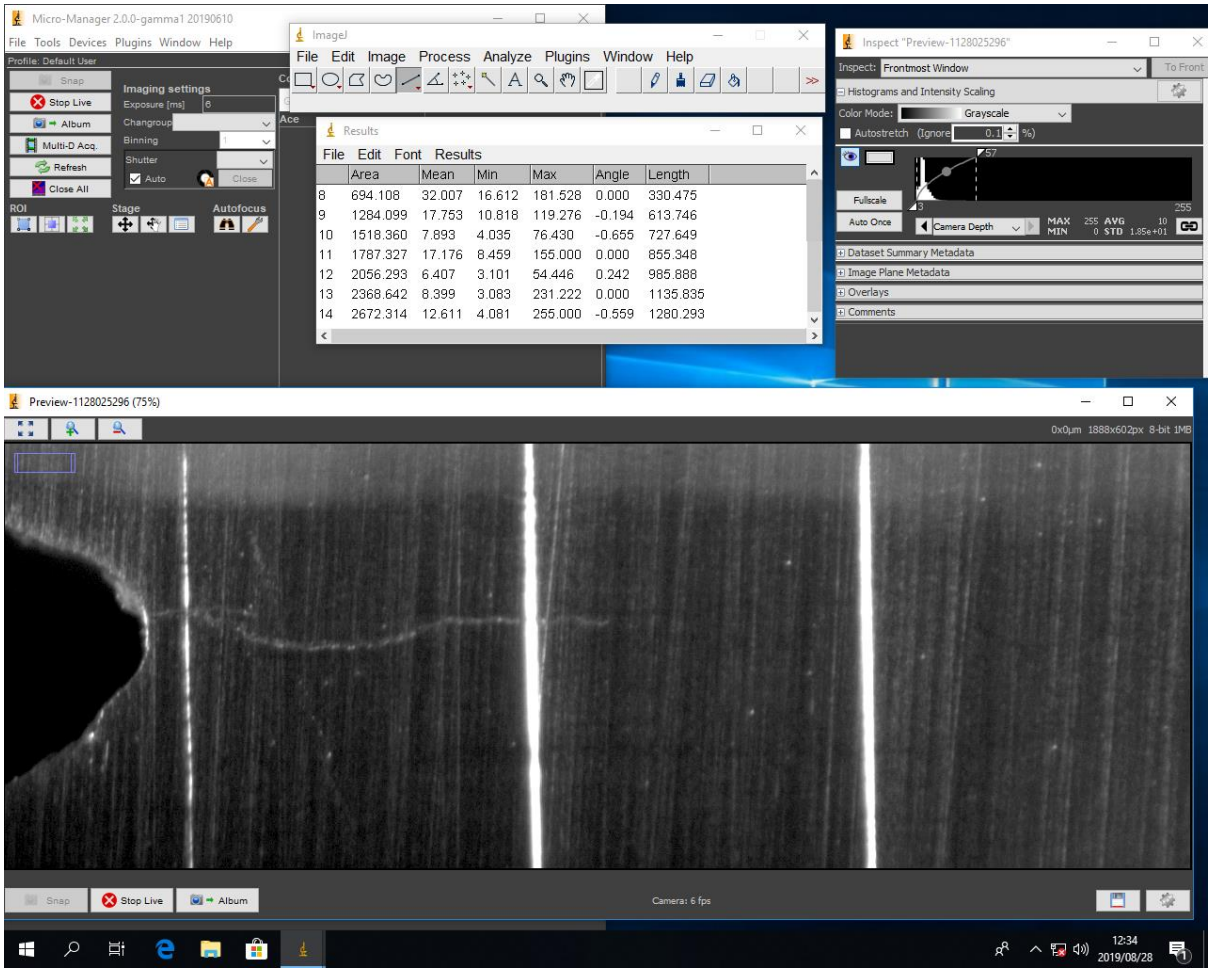

Figure 3.33: Micro-Manager User interface

In Figure 3.33 above, the interface for the Micro-Manager software can be seen. The bottom half of the image shows the live image of the test region with a fatigue crack growing. It is possible to obtain a still, live image of the sample during testing by setting the frame rate of the camera to the FCGR test frequency. Since 7 Hz was used as the test frequency, the camera frame rate was set to 7 frames per second and therefore, the camera would be taking a picture at the same position every second which

results in a still, live image. The upper left section in the figure above displays the controls for starting and stopping the live imaging and also controls for selecting the region of interest of the live image. Exposure adjustment settings can also be found here. The upper middle portion of the interface shows the measurements panel. This panel pops up when measurements are recorded during the test. Various shapes can be drawn using ImageJ which is located above the measurements panel. A scale can be set (unit per pixel) using the “Analyze” tab and regular measurements can be made by using the line shape and the measuring tool which is also located under the “Analyze” tab. The upper right portion of the interface shows the image properties of the live image which include light and contrast adjustments as well as colour adjustments if a colour camera is used. These settings can be changed to obtain an image that clearly highlights the fatigue crack.

4. Experimental testing methodology for IN718

In this section, the methodology followed throughout the preparation and testing of IN718 material will be described in detail.

4.1. Testing matrix

For this project, two different material conditions will be tested, each comprised of three different build orientations. The testing matrix to be used in this project for the fatigue crack growth rate and fracture toughness tests is shown in Table 4.1 below.

Table 4.1: Testing matrix for FCGR and FT tests

	Build orientations		
Material condition	**XY**	**XZ**	**ZX**
As-built	XY1, XY2, XY3, XY4, XY5, XY6, XY7	XZ1, XZ2, XZ3	ZX1, ZX2, ZX3
Solution treated and aged	XY8, XY9, XY10, XY11, XY12, XY13, XY14	XZ4, XZ5, XZ6	ZX4, ZX5, ZX6

The testing matrix for the tensile tests is shown in Table 4.2 below.

Table 4.2: Testing matrix for tensile tests

Material condition	**Number of specimens**
As-built	4
Solution treated and aged	4

The testing matrix above displays the number of samples for the tensile tests for the two material conditions.

4.2. Specimen parameters

The details regarding the production and preparation of the IN718 CT specimens will be outlined in this section. This includes details of the manufacturing process of the source material as well as the specimen preparation for fatigue crack growth rate and fracture toughness testing.

4.2.1. Material production details

The building process for the source material was conducted at the National Laser Centre in Pretoria. The IN718 material was built into solid blocks as shown in Figure 4.1 using a LENS system manufactured by Optomec.

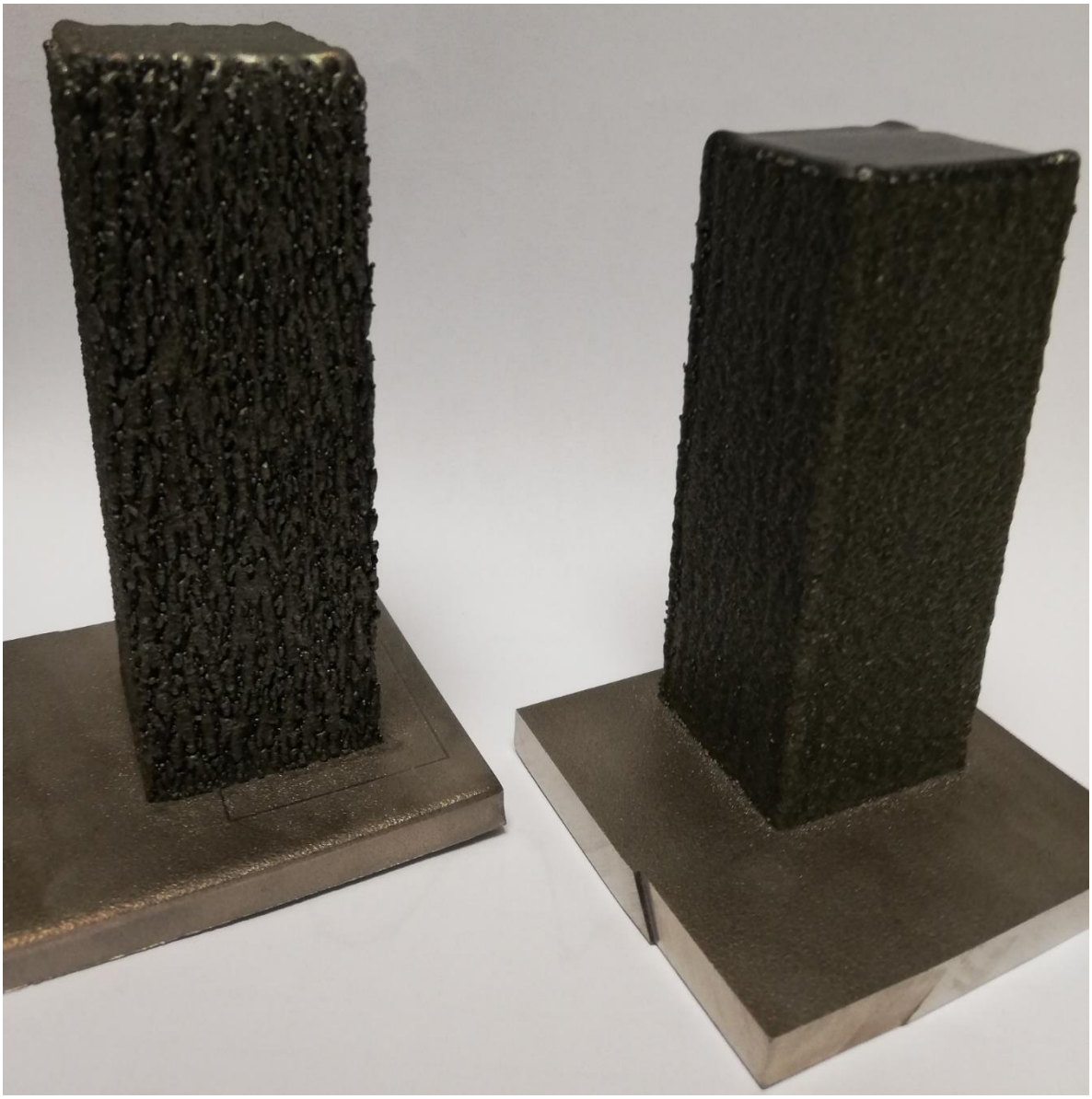

Figure 4.1: IN718 blocks built by the National Laser Centre via the LENS process for the XY orientation

IN718 powders were sourced externally and were used to make the required builds. Different build parameters were used to build the blocks that corresponded to the different build orientations due to the stability issues during the building process. Figure 4.1 above corresponds to the XY build orientations. The build parameters for these blocks are listed below.

- Laser power – 400 W
- Feed rate – 7.15 g/min
- Scan speed – 12.7 mm/s
- Layer thickness – 0.330 mm
- Hatch spacing – 0.530 mm

These parameters were used to build the specimens XY1-XY12 excluding XY7.

Figure 4.2 shows the blocks built for the XZ and ZX build orientations.

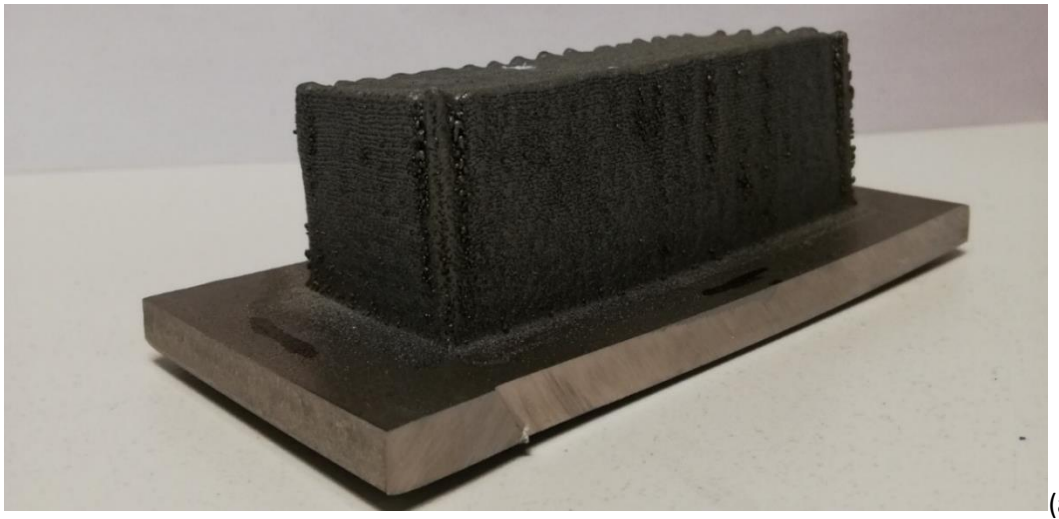

(a)

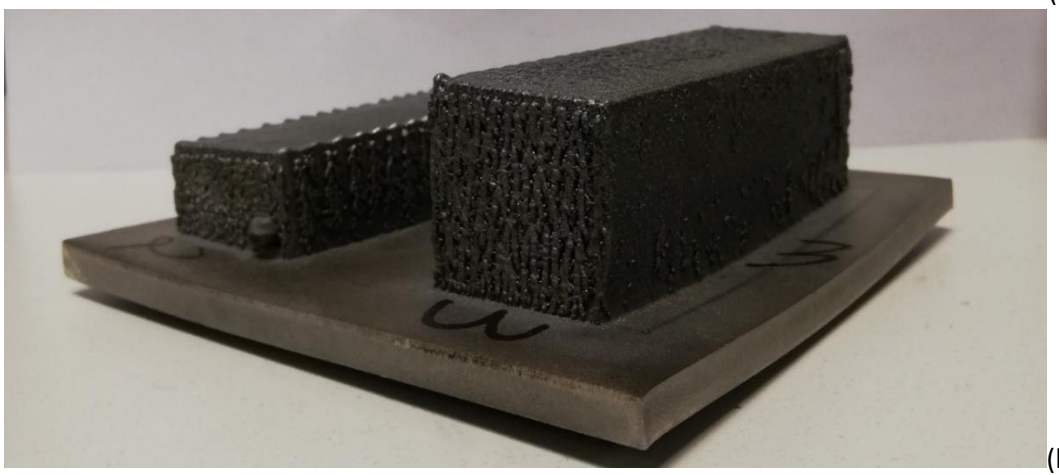

(b)

Figure 4.2: IN718 blocks built by the National Laser Centre via the LENS process for the XZ orientation (a); ZX and XY orientations (b)

In Figure 4.2 above, three blocks can be seen that are labelled 1, 2 and 3.

Block 1 was used to form the XZ orientated CT specimens and the build parameters are listed below.

- Laser power – 400 W
- Feed rate – 6.6 g/min
- Scan speed – 12.7 mm/s
- Layer thickness – 0.3302 mm
- Hatch spacing – 0.8636 mm

Specimens XZ1 – XZ6 were built using these build parameters.

Blocks 2 and 3 corresponded to the ZX and XY build orientation respectively and the parameters are listed below.

- Laser power – 400 W
- Feed rate – 7.15 g/min
- Scan speed – 12.7 mm/s
- Layer thickness – 0.2032 mm
- Hatch spacing – 0.635 mm

Specimens ZX1 – ZX6 were harvested from block 2 and specimens XY7, XY13 and XY14 were harvested from block 3.

All builds were conducted on IN718 base plates. The scanning strategy for each build was the same crosshatch pattern with the X direction being at 0 degrees and the Y direction being at 90 degrees.

4.2.2. Specimen preparation details

The source material in the form of blocks shown in Figure 4.1 and Figure 4.2 above required a machining and surface preparation process before testing could be conducted. The process outlined below was used to prepare the M201 dummy specimens for preliminary testing as well.

4.2.2.1. Specimen geometry

The IN718 as-built blocks were machined to the required specimen size as specified by ASTM E647 and E399. The dimensions for the specimen size used in this project are shown in Figure 4.3 below.

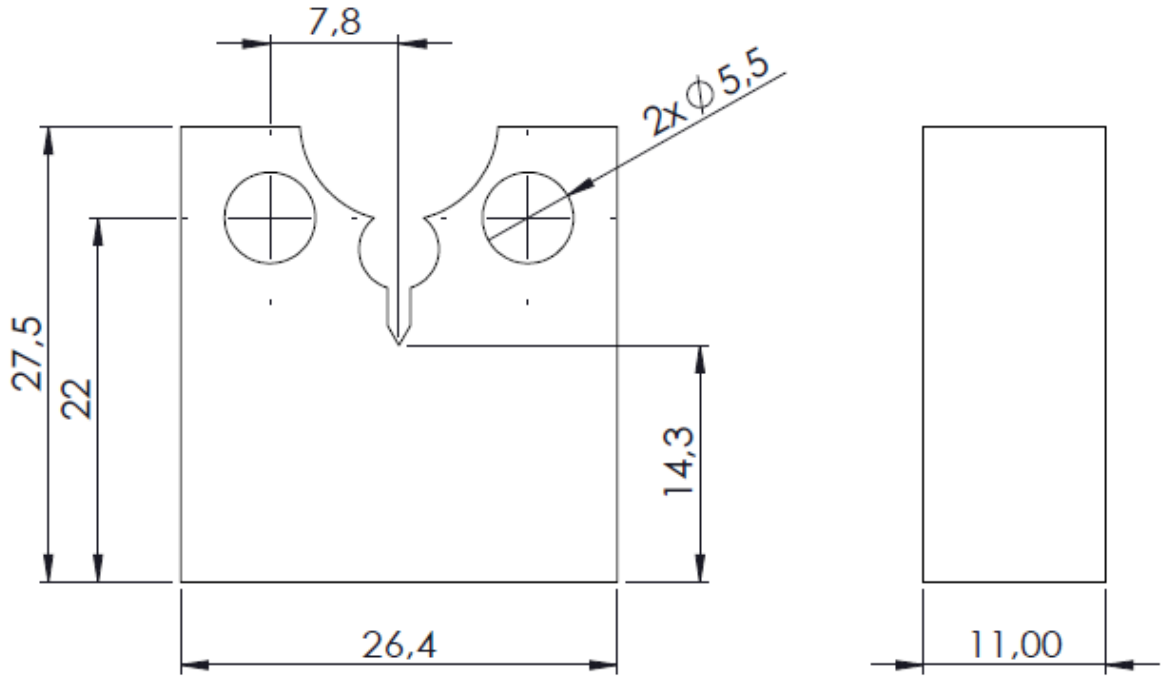

Figure 4.3: IN718 CT specimen geometry (in millimetres)

The specimen geometry is small in order to minimise costs with sufficient thickness for the test to theoretically be in the plane strain condition. The notch is designed in such a way that a clip gauge can be attached during the fracture toughness test for displacement readings.

The complex notch detail was machined by wire cutting (EDM) according to the drawing shown above and the holes were drilled and reamed to the specified dimensions. Wire cutting is a non-contact process that allows for a complex geometry profiles to be achieved with high accuracy [aa][ab]. This process is recommended by both ASTM E647 and ASTM E399 for machining the starter notch for these specimens. Furthermore, there is no risk of temperature induced stresses on the surface of the material and any irregularities are negligible since the internal portion of the material is of importance and not the machined surface. A total of 26 IN718 specimens were machined this way according to the test matrix shown in section 4.1. A composite image of the solid blocks and the machined CT specimens can be seen in Figure 4.4.

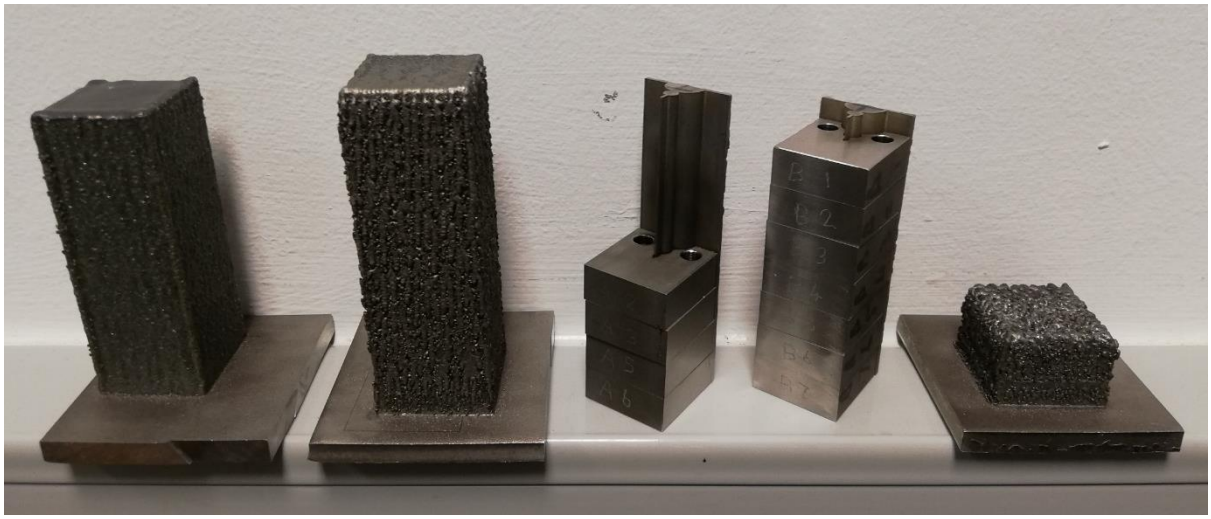

Figure 4.4: Transformation of IN718 blocks to CT specimens

4.2.2.2. Surface preparation: Polishing and marking

Before testing the specimens, a surface preparation process is required. This process was also used for the M201 dummy specimens.

Polishing of the test specimen is essential as it allows for accurate observation of the crack propagation during the test. A well-polished surface with a mirror finish prevents any visible surface defects from being observed during the test which may be mistaken for a fatigue crack. The polishing process is a sequential abrasion process.

The specimens were received after machining which was followed by a polishing procedure using the Struers LaboPol-25. A 1200 grit sandpaper was used on this machine to remove the marks generated from the machining process. The machine was operated at 300 rpm and the water tap was opened for lubrication and cooling of the sample. Both sides of the specimen were polished.

The specimen underwent a second polishing procedure to obtain a mirror finish on the surface. This was executed with the use of a Metaserv universal polisher with a 3 µm pad and a 3 µm DP paste. Only one side of the specimen was polished with this method as this would be the side facing the camera for crack length measurement.

The CT specimens were then marked at 1 mm intervals on both sides to be used as a reference during the fatigue crack propagation test as well of for the calibration of the camera crack measurement system. Highly accurate markings were not required as the calibration of the crack measurement system accounted for any inaccuracies. The markings were made with the use of a scribe, a Vernier calliper for measurement and a vice to hold the specimen in place. A marked dummy specimen can be seen in Figure 4.5.

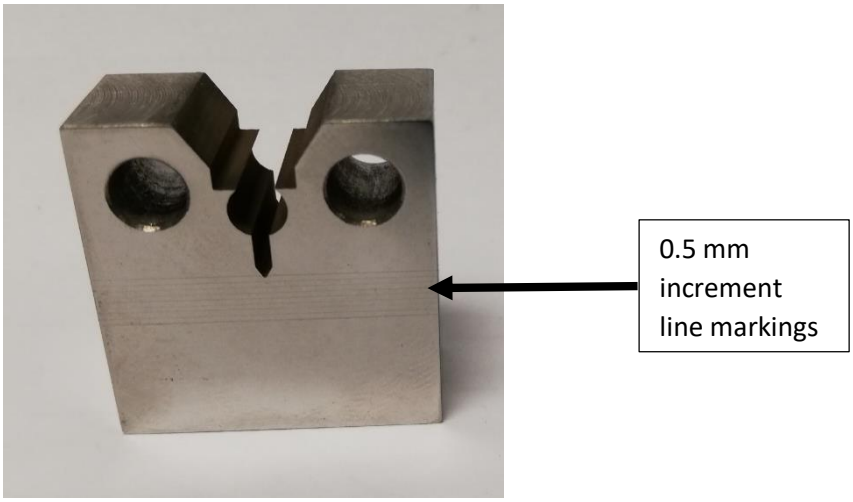

Figure 4.5: 0.5 mm markings on CT specimen

The markings on the specimen shown in Figure 4.5 above can be seen below the notch tip at 0.5 mm increments.

4.3. Tensile testing

Mini tensile specimens were harvested from unused CT specimens. The testing of the test specimens was performed at the Centre for Materials Engineering at the University of Cape Town, according the ASTM E8 test standard [47]. The tests were performed on the Instron 3365 at room temperature. A 5 kN load cell was used with a cross head speed of 2 mm/min until failure occurred. The ultimate tensile strength was extracted from the results of the test for each specimen.

The size of the mini tensile test specimens was restricted by the size of the unused CT specimens. The mini tensile specimen with respect to build direction is shown in the figure below.

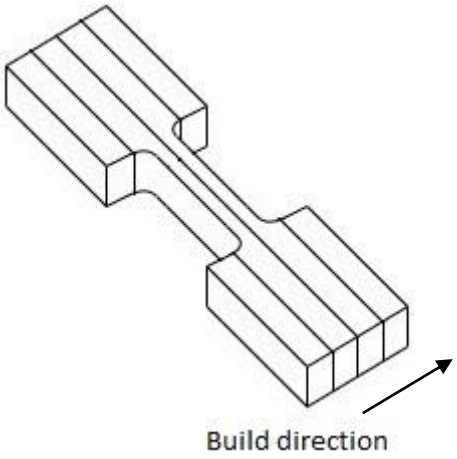

Figure 4.6: Mini tensile specimen build direction

The drawing of the mini tensile specimen is shown in Figure 4.7.

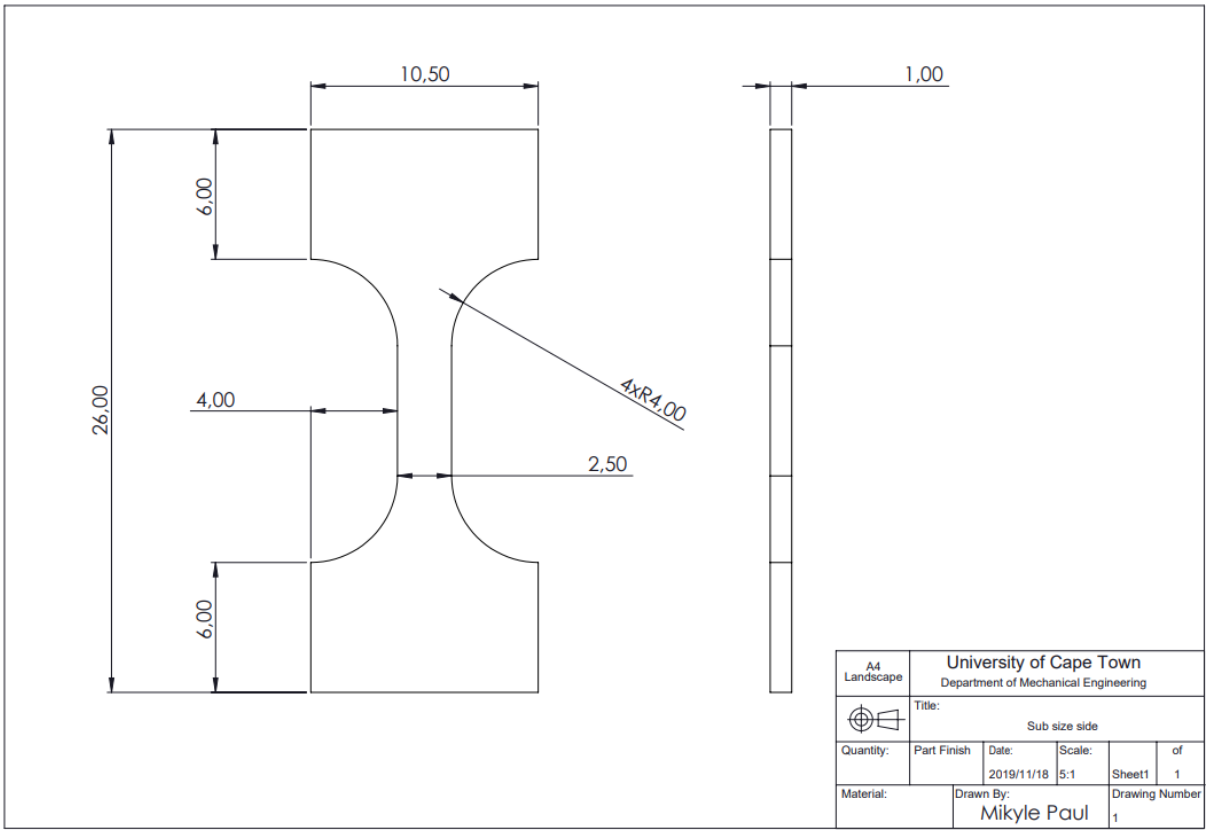

Figure 4.7: Drawing of mini tensile test specimen (dimensions in millimetres)

The tensile specimens were harvested from the CT specimens according to the drawing above with the use of a wire cutter. A wire cutter was used due to the small size of the specimens and the dimensional accuracy associated with wire cutting. A finished specimen with a prepared surface for testing is shown in the figure below.

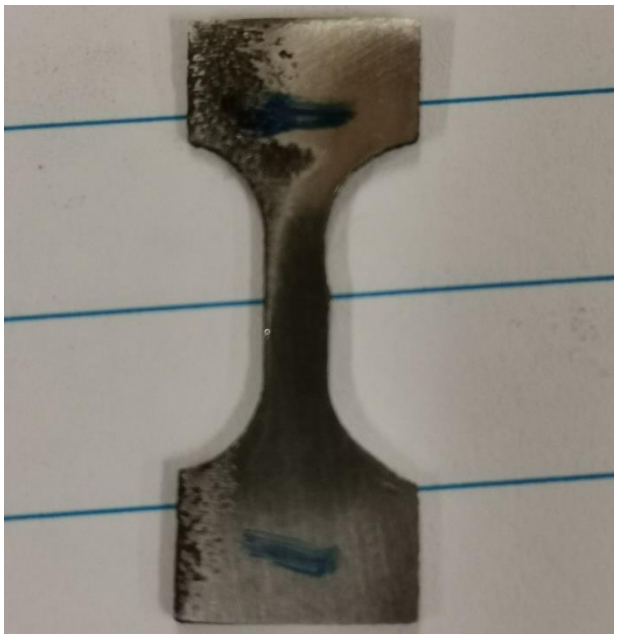

Figure 4.8: Mini tensile test specimen with prepared surface

4.4. Heat treatment protocols

The heat treatment protocol for the IN718 material was tested and optimised in Section 3.3. The heat treatment protocol to be used in this project was a solution treatment at 1200 °C for 2 hours followed by water quenching. The samples were slow heated at 100 °C/hour to 1200 °C. Thereafter, an ageing procedure at 650 °C for 16 hours was conducted followed by air cooling to room temperature. Figure 4.9 below shows the heat treatment cycle schematically.

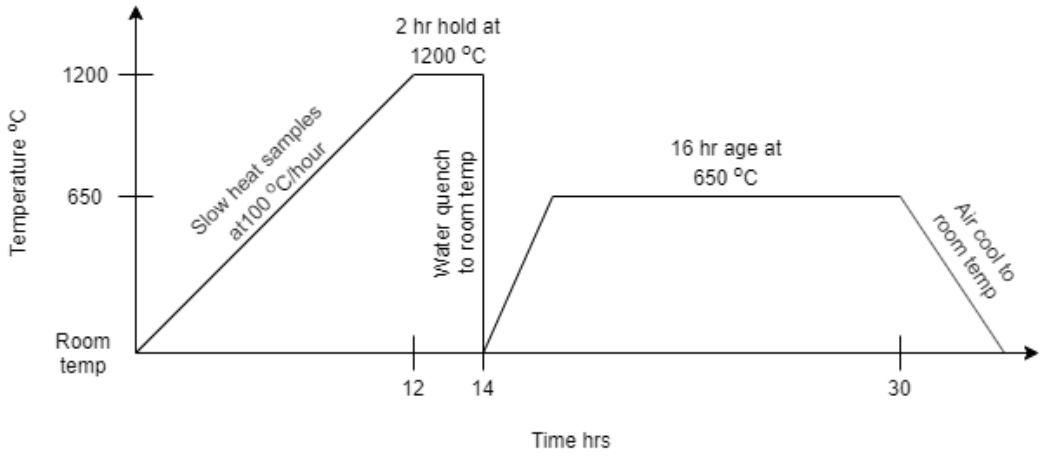

Figure 4.9: Heat treatment protocol used for the IN718 material

The 1200 °C high temperature solution treatment was performed using a Gallenkamp furnace which is shown in Figure 4.10 below.

Figure 4.10: Gallenkamp furnace

Ageing was conducted at 650 °C for 16 hours in a muffle furnace supplied by Kiln contracts which is shown in Figure 4.11 below.

Figure 4.11: Muffle furnace

The heat treatment shown above was applied to the relevant CT specimens according to the testing matrix shown in Section 4.1. The specimen dimensions were measured after heat treating to ensure that they complied with the specified drawing and there was no permanent deformation due to warping during the heat treatments.

4.5. Fatigue crack growth rate testing

The fatigue crack growth rate testing portion of this project followed the ASTM E647 guidelines. The ESH servo hydraulic testing machine was used to perform the fatigue crack growth rate tests, which is run by an Instron 8800 control system. The Instron Wave Matrix program was used to set up the test parameters and to conduct the tests. A picture of the machine can be seen in Figure 4.12.

Figure 4.12: ESH servo-hydraulic testing machine

The fatigue crack growth rate test was performed at a constant load amplitude and frequency for each test sample and evaluated the properties of the material for crack growth rates above 10^{-8} m/cycle as specified in the ASTM E647 test standard. Crack growth rates greater than 10^{-8} m/cycle were employed for the testing of the AM produced IN718 samples to reduce scatter in the data. At very low crack growth rates the variability in $\left(\frac{da}{dN}\right)$ can increase to about of a factor of five or more, whereas for higher crack growth rates, this variability reduces to about a factor of two. This occurs because of the increased sensitivity to small variations in ΔK which can be compounded by microstructural changes in the material, residual stresses, crack tip geometry, precision within the testing grips, fixtures and load application, and even the environmental conditions. Since AM manufactured components are known to produce slightly anisotropic microstructures, it is best to test at higher crack growth rates.

The procedure for fatigue crack growth rate testing is described in full detail in section 8 of the ASTM E647 test standard [43]. The fatigue crack growth rates were determined for DED manufactured IN718 CT specimens built in 3 different build orientations namely the XY, XZ and ZX build orientations as described in Section 2.8.3. Each of the build orientations consisted of as-built samples as well as heat treated samples that were all tested under similar conditions to determine the differences between as-built and heat-treated samples of different build orientations.

The specimens were loaded into the clevis as shown in Figure 4.13.

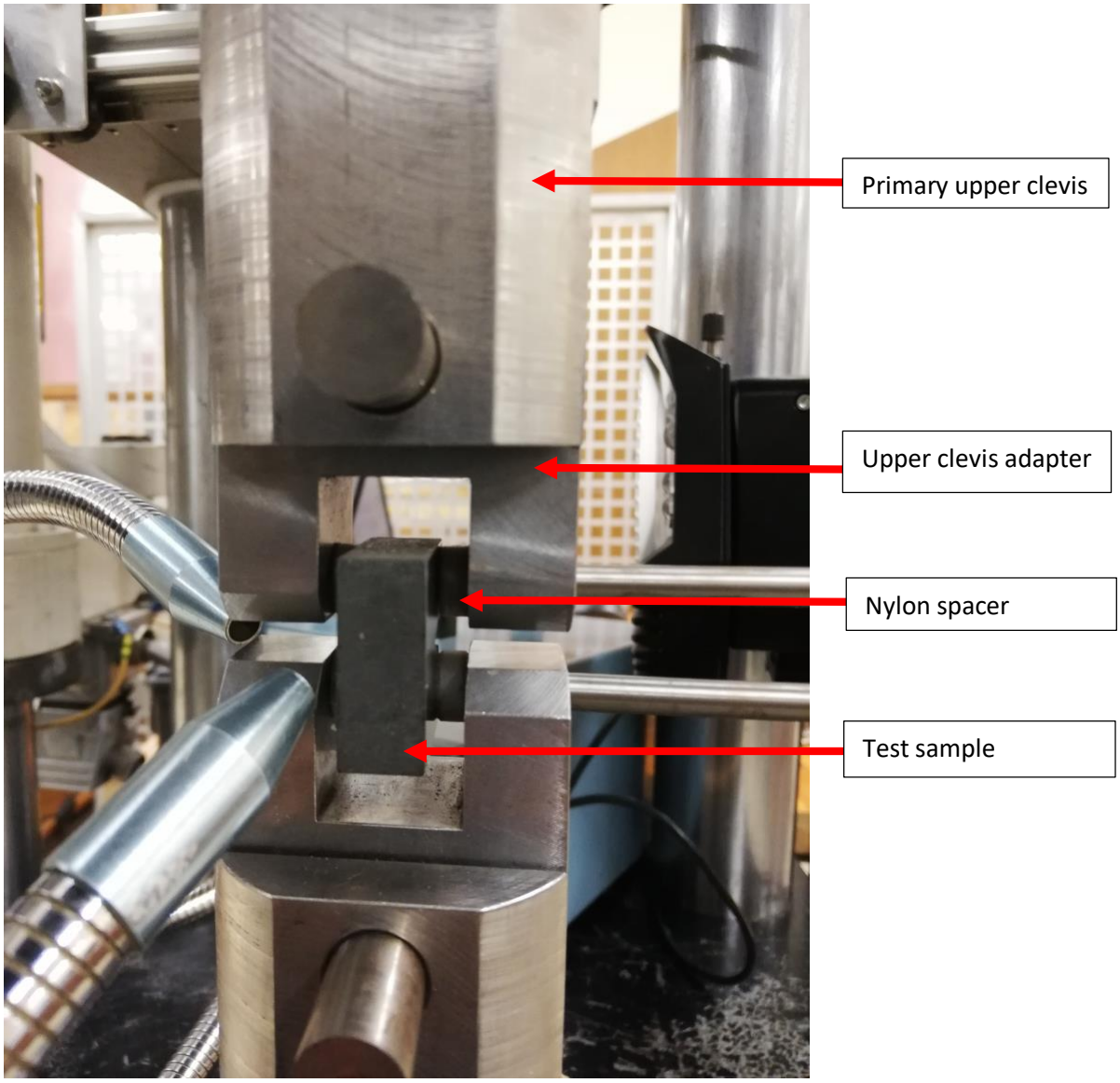

Figure 4.13: Specimen mounted into the clevises of the testing machine

Figure 4.13 above shows the test specimen in the adapter clevis, which is then fixed to the primary clevis on the ESH testing machine. It is to be noted that the specimen is fixed in place with the use of nylon spacers on either side of the specimen to provide accurate location of the specimen within the clevis and to promote stable and linear cracking. The nylon spacers are marked with the use of arrows in the figure above. The Ø5.50 mm pins were oiled before fixing the test specimen in the clevis adapter to ease the insertion process and to prevent the pins from fretting due to the cyclic loading and failing prematurely. Oiling significantly increased the life of the pins.

The majority of the test specimens were tested at a constant loading range of 7.2 kN with a stress ratio of 0.1 and test frequency of 7 Hz with a sinusoidal waveform at room temperature with some specimens being tested at slightly higher and lower load ranges. The starting stress intensity factor (SIF) range for each specimen was approximately 28 $MPa\sqrt{m}$ for the load range and notch geometry used in this experiment. Pre-cracking was conducted on each specimen until the total crack length *"a"* was approximately 8 mm for each sample. This eliminated the effects of the machined notch geometry and unified each test. Extensive pre-cracking for the recommended range as specified by both ASTM E647 and ASTM E399 was not possible due to the small sample size used. Pre-cracking was not

conducted as the specimen was not big enough to perform a pre-cracking procedure in conjunction with a FCGR test and to provide the specimen with enough uncracked ligament *(W – a)* for the proceeding fracture toughness test.

Each specimen was tested until a total crack length *"a"* of approximately 12.1 mm was obtained as specified by ASTM E399. Once this end condition was reached, the load was lowered, and the sample was cycled for a further 2000 cycles to prevent any work-hardening effects from occurring that could compromise the proceeding fracture toughness test. During the test, the number of cycles *(N)* was recorded. Crack length measurements *"a"* were taken using the crack measurement technique developed in this project (outlined in Section 3.4 of this report). This technique provided extremely accurate crack length measurements to micron accuracy using ImageJ as an image analysis, calibration and measurement platform. Any scatter in the measurements obtained was reduced by using a 3-point moving average for the crack length measurements. The 3-point moving average is calculated as shown in Equation 4.1 below.

$$\acute{a}_i = \frac{a_{i+1} + a_i + a_{i-1}}{3}$$

Equation 4.1: 3 point moving average

The number of cycles versus fatigue crack length were plotted on a graph thereafter. The fatigue crack growth rate $\left(\frac{da}{dN}\right)$ was calculated and plotted against the cyclic stress intensity factor range (ΔK) throughout the duration of the test using the smoothened crack length data from the 3-point moving average. From these results, the relevant Paris equation constants and coefficients were determined and the results for each material condition were compared. The specific testing parameters for each test specimen can be found in Appendix 11.4. The results obtained during these tests will be shown in Section 5.2 of this report.

4.6. Fracture toughness testing

Plain strain fracture toughness tests were to be performed in compliance with ASTM E399 test standard for the determination of the plain strain fracture toughness of metallic materials. The dummy specimens that were tested complied with the test standard as they behaved in a linear elastic manner however, when the IN718 CT samples were tested, the behaviour was of an elastic plastic relationship. Therefore, the ASTM E399 test method could not be used to conduct the tests. The ASTM E1820 test standard was therefore used as a guideline to perform the fracture toughness tests in conjunction with BS 7448: Part 1 [48]. The fracture toughness was expressed in terms of a comparative J_{max} value. J_{max} corresponds to the value of J at the maximum load during the fracture toughness test. For argumentative purposes, this J_{max} value was used, which follows from COD procedures when COD at the crack initiation δ_i is too conservative as in BS 7448: Part 1 [48]. Hence, COD at max loading so called "δ_{max}" is used and is sufficiently conservative because δ_i is too conservative. This is applied to J and J_{max} where J_{max} is still conservative enough for the present study. Construction of an R-curve which can be used to determine the J_{1C} will not be investigated in this project.

As mentioned in the preliminary test section of this report, the same samples that underwent the fatigue crack growth rate test would be used for the fracture toughness test. This meant that the FCGR test could not run until fracture and had to be stopped prematurely. It was decided that the pre-crack that is required for the fracture toughness test would be used to obtain the fatigue crack growth rate data. Similarly, with the FCGR test, the ESH servo hydraulic testing machine was employed to perform the fracture toughness tests on all DED produced IN718 test samples that underwent a FCGR test. The Instron 8800 control system was used to control the machine and the Instron Bluehill software was

used to set up the fracture toughness test and to record the load and displacement values throughout the test. An Instron 2670-116 displacement gauge was used to record crack opening displacement readings throughout the tests. Figure 4.14 shows the clip gauge attached to the sample prior to testing.

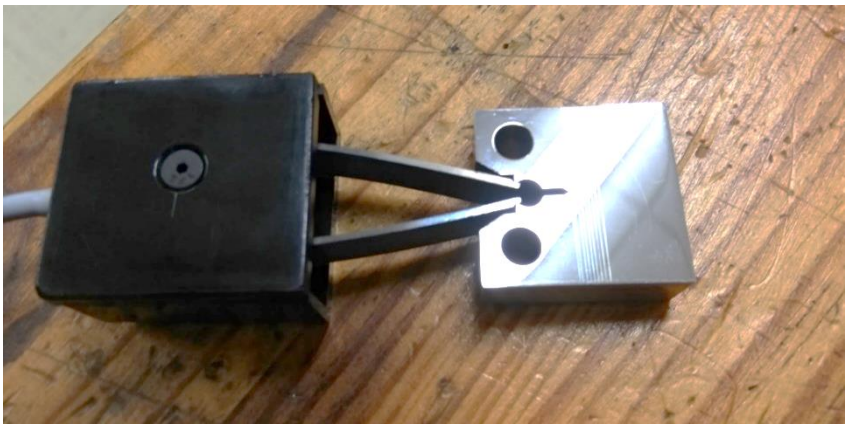

Figure 4.14: Clip gauge attached to a dummy specimen

As mentioned in Section 3.1.3, there was some discrepancy in the preliminary fracture toughness test parameters and data. It was seen that the test results were invalid for a definitive K_{1C} result due to the specimen being slightly undersized. In conjunction with this, the clip gauge was required to work below its specified working range as mentioned in Section 3.2.2. With all these factors taken into consideration, it was decided that the tests would be run as per normal according to the guidelines of testing procedure of ASTM E1820 for the IN718 samples and the data be used as comparative data since all specimens would be exposed to the exact same testing conditions. The J_{max} values could then be compared since this study is comparative.

After the FCGR test, the same samples underwent the fracture toughness test. The samples were not altered in any way during this time. Each sample was exposed to the same test parameters that were inputted into the Bluehill software. Tests were performed at room temperature and the same clevises and clevis adapters from the FCGR test were used for the FT tests. The test was set up in the same fashion as the FCGR test. Pre-cracking was conducted by means of the FCGR test mentioned in the previous section. To avoid the crack tip from becoming a work-hardened region at the end of the FCGR test, the load was lowered at the end of the FCGR test for 2000 cycles to sharpen the fatigue crack and to prevent any work-hardening from affecting the fracture behaviour of the material. As seen from the preliminary fracture toughness testing, the desired rate of increase in stress intensity factor was not possible to maintain, as the Bluehill software does not have this type of load control. After preliminary testing, a cross head speed of 0.5 mm/min (approximately 0.6 MPa√m/s for the dummy specimens) was desired however, once the first IN178 sample was tested and once it was realised that the behaviour of the material was elastic plastic, the cross-head speed was changed to 2 mm/min (in the range of 0.8 to 2.0 MPa√m/s for the as-built and heat-treated specimens respectively). This loading rate was determined by calculating J at the point of peak loading and recording the time taken to reach this peak load. The relationship $\dot{K} = \frac{\sqrt{EJ}}{t}$ was then used to determine the loading rate in MPa√m/s. Each test was run until the maximum load was reached. The material as then allowed to deform more under tension until the clip gauge reading was 8 mm. The test was then stopped manually, and the specimen was broken into two pieces by moving the cross-head upwards. The material did not experience fast fracture due to its ductile behaviour.

The load experienced during the test was plotted against the load line displacement that was captured by the clip gauge. This curve was then analysed according to the appropriate method for J-integral calculation. Octave and Microsoft Excel were used to perform the data analysis. The results obtained during these tests will be shown in Section 5.3 of this report.

After FT testing, one half of the sample was used for post-test analysis and the fracture surface of the other half was skimmed off with a mill to make a smooth surface for density and hardness tests to be performed.

4.7. Density testing

The density of each test specimen was determined according to the ASTM B311-17 test standard [49]. This test standard is used for determining the density of powder metallurgy materials containing less than two percent porosity. The density was determined in this study to quantify any major differences in the final density between the different build orientation as well as the different build parameters. The density is determined based on Archimedes principle. The skimmed half of the CT specimens were used as the surface is required to be as smooth as possible to prevent air bubbles from forming on the fracture surface of the sample which could affect the buoyancy and hence, the density result. Figure 4.15 below shows the skimmed samples that were used to perform the density tests.

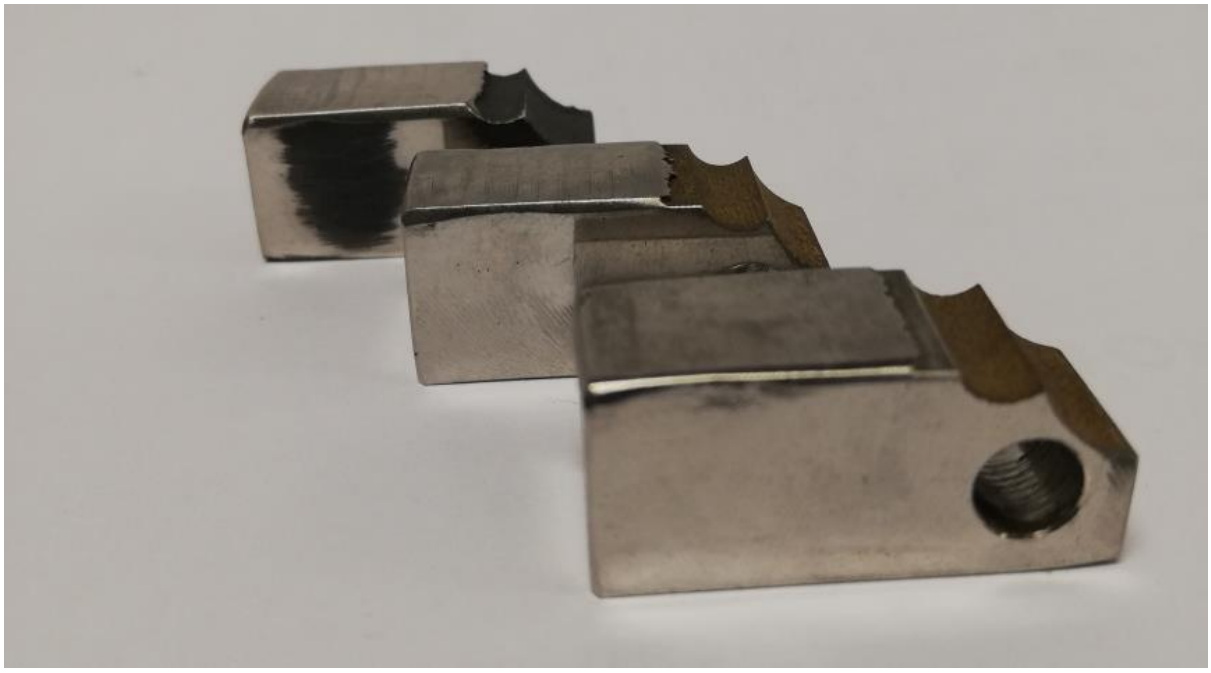

Figure 4.15: Density test specimens

Before performing the density tests, all test samples were rinsed thoroughly in ethanol to remove any oils and impurities that may have been on the surface of the material during machining. The samples were then weighed using a scale and basket support arrangement as stipulated in section 6 of ASTM B311-17. This arrangement is shown in Figure 4.16.

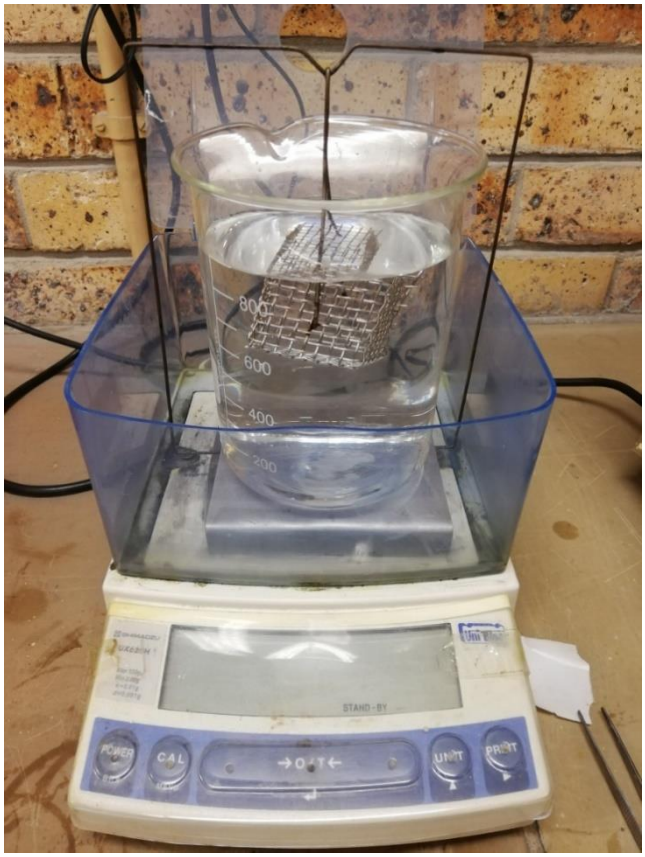

Figure 4.16: Basket support arrangement for density testing

The procedure to obtain mass measurements to calculate the density was as follows. The temperature of the water was measured prior to testing as the density of water differs as the water temperature changes. Testing was conducted at a water temperature of 22 °C, which results in a density of water of 0.9978 g/cm^3 according to table 3 in ASTM B311-17. The scale reading was then zeroed while the basket support was on the scale. The sample was placed into the basket and the mass of the sample in air was recorded on the scale. This is mass A. The beaker containing distilled water was then placed on the metal bridge as shown in Figure 4.16 and the basket was allowed to hang in the distilled water. The mass of the basket support in the water was then recorded. This is mass C. This would be a negative mass as the buoyancy effect occurs which drops the mass of the apparatus below the zero value. Thereafter, the sample was placed back into the basket and the mass was recorded on the scale. This is mass B and is the apparent mass of the sample and the basket supporting apparatus in water. The density is then calculated according to Equation 4.2.

$$\rho_{IN718} = \frac{m_A \times \rho_{water}}{m_A - (m_B - m_C)}$$

Equation 4.2: Determination of density using Archimedes priciple

Once this was complete, the process was repeated for each test specimen. According to ASTM B311-17, the density is to be reported in g/cm³ and rounded off to the nearest 0.01 g/cm³.

4.8. Hardness testing

Each IN718 CT specimen manufactured by the LENS process underwent a Vickers hardness test. This was performed on the Zwick/Roell ZHV hardness testing machine and can be seen in Figure 4.17.

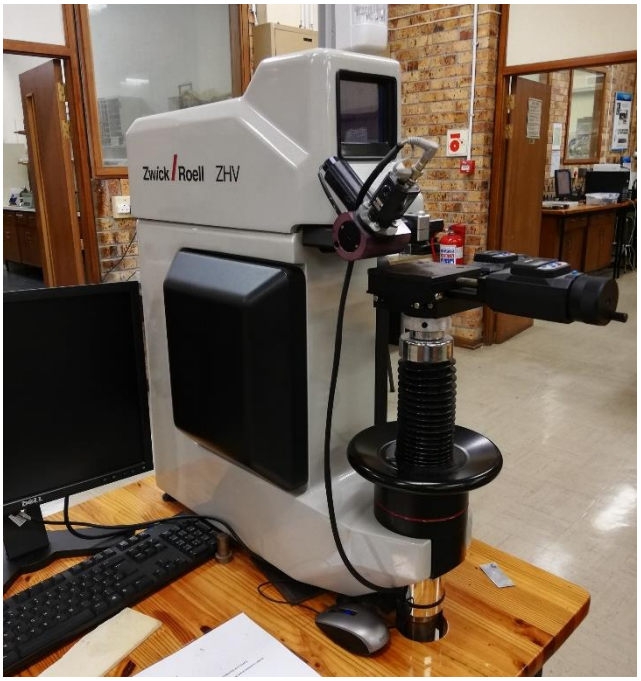

Figure 4.17: Zwick/Roell ZHV hardness testing machine

The Vickers hardness test was performed at room temperature on each IN718 specimen using a 10 kg load for 10 seconds. The skimmed surface of the fractured CT specimens were used for the hardness tests, to eliminate the effect of. An oxide layer introducing error into the actual material hardness. A total of five hardness readings were recorded for each specimen and an average was calculated thereafter.

4.9. Microscopy

The preparation for microscopy as well as the microscopy techniques will be outlined below.

4.9.1. Preparation

The IN718 material was prepared for microscopy in order to view the microstructure of the material in the three different build orientations, in both the as-built and heat-treated conditions. Three views of each material condition were prepared by slicing the material in three orthogonal directions. This can be seen in Figure 4.18 below.

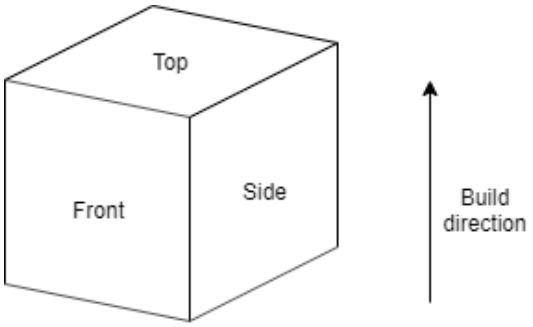

Figure 4.18: Different views of the built material with respect to the build orientation

The as-built; solution treated and quenched; and the solution treated, quenched and aged material conditions were looked at to determine microstructural differences.

A Buehler IsoMet low speed saw was used to cut the material to a suitable size for analysis. The blade used to cut the material was diamond tipped and was constantly lubricated. This low speed saw was

used to prevent the build-up of heat and plastic deformation in the specimen which could potentially alter its microstructure. Once the specimen was cut to the required size, it was hot mounted in resin with the use of a Struers LaboPress-3. This device applies a 20 kN load at a temperature of 180 °C for 8 minutes to cure the resin followed by cooling for a further 8 mins. Once the sample was mounted, it was hand-polished using a 1200 grit grinding paper on a Struers LaboPol-25. Next, the mounted specimens were polished with a Struers Tegramin-25 automatic polisher. There were various sequential polishing procedures to obtain the final surface condition utilising different polishing pads. These steps are listed below.

- MD Allegro pad (9 µm) for 10 minutes with water lubrication and cooling.
- MD Dac pad (3 µm) two times for 6 minutes each with DiaDuo2 lubricant. After the first six minutes, the pad was cleaned with soapy water and a brush and replaced for the next six minutes polish.
- MD Chem with OP suspension for 3 minutes followed by 1 minute with boiling water.

4.9.2. Techniques

In this project, light microscopy and scanning electron microscopy (SEM) were used to examine the microstructure of the material.

4.9.2.1. Light microscopy

Light microscopy was performed using a Nikon Eclipse MA200 to view the surface of the material condition in each of the views shown in Figure 4.18 above. Images were captured using a Nikon DS-Fi2 at magnifications of 100x and 500x. A Nomarski prism was used to clearly distinguish between grain boundaries, precipitates and pores that were present in the samples. The images taken for each material condition for the front view were compared with each other, the same occurred for the side and top views.

4.9.2.2. Scanning electron microscopy (SEM)

Scanning electron microscopy was performed using a Nova NanoSEM 450 to view the surface features of the material in greater detail and in higher magnification than the light microscopy. The same samples used for light microscopy were used for SEM and therefore, no further polishing was required. Electrodag 1415 was applied to the samples to prepare them for SEM which allows electromagnetic compatibility during the SEM process.

Backscattered electrons were employed during SEM to provide a high contrast between different surface features that were expected in the material such as porosity and precipitates.

Energy dispersive X-ray spectroscopy (EDS) was also employed during SEM to confirm the chemical composition of the IN718 material and to confirm the presence of porosity and precipitate distribution.

4.10. Fractography

Fractographs of the fracture surface for each build orientation and material condition were obtained using the scanning electron microscope. In this context, the fracture surface refers to exposed region within the CT specimen after it is torn apart. This was performed on one half of the fractured CT specimen as the other half was used for the density and hardness tests. The fracture surface of one sample per build orientation and material condition was examined, a total of six samples. Sample preparation was not required for this analysis because the fracture surface was to be observed as it was after fracture occurred during the FT test.

5. Results

In this section, the experimental results pertaining to the fatigue crack growth rate and fracture toughness testing of DED produced IN718 in varying build orientations will be presented along with the validity of the tests. The results from the tensile tests conducted will also be presented as well as hardness test data, microstructural observations and density.

5.1. Tensile test results

The results obtained for the tensile tests will be shown in this section for the as-built and heat-treated conditions. Stress versus strain curves were generated, as shown below. The cross sectional area of each test specimen was determined prior to testing.

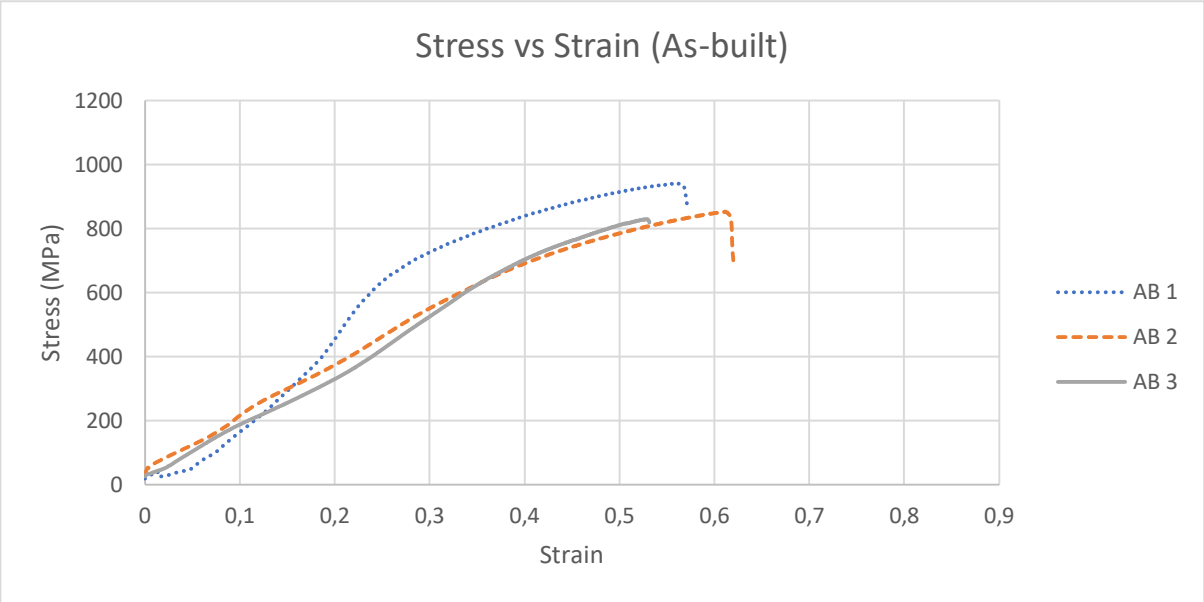

Figure 5.1: Stress vs strain curves for as-built condition

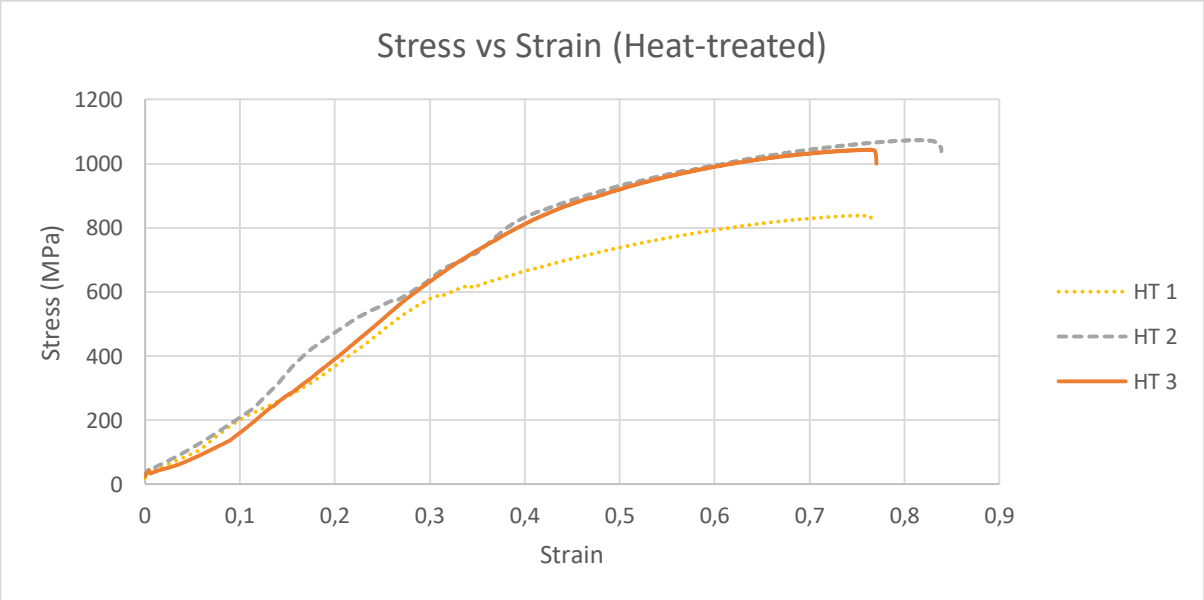

Figure 5.2: Stress vs strain curves for heat-treated condition

Table 5.1 summarises the ultimate tensile strengths for each material condition.

Table 5.1: Ultimate tensile strengths for as-built and heat-treated conditions

Specimen	Ultimate tensile strength (MPa)
AB 1	939
AB 2	853
AB 3	829
Average (AB)	**874**
HT 1	837
HT 2	1073
HT 3	1044
Average (HT)	**985**

The results shown in the table above will be discussed in greater detail in Section 6.1.

5.2. Fatigue crack growth rate test results

The results obtained during the fatigue crack growth rate tests of both the as-built and heat-treated specimens in the three different build orientations will be shown in the sections below. All specimens were not tested to failure as mentioned in Section 4.6, but were tested until the desired total crack length of approximately 12 mm was reached.

5.2.1. XY

This section contains the data obtained for both material conditions in the XY build orientation. Figure 5.3 and Figure 5.4 below represents the crack length vs number of cycles for the XY as-built and heat-treated specimens respectively.

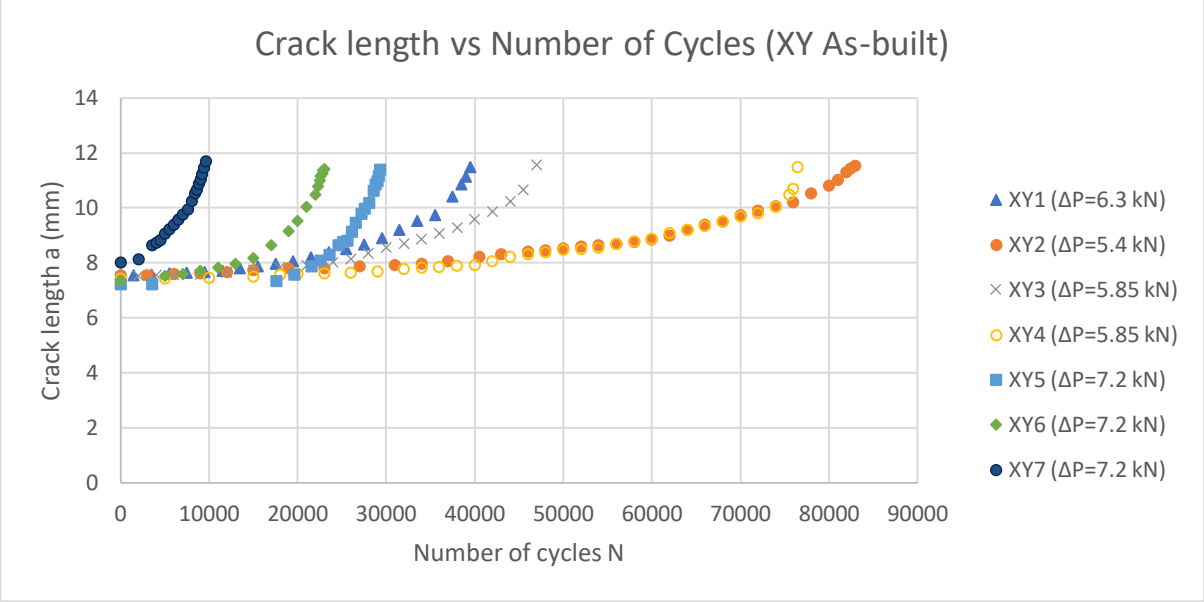

Figure 5.3: Crack length vs number of cycles for XY as-built orientation

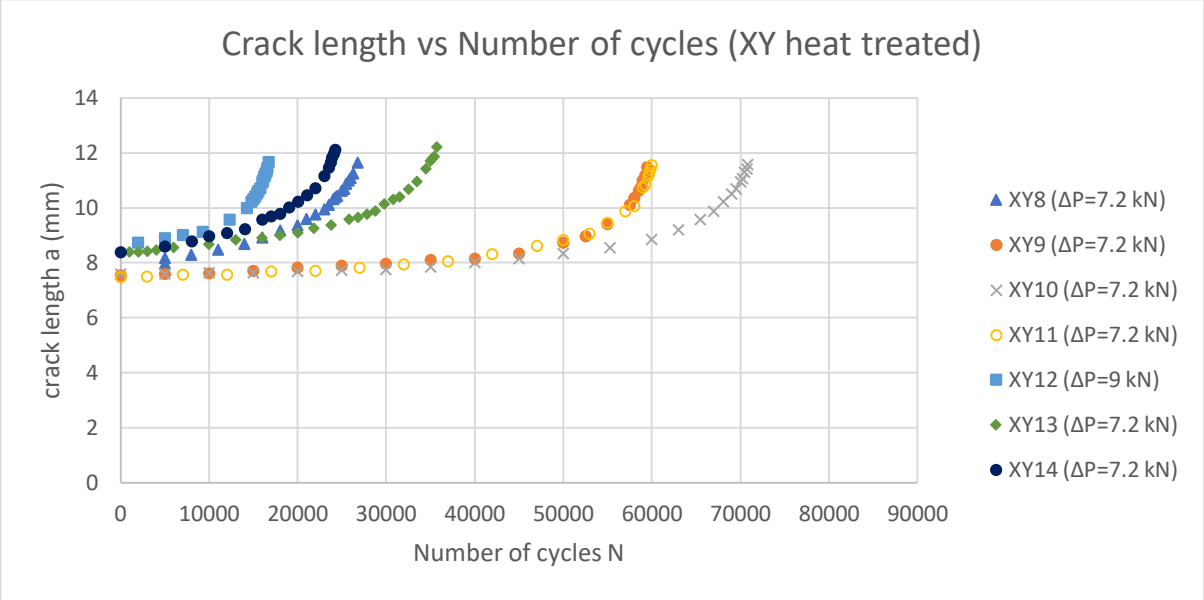

Figure 5.4: Crack length vs number of cycles for XY heat-treated orientation

It is to be noted that some of the as-built XY specimens were tested at different loads as can be seen in the figures above and according to Appendix 11.4. This explains the variation seen in the number of cycles to test end for some of the as-built samples. Other variations in the end point for each test include microstructural differences and starter notch differences.

The Paris region of each of the test specimens in both the as-built and heat-treated conditions were also plotted and can be seen in Figure 5.5 and Figure 5.6 below. The Paris region was of interest in this project and therefore, only the linear region of the curve on a log-log scale was plotted.

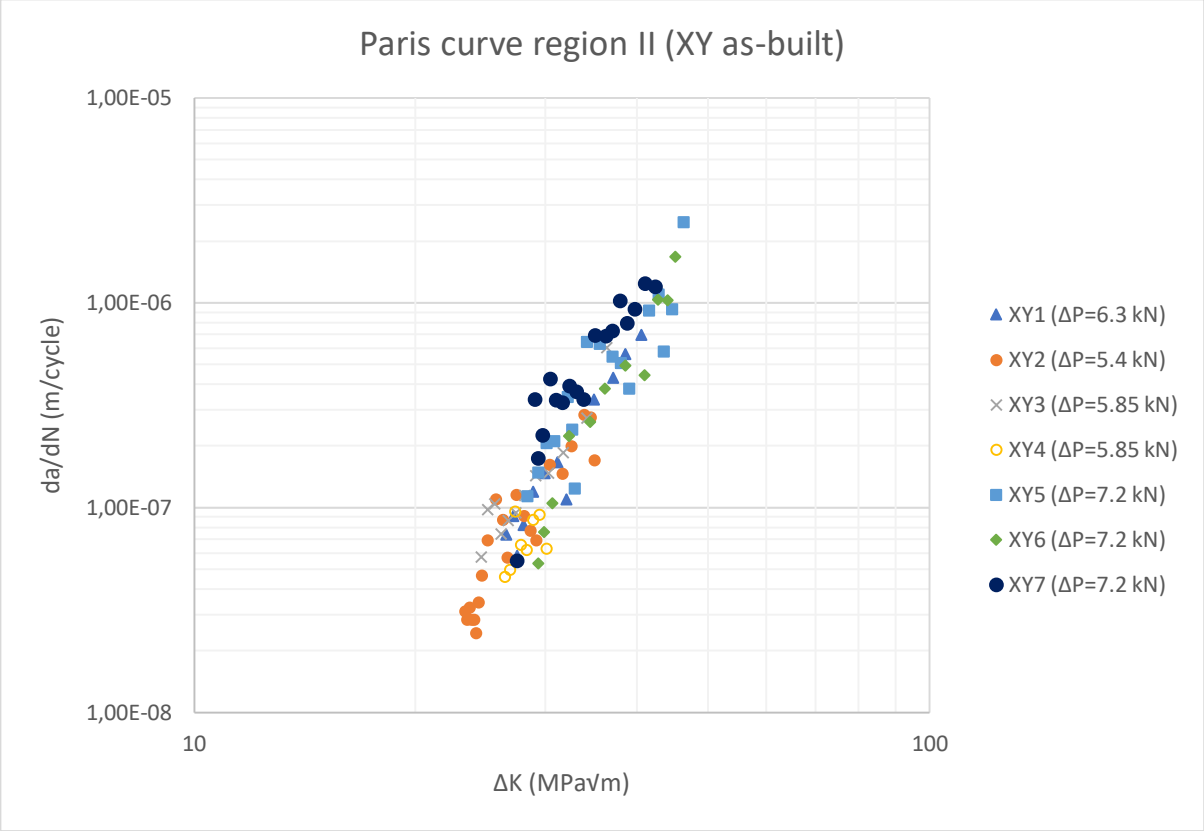

Figure 5.5: Paris curve for XY as-built orientation

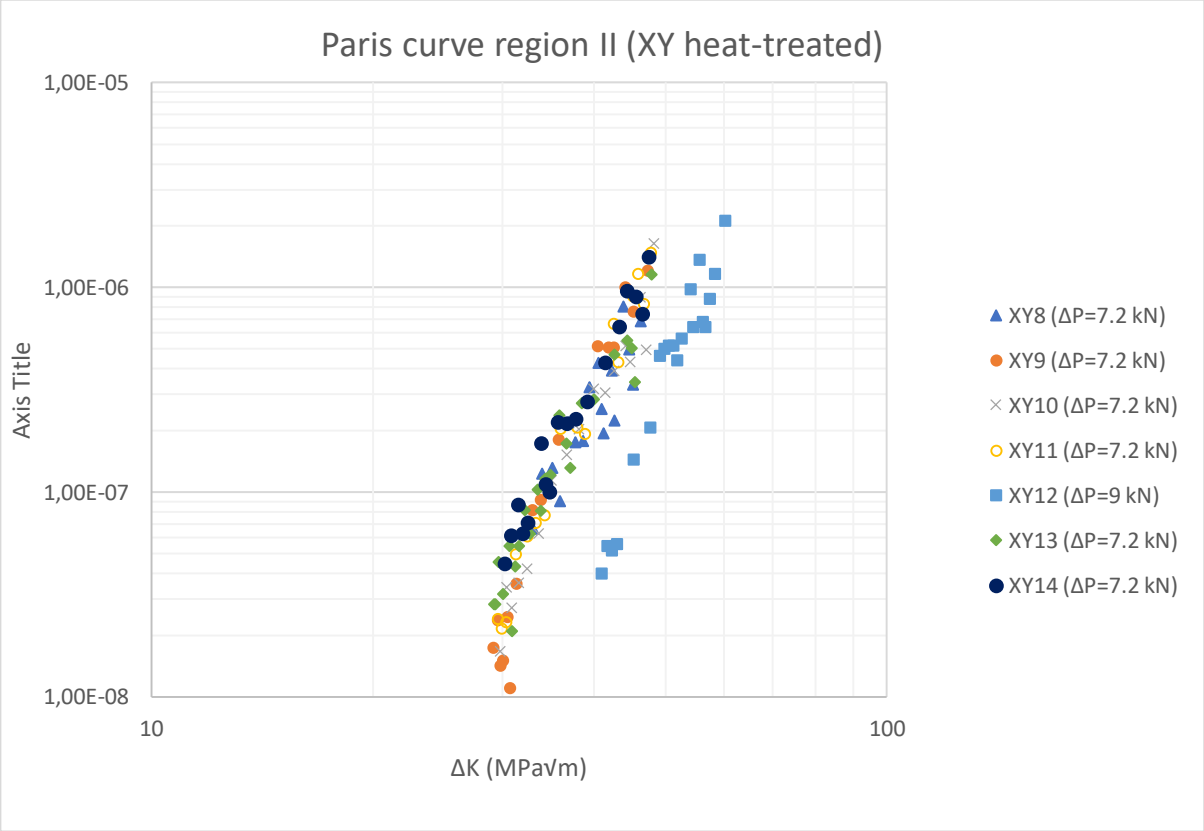

Figure 5.6: Paris curve for XY heat-treated orientation

The data above was plotted for a stress intensity factor range of between 20 and 50 MPa√m. Specimen XY12 was an exception where the stress intensity factor was plotted for a range between 40 and 60 MPa√m, as the load range was increased to 9 kN due to the high fatigue resistance of the sample. All XY build orientation samples displayed similar levels of scatter for the as-built condition. A significant reduction of scatter could be seen in the heat-treated samples.

The Paris equation for both material conditions was developed from the data obtained during the FCGR tests. The Paris equations can be seen in Table 5.2 below.

Table 5.2: Paris equations for XY orientation

Specimen	**Material condition**	**Paris Equation**
XY1	As-built	$\frac{da}{dN} = (3.14 \times 10^{-15})\Delta K^{5.19}$
XY2		$\frac{da}{dN} = (2.21 \times 10^{-16})\Delta K^{5.88}$
XY3		$\frac{da}{dN} = (5.26 \times 10^{-16})\Delta K^{5.72}$
XY4		$\frac{da}{dN} = (8.81 \times 10^{-13})\Delta K^{3.38}$
XY5		$\frac{da}{dN} = (1.07 \times 10^{-15})\Delta K^{5.52}$
XY6		$\frac{da}{dN} = (9.08 \times 10^{-16})\Delta K^{5.60}$
XY7		$\frac{da}{dN} = (3.62 \times 10^{-15})\Delta K^{5.29}$
Average		$\frac{da}{dN} = (15.8 \pm 5) \times 10^{-16}\Delta K^{5.53 \pm 0.1}$
XY8	Heat-treated	$\frac{da}{dN} = (3.38 \times 10^{-20})\Delta K^{7.99}$
XY9		$\frac{da}{dN} = (2.64 \times 10^{-21})\Delta K^{8.75}$
XY10		$\frac{da}{dN} = (1.68 \times 10^{-22})\Delta K^{9.50}$
XY11		$\frac{da}{dN} = (5.17 \times 10^{-21})\Delta K^{8.61}$
XY12		$\frac{da}{dN} = (1.21 \times 10^{-23})\Delta K^{9.69}$
XY13		$\frac{da}{dN} = (2.11 \times 10^{-19})\Delta K^{7.58}$

XY14		$\frac{da}{dN} = (9.33 \times 10^{-19})\Delta K^{7.26}$
Average		$\frac{da}{dN} = (1.69 \pm 1) \times 10^{-19}\Delta K^{8.48 \pm 0.3}$

XY4 was excluded from the calculation of the average as the results obtained during the FCGR test of XY4 were anomalous. The fatigue crack split several times during the test, resulting in several decreases of crack growth rate. This prevented a linear Paris region from forming. This will be outlined in greater detail in Section 6.2.

5.2.2. XZ

The results obtained from the FCGR testing of the XZ build orientation in both material conditions will be shown below. Figure 5.7 and Figure 5.8 display the number of cycles vs crack length for the as-built and heat-treated conditions respectively. It is also to be noted that the sample space for this build orientation is much less than the XY orientation due to the lack of test specimens therefore, three specimens were tested per material condition.

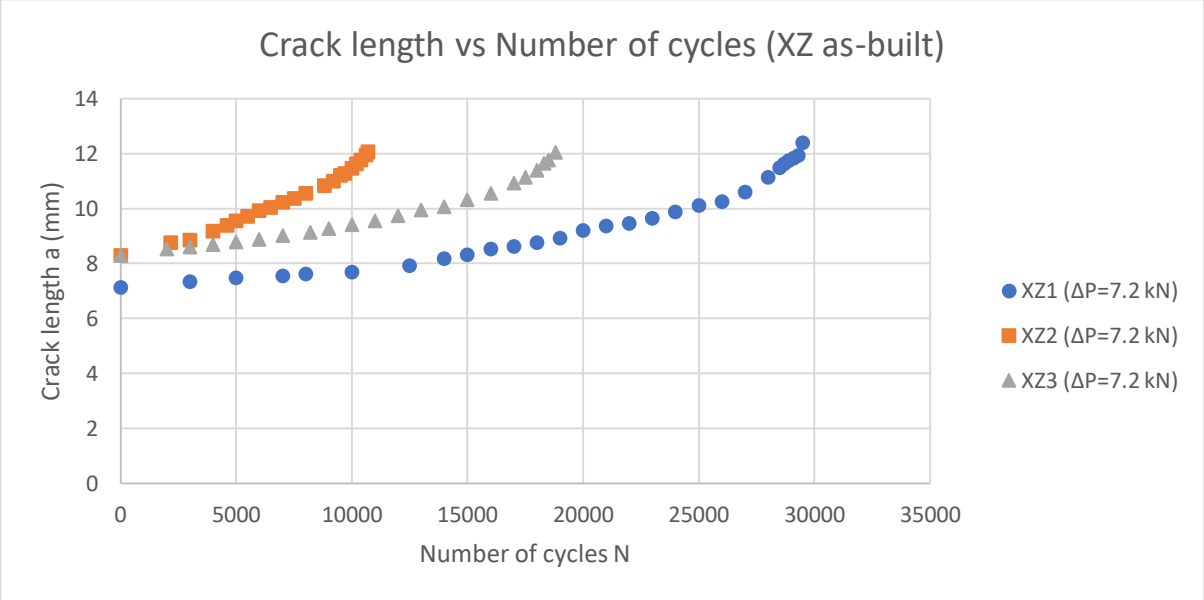

Figure 5.7: Crack length vs number of cycles for XZ as-built orientation

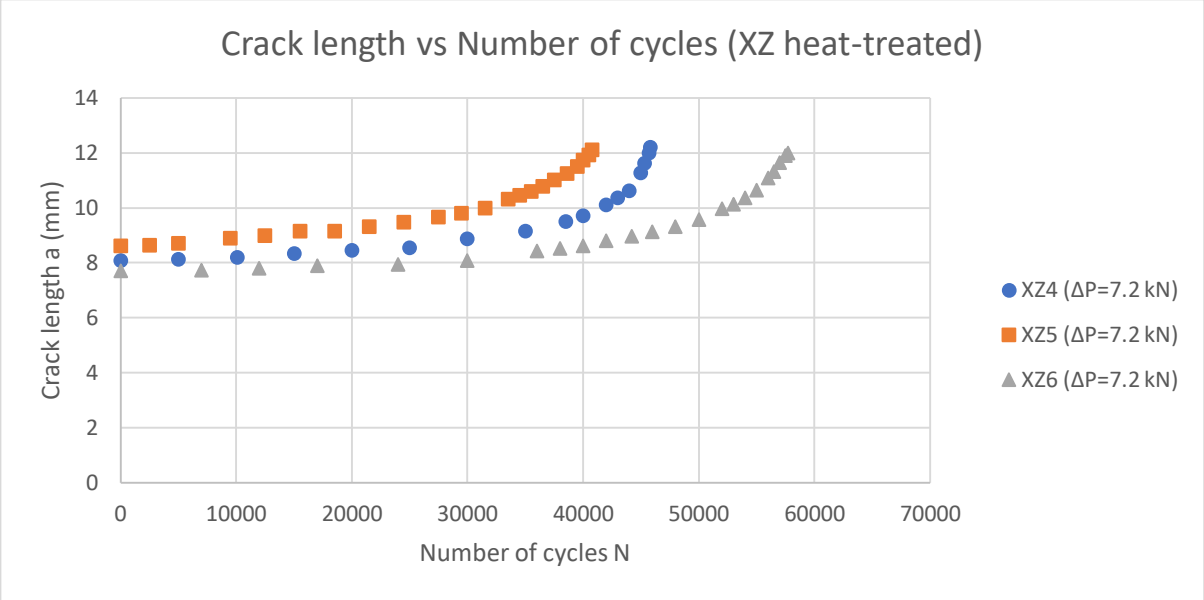

Figure 5.8: Crack length vs number of cycles for XZ heat-treated orientation

All tests were performed under identical loads but a wide variation in the fatigue crack growth behaviour can be seen in both the as-built and heat-treated conditions. This variation was similar to that of the XY orientation when comparing specimens tested under the same loads. The difference is significantly less in the heat-treated condition.

The Paris region of both material conditions in the XZ orientation can be seen in Figure 5.9 and Figure 5.10 below. These were plotted in the same fashion as the XY orientation.

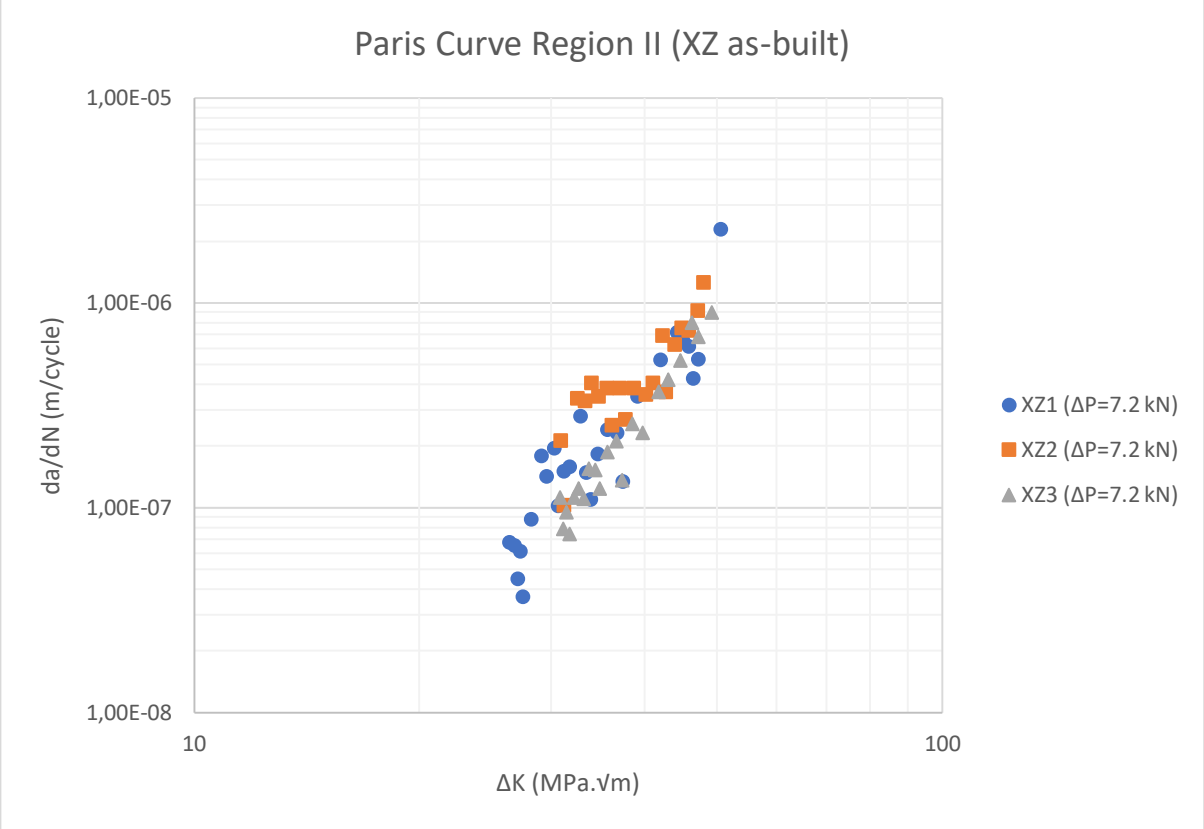

Figure 5.9: Paris curve for XZ as-built orientation

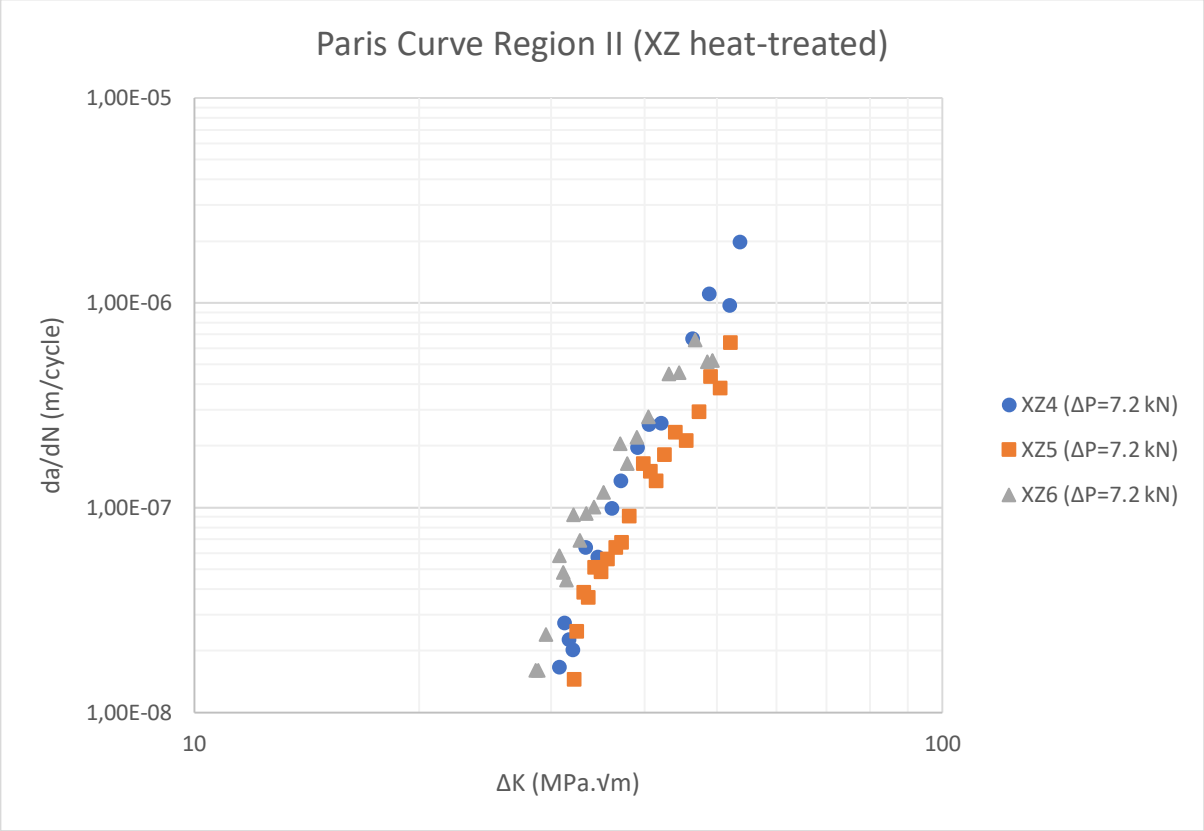

Figure 5.10: Paris curve for XZ heat-treated orientation

The level of scatter in the data of the as-built condition is much higher than that of the heat-treated condition. The heat-treated condition demonstrates a more linear correlation than the as-built condition.

The Paris equation for each of the XZ test specimens was developed using the linear range of the data shown in Figure 5.9 and Figure 5.10 above. A summary of the Paris equations is shown in Table 5.3 below.

Table 5.3: Paris equations for XZ orientation

Specimen	**Material condition**	**Paris equation**
XZ1	As-built	$\frac{da}{dN} = (2.45 \times 10^{-15})\Delta K^{5.26}$
XZ2		$\frac{da}{dN} = (1.61 \times 10^{-16})\Delta K^{5.83}$
XZ3		$\frac{da}{dN} = (2.75 \times 10^{-15})\Delta K^{5.03}$
Average		$\frac{da}{dN} = (17.8 \pm 7) \times 10^{-16}\Delta K^{5.38 \pm 0.2}$
XZ4	Heat-treated	$\frac{da}{dN} = (3.91 \times 10^{-20})\Delta K^{7.92}$

XZ5		$\frac{da}{dN} = (9.81 \times 10^{-19})\Delta K^{6.88}$
XZ6		$\frac{da}{dN} = (2.50 \times 10^{-18})\Delta K^{6.84}$
Average		$\frac{da}{dN} = (11.7 \pm 6) \times 10^{-19}\Delta K^{7.22 \pm 0.3}$

Each XZ test specimen was tested with the same load range of 7.2 kN with a load ratio of 0.1. The stress intensity factor range of interest for these tests ranged from approximately 20 to 50 MPa√m. Improvements in the fatigue crack resistance and stability were seen in the heat-treated condition.

5.2.3. ZX

The results obtained from the FCGR testing of the ZX test specimens in the as-built and heat-treated conditions are shown in this section. The number of samples (sample space) for this build orientation is the same as the XZ condition due to the quantity of supplied material. The number of cycles vs crack length data can be seen in Figure 5.11 and Figure 5.12 below.

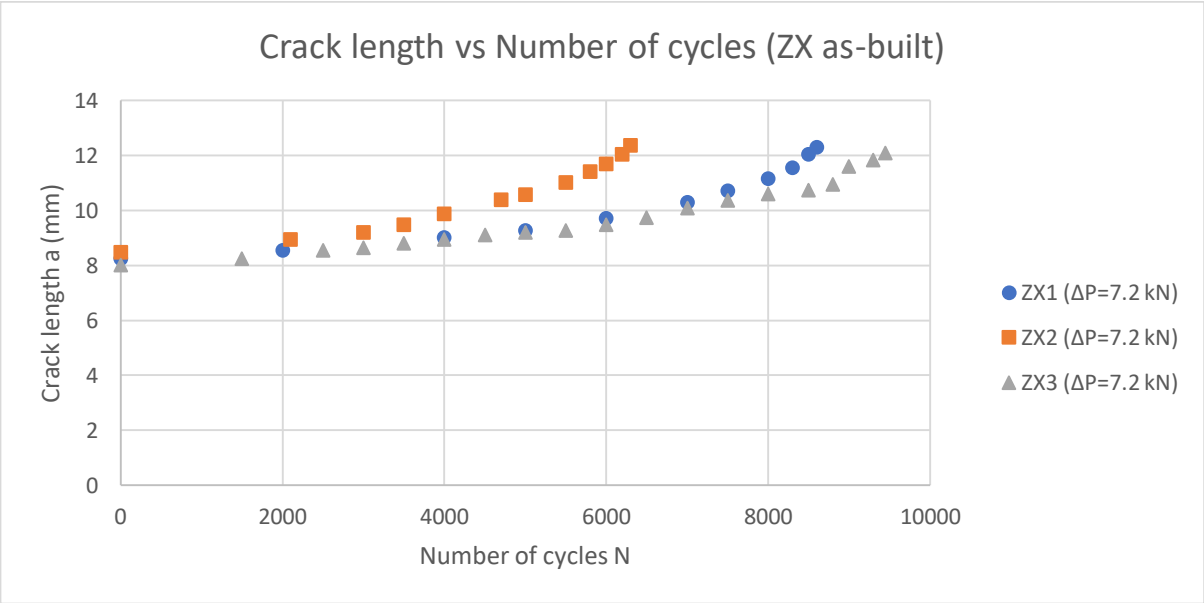

Figure 5.11: Crack length vs number of cycles for ZX as-built orientation

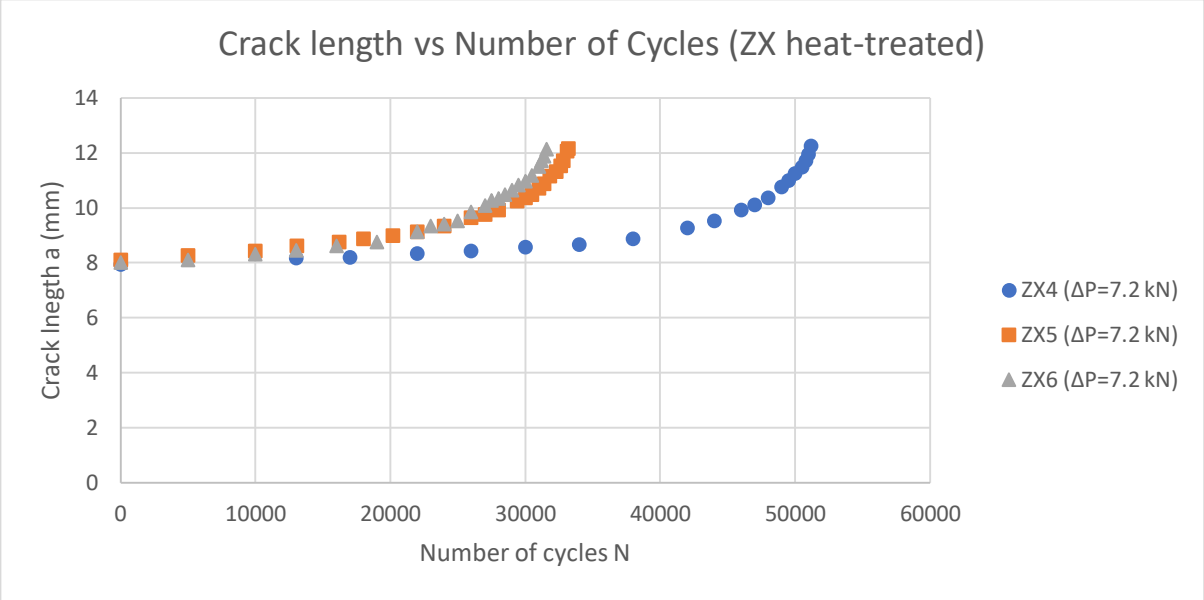

Figure 5.12: Crack length vs number of cycles for ZX heat-treated orientation

The fatigue resistance of the as-built condition is significantly less than that of the heat-treated condition. It is to be noted that the X-axis scale of the as-built condition extends to 10 000 cycles whereas the X-axis scale of the heat-treated condition extends to 60 000. There was a significant improvement in the fatigue performance after the heat treatment. The Paris region of both material conditions can be seen in Figure 5.13 and Figure 5.14 below.

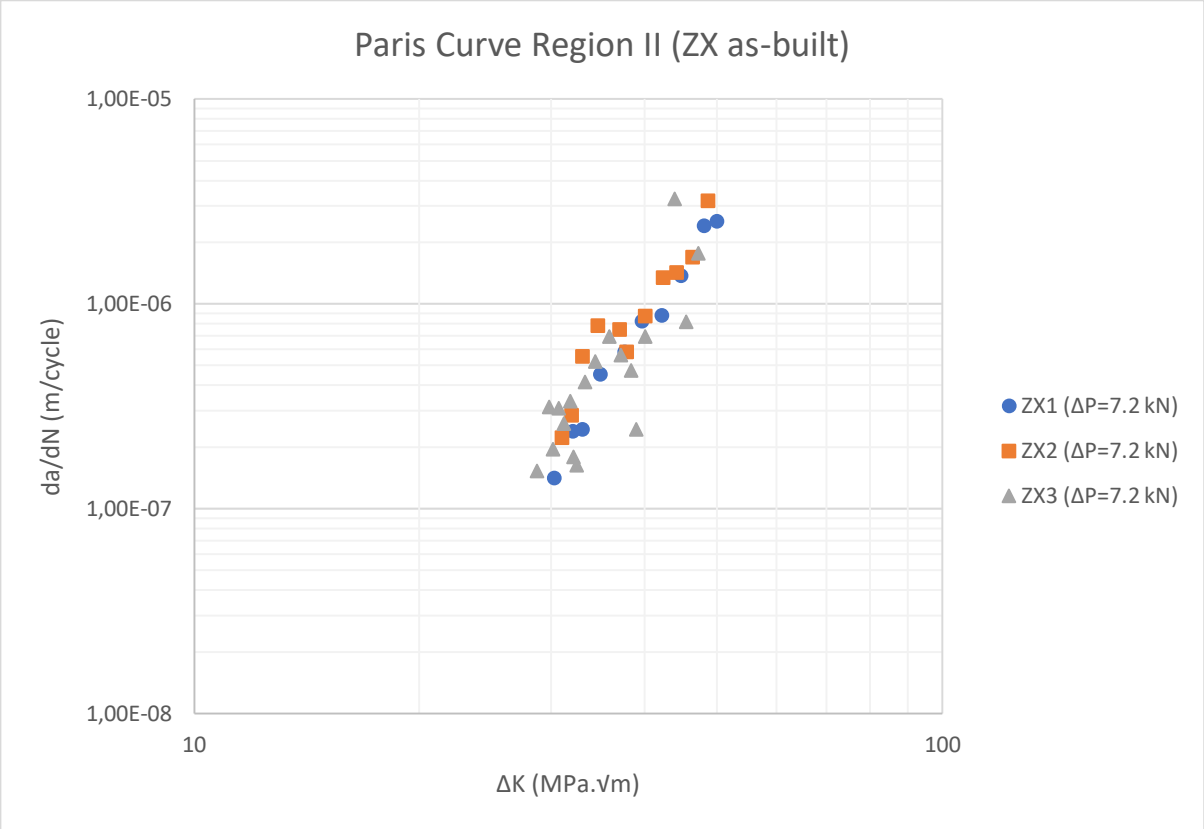

Figure 5.13: Paris curve for ZX as-built orientation

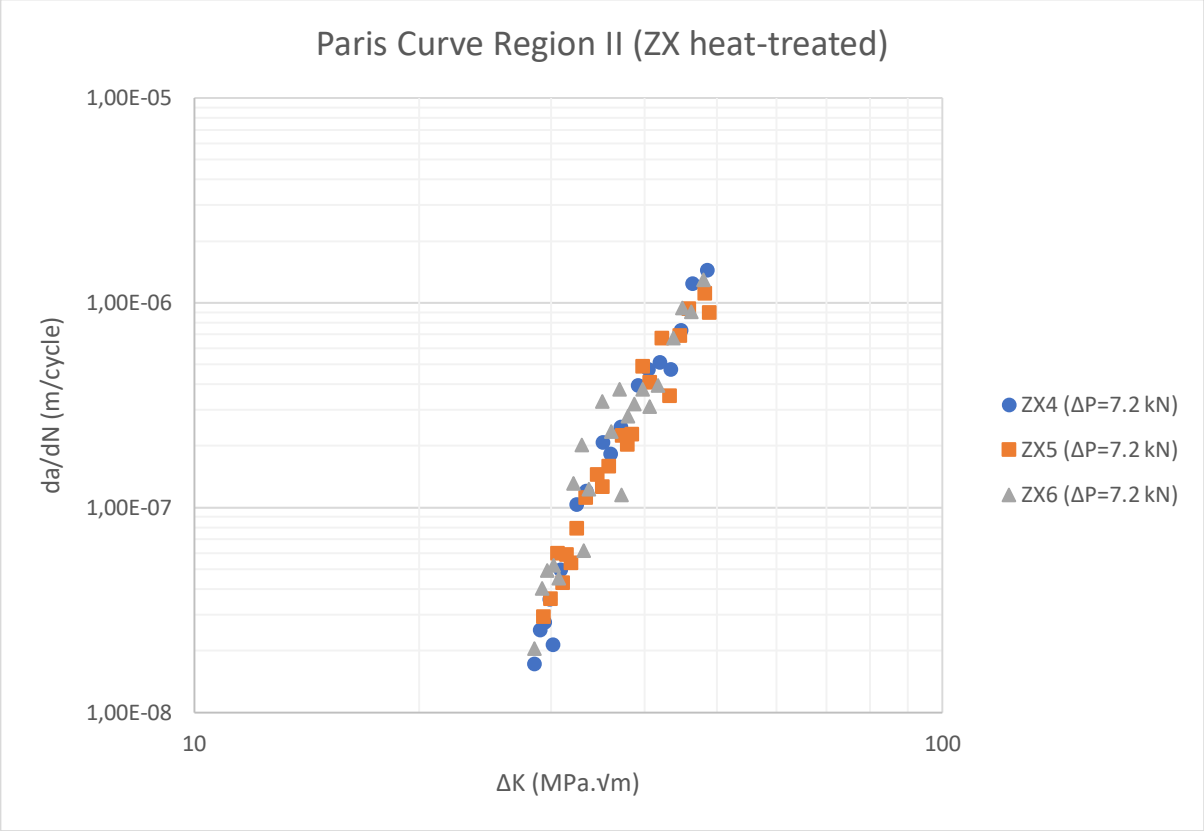

Figure 5.14: Paris curve for ZX heat-treated orientation

From Figure 5.13 and Figure 5.14 above, a greater correlation of the data can be seen in the heat-treated condition when compared to the as-built condition which is similar to the XY and XZ build orientations. A summary of the Paris equations developed from the results obtained is shown in Table 5.4 below.

Table 5.4: Paris equations for XZ orientation

Specimen	**Material condition**	**Paris equation**
ZX1	As-built	$\frac{da}{dN} = (1.14 \times 10^{-16})\Delta K^{6.14}$
ZX2		$\frac{da}{dN} = (3.18 \times 10^{-16})\Delta K^{5.93}$
ZX3		$\frac{da}{dN} = (1.92 \times 10^{-17})\Delta K^{6.84}$
Average		$\frac{da}{dN} = (15.1 \pm 7) \times 10^{-17}\Delta K^{6.30 \pm 0.2}$
ZX4	Heat-treated	$\frac{da}{dN} = (1.80 \times 10^{-20})\Delta K^{8.30}$
ZX5		$\frac{da}{dN} = (1.22 \times 10^{-19})\Delta K^{7.76}$

ZX6		$\frac{da}{dN} = (5.73 \times 10^{-20})\Delta K^{7.94}$
Average		$\frac{da}{dN} = (6.60 \pm 2) \times 10^{-20}\Delta K^{8.00 \pm 0.1}$

The ZX test specimens were all tested with a load range of 7.2 kN and a load ratio of 0.1 as with the XZ specimens. The stress intensity factor range of the ZX was also in the range of 20 to 50 MPa√m.

5.2.4. Summary and comparison between XY, XZ and ZX

It was intended for all test specimens, as-built and heat treated, for all build orientations to have identical test starting conditions in terms of starter notch length and root radius, starting stress intensity factor range and loading conditions. Slight variations were seen in the starting conditions owing to inconsistencies in the wire cutting of the notches, resulting in variations in root radii and starter notch depth. Each sample was therefore pre-cracked to a total crack length, as measured from the load line, of approximately 8 mm, giving a starting stress intensity factor range of approximately 28 MPa√m. A summary of the average FCGR test results for each build orientation can be seen in Table 5.5 below.

Table 5.5: Summary of average Paris equations

Build orientation	**Average as-built Paris equation**	**Average heat-treated Paris equation**
XY	$\frac{da}{dN} = (15.8 \pm 5) \times 10^{-16}\Delta K^{5.53 \pm 0.1}$	$\frac{da}{dN} = (1.69 \pm 1) \times 10^{-19}\Delta K^{8.48 \pm 0.3}$
XZ	$\frac{da}{dN} = (17.8 \pm 7) \times 10^{-16}\Delta K^{5.38 \pm 0.2}$	$\frac{da}{dN} = (11.7 \pm 6) \times 10^{-19}\Delta K^{7.22 \pm 0.3}$
ZX	$\frac{da}{dN} = (1.51 \pm 0.7) \times 10^{-16}\Delta K^{6.30 \pm 0.2}$	$\frac{da}{dN} = (0.66 \pm 0.3) \times 10^{-19}\Delta K^{8.00 \pm 0.1}$

The differences between the three different build orientations in both the as-built and heat-treated conditions can be seen graphically in the figures below for specimens tested at a load range of 7.2 kN. This was done to highlight the differences observed whilst testing the different build orientations.

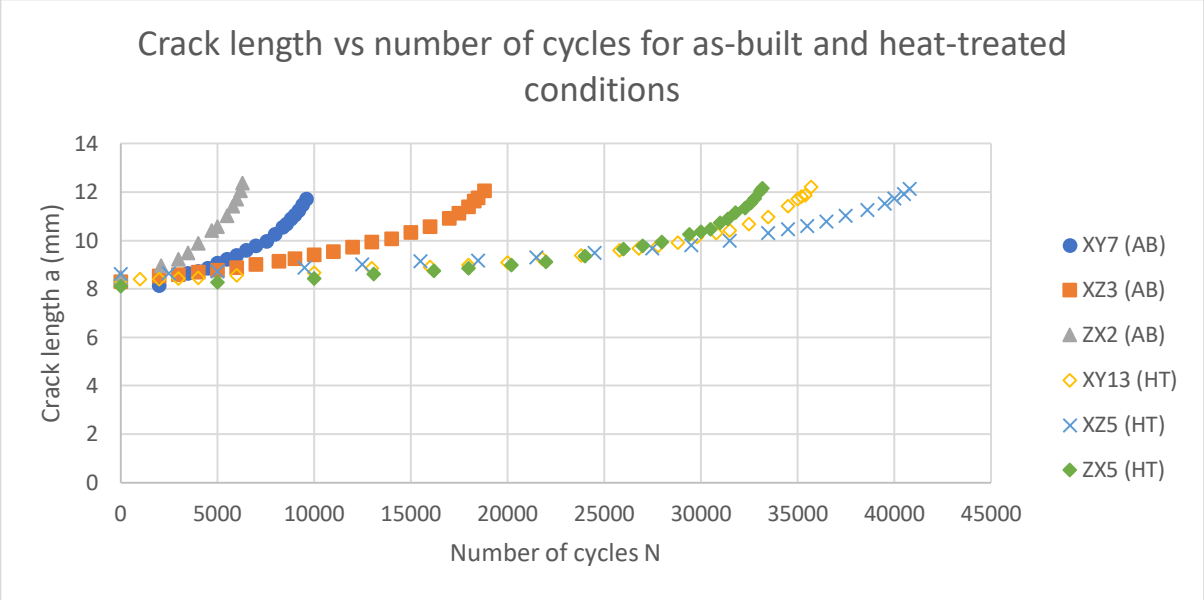

Figure 5.15: Crack length vs number of cycles for as-built and heat-heated conditions tested at a load range of 7.2 kN

In the figure above it is to be noted that "AB" and "HT" represent the as-built and heat-treated conditions respectively. Paris curves corresponding to the specimens shown in the figure above were also plotted and are shown in the figure below for the as-built and heat-treated specimens tested at a load range of 7.2 kN.

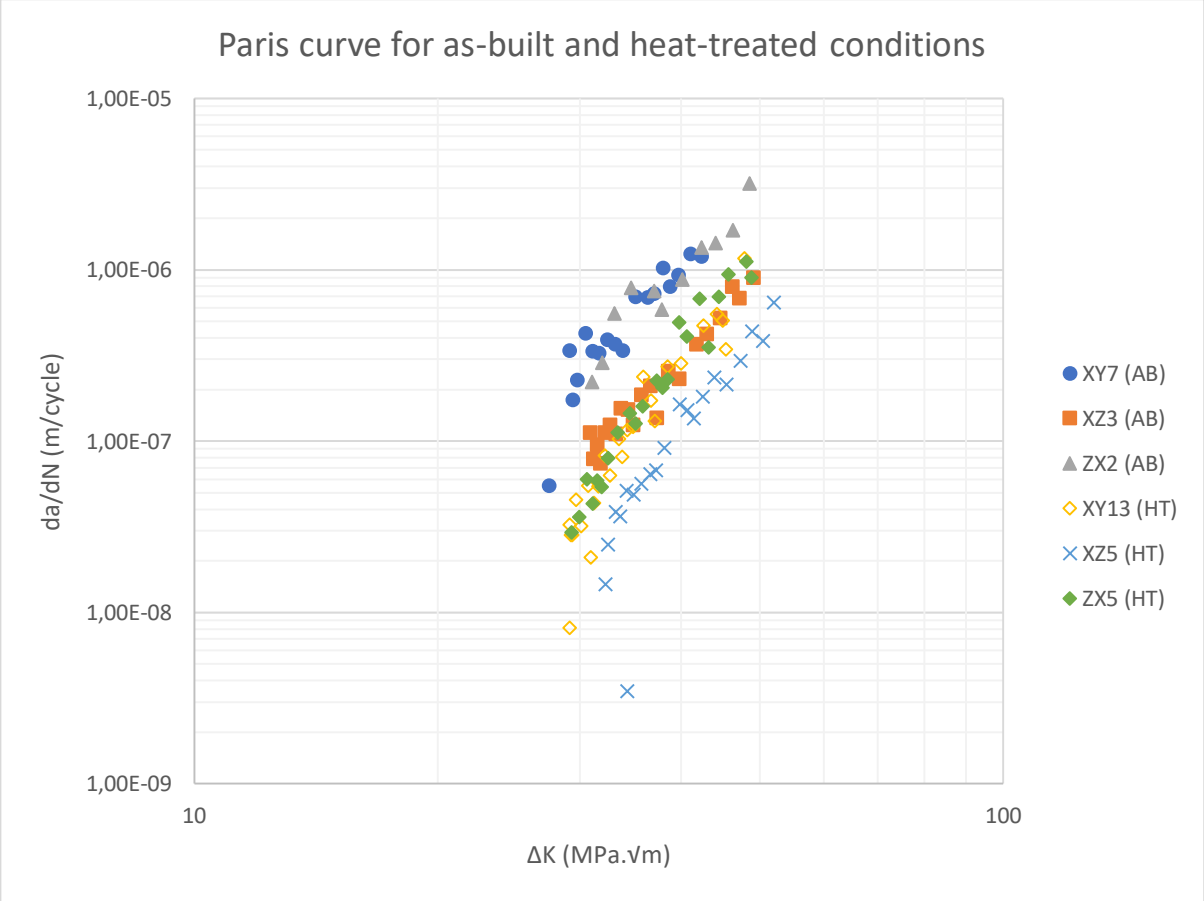

Figure 5.16: Paris curve for as-built and heat-treated conditions tested at a load range of 7.2 kN

5.2.5. Fatigue cycling to failure

Four CT specimens were cycled to failure and were not used to conduct FT tests. Specimens XY3, XY6, XY9 and XY10 were used to perform these tests to observe the behaviour of the material in the fast fracture regime (region III on the Paris curve). These tests were also performed to observe whether a two stage Paris region is observed, as mentioned in Section 2.12. Only specimens from the XY orientation were used to conduct these tests, as there was an abundance of XY specimens manufactured. There were only limited XZ and ZX specimens, thus this testing could not be performed for the XZ and ZX directions. The Paris curves obtained for these specimens are shown in Figure 5.17 below.

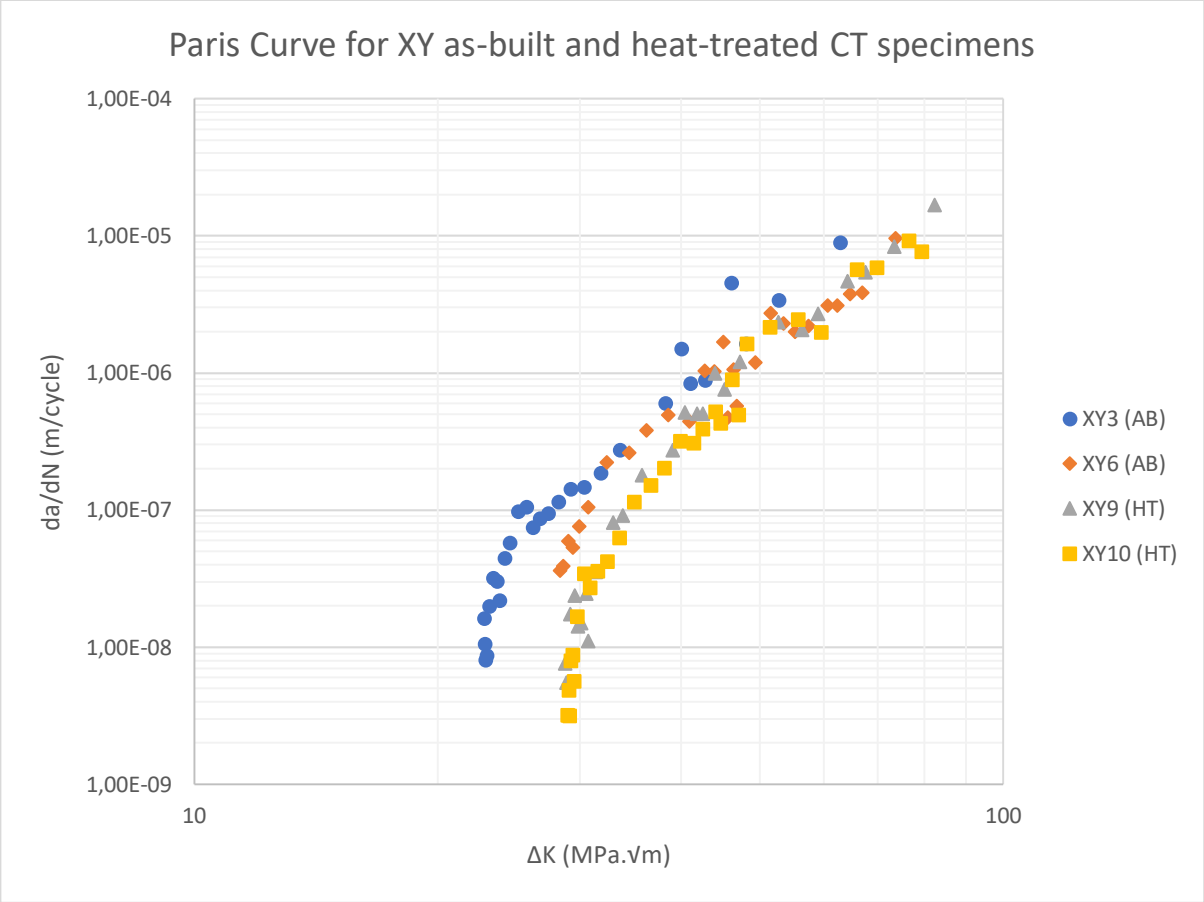

Figure 5.17: Paris curve for specimens tested to failure

The figure above displays the full range of data for four XY orientated CT specimens. The as-built specimens (XY3 and XY6) can be seen on the same graph as the heat-treated specimens (XY9 and XY10). As a result, the difference in the fatigue crack growth behaviour can be seen more clearly as the heat-treated material has a steeper slope that the as-built. This correlates well with the Paris equations shown in Section 5.2.1 as the steeper slope infers a larger *m* value. A more detailed analysis of these results will be given in Section 6.2.

5.3. Fracture toughness test results

The results obtained after the fracture toughness testing will be shown in this section. Fracture toughness tests were performed on the same CT specimens that were used for the FCGR tests. The tests were conducted according to the method described in section 4.6. The analysis of the results for determining J_{max} is lengthy and therefore, the data reduction method will be shown below for one test specimen. The data for the remaining test specimens can be located in Appendix 11.6.

A load vs load line displacement graph was obtained from the test data. This graph was used to calculate the corresponding J_{max} value to be compared for each test sample. Figure 5.18 below shows the load vs load line displacement graph for specimen XY2.

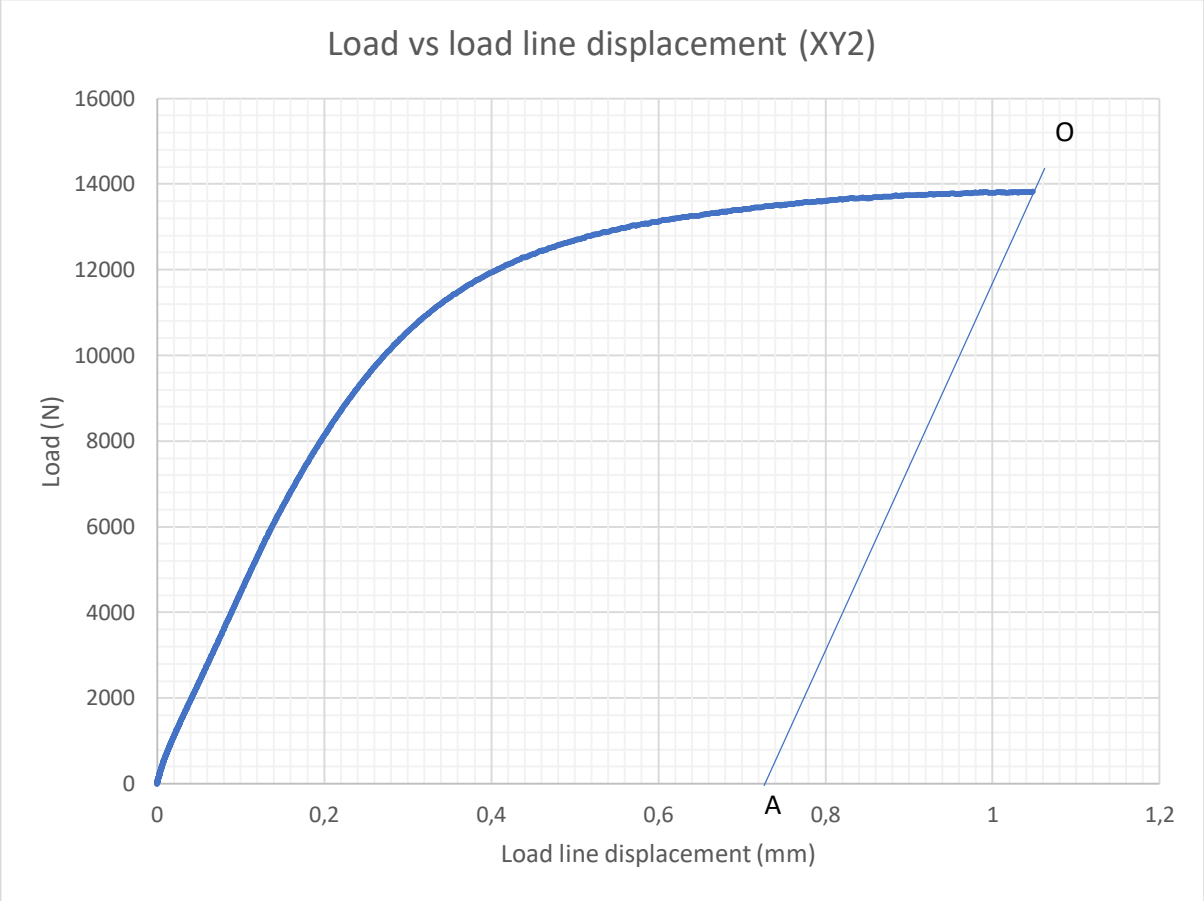

Figure 5.18: Load vs load line displacement for XY2

The line OA in the figure above encloses the area under the graph and has a gradient equal to that of the elastic portion of the graph. The intercept of this line with the X-axis is used for the calculation of J_{max}. The area enclosed by the curve, line OA and the X-axis is also required for the determination of J_{max} and is calculated using the "trapz" function in Octave. The script used to perform all J calculations can be found in Appendix 11.8.

The length of the fatigue pre-crack is also required for the determination of J_{max}. This is calculated by measuring the length from the load line to the crack front at nine equally spaced points on the crack front as shown in Figure 5.19 below.

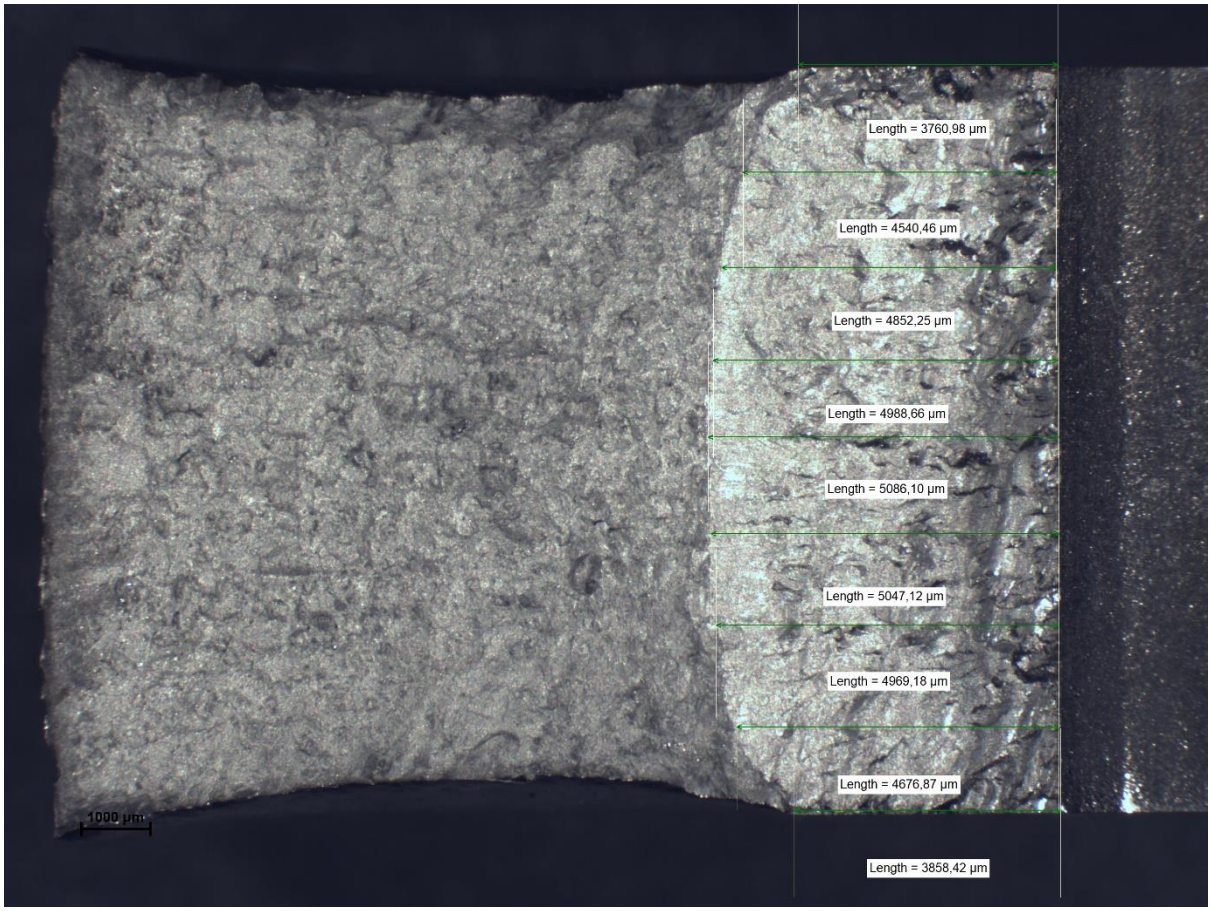

Figure 5.19: Measurement of crack length after fracture

The average of these measurements is then used as the average crack length for the determination of J_{max}. The measurements for each test specimen can be found in Appendix 11.7.

5.3.1. XY

A total of five specimens for each material condition (as-built and heat-treated) were tested for the XY build orientation.

A summary of the fracture toughness results obtained can be found in Table 5.6 below. These results include both the as-built and heat-treated condition.

Table 5.6: Fracture toughness results for XY orientation

Specimen	**Material condition**	**P_{max} (N)**	**Average crack length (mm)**	**K (MPa√m)**	**J_{max} (kJ/m²)**
XY1	As-built	15358	11,84	105	239
XY2		13822	12,18	99	236
XY4		14600	12,08	104	466
XY5		14130	12,09	101	247
XY7		14172	12,85	99	212
				Average	**234 ± 6**

XY8	Heat-treated	15271	12,74	124	268
XY11		14378	12,77	116	276
XY12		13822	12,31	114	262
XY13		14324	13,11	110	318
XY14		14449	13,38	117	301
				Average	**285 ± 9**

The table above displays some important parameters that were used in the determination of J_{max}. These parameters are the maximum load experienced during the test (P_{max}), the average crack length as determined from the average value of the measurements shown in Figure 5.15 above and the value of K corresponding to the maximum load experienced. The average J_{max} for each material condition was calculated and can be seen in bold in the table above. There is a distinct increase in the average J_{max} after the heat-treatment is applied to the material. XY4 was excluded as the material behaved in an anomalous fashion with a large plastic region. Specimens XY7, XY13 and XY14 were manufactured using the same scanning parameters as the ZX orientated specimens. These scanning parameters were different to that of the other XY test specimens.

5.3.2. XZ

A total of six specimens were tested for the XZ build orientation. Three specimens per material condition were tested. All specimens were harvested from the same block of source material and hence, have the same build parameters. Table 5.7 below summarises the fracture toughness results for the XZ build orientation.

Table 5.7: Fracture toughness results for XZ orientation

Specimen	**Material condition**	**P_{max} (N)**	**Average crack length (mm)**	**K (MPa√m)**	**J_{max} (kJ/m^2)**
XZ1	As-built	12968	13,14	103	371
XZ2		14567	12,58	105	321
XZ3		13848	12,81	107	276
				Average	**323 ± 22**
XZ4	Heat-treated	11682	13,70	115	338
XZ5		16900	12,26	125	454
XZ6		13530	13,11	111	381
				Average	**391 ± 28**

From the fracture toughness results shown in Table 5.7 above, a clear difference can be seen between the as-built and heat-treated conditions. XZ5 displays a significantly higher maximum load and hence, a high J_{max}. If XZ5 is taken as anomalous, then the average between ZX4 and XZ6 will still be greater than the average of the as-built specimens therefore the result is still conclusive. An increase in J_{max} can be seen in both material conditions when compared to the XY build orientation however, the build parameters were different for the XY and XZ build orientations which could affect the fracture toughness of the material.

5.3.3. ZX

Six specimens were tested for the ZX build orientation with three being as-built and three in the heat-treated condition. These specimens were all harvested from the same block of material and therefore have the same build parameters. The build parameters for the ZX test specimens differed from build parameters of the XZ and XY specimens. Specimens XY7, XY13 and XY14 shared common build parameters as the ZX orientation as they were manufactured during the same build. A summary of the fracture toughness results for the ZX orientation can be seen in Table 5.8 below.

Table 5.8: Fracture toughness results for ZX orientation

Specimen	**Material condition**	**P_{max} (N)**	**Average crack length (mm)**	**K (MPa√m)**	**J_{max} (kJ/m^2)**
ZX1	As-built	11440	13,17	92	233
ZX2		11891	13,35	94	185
ZX3		10229	13,74	88	211
				Average	**210 ± 11**
ZX4	Heat-treated	13323	13,54	111	220
ZX5		13998	13,38	116	249
ZX6		14215	13,17	111	264
				Average	**245 ± 10**

The ZX build orientation displays the lowest J_{max} average for both the as-built and heat-treated conditions however, the heat-treated condition does display an increase in fracture toughness when compared to the as-built condition.

A significant difference in the fracture toughness of the different build orientations was noticed with the XZ orientation possessing the highest fracture toughness and the ZX possessing the lowest. This could be attributed to the building parameters such as layer thickness and hatch spacing or the build orientation itself. Significant increases in the fracture toughness result were seen when the specimens were in the heat-treated condition. The standard error in the XZ results was significantly higher than that of the XY and ZX orientations. This could be as a result of the inhomogeneity of the microstructure or the minimal number of test specimens. A summary of the fracture toughness test results is shown in Table 5.9 below.

Table 5.9: Summary of fracture toughness results

Build orientation	Average as-built J_{max} (kJ/m^2)	Average heat-treated J_{max} (kJ/m^2)
XY	234 ± 6	285 ± 9
XZ	323 ± 22	391 ± 28
ZX	210 ± 11	245 ± 10

5.4. Density test results

Density tests were performed according to the testing procedure outlined in Section 4.7. A summary of the density test results per build orientation and material condition can be seen in Table 5.10 below. A more detailed results table with individual mass measurements per test sample can be found in Appendix 11.9.

Table 5.10: Summary of density test results for all orientations and material conditions

Build orientation	As-built density (g/cm^3)	Heat-treated density (g/cm^3)	Average density for build orientation (g/cm^3)
XY	8.25 ± 0.03	8.25 ± 0.01	8.25 ± 0.01
XZ	8.22 ± 0.00	8.25 ± 0.01	8.23 ± 0.01
ZX	8.24 ± 0.00	8.25 ± 0.00	8.25 ± 0.00

From Table 5.10 above, it can be seen that all build directions display very similar densities. It is also to be noted that these some samples were built with different build parameters. The quoted density of 8.22 g/cm^3 is also consistent with the results obtained. A slight increase in the obtained value when compared to the quoted value can be due to experimental error in terms of the mass measurement and specimen preparation.

5.5. Hardness test results

Vickers hardness tests were conducted according to the method outlined in Section 4.8. A summary of the Vickers hardness test results per build orientation and material condition can be seen in Table 5.11 below. A more detailed table containing the Vickers hardness for each indentation can be found in Appendix 11.10.

Table 5.11: Summary of Vickers hardness test results for all orientations and material conditions

Build orientation	As-built Vickers hardness (HV10)	Heat-treated Vickers hardness (HV10)	Average Vickers hardness gained (HV10)
XY	355 ± 5	461 ± 13	106
XZ	461 ± 6	555 ± 9	94
ZX	366 ± 4	471 ± 7	105

The Vickers hardness obtained for each build orientation can be seen to differ quite significantly. There is a distinct increase in the Vickers hardness after heat treating for all build orientations.

From Table 5.11 above, the as-built Vickers hardness can be seen to vary amongst the three build orientations with the XY and ZX orientations exhibiting similar average Vickers hardness readings. This is similar when the heat-treated Vickers hardness readings are compared. The XY and ZX specimens were built using similar build parameters in terms of layer thickness and hatch spacing which could be the reason why the hardness readings were so similar. The hardness readings were obtained from the inner region of each test specimen to get the most accurate hardness reading which negated the effects of polishing and the oxide scale that was produced during heat-treating. These readings displayed similarities to the readings obtained by Murr *et al.* [50] which were in the range of 500 HV for SLM produced IN718.

The last column of the table above shows the increase in average Vickers hardness after heat-treating. Here it can be seen that the overall gain in hardness in all build orientations is quite consistent and proves that precipitation hardening was successful. It is not clear whether the build orientation has a definite impact on the material hardness as all orientations were built with slightly different build parameters, but the gain in hardness as a result of the heat-treatment is consistent in all orientations regardless of the build parameters. The Vickers hardness test was also performed to provide an indication on the tensile properties of the material however, due to the findings from the FCGR and FT tests, the material seems to behave differently depending on the build orientation and therefore, the hardness may not be an appropriate indicator of the tensile properties. Multiaxial hardness tests could potentially be performed on test specimens to observe whether there is a difference in the hardness readings depending on which surface of the material the indentation is made. This can be conducted for future work.

5.6. Microstructure

The microstructural results obtained from light microscopy and SEM will be shown in this section.

5.6.1. Light microscopy

The microstructure of the material was firstly investigated with the use of a light microscope as mentioned in Section 4.9.2. Differential interference contrast was utilised through the use of a Normarski interference prism in the microscope to provide greater contrast of grain boundaries and other surface features. The front, top and side view for each material condition (as-built and heat treated) will be shown below.

5.6.1.1. As-built condition

The three views of the as-built material can be seen in Figure 5.20.

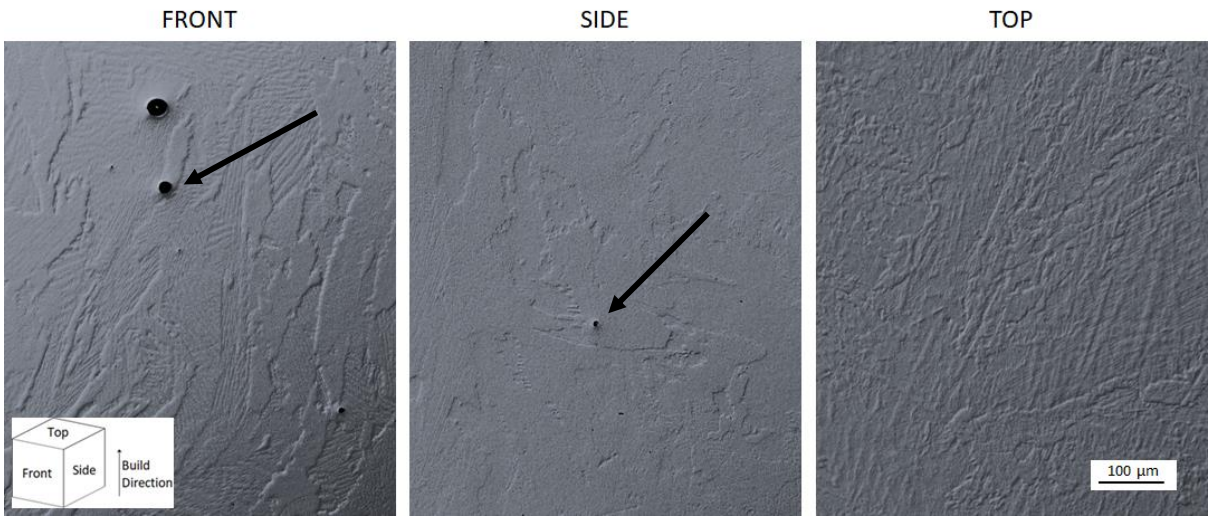

Figure 5.20: Light microscope images of as-built specimen Showing front, side and top views at 100X magnification

The front view seen in Figure 5.20 above shows elongated columnar grains characteristic of AM metallics. The large spherical hole-like structures identified by the black arrow, are pores which would have formed as a result of the LENS process. The grains visible in the figure above are irregular in shape and seem to possess “rough” edges.

The side view displays, a similar grain structure to the front view with the grains possessing rough edges and an irregular shape. It was expected that the side and front view be similar in structure since they are both cross sections of the material. Porosity can be identified in the figure and is shown by the arrow.

The top view of the material as seen in Figure 5.20 displays an irregular microstructure, but similar dendrite cores were seen by Raghavan *et al.* [20]. The top view of an AM part would usually show the scanning tracks of the building process in high clarity however, for DED manufactured parts, the scanning width is much greater than in processes such as SLM. As a result, the tracks cannot be been under the light microscope with such high magnification. A stereomicroscope was used to acquire an image with less magnification to look at the scanning tracks. This can be seen in Figure 5.21.

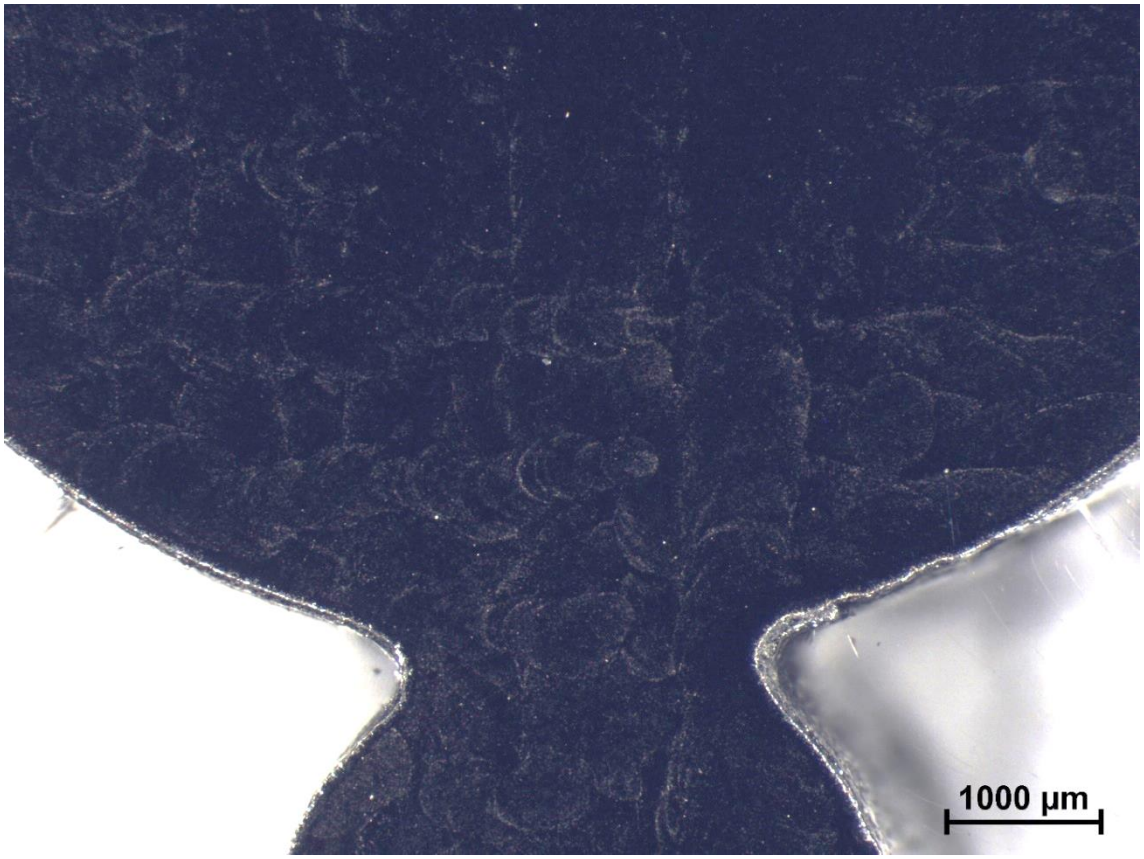

Figure 5.21: Stereomicroscope image of top view with low magnification

In Figure 5.21 above, the cross-hatch pattern of the build process can be seen clearly with a hatch spacing of approximately 0.5 mm as specified by the LENS machine.

5.6.1.2. Heat treated condition

The three views of the heat-treated material are shown below. The heat treatment protocol used in this project was a 1200 °C solution treatment for 2 hours followed by a water quench. Thereafter, an ageing procedure was conducted at 650 °C for 16 hours followed by air cooling to room temperature.

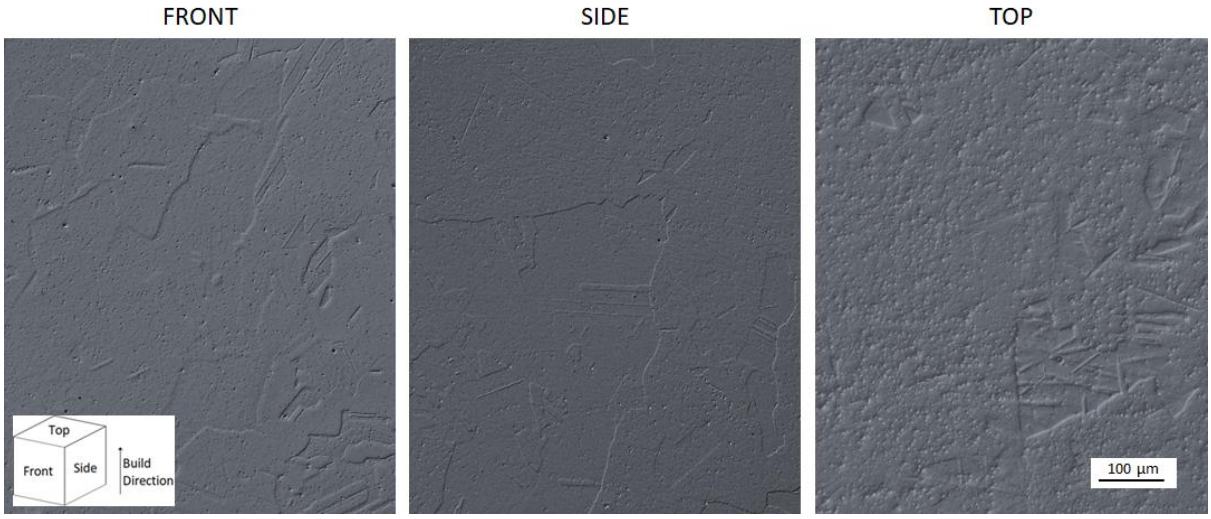

Figure 5.22: Light microscope images of heat-treated specimen showing front, side and top views at 100X magnification

The heat-treated front view of the material displays a much more uniform grain structure. The grain edges appear smoother, which can be attributed to the diffusion and homogenisation of the undesirable niobium-rich Laves phase. The side view appears similar to the front view, which was expected. The presence of porosity is still obvious.

The top view of the heat-treated material has an extremely rough surface that was littered with small holes or indents. These should not be mistaken for precipitates due to the size of the features and the contrast that can be seen with the Nomarski prism and polarised light, but may be an effect of corrosive attack at high energy locations, possibly precipitates or porosity, within the grain during the polishing process (as OP colloidal silica is known to etch the surface during polishing).

Figure 5.22 displays a top view microstructure with a higher concentration of porosity. Instances of clustering of porosity was noticed, which correlates with the shape and curvature of the melt pool. This can be seen clearly in Figure 5.23 below, highlighted by the black oval.

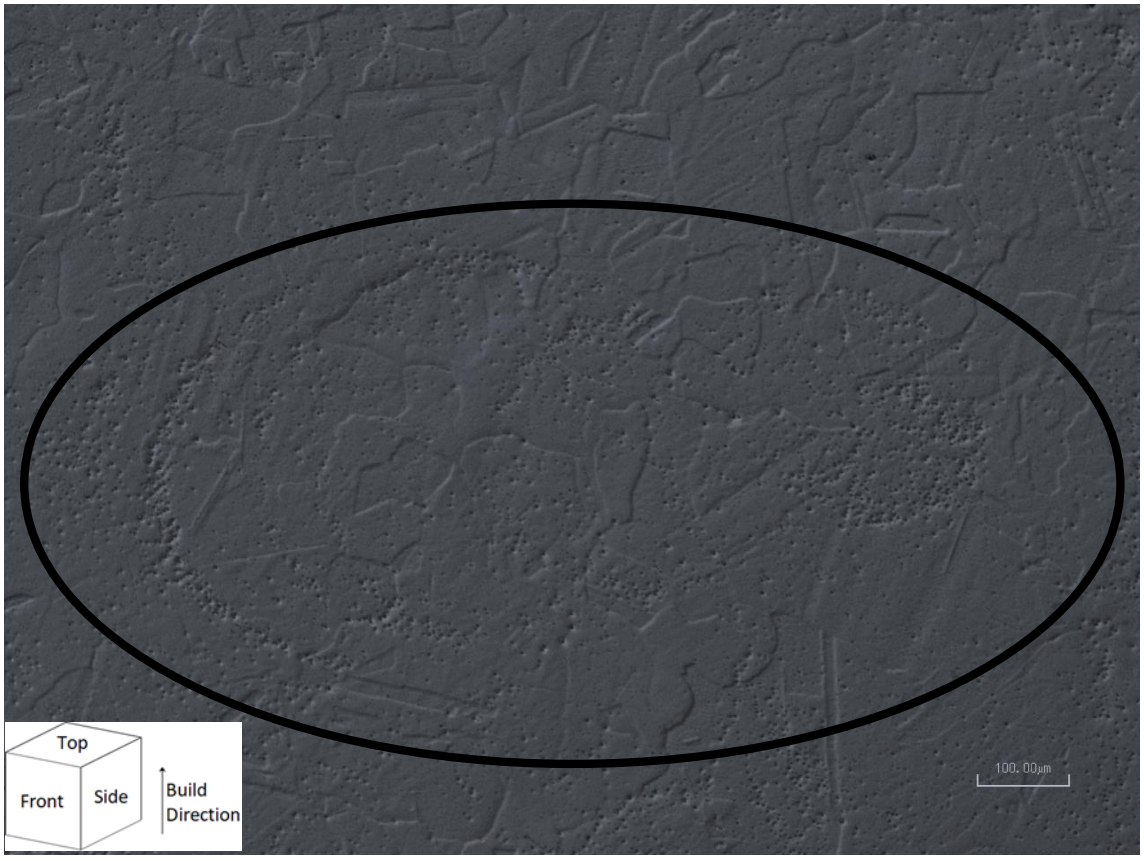

Figure 5.23: Light microscope image of heat-treated top view showing the shape of the melt

5.6.2. Scanning electron microscopy

A scanning electron microscope was employed to investigate the surface of the material at a higher magnification and to investigate features that could not be clearly identified using light microscopy. Magnifications of between 1 000X and 10 000X were used for imaging in the SEM. The front, side and top views of both material conditions were investigated. The SEM images for these samples are shown below.

5.6.2.1. As-built condition

The SEM images of the front, side and top views of the as-built material will be shown below.

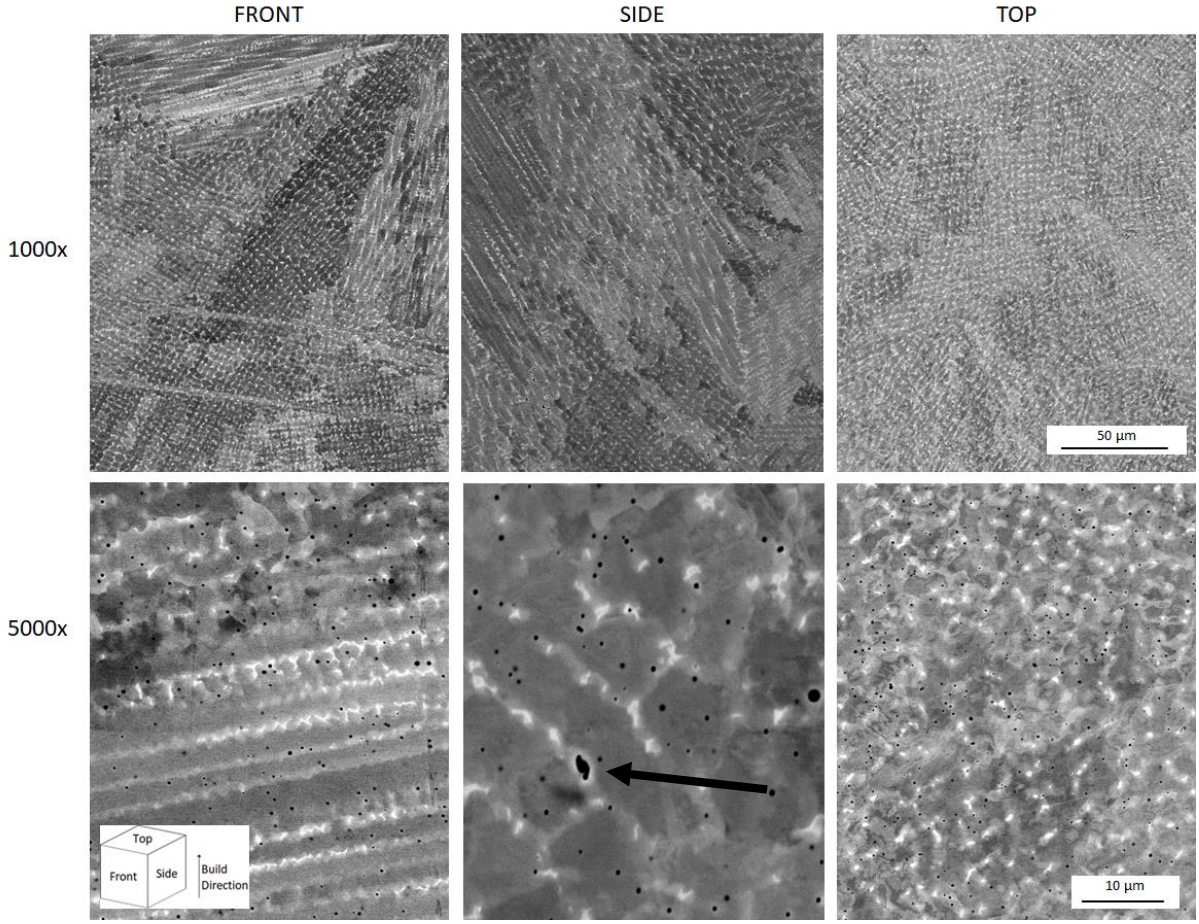

Figure 5.24: SEM images of as-built condition at two different magnifications

The grains in the front view of the material can be identified by the large patches of varying contrast. Each grain also possesses many white patches, which were confirmed by EDS to be a niobium-rich phase. The grains in the front view are long and elongated. The higher magnification of the front view (5000x) shows the patches of a niobium-rich phase that take the form of the Laves phase. This confirms that the high solidification rates and rapid cooling cause the niobium to diffuse out of the solid solution and form the Laves phase. This is not beneficial for precipitation hardening as the precipitation requires an even distribution of niobium throughout the alloy to bond with the nickel base. The black dots that were seen during light microscopy can also be seen in all the images at 5000x magnification shown above. These black dots, which were assumed to be either porosity or precipitates, were confirmed with EDS to be porosity due to the presence of all alloying elements within the holes, indicating the EDS is sampling from an interaction volume that is homogeneous and in line with the base material composition.

The as-built side and front views appear similar. These similarities include elongated grains in the direction of layer addition (Z-axis), Laves phase in the form of niobium that has diffused out of the solid solution and a fine dispersion of porosity throughout the material. An irregular shape, which is identified in Figure 5.24 above by the black arrow, is unlikely to be porosity due to its irregular shape since porosity tends to be spherical. This shape could have formed during the polishing process where a niobium-rich particle was removed from the material and left a large irregularly shaped void in its place that corresponds well to the shape of the niobium-rich particles. The void is also surrounded by

a region with a lighter contrast value, which correlates with an increase in niobium content in that region.

The top view at 1000X magnification shows a dispersion of features that can be identified by the large dark and light patches. These features form part of a single grains. The grains are not elongated as seen in the front and side view. This is expected as the direction of grain growth is orthogonal to the top view (grows into the page). A regular array of niobium-rich phase can be seen at both magnifications above, as well as the presence of porosity, which is identified by the black dots.

5.6.2.1.1. EDS of as-built condition

Energy dispersive X-ray spectroscopy (EDS) was utilised to confirm the chemical composition of the alloy and to analyse the surface features that were observed during light and scanning electron microscopy. The feature identified during microscopy that needed further investigation were the small black dots that were scattered throughout the surface of all samples and the white patches that were observed during SEM. Different sites were scanned in order to obtain enough data to observe the composition of the material accurately. Three large spectrums were analysed for composition deduction (baseline composition) and an example of spectrum 1 is shown in Figure 5.25 below.

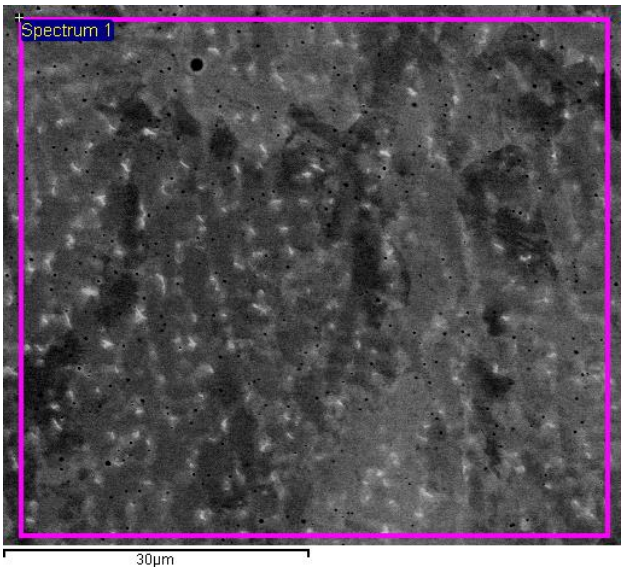

Figure 5.25: EDS spectrum on as-built condition

The chemical composition of the material can be seen in Table 5.12 below.

Table 5.12: EDS analysis of as-built condition

Element	Al	Ti	Cr	Fe	Ni	Nb	Mo	Total
Spectrum 1	0,6300	0,9900	19,48	18,02	51,13	6,050	3,710	100.0
Spectrum 2	0,5800	1,010	19,40	18,04	50,94	6,290	3,730	100.0
Spectrum 3	0,6800	1,040	19,42	17,80	51,22	6,210	3,630	100.0
Average	0,6300	1,010	19,43	17,95	51,09	6,180	3,690	100.0

The EDS analysis picked up about 5 % of carbon in the total composition. This could be due to carbon contamination during SEM. IN718 should only contain up to 0.08 %C and therefore the peak of carbon

measured here was disregarded when determining the composition of the material as trace amounts of carbon cannot be reliably measured in the SEM using EDS. The primary use for EDS was for comparative purposes such as determining the niobium-rich Laves phases.

The black dots were also scanned at three different sites which can be seen in the figure below.

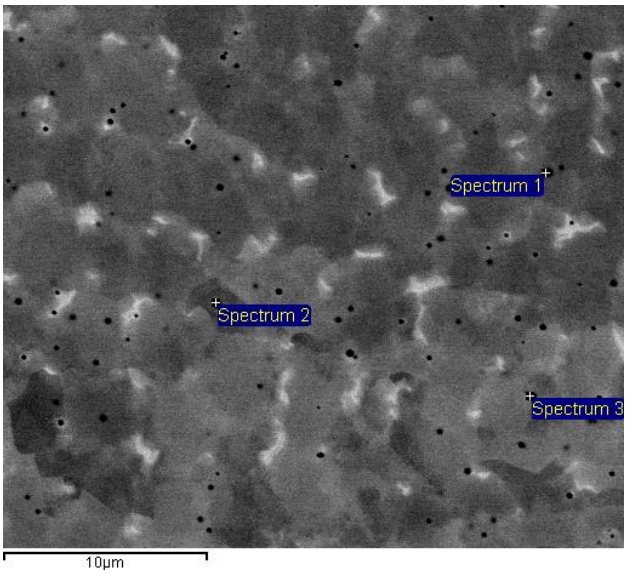

Figure 5.26: Different spectrum sites for EDS analysis of black dot features

The EDS results obtained for each of the three sites shown in Figure 5.26 are displayed in Table 5.13.

Table 5.13: EDS analysis on black dot features

Element	**Al**	**Ti**	**Cr**	**Fe**	**Ni**	**Nb**	**Mo**	**Total**
Spectrum 1	3,900	3,670	19,28	17,89	47,83	4,400	3,050	100.0
Spectrum 2	1,500	3,880	19,37	18,46	48,95	4,880	2,950	100.0
Spectrum 3	1,470	0,9400	19,43	18,13	50,71	5,680	3,630	100.0
Average	2,290	2,830	19,36	18,16	49,17	4,990	3,210	100.0

From the spectrums above, it can be seen that the black dots resemble the overall chemical composition of the material quite closely. This confirms that the dots are not embedded particles and are pores within the material due to their near perfect spherical shape.

The white patches were scanned with EDS and five spectrums were considered. The sites for each spectrum are shown in Figure 5.27 followed by the EDS results obtained for each spectrum in the table.

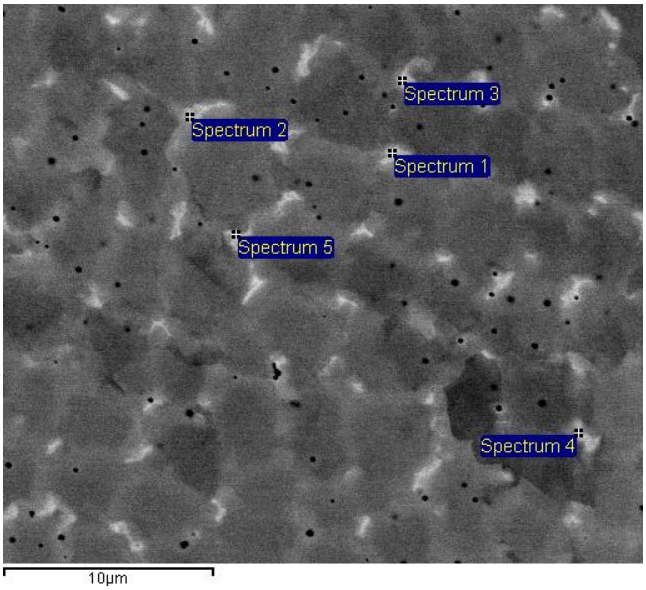

Figure 5.27: Different spectrum sites for EDS analysis of white patch features

The EDS results obtained for each spectrum shown in Figure 5.27 above can be seen in Table 5.14 below.

Table 5.14: EDS analysis on white patch features

Element	Al	Si	Ti	Cr	Fe	Ni	Nb	Mo	Total
Spectrum 1	0,4100	0,2200	1,490	14,95	12,90	44,50	20,42	5,110	100.0
Spectrum 2	0,4200	0,2300	1,450	14,93	13,15	44,62	20,23	4,980	100.0
Spectrum 3	0,5000	0,1700	1,320	16,89	15,15	48,29	13,41	4,270	100.0
Spectrum 4	0,5100	0,1600	1,480	15,62	13,81	45,97	17,97	4,480	100.0
Spectrum 5	0,6200	0,0000	1,140	18,85	17,03	50,15	8,220	3,990	100.0
Average	0,4900	0,1600	1,380	16,25	14,41	46,71	16,05	4,570	100.0

Table 5.14 above shows a significant increase in the niobium content. This proves that the white patches are primarily composed of niobium which has diffused out of the solid solution during rapid solidification and the high temperature gradient that is experienced.

5.6.2.2. Heat treated condition

The SEM micrographs for the heat-treated front, side and top views are shown in Figure 5.28.

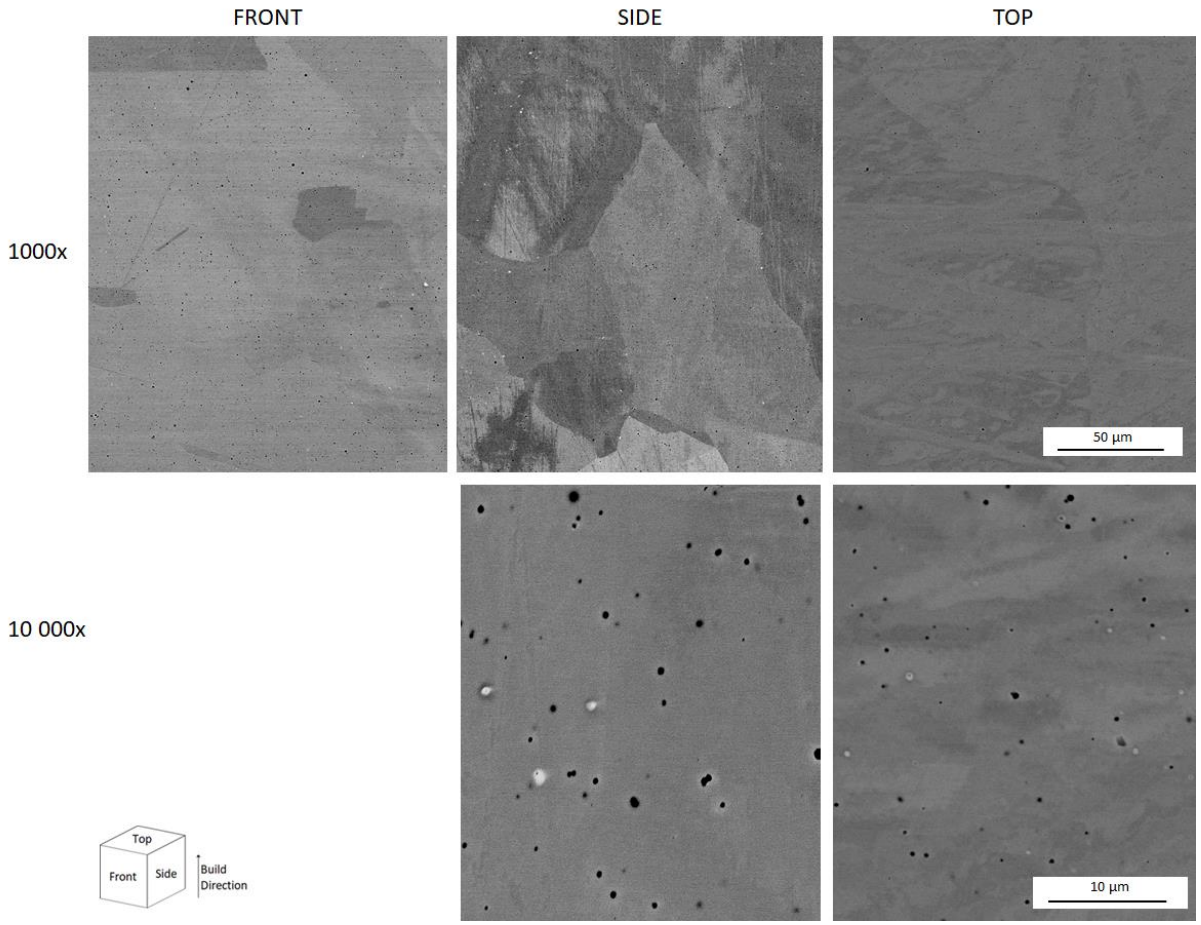

Figure 5.28: SEM images of heat-treated material at two magnifications

The microstructure seen in the front view of the material is more uniform when compared to the as-built condition with larger grains and less contrast between grains. This lack of contrast is owed to the reduction of Laves phase after the high temperature solution treatment and quenching which generates a more homogenous microstructure. The white patches that were identified in the as-built condition to be Niobium by EDS are not present in the figure above. Porosity can still be seen in the form of the black dots which was confirmed by EDS.

In the side view above, the grain structure can be seen more clearly than in the front view as the contrast was altered. The side view at a magnification of 1000X above shows traces of white and black dots that were confirmed by EDS to be niobium-rich phases and porosity. During the ageing process, the niobium precipitates to form the γ'' strengthening phase. These findings were similar to that of the front view. A higher magnification of the side view is shown in the figure above which clearly shows the white and black dots mentioned above.

The grain structure seen in the top view is similar to the as-built condition where the grains are irregular in shape since they are grown in the direction orthogonal to the build direction (into the page). It can also be seen that the white patches of Niobium are no longer present in the microstructure as they have diffused back into the solution during the high temperature solution treatment and formed precipitates during the ageing process. The black dots which correspond to porosity are also present. A higher magnification of the heat-treated top view can also be seen in the figure above. The porosity can be clearly seen along with small white patches which are precipitated Niobium. These findings support the findings from the heat-treated front and side views.

5.6.2.2.1. EDS of heat-treated condition

The heat-treated material was also analysed with EDS to confirm certain surface features and chemical composition. The chemical composition would not be expected to change as the material has not changed. As with the as-built EDS scan, the heat-treated sample was scanned at three different sites to gain an overall chemical composition of the material in the heat-treated form. An example of one of the sites is shown in Figure 5.29 below.

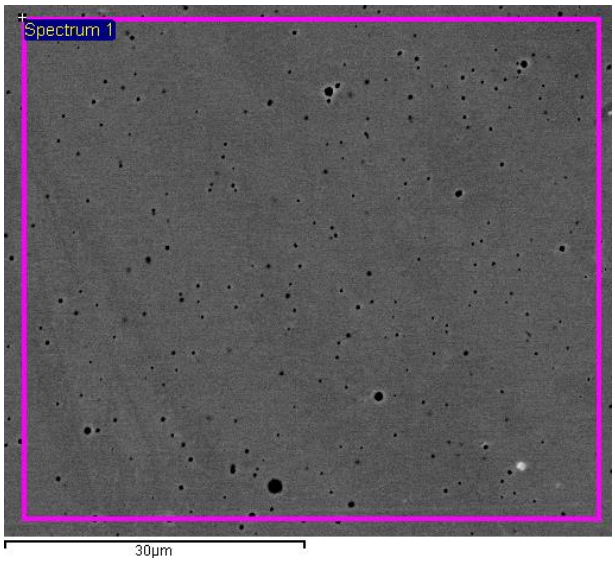

Figure 5.29: EDS spectrum on heat-treated condition

The chemical composition of the material can be seen in Table 5.15 below.

Table 5.15: EDS analysis of heat-treated condition

Element	Al	Ti	Cr	Fe	Ni	Nb	Mo	Total
Spectrum 1	0,6500	0,9800	19,50	17,99	51,11	5,990	3,780	100.0
Spectrum 2	0,6100	0,9800	19,42	17,86	51,42	6,170	3,550	100.0
Spectrum 3	0,6200	1,080	19,36	18,10	51,16	6,050	3,620	100.0
Average	0,6200	1,010	19,43	17,98	51,23	6,070	3,650	100.0

From Table 5.15 above, it can be seen that the chemical composition is consistent when compared to the as-built condition which was expected. Trace levels of carbon were found in the heat-treated condition that is similar to the findings of the as-built condition, but this carbon content was omitted as carbon cannot be reliably measured in the SEM using EDS, and is likely affected by carbon contamination. An EDS scan of some of the surface features was performed. Five spectrums were analysed at five different sites. These sites are shown in Figure 5.30.

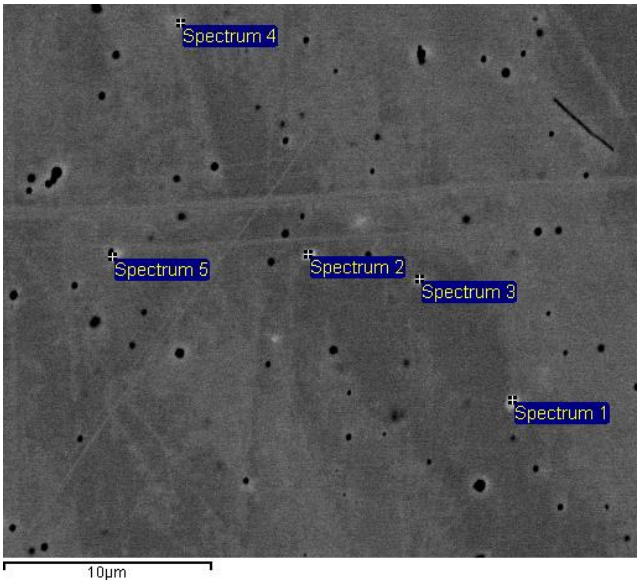

Figure 5.30: Different spectrum sites for EDS analysis of surface features

Table 5.16 below summarises the EDS results for each of the five sites above.

Table 5.16: EDS analysis on sites shown above

Element	Al	Ti	Cr	Fe	Ni	Nb	Mo	Total
Spectrum 1	0,5300	1,640	18,16	16,60	46,31	13,23	3,530	100.0
Spectrum 2	0,5300	1,040	19,35	18,02	51,01	6,460	3,600	100.0
Spectrum 3	0,5800	0,9500	19,51	18,09	51,18	6,050	3,640	100.0
Spectrum 4	0,6100	0,9000	19,62	17,85	51,30	5,970	3,750	100.0
Spectrum 5	0,6500	0,9300	19,40	18,04	51,30	5,940	3,730	100.0
BASE MATERIAL	0,6300	1,010	19,43	17,98	51,23	6,070	3,650	100.0

Spectrum 1 was on a white dot surface feature which explains the high level in the niobium content of the site. Each of the other four sites were on the black dot surface features which corresponded to porosity as the composition was similar to the base material composition.

5.7. Fractography

Fractographs of the fracture surface for each build orientation and material condition were obtained using the scanning electron microscope. These fractographs can be seen in Figure 5.31.

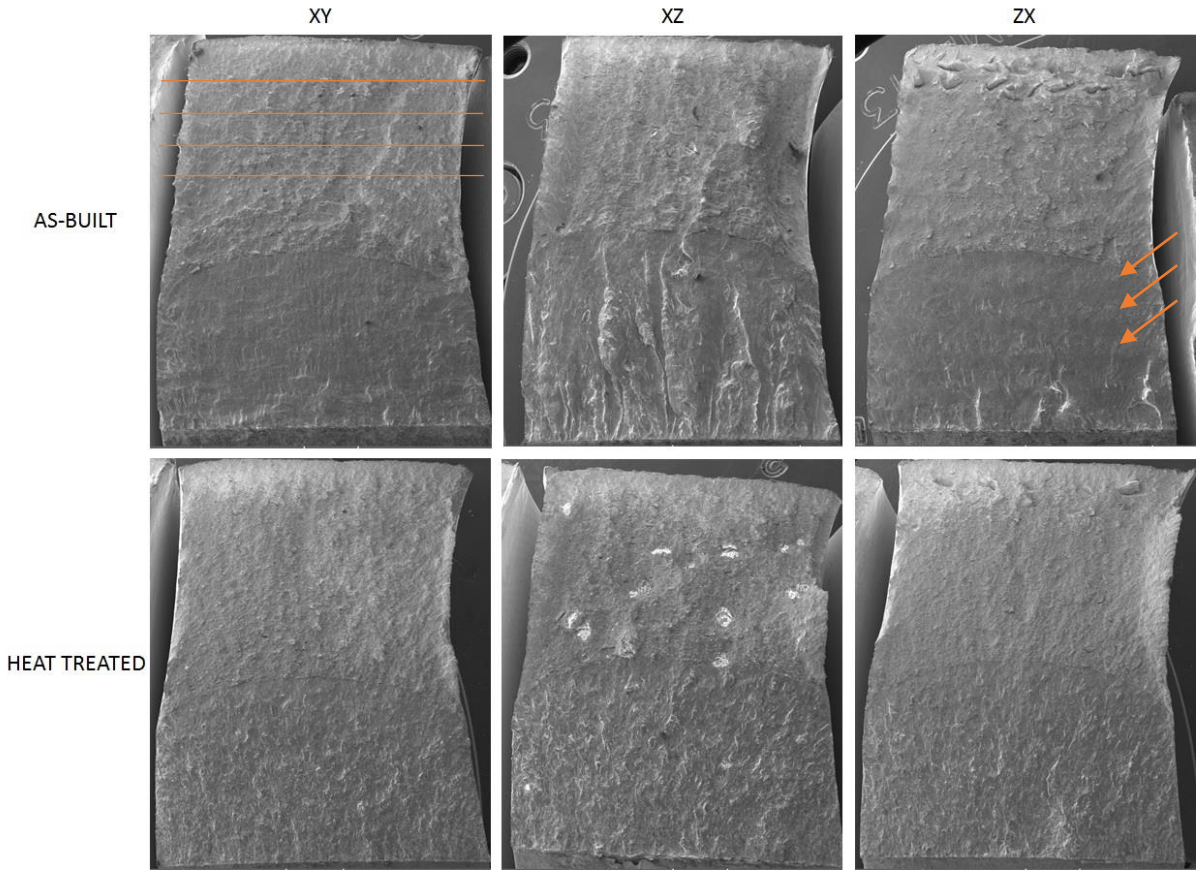

Figure 5.31: Fractographs of all three build orientations in the as-built and heat-treated conditions

Figure 5.31 above displays some differences between the as-built and heat-treated conditions. Looking at the XY orientation, the fatigue pre-crack region is easily distinguishable. In the XY orientation, the most noticeable differences are the scanning tracks that can be seen more clearly in the as-built condition. These are highlighted by the orange lines in the as-built view. The fracture surface within the fast fracture region of the as-built specimen appears to be rougher than the heat-treated specimen, which may be the results of the segregated microstructure and the ductility of the fracture. The uniform fracture surface of the heat-treated specimen also indicates that homogenisation was achieved after the heat-treatment.

The XZ orientated specimens displayed a rough fracture surface in the fast fracture region and ratchet marks are clearly visible in the fatigue pre-crack region. This was more prominent in the as-built condition where the pre-crack region was extremely uneven and possessed evenly spaced ratchet grooves on the surface what would have been multiple crack initiation sites at the notch tip. The ratchet marks correlated reasonably well with the hatch spacing of this build which was approximately 0.8 mm, thus crack initiation would have been influenced by the scanning pattern and melt pools. Each ratchet groove was approximately 0.8 to 1 mm apart. The ratchet marks are associated with ductile tearing.

The ZX orientation displayed similar fracture surfaces and pre-crack regions to the XY specimens as the build parameters were similar. A more homogenous microstructure was seen in the as-built condition when compared to that of the XZ orientation. The scanning tracks can be seen in the direction perpendicular to the crack growth, which were similar to those seen in the XY orientation and is identified in the figure above by the orange arrows. A slightly rough surface within the fast fracture region was seen on the as-built specimen, which indicates ductile behaviour. This was similar

to the XY and the XZ orientations but did not possess the same ratchet marks as the XZ orientation. The heat-treated specimen showed homogeneity in the fracture surface and the fatigue pre-crack region. This was similar to the XY orientation.

All heat-treated specimens displayed significant improvements in the homogeneity of their microstructure. This was an expected outcome of the high temperature solution treatment.

6. Discussion

In this section, the results obtained from the different tests will be analysed and the behaviour of the material will be discussed. The trends and relationships observed between different material conditions will also be discussed.

6.1. Tensile behaviour

The tensile test results showed noticeable differences between the as-built and heat-treated conditions. The tensile properties for various build orientations were not compared. A summary of the average ultimate tensile strengths for each material condition can be seen in the table below.

Table 6.1: Summary of average tensile test results

Material condition	Average Ultimate Tensile Strength (MPa)
As-built	874
Heat-treated	985

From the table above, it can be seen that the average UTS for the as-built condition is slightly lower than the heat-treated condition. The increase in ultimate tensile strength is not as high as seen by Wang *et al.* [32] and this could be due to the heat treatment protocol used for the current study. The protocol used for this study may not have completely dissolved the Laves phases that formed during the LENS process. Therefore, precipitation of the Ni_3Nb strengthening phase may not have been fully promoted however, strengthening did occur. The correlation of the heat-treated specimens was seen to be greater than the as-built specimens and this indicates a greater stability in the microstructure of the heat-treated material and a more uniform set of results.

The validity of the tensile test results according to ASTM E8 is also a concern due to the small size of the test samples however, a study by Kumar et al [51] has shown that the yield and ultimate tensile strengths of a material differ slightly among full size, sub-size and miniature tensile specimens. The UTS was seen to be between 2%-4.5% lower than full size test specimens. For the current application of comparative purposes, this observation is acceptable. Uniaxial standardised testing procedures for miniature specimens will need to be developed.

Further investigation into the tensile properties will have to be performed on larger test specimens to obtain a full range of data, encompassing the yield strength, percentage elongation and also to prevent slippage of the specimen in the grips of the testing machine. Slippage was seen during the tests and is clearly illustrated in the graphs as the elastic region is not perfectly linear. This can be overcome with a larger gripping area on a bigger test specimen. The development of robust adequate grips and fixtures is highly recommended to prevent slippage during testing. The tensile test should also be performed for all build orientations in order to investigate the effect of build orientation on the mechanical properties in both the as-built and heat treated conditions.

6.2. Fatigue crack growth rate behaviour

Three different build orientations were examined during the FCGR tests. The aim of the experiment was to determine whether the build orientation affected the fatigue crack growth rate properties of the material and whether the application of a heat treatment was sufficient to homogenise the material enough to negate the effects of the build orientation, if there was a significant difference. This information is required to address the question of whether DED can be used to manufacture high speed micro gas turbine blisks from IN718, as fatigue crack resistance and fatigue crack propagation characteristics can be an indication of the longevity of the part.

6.2.1. Differences within the as-built condition

After completion of the FCGR tests, it was seen that there was a difference in the fatigue performance of the material depending on its build orientation. This was shown in Table 5.5 in terms of the Paris equation with constants *C* and *m* being the defining characteristics to gauge the differences between the build orientations. The summary of the FCGR test results are shown in Table 6.2 for reference in this section.

Table 6.2: Summary of average Paris equations

Build orientation	Average as-built Paris equation	Average heat-treated Paris equation
XY	$\frac{da}{dN} = (15.8 \pm 5) \times 10^{-16} \Delta K^{5.53 \pm 0.100}$	$\frac{da}{dN} = (1.69 \pm 1) \times 10^{-19} \Delta K^{8.48 \pm 0.320}$
XZ	$\frac{da}{dN} = (17.8 \pm 7) \times 10^{-16} \Delta K^{5.38 \pm 0.190}$	$\frac{da}{dN} = (11.7 \pm 6) \times 10^{-19} \Delta K^{7.22 \pm 0.290}$
ZX	$\frac{da}{dN} = (1.51 \pm 0.7) \times 10^{-16} \Delta K^{6.30 \pm 0.230}$	$\frac{da}{dN} = (0.66 \pm 0.3) \times 10^{-19} \Delta K^{8.00 \pm 0.130}$

Firstly, looking at the average Paris equation in the as-built condition for each build orientation, slight differences in the *m* and *C* values per orientation are noticed. The XY and XZ orientations exhibit similar Paris equations in the as-built condition whereas the ZX orientation exhibits a steeper gradient of Paris region II by means of an increased *m* value. Although the difference appears small, this does indicate that build orientation plays a role in FCGR properties. During testing of all the as-built test samples, the fatigue performance was erratic and not consistent. This erratic performance refers to the variation in the duration of each fatigue test and the variation in the test end condition. For a uniform material, the number of cycles to the end of test condition of approximately 12.1 mm of crack length should have been consistent or at least in a suitable range. However, the range of cycles to test end was quite irregular. Table 6.3 below displays a summary of the number of cycles taken to the reach the test end condition for the as-built samples that were tested at a load range of 7.2 kN.

Table 6.3: Cycles to test-end for as-built condition

Specimen	Number of cycles to test end (ΔP = 7.2 kN)	Cycle range	Cycle range as a percentage of max cycles
XY5	29 300	19 700	67%
XY6	24 000		
XY7*	9 600		
XZ1	29 500	10 700	36%
XZ2	10 700		
XZ3	18 800		
ZX1	8 600	3 150	33%
ZX2	6 300		

ZX3	9 450		

**Samples with different build parameters (see Section 4.2.1 for details)*

Looking at the XY build orientation, the specimens that were tested at a load range of 7.2 kN (specimens XY5, XY6, and XY7) experienced completely different end points with XY5 ending at 29 300 cycles, XY6 ending at 24 000 cycles and XY7 ending as low as 9 600 cycles. XY5 and XY6 are in an acceptable range as all specimens would not behave in the exact same manner. XY7 however, was built with different build parameters to XY5 and XY6. This was mentioned in section 4.2.1. A range of scatter can also be seen in both the XZ and ZX build orientations, where the number of cycles to test end varies from 10 700 cycles to 29 500 cycles for the XZ orientation and 6 300 and 9 450 cycles for the ZX orientation. This is a significant difference, more so in the XZ orientation, considering that the specimens are manufactured from the same block of source material. Furthermore, the last column in Table 6.3 above shows the cycle range as percentage of the maximum number of cycles for that build orientation. This is simply to show the extent to which the level of scatter in the data occurs. A higher percentage indicates that there is more scatter in the data. This shows that the microstructure of the material lacks homogeneity in the as-built state as the material struggles to behave in a uniform manner and could be attributed to the presence of residual stresses in the material after building, and the presence of Laves phase that is indicative of a lack of precipitation of the secondary phase precipitates. The fatigue crack path is also a good indicator of the microstructure homogeneity. This will be looked at later and compared to the crack path of the heat-treated material.

6.2.2. Differences within the heat-treated condition

Comparing the Paris equations obtained for the heat-treated condition, there is still a difference between the different build orientations. The magnitude of the gradient for each build orientation can be seen to have increased from approximately 5 to approximately 8. As mentioned in Section 4.2.1, the build parameters for XY13 and XY14 were different when compared to the other XY specimens. As a result, the standard error on the average Paris equation constants, m and C, for the XY orientation is slightly more than the XZ and ZX. This is due to the XY orientation having specimens that were built with different build parameters which introduces another variable into the experiment – that being the build parameters. Specimens XY8 to XY12 possessed gradients ranging from approximately 8 to 9.7 with the majority of specimens being in the upper 8 regions. Specimens XY13 and XY14 possessed gradients of 7.6 and 7.2 respectively. This is a significant reduction in the gradient considering that all specimens were heat-treated according to identical heat-treatment protocols. Therefore, the build parameters affected the fatigue crack growth rate properties of the material and require further investigation, which is not within the scope of this project. Specimens XY13 and XY14 were manufactured using the same build parameters as the ZX orientated specimens. Comparing these two XY orientated specimens with the heat-treated ZX specimens, they can be seen to correlate more closely with each other and exhibit a similar test end point of approximately 30 000 cycles. Table 6.4 below is similar to Table 6.3 shown above but displays the heat-treated data.

Table 6.4: Cycles to test-end for heat-treated condition

Specimen	Number of cycles to test end (ΔP = 7.2 kN)	Cycle range	Cycle range as a percentage of max cycles
XY8	26 750	46 670	66%
XY9	59 500		

XY10	70 850		
XY11	59 950		
XY13*	35 700		
XY14*	24 180		
XZ4	45 800	16 900	29%
XZ5	40 800		
XZ6	57 700		
ZX4	51 200	19 600	38%
ZX5	33 200		
ZX6	31 600		

** Samples with different build parameters (see Section 4.2.1 for details)*

From the data shown in Table 6.4 above, the XY orientation exhibits a greater level of scatter which is owed to the specimens XY13 and XY14 having different build parameters. Specimen XY8 does also exhibit a much shorter fatigue life than the other similar specimens but the FCGR test conducted on XY8 was not uniform. The test was initially conducted at a load range of 5.85 kN but this was changed to 7.2 kN due to the crack growing unreasonably slowly. This essentially gave the fatigue crack a start advantage which is why the life is much lower than the others. Specimen XY12 was omitted from the table above as it was tested at a load range of 9 kN and therefore, the life was significantly lower than those tested at 7.2 kN. The life of the ZX specimens can be seen to correlate quite well with XY13 and XY14, which shows that the was some homogenisation in the material after the heat treatment since the specimens are built with two different build orientations but display similar Paris data. This finding was beneficial as it shows that two different build orientations can be homogenised with a heat-treatment and display uniform properties within an acceptable range.

6.2.3. As-built vs heat-treated behaviour

Comparing both material conditions, the heat treatment significantly improves the fatigue crack growth resistance of the material. This is owed to the precipitation hardening of the material during heat-treating. The mechanism for this will be outlined more in Section 6.5. The duration of the FCGR test was extended by at least a factor of 2 in most cases with the application of the heat-treatment. This indicates that the material should undergo a post manufacture heat-treatment to strengthen the material and to improve its fatigue crack growth resistance. The as-built condition does display a decent level of fatigue crack growth resistance but not to the extent of the heat-treated specimens. Comparing the Paris regions of both material conditions, it can be clearly seen that there is less scatter in the data plot of the heat-treated specimens. The linear region of the heat-treated specimens appears to be much more linear than the as-built specimens and hence a much closer correlation. This trend can be seen for all build orientation and is illustrated in Figure 6.1 and Figure 6.2 with reference to the Paris curves for the ZX build orientation.

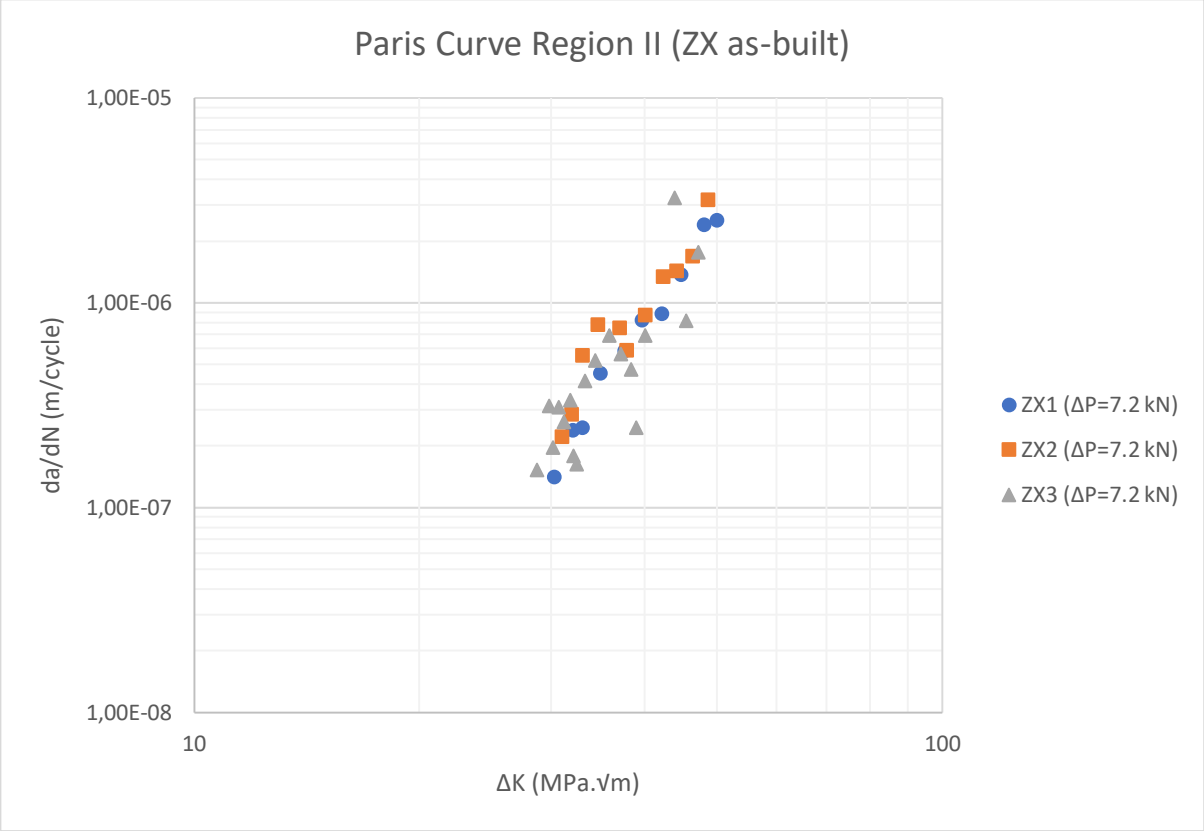

Figure 6.1: Paris curve for ZX as-built orientation

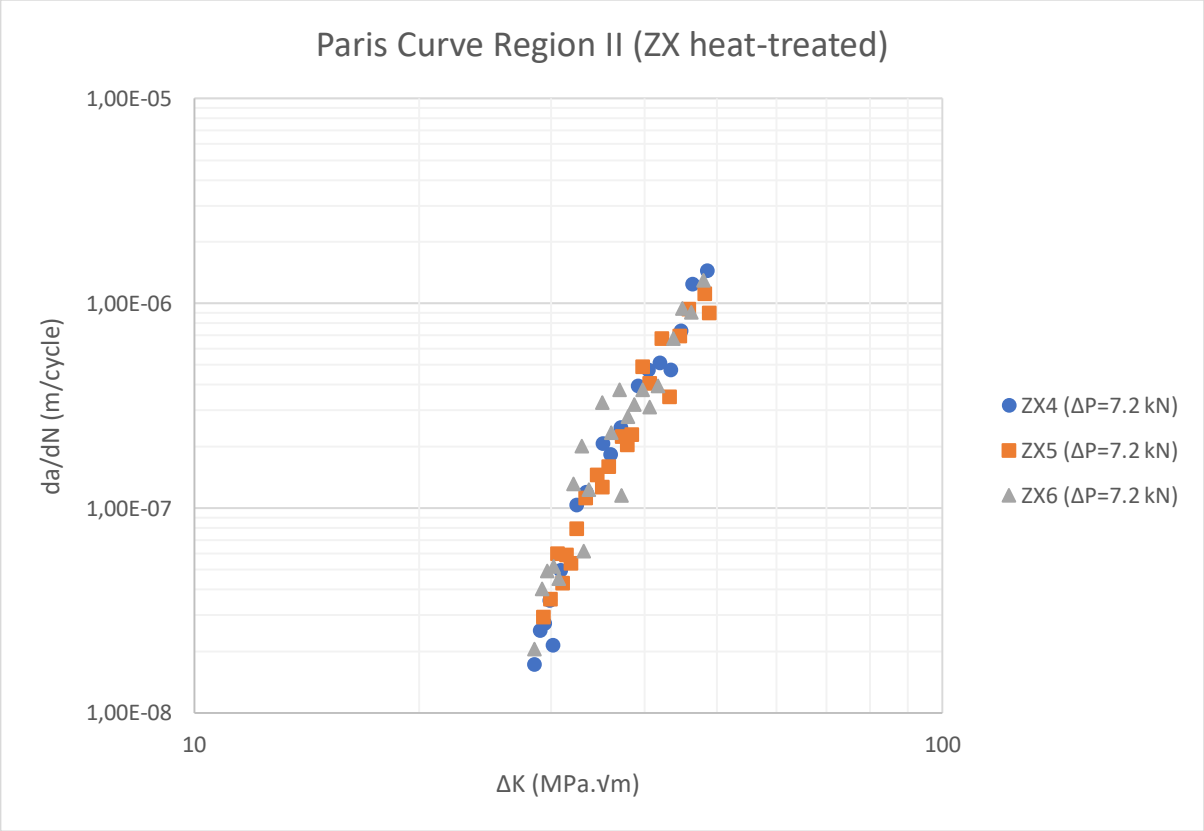

Figure 6.2: Paris curve for ZX heat-treated orientation

The crack growth stability (qualitatively determined from the crack path relative to the horizontal plane) of the heat-treated specimens showed significant improvements when compared to the as-built specimens. Examples of which can be seen in the figures below.

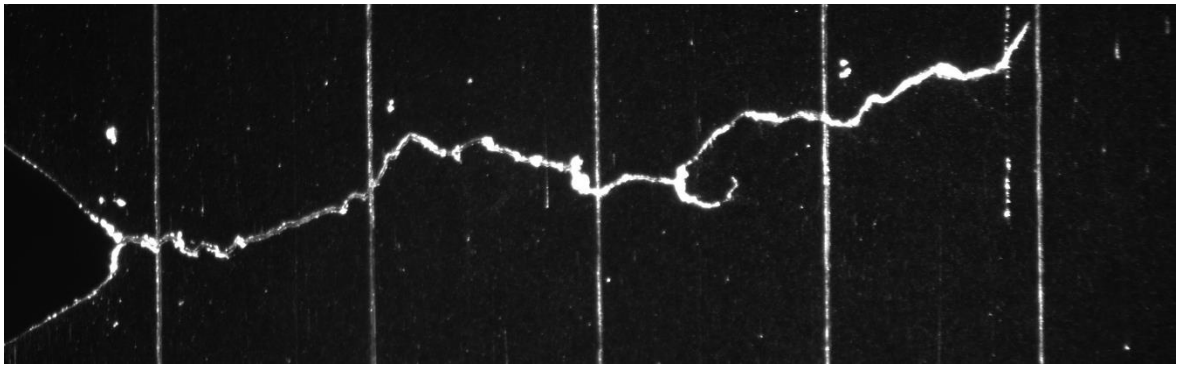

Figure 6.3: Fatigue crack path for as-built specimen

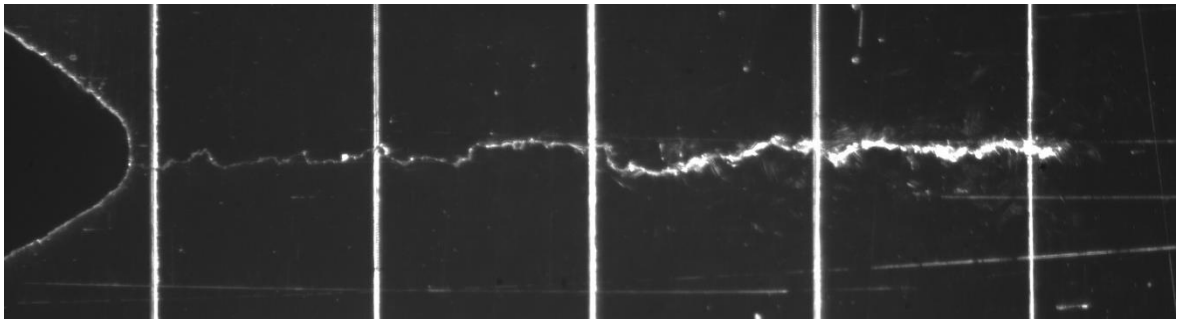

Figure 6.4: Fatigue crack path for heat-treated specimen

Figure 6.3 and Figure 6.4 above display the fatigue crack path of specimens XY2 and XY12 which are in the as-built and heat-treated conditions respectively. Both specimens were built using the same build parameters. The instability in crack growth can be seen in the as-built condition as the crack deviates from the horizontal (crack plane) frequently and struggles to maintain a steady path. In this context, steady refers to the degree of crack deviation away from the crack plane. A steady crack will not deviate significantly from the crack plane as shown in Figure 6.4, whereas in Figure 6.3, the crack deviates approximately 1 mm away from the horizontal crack plane. After the heat-treatment, the crack growth is much more stable and maintains a steady path along the horizontal. This indicates that the heat-treatment homogenises the microstructure of the material and is far more stable than the as-built condition. This relationship was noticed in all build directions.

As mentioned in Section 5.2.1, specimen XY4 was omitted from the analysis because the fatigue crack path deviated on more than one occasion. This is highlighted by the white circles in Figure 6.5 below.

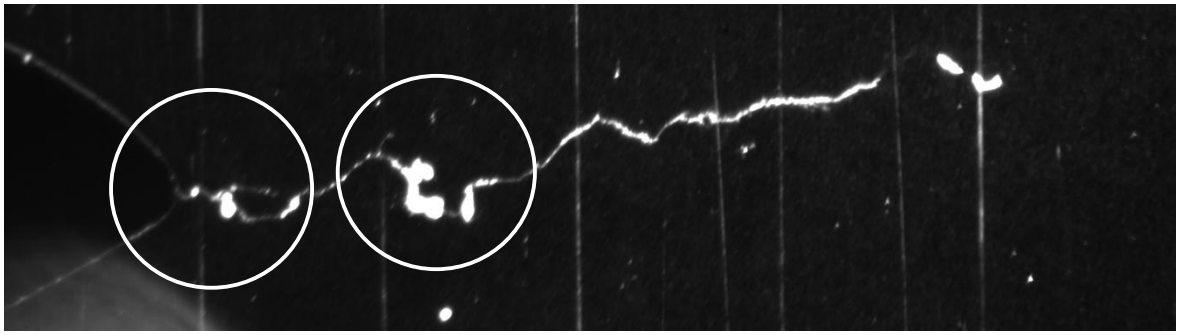

Figure 6.5: Fatigue crack path for XY4 highlighting deviations in crack

These deviations caused the energy in the material to be shared by two cracks instead of one, which in turn essentially halves the crack growth rate. This false indication of crack growth rate resulted in the data being invalid as the correlation of the data was too low to determine reasonable Paris constants. The fatigue crack deviation occurred in more than one test specimen more so in the as-built conditions. The images of the final crack for each of the test specimens tested can be found in Appendix 11.5.

The heat-treated specimens developed an oxide scale on the surface of the specimens after the heat-treatment. This was formed during the 1200 °C solution treatment. After polishing the specimens for FCGR testing, it was noticed that an underlying grain structure was revealed. This is shown in Figure 6.6 below.

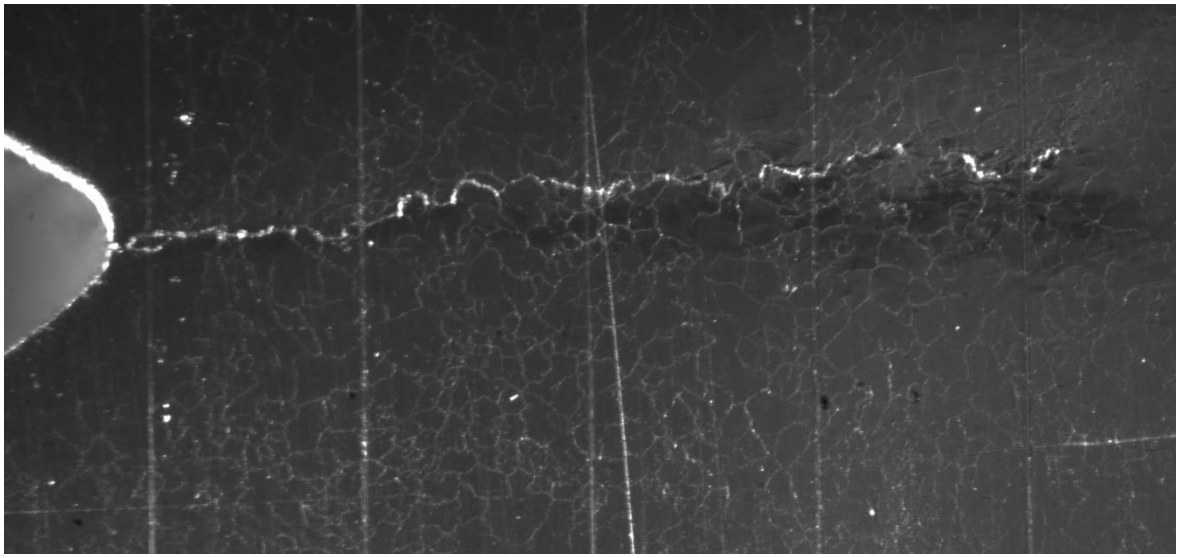

Figure 6.6: Underlying grain structure on the surface of heat-treated specimen XY11

Figure 6.6 above shows the fatigue crack grown for specimen XY11. During the heat treatment, the oxide layer that was formed penetrated the surface of the material at high energy locations. These high energy locations were the grain boundaries. After polishing the oxide layer away, the grain boundaries that were penetrated by the oxide were exposed and therefore, the grain structure could be easily seen. Greater surface material removal would have removed these features.

Considering all build orientations and all material conditions, the Paris data for the ZX and XY orientations displayed a greater correlation than the XZ orientation. This could be owed to the direction of grain growth within the material when being built as AM produced material generally forms columnar grains. This was seen during the microstructural analysis in Section 5.6. The microstructural findings will be discussed in greater detail in Section 6.5.

6.2.4. Paris region

In Section 2.12, the two-stage Paris region was introduced, which was seen in BS 7910:1999. This type of behaviour was expected during testing since the gradient of the Paris region was very high when compared to other sources of literature. Therefore, specimens XY3, XY6, XY9 and XY10 were cycled in fatigue to failure. The trend to expect for a two-stage Paris region was shown in Figure 2.41. The figure below displays the Paris curve to failure for XY3, XY6, XY9 and XY10.

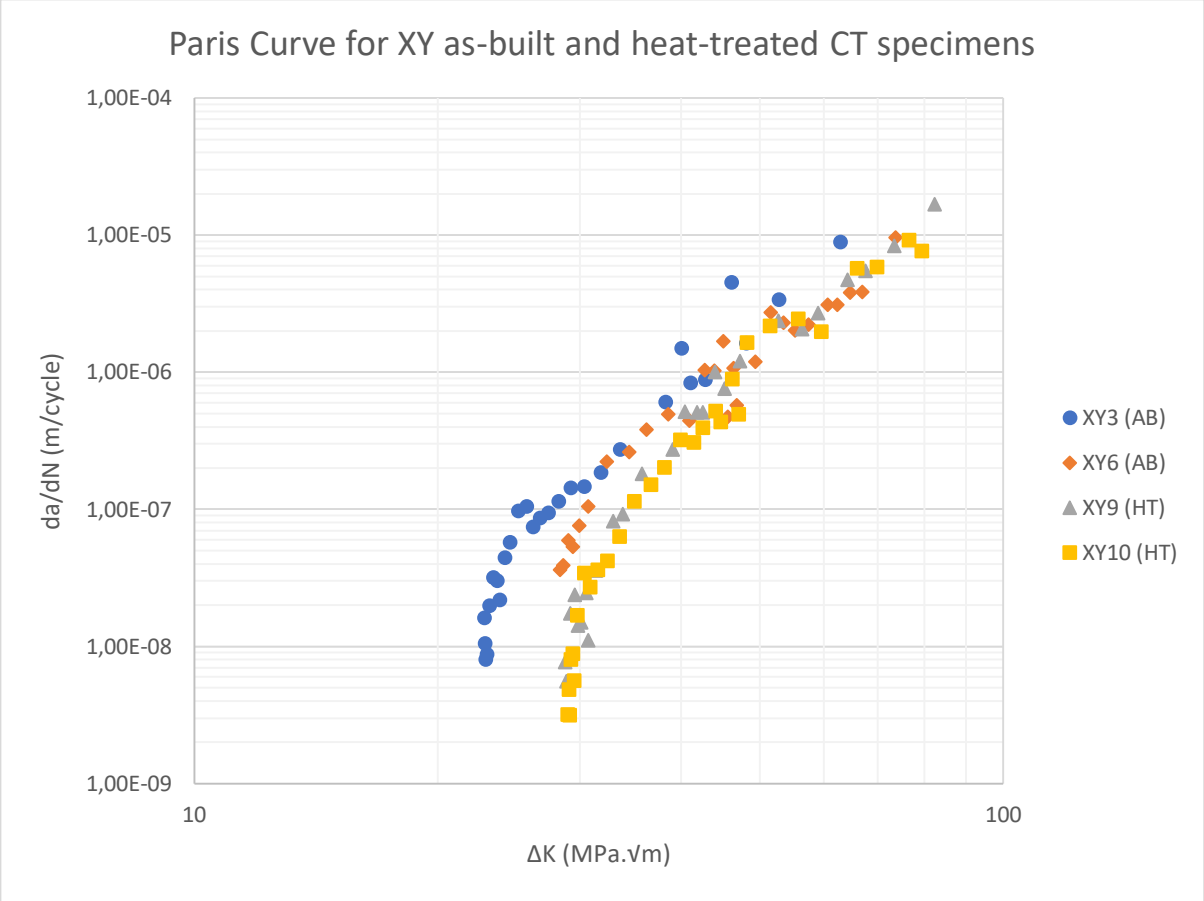

Figure 6.7: Paris curve for specimens tested to failure

The Paris curves seen in Figure 6.7 clearly display the primary Paris region where crack initiation occurs. This is usually known as the threshold stress intensity factor but in the case of this project, the actual threshold was not determined. The secondary Paris region can also be clearly seen as the linear region of the curve. It is difficult to determine whether the curve does exhibit a two-stage Paris region as the crack growth rate increased rapidly towards the end of the test. This can be seen in the amount of scatter present in the latter portion of each Paris curve. As a result, the BS 7910 two-stage Paris behaviour was rejected due to scatter in the data. Fast fracture which was expected for this material did not occur. It was observed that the material failed in a completely ductile manner with no fast fracture region being observed. This was peculiar as the dummy stainless-steel specimens that were tested to failure experienced fast fracture with a snapping noise. This noise was not heard for the IN718 specimens and the material simply stretched apart. This was observed in both the as-built and heat-treated conditions.

Gradients as high as 7 and above are usually indicative of very brittle materials however, the IN718 material behaved in a completely ductile manner. The high gradient of the Paris region could owe to the material being highly resistant to fatigue crack growth since IN718 is a strong alloy with a high tensile strength. As mentioned in Section 2.12, the gradients observed by Ganesh *et al.* [40] for LRM IN625 were seen to have a magnitude of approximately 5. The material in this study exceeds this by a large margin despite being a different alloy.

6.3. Fracture toughness behaviour

The elastic-plastic behaviour of the material during the fracture toughness tests was not expected prior to testing as the experiment was designed for a plain strain fracture toughness test. Therefore,

the focus was shifted from plain strain fracture toughness to J-integral fracture toughness. It is known that a thick test specimen is required to obtain a valid K_{1C} value, which can result in unreasonably large test specimens to be manufactured. Large specimens were not an option owing to the high cost of the nickel-based super alloy material. Since the specimen was designed to be as small as possible (while still adhering to the ASTM standard), the thickness might not have been large enough to determine the plain strain fracture toughness. Therefore, the values obtained for K would be higher than the true material K_{1C} as shown in Section 2.11.2.1. This could explain why the fatigue crack growth rate tests were able to reach such high ΔK values and correspond to high m and low C values. The stress intensity factor was not reaching the true plain strain fracture toughness value because the sample may have been in slight plane stress conditions.

A summary of the FT test results is shown in Table 6.5 below. These results were shown in Section 5.3.

Table 6.5: Summary of fracture toughness results

Build orientation	Average as-built J_{max} (kJ/m^2)	Average heat-treated J_{max} (kJ/m^2)	Increase in J_{max} after heat treating (kJ/m^2)
XY	234 ± 6	285 ± 9	51
XZ	323 ± 22	391 ± 28	68
ZX	210 ± 11	245 ± 10	35

The fracture toughness properties are required as they indicate the material's resistance to brittle fracture. This is beneficial for DED produced IN718 as existing flaws in the material can propagate under high loading conditions such as in a micro gas turbine engine. If an AM produced material is able to resist crack propagation and ultimately fracture, then it will benefit its' suitability in gas turbine engine applications.

6.3.1. As-built behaviour

There is a distinct difference in the J_{max} values for the different build orientations. It is also to be noted that different build parameters were used to build certain specimens as mentioned in Section 4.2.1. These build parameters could have affected the fracture toughness behaviour of the material in the same way that the fatigue crack growth behaviour was affected. The XY orientation exhibited a low standard error as compared to the XZ and ZX orientations. This indicates that the response of the material to ductile tearing was stable. Furthermore, XY7 was built with the same build parameters as the ZX orientation. Comparing the J_{max} of XY7 (213 kJ/m^2) and ZX1-ZX3 (233, 185 and 211 kJ/m^2) in isolation, it was seen that XY7 displayed a similar J_{max} to the ZX orientation meaning that the build orientation did not affect the fracture toughness to a great extent. However, it is not conclusive whether this is truly the case as the sample space is too small. A greater number of test specimens all having the same build parameters should be used to eliminate the effects of build parameters on the test results.

The XZ orientation exhibited the greatest average J_{max} in the as-built condition but also exhibited the greatest standard error. A greater number of test specimens would be beneficial to eliminate the scatter within the data, but the error could also be as a result of the microstructure obtained after printing. The XZ specimens possessed the greatest layer thickness and hatch spacing. This could result in inconsistencies within the microstructure of the material by means of porosity.

The data from all orientations in the as-built condition indicates that there is a difference in the fracture toughness properties in terms of J_{max} between the different orientations. It is not conclusive to what extent the build parameters affected these fracture toughness results. Similar findings were observed by Cain *et al.* [17] in terms of the effect of build orientation on the fracture toughness, however these tests were conducted in the plain strain condition and hence, K_{1C} results were obtained. The ZX orientation in the work by Cain *et al.* [17] exhibited the lowest fracture toughness, which is similar to the findings of the current study. The XY orientation according to Cain exhibited the highest fracture toughness whereas in the current study, the XZ orientation exhibited the highest fracture toughness properties in terms of J_{max}. The different build parameters however could have affected the fracture toughness properties, as mentioned previously.

6.3.2. Heat-treated behaviour

The heat-treated fracture toughness test results indicate very similar findings to that of the as-built condition. It was seen that J_{max} increased in all three build orientations, indicating that a greater amount of energy is required for crack extension. This demonstrates that the material was strengthened during the heat-treatment and precipitation hardening was successful. The last column in Table 6.5 above shows the increase in J_{max} as a result of the heat-treatment. The increases for each build orientation are within the same range and are thus comparable. This indicates that the hardening effects were relatively consistent throughout the build orientations regardless of the build parameters.

The homogenisation effects achieved after heat-treating cannot be clearly seen when looking at the data because not all specimens had the same build parameters. The homogenisation effects however, could be seen on the fracture surfaces of the test specimens and this will be shown in Section 6.3.3 below.

6.3.3. Fracture surfaces

The fracture surfaces observed between the as-built and heat-treated material were completely different. The homogenisation effects from the heat treatment can be clearly seen from the SEM fractographs that were shown in Section 5.7. The differences between the fracture surfaces of the various build orientations were also be seen. Figure 6.8 (a) and (b) is adapted from Section 5.7 and highlight the main differences in the fracture surfaces between the heat-treated and as-built material.

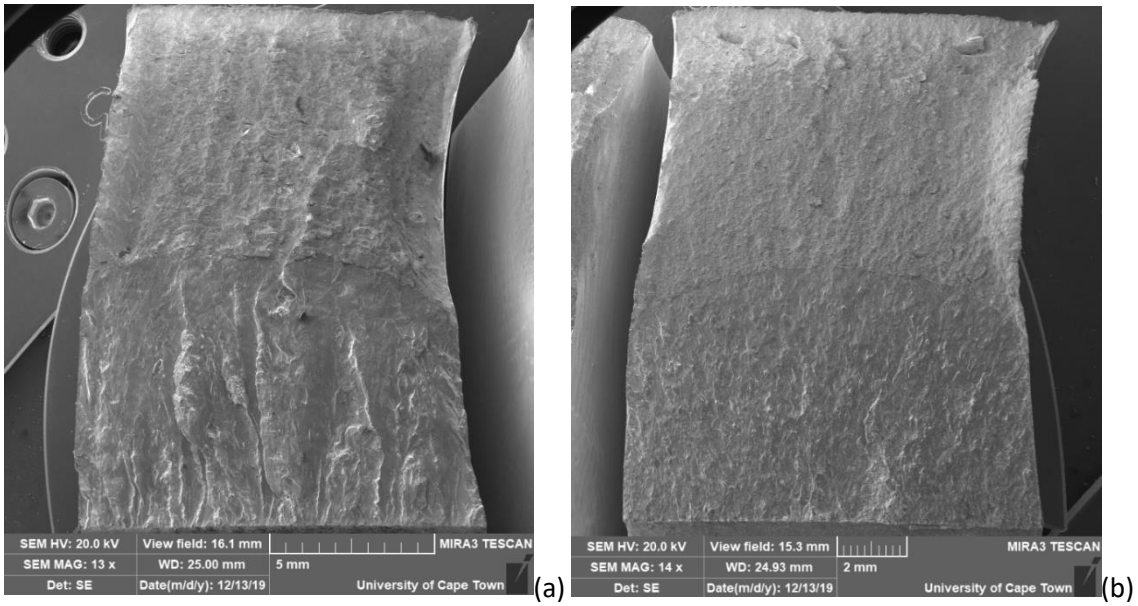

Figure 6.8: Fracture surface comparison between XZ as-built (a) and ZX heat-treated (b)

The as-built XZ specimen can be seen in (a) and the heat-treated ZX specimen can be seen in (b). These two specimens were chosen to be compared here, even though they are from different build directions, as they possessed the greatest contrast in fracture surfaces and clearly highlight the major differences between the as-built and heat-treated material. The as-built material can be seen to possess ratchet marks on the fracture surface within the fatigue crack propagation region which is indicative of multiple crack initiation sites at the notch tip, but may also be influenced by the porosity and microstructure of the AM specimens. Ratchet line are formed by the intersection of fatigue cracks propagating from multiple origins. They are most commonly associated with brittle materials. The size and location of the ratchet lines could also owe to the direction of grain growth of the XZ specimen as the columnar grains grew in the direction of crack growth. This can be compared to chopping a piece of wood along the grain which is easier than against the grain.

6.4. Effectiveness of the developed crack measurement technique

The overall effectiveness of the new crack measurement technique needed to be evaluated in order to establish whether the system was an improvement of the existing system and if so, by how much. Fatigue crack growth rate tests were therefore performed using the new crack measurement system to take measurements of the crack length at regular intervals and the data was then compared to that of the initial data. For reference, the data obtained from SS9 will be compared to the data obtained from another dummy specimen, SSN2, which was tested using the new crack measurement technique. This data will be shown in Figure 6.9 and Figure 6.10.

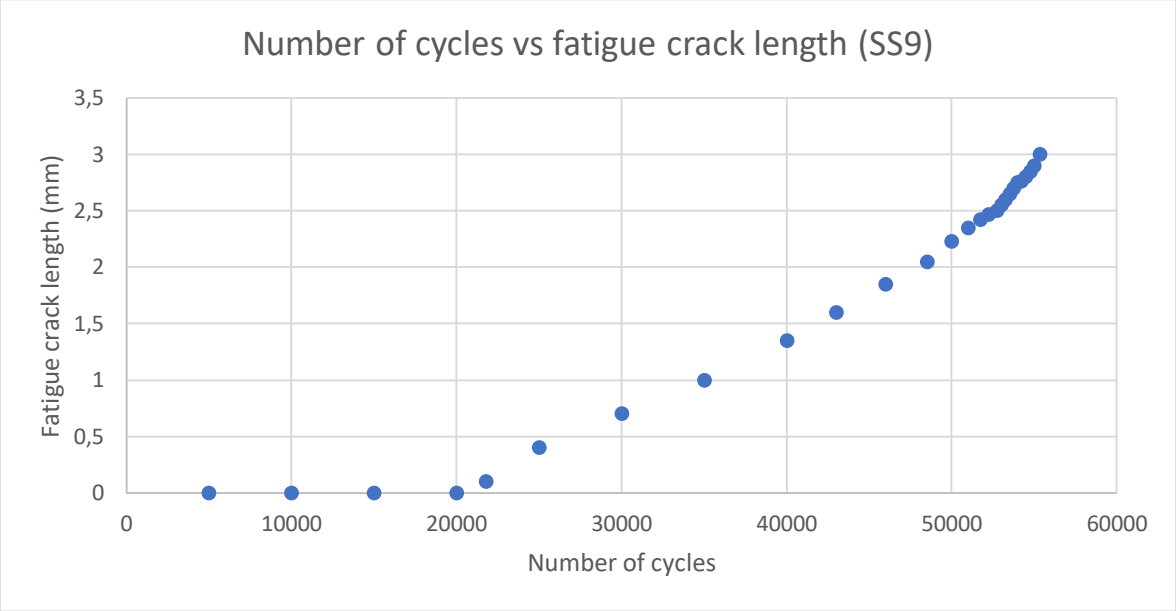

Figure 6.9: Number of cycles vs fatigue crack length for SS9 without camera system

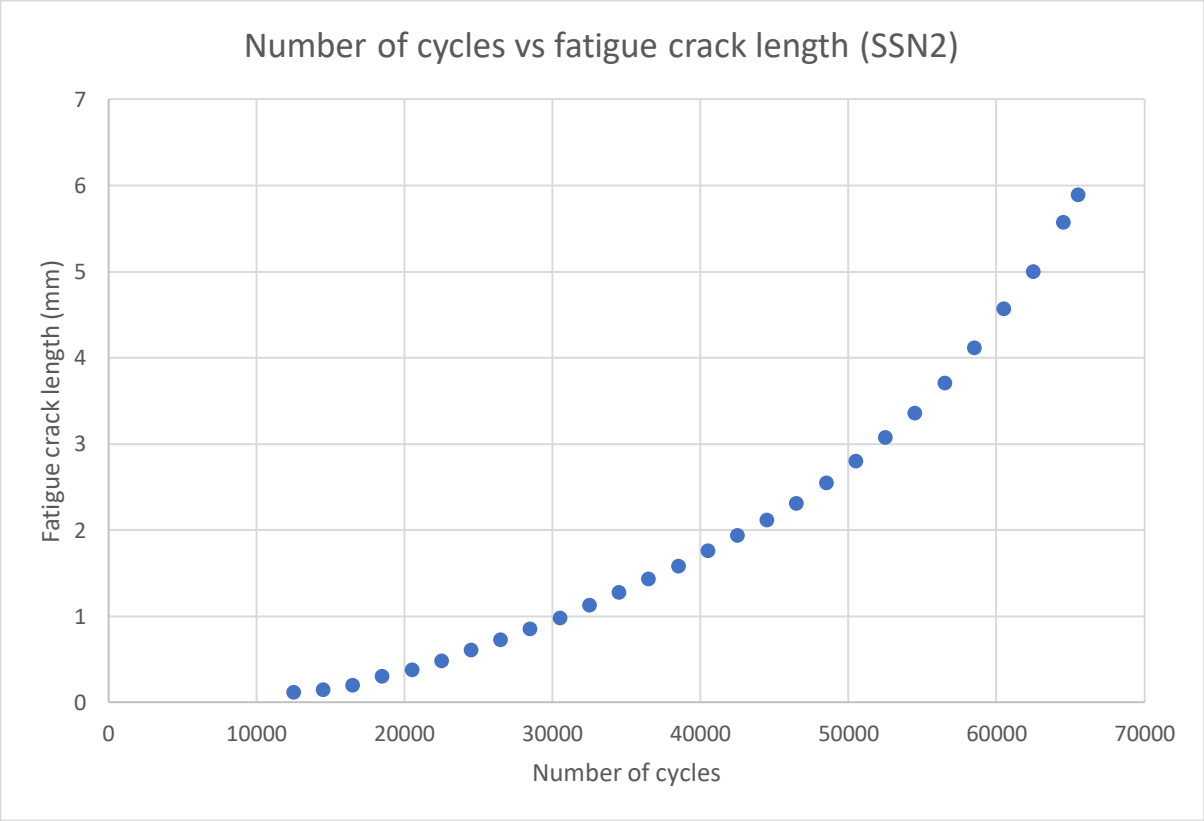

Figure 6.10: Number of cycles vs fatigue crack length for SSN2 with camera system

Figure 6.9 and Figure 6.10 above show the curves for the number of cycles vs fatigue crack length for both SS9 and SSN2. The results for SSN2 using the new crack measurement technique are clearly more representative of the expected curve, which can be seen in Section 2.12, and there is less scatter in the data as compared to the data obtained for SS9.

The ΔK vs $\left(\frac{da}{dN}\right)$ comparison can be seen in Figure 6.11 and Figure 6.12.

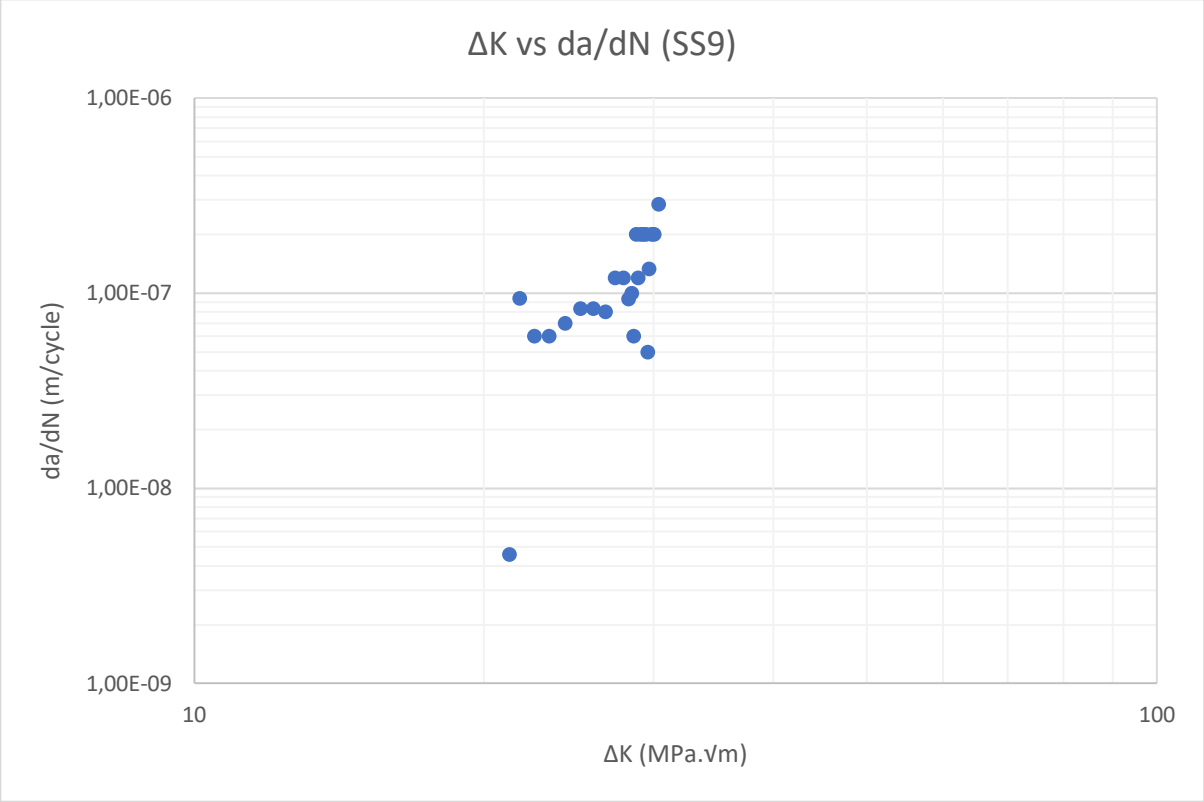

Figure 6.11: Paris curve for SS9 without camera system

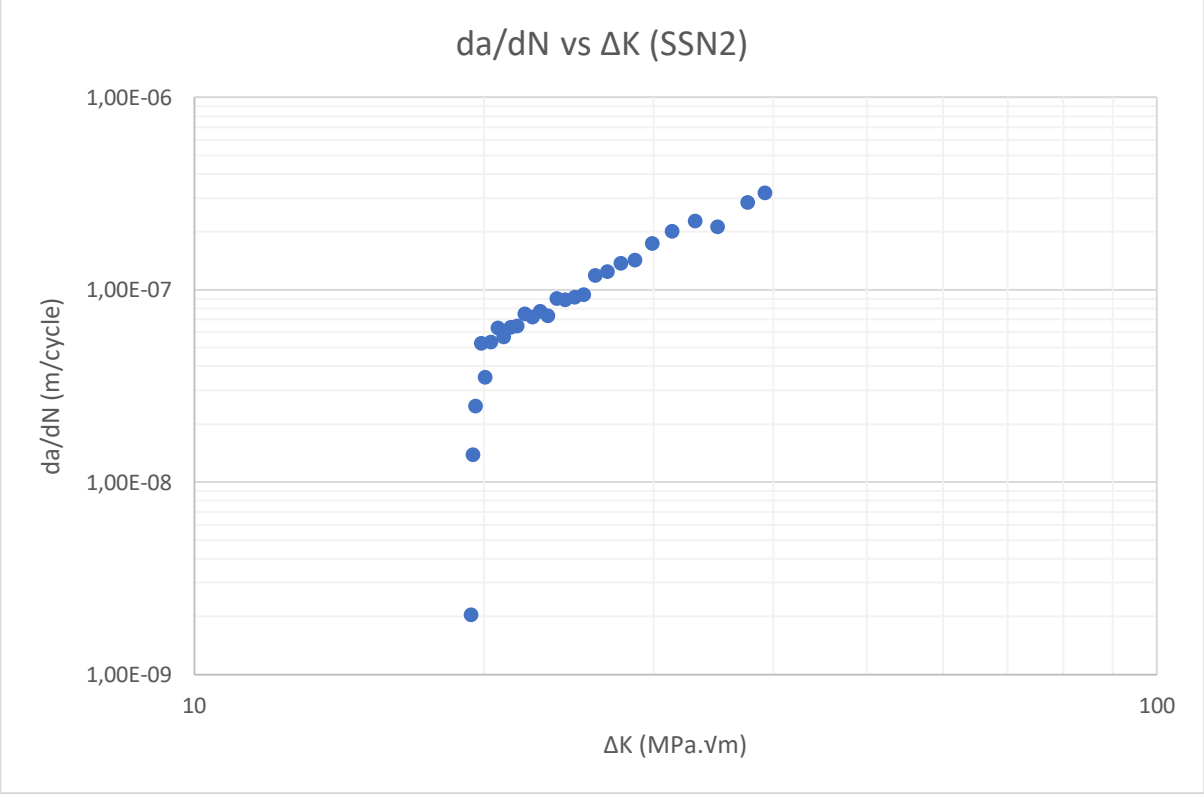

Figure 6.12: Paris curve for SSN2 with camera system

It is clear to see that the data obtained for SS9 has almost no correlation and is due to inaccurate crack measurements during the fatigue crack growth rate test. The data obtained for SSN2 is almost

completely representative of the expected curve which was shown in Section 2.12 and displays a clear region I, II and partial region III crack growth. The Paris region can also be clearly seen, which is indicative of accurate data collection.

The overall accuracy of the crack measurement system was compared to NIS elements, which is a calibrated system. The crack measurement system could potentially possess some inaccuracies within the ImageJ software itself or instabilities in the rig that could cause the calibration to deviate. It was found that the deviation from the NIS elements system was no more than 2% in the ImageJ results. This indicates that the crack measurement system is accurate enough to perform fatigue crack growth tests with an acceptable level of accuracy. Details for calculation of this accuracy can be found in Appendix 11.11. The new crack measurement technique can provide data that is significantly more accurate than that of the existing visual technique. The crack measurement is also a seamless and user-friendly process.

6.5. Microstructure

The microstructural differences between the as-built and heat-treated material were significant. From the micrographs seen in Section 5.6, the as-built built material can be seen to have a fine grain structure with the grains being elongated in the build direction (Z-axis). This is a characteristic of additively manufactured metallic alloys. The fine grains are advantageous since there are more grains which lead to more grain boundaries to prevent dislocations from moving past each other. This results in an increase in overall strength of the material. The microstructure after heat-treating was seen to result in the coalescence of grains which results in fewer grain boundaries to obstruct dislocation movement. The extent to which was not as severe as the grain size did not increase in size significantly. This can be seen in the SEM micrographs in Figure 6.13 (a) and (b) below which are repeated for reference.

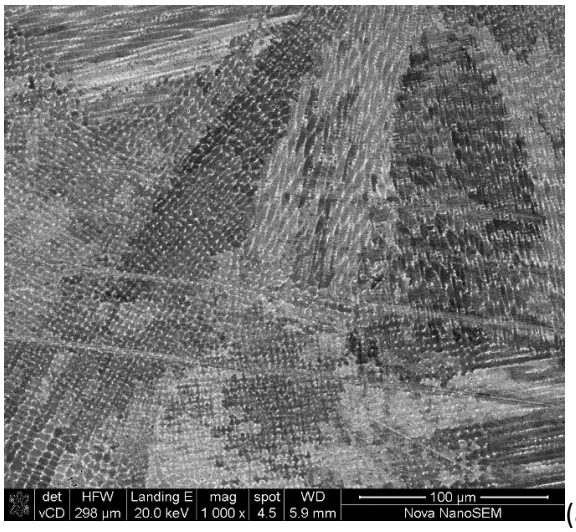

(a)

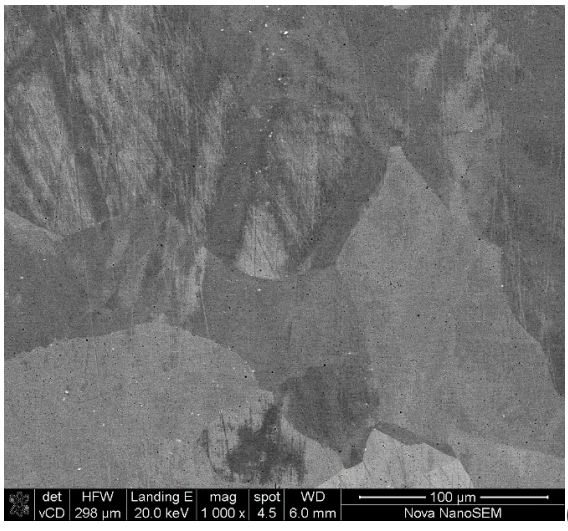

(b)

Figure 6.13: Comparison between as-built (a), and heat-treated microstructures (b)

IN718 is a precipitation hardening alloy and requires a fine distribution of secondary phase precipitates for strengthening purposes. According to the SEM images and EDS spectrographs, the Niobium was seen to have diffused out of the solid solution and formed Laves phase within the as-built material. This was identified by the white patches throughout the grains structure and can be seen clearly in the figures above. As this does provide some form of strengthening to the material, the effects are far less than obtaining a fine distribution of the secondary phase in the alloy. The heat-treatment was seen to have eliminated the Laves phase and all the Niobium particles that were

clustered together as a result of the AM building process. This means that the heat treatment was firstly able to solutionise the alloy and enabled precipitation of the niobium-rich γ'' phase thereafter to harden the material. This increase in hardness was confirmed during the hardness testing of the material, with a hardness increase of approximately 100HV for all build directions. This increase in strength was owed to the precipitation hardening effect that accounted for the increase in material hardness and resistance to fatigue crack propagation.

A significant level of porosity was observed in the material in both the as-built and heat-treated conditions. This type of porosity is common in AM produced metallic alloys and was outlined in Section 2.8.6. The porosity can be seen in the SEM micrographs in Figure 6.14 (a) and (b) below in the as-built and heat-treated orientations.

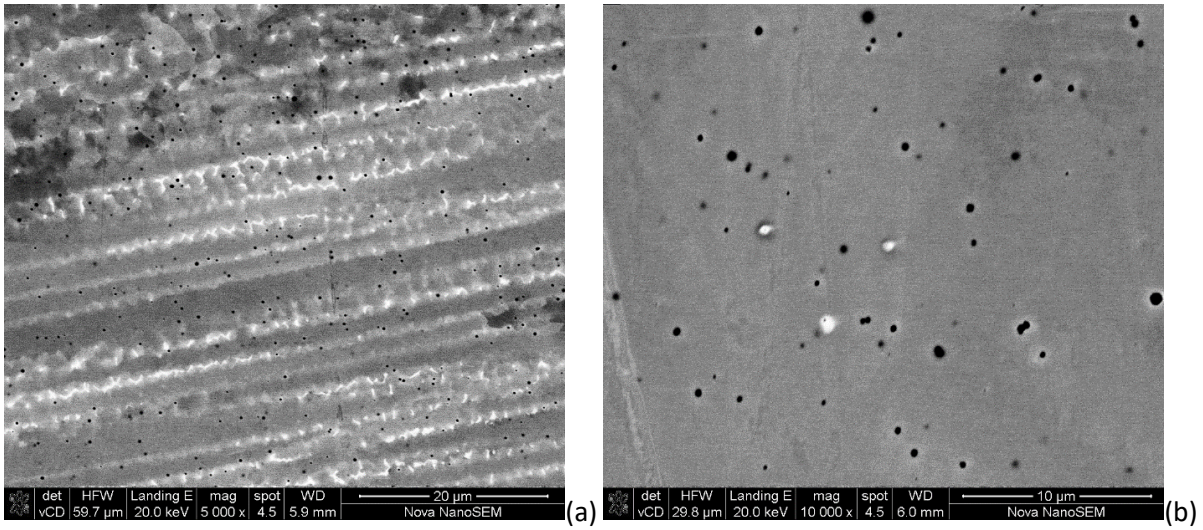

Figure 6.14: Comparison of the porosity seen in as-built (a), and heat-treated microstructures (b)

The heat-treatment did not significantly decrease the visual level of porosity by enabling diffusion of trapped gasses out of the alloy. The density test results did show an improvement in density especially in the XZ orientation however, this would require further investigation to confirm that the heat-treatment was responsible for the increase in density. The exact cause of the porosity observed in this project was not investigated but could be as a result of the build and laser parameters or the quality of the powders used for the DED process.

Other Inconel alloys such as IN625 exhibit similar as-built microstructures and can be seen in the figure below.

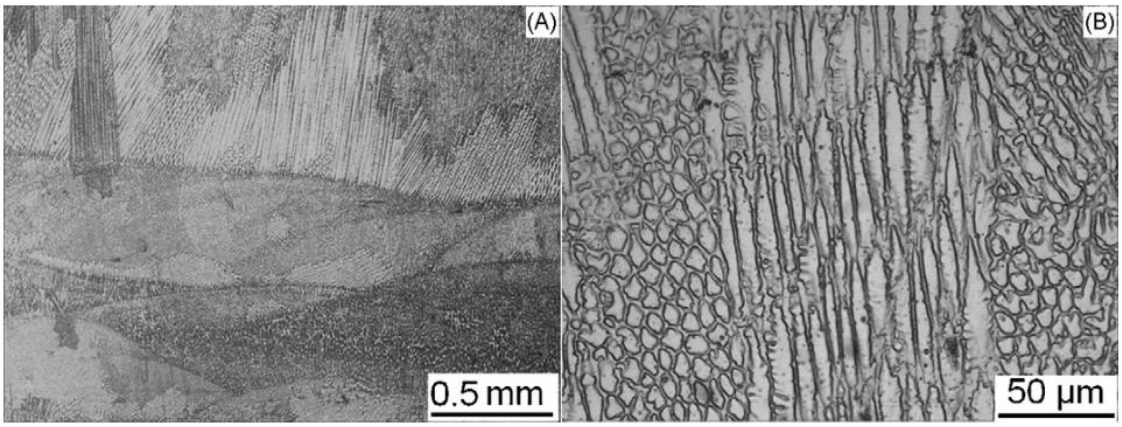

Figure 6.15: Microstructure of as-built IN625 [62]

IN625 derives its' strength from the stiffening effect of Mo and Nb on the Ni-Cr matrix. As a result, precipitation hardening heat treatments are not required. Light and dark patches can be seen in both IN718 in the current study as well as in IN625 as well as long columnar grains. According to a study by Zhao *et al*. [52], the grains of IN718 produced by SLM tend to coarsen less after heat treating when compared to that of wrought IN718. This is beneficial for AM produced parts in general as the finer grain structure can be retained after solution treating which further promotes the growth of secondary phase precipitates during the subsequent ageing process. A higher material hardness and strength can therefore be achieved by SLM produced IN718 as compared to its wrought counterpart [52]. A harder and stronger material would be beneficial for longevity purposes as the material will be more robust and resistant to fatigue crack initiation and crack propagation. This can most likely be applied to other forms of AM processes. In addition, due to the increase in defects induced by AM processes such as pores and voids, as well as the poor surface quality of the finished product, the fatigue performance of the material would generally be poorer than the wrought material in the as-built state, but can be overcome with optimised processing parameters and heat treatment protocols [53].

The images obtained during SEM indicate that a component manufactured from IN718 utilising the DED procedure would be more stable after heat treating was conducted on the material. This is seen in the SEM micrographs as the Laves phase was almost completely dissolved after the heat treatment protocol used in the current study. Stability in this context refers to the uniformity of the microstructure and distribution of all alloying elements. The structural integrity of a component manufactured this way may not be entirely stable in the as-built condition due to the lack of precipitation of the γ'' phase as well as the presence of porosity in the material which was seen to cause significant deviation in the crack path during FCGR testing. The porosity could also be attributed to the scanning parameters during the build that could have trapped gasses in the material during solidification. Since the Laves phase was almost completely dissolved after heat treating and precipitation hardening was achieved, the structural integrity of the component would increase. In the specific case of a gas turbine application where high rotational speeds are experienced, structural integrity is vital for the component and therefore, heat treating the material after building is evidently essential.

7. Conclusions

The results indicate that build orientation in DED produced Inconel 718 does have an effect on the room temperature fatigue and fracture properties of the material, with the XZ build orientation performing better than XY and ZX. The application of a post-build heat treatment results in an improved fatigue performance and increased fracture toughness properties. The heat treatment resulted in a consistent improvement in fatigue and fracture properties for all build orientations.

In order to achieve this aim, the following conclusions were drawn relating to the overall objectives of this work.

- The crack monitoring procedure incorporated a bolt-on rig to hold a stereo-microscope which allowed for real time monitoring and measurement of the crack growth during testing. The rig was able to achieve an accurate measurement increment of 1µm. The fatigue crack measurement technique developed during this project significantly improved the accuracy of the FCGR tests. This was highlighted by the improvement of the Paris data obtained during the preliminary and final testing phases of this project. It can also be concluded that the system was successfully integrated into the ESH testing machine.

- A heat treatment protocol, based on parameters extracted from literature, was successfully used that incorporated a solution treatment at 1200 °C for 2 hours, water quenching and ageing at 650 °C for 16 hours. The heat treatment effectively removed the segregation of the niobium-rich Laves phase, which was seen in the as-built structures. The hardness results show a consistent increase of approximately 100HV after heat treatment, which is attributed to the precipitation strengthening of the IN718. This heat treatment did not result in a peak hardened condition but showed that strengthening can be achieved through a post-build heat treatment.

- The microstructure of the material was investigated using light microscopy and scanning electron microscopy (SEM) with energy dispersive X-ray spectroscopy (EDS). It can be concluded that the material in the as-built condition contains a high concentration of niobium-rich Laves phase as confirmed by EDS. A fine grain structure with grains elongated in the build direction (Z-axis) was noticed. The heat treatment protocol was seen to have eliminated the niobium-rich Laves phase and a more homogeneous microstructure was observed. The heat treatment protocol homogenises the microstructure of the material regardless of the build orientation. A high level of spherical porosity was identified in the micrographs in both the as-built and heat-treated conditions that would have formed during the building process where gas was trapped during rapid solidification.

- The fatigue properties of the material were characterised through the development of the Paris equation for each build orientation. Variations in the Paris equations of the as-built material were seen throughout each orientation and the within lot variability per orientation was high. This indicated that the crack growth stability in the material fluctuated in the as-built condition for each orientation. The instability of crack growth in the as-built condition was seen in the fatigue crack path images obtained during testing, where the path of the crack deviated several times. The fatigue performance of the heat-treated material significantly increased. The variability in the results was more stable over the range of heat-treated test specimens in all build orientations. The Paris equations obtained for each heat-treated test specimen was more uniform, for all build directions. The heat treatment also increases the material's resistance to fatigue crack initiation and propagation and resulted in a more stable

crack path being followed. This increase in fatigue performance can be attributed to precipitation hardening and strengthening as a result of the heat treatment process.

The XZ build orientation was seen to possess the best fatigue properties in the as-built and heat-treated conditions due to the low variation in number of cycles to test end. For the as-built condition, the average fatigue life was 19 667 cycles at a load range of 7.2 kN. The Paris equation constants, C and m, were seen to be $(17.8 \pm 7) \times 10^{-16}$ and 5.38 ± 0.2 respectively. For the heat-treated condition, the average fatigue life was 48 100 cycles at a load range of 7.2 kN. The Paris equation constants, C and m, were seen to be $(11.7 \pm 6) \times 10^{-19}$ and 7.22 ± 0.3 respectively.

- The fracture toughness of the material was characterised through a comparative J-integral fracture toughness test as the material displayed an elastic-plastic behaviour. J_{max} values for each build orientation in the as-built condition were compared. It was seen that there was a significant variation in the average J_{max} values for each build orientation. The fracture toughness properties of the heat-treated material were also seen to improve when compared to the as-built equivalent orientations. It can be concluded that the J_{max} for each build orientation increases by a similar factor after the heat treatment. This indicates that a similar level of hardening is achieved by all build orientations as the increase in J_{max} is consistent.

  The XZ build orientation was shown to possess the best fracture toughness properties in both the as-built and heat-treated conditions in terms of the J_{max} values obtained. The as-built and heat-treated conditions exhibited a J_{max} of 323 ± 22 kJ/m^2 and 391 ± 28 kJ/m^2 respectively.

- The build parameters were also seen to affect the fatigue and fracture properties of the material. Specimens built with the same build orientation, but with different build parameters such as scanning width and hatch spacing were seen to behave differently. This directly affected the fatigue performance of some specimens namely XY7, XY13 and XY14 that were manufactured with different build parameters than the rest of the XY orientated specimens. The Paris equations for these specimens were seen to be outliers within the XY lot. The effect was similar for the fracture toughness results as specimens manufactured with the same build parameters were seen to correlate closely.

- This study used a combination of fatigue crack growth rate and fracture toughness tests to quantify two mechanical properties of a material using one test specimen. It can be concluded that this is a suitable method for determining comparative fatigue and fracture data, but not suitable if a full range of data is required. The full Paris curve encompassing primary, secondary and tertiary crack propagation cannot be determined in a combination test as the specimen cannot be tested to fracture.

8. Recommendations

Upon completion of the project, the following recommendations are provided for future work.

- It is recommended that height adjustability of the supporting rig for the crack measurement technique developed in this project should be developed to improve the ease of use by the user.
- It is recommended that material manufactured using the LENS process be built at a higher chamber temperature, a higher platform temperature or both of the aforementioned. The higher temperature will prevent rapid solidification and therefore reduce or eliminate the level of thermal residual stress in the material. This will reduce permanent deformation and warping of the material during building. In conjunction with this recommendation, the residual stress in the as-built material should also be measured with and without using an increased build temperature to quantify the differences between the two. Residual stress can also be measured in the as-built and heat-treated condition to determine the level of stress relief after heat treating.
- Hot isostatic pressing (HIP) pressing is recommended as a post-build treatment as it has the potential to increase the density and hardness of the AM produced material and to decrease the porosity within the material that can benefit the fatigue and fracture properties of the material [31].
- It is recommended that a double ageing heat treatment protocol for IN718 be used to increase the level of γ'' precipitation. The heat treatment protocol recommended is a solution treatment (980 °C for 1 hour, air cooling), followed by double ageing (720 °C for 8 hours, furnace cooling and 620 °C for 8 hours, air cooling). It is recommended that larger CT specimens be used for both FCGR and FT tests in order to pass the validity checks for the relevant ASTM test standards.
- Separate FCGR and FT test specimens are recommended to obtain a full range of fatigue data (primary, secondary and tertiary crack growth), and a thicker specimen is required for the determination of K_{1C}. Separate test specimens also prevents the formation of a work hardened region at the crack tip which could affect the FT results.
- Larger tensile test specimens are recommended to increase the gripping area of the test specimens during testing. This will increase the accuracy of the results and reduce slippage of the grips on the test specimen. An alternative would be for tensile specimens to be built according to a Hounsfield type cylindrical geometry, which will minimise the slippage during tensile testing.
- It is recommended that the fracture toughness (J_{1C}) of the material be determined using the J-integral resistance curve (R-curve) method as the material exhibits an elastic-plastic nature.
- Since IN718 is required to operate at very high temperatures, it is recommended that high temperature FCGR and FT tests are performed.
- In conjunction with the above recommendation, it is further recommended that the effect of build orientation on the creep properties of the material be investigated by means of a creep test on AM produced IN718 in the as-built and heat-treated condition.

9. References

[1] F. Oppong, (supervisors S. van der Spuy, and T. von Backström), “An overview of micro gas turbine engine performance investigation,” M. Eng thesis, University of Stellenbosch, 2017.

[2] M. J. Donachie and S. J. Donachie, *Superalloys: A Technical Guide. ASM International, 2008.*, Second Edi. ASM International, 2002.

[3] A. K. Roy and A. Venkatesh, “Evaluation of yield strength anomaly of Alloy 718 at 700-800 °C,” *J. Alloys Compd.*, vol. 496, no. 1–2, pp. 393–398, Apr. 2010, doi: 10.1016/j.jallcom.2010.02.023.

[4] N. Rao Muktinutalapati, “Materials for Gas Turbines-An Overview,” *Adv. Gas Turbine Technol.*, pp. 293–314, 2011, doi: 10.5772/664.

[5] P. M. Mignanelli *et al.*, “Gamma-gamma prime-gamma double prime dual-superlattice superalloys,” *Scr. Mater.*, vol. 136, pp. 136–140, Jul. 2017, doi: 10.1016/j.scriptamat.2017.04.029.

[6] H. Okamoto, “Nb-Ni (Niobium–Nickel),” *J. Phase Equilibria Diffus.*, vol. 29, no. 2, pp. 210–210, Apr. 2008, doi: 10.1007/s11669-008-9277-0.

[7] M. Weeks, “Design and Environmental Factors Contributing to the Failure of Thermal Barrier Coating Systems,” Doctor of Philosophy dissertation, University of California, Irvine 2011.

[8] N. Boutarek, D. Saïdi, M. A. Acheheb, M. Iggui, and S. Bouterfaïa, “Competition between three damaging mechanisms in the fractured surface of an Inconel 713 superalloy,” *Mater. Charact.*, vol. 59, no. 7, pp. 951–956, 2008, doi: 10.1016/j.matchar.2007.08.004.

[9] T. J. Carter, “Common failures in gas turbine blades,” *Eng. Fail. Anal.*, vol. 12, no. 2, pp. 237–247, 2005, doi: 10.1016/j.engfailanal.2004.07.004.

[10] R. S. Bunker, “Axial turbine blade tips: Function, Design, and Durability,” *J. Propuls. Power*, vol. 22, no. 2, 2006.

[11] OPTOMEC, “Superalloy Metallurgy Using the LENS Process,” Information brochure, Alburquerque, 2015.

[12] B. Almangour, D. Grzesiak, and J. M. Yang, “ Effect of scanning methods in the selective laser melting of 316L/TiC nanocomposites.” Solid Freeform Fabrication 2016: Proceedings of the 27th Annual International - An additive manufacturing conference, Reviewed Paper, pp. 566-573, 2016.

[13] L. Bian, S. M. Thompson, and N. Shamsaei, “Mechanical Properties and Microstructural Features of Direct Laser-Deposited Ti-6Al-4V,” *Jom*, vol. 67, no. 3, pp. 629–638, Mar. 2015, doi: 10.1007/s11837-015-1308-9.

[14] A. Kulkarni, “Additive Manufacturing of Nickel Based Superalloys,” Michigan Technological Univeristy, Houghton, 2018.

[15] ASTM E 399 - 90. Standard Test Method for Plane-Strain Fracture Toughness of Metallic Materials,” vol. 03, no. Reapproved 1997, 2003.

[16] M. Simonelli, Y. Y. Tse, and C. Tuck, “Effect of the build orientation on the mechanical properties and fracture modes of SLM Ti-6Al-4V,” *Mater. Sci. Eng. A*, vol. 616, pp. 1–11, 2014, doi: 10.1016/j.msea.2014.07.086.

[17] V. Cain, L. Thijs, J. Van Humbeeck, B. Van Hooreweder, and R. Knutsen, “Crack propagation

and fracture toughness of Ti6Al4V alloy produced by selective laser melting," *Addit. Manuf.*, vol. 5, pp. 68–76, 2015, doi: 10.1016/j.addma.2014.12.006.

[18] P. Mercelis and J. P. Kruth, "Residual stresses in selective laser sintering and selective laser melting," *Rapid Prototyp. J.*, vol. 12, no. 5, pp. 254–265, 2006, doi: 10.1108/13552540610707013.

[19] K. N. Amato *et al.*, "Microstructures and mechanical behavior of Inconel 718 fabricated by selective laser melting," *Acta Mater.*, vol. 60, no. 5, pp. 2229–2239, 2012, doi: 10.1016/j.actamat.2011.12.032.

[20] S. Raghavan *et al.*, "Materials and Manufacturing Processes Effect of different heat treatments on the microstructure and mechanical properties in selective laser melted INCONEL 718 alloy," *Materials and manufacturing processes*, vol. 32, no. 14, pp. 1588-1595 2017, doi: 10.1080/10426914.2016.1257805.

[21] D. Deng, "Additively Manufactured Inconel 718 ： Microstructures and Mechanical Properties," Licentitate thesis, Linköping University, 2018.

[22] H. Xiao, S. Li, X. Han, J. Mazumder, and L. Song, "Laves phase control of Inconel 718 alloy using quasi-continuous-wave laser additive manufacturing," *Mater. Des.*, vol. 122, pp. 330–339, May 2017, doi: 10.1016/j.matdes.2017.03.004.

[23] W. Huang, Z. Wang, J. Yang, H. Yang, and X. Zeng, "Effects of process paramaters and heat treatement on the microstructure and mechanical properties of selective laser melted Inconel 718." Solid Freeform Fabrication 2018: Proceedings of the 29th Annual International Solid Freeform Fabrication Symposium – An Additive Manufacturing Conference. pp. 1268-1276

[24] M. Yakout, M. A. Elbestawi, and S. C. Veldhuis, "Density and mechanical properties in selective laser melting of Invar 36 and stainless steel 316L," *J. Mater. Process. Technol.*, vol. 266, pp. 397–420, Apr. 2019, doi: 10.1016/j.jmatprotec.2018.11.006.

[25] B. Song *et al.*, "Differences in microstructure and properties between selective laser melting and traditional manufacturing for fabrication of metal parts: A review," *Front. Mech. Eng*, vol. 10, no. 2, pp. 111–125, 2015, doi: 10.1007/s11465-015-0341-2.

[26] C. Beckermann, "Macrosegregation," in *Encyclopedia of Materials: Science and Technology*, K. H. J. Buschow, R. W. Cahn, M. C. Flemings, B. Ilschner, E. J. Kramer, S. Mahajan, and P. Veyssière, Eds. Oxford: Elsevier, 2001, pp. 4733–4738.

[27] W.-C. Huang *et al.*, "Microstructure-controllable Laser Additive Manufacturing Process for Metal Products," *Phys. Procedia*, vol. 56, pp. 58–63, Jan. 2014, doi: 10.1016/J.PHPRO.2014.08.096.

[28] B. Van Hooreweder, D. Moens, R. Boonen, J.-P. Kruth, and P. Sas, "Analysis of Fracture Toughness and Crack Propagation of Ti6Al4V Produced by Selective Laser Melting," *Adv. Eng. Mater.*, vol. 14, no. 1–2, pp. 92–97, Feb. 2012, doi: 10.1002/adem.201100233.

[29] M. Thöne, S. Leuders, A. Riemer, T. Tröster, and H. A. Richard, "Influence of heat-treatment on Selective Laser Melting products – e.g. Ti6Al4V," *Solid Free. Fabr. Symp. SFF, Austin Texas. Aug.*, 2012.

[30] J. S. Zuback and T. Debroy, "The Hardness of Additively Manufactured Alloys," *Materials (Basel).*, vol. 11, p. 2070, 2018, doi: 10.3390/ma11112070.

[31] S.-H. Chang, "Effects of Gamma Prime Precipitation on the Structure and Properties of 713LC

Superalloy via HIP Treatment," *Mater. Trans.*, vol. 53, no. 2, pp. 446–452, 2012, doi: 10.2320/matertrans.M2011287.

[32] Z. Wang, K. Guan, M. Gao, X. Li, X. Chen, and X. Zeng, "The microstructure and mechanical properties of deposited-IN718 by selective laser melting," *J. Alloys Compd.*, vol. 513, pp. 518–523, Feb. 2012, doi: 10.1016/j.jallcom.2011.10.107.

[33] N. M. Dhansay, "Fracture mechanics based fatigue and fracture toughness evaluation of SLM Ti-6Al-4V," Master of Science thesis, University of Cape Town, 2015.

[34] H. Zhang, H. Zhang, X. Zhao, Y. Wang, and N. Li, "Study of Thickness Effect on Fracture Toughness of High Grade Pipeline Steel," MATEC Web of Conferences 67, 03016, SMAE, 2016 doi: 10.1051/03016.

[35] I. A. Essienubong, O. Ikechukwu, P. O. Ebunilo, and E. Ikpe, "Material Selection for High Pressure (HP) Turbine Blade of Conventional Turbojet Engines," *Am. J. Mech. Ind. Eng.*, vol. 1, no. 1, pp. 1–9, Jun. 2016, doi: 10.11648/J.AJMIE.20160101.11.

[36] M. Srinivasan and S. Seetharamu, "Fracture Toughness of Metal Castings," in *Science and Technology of Casting Processes*, InTech, 2012, pp. 285–312.

[37] Cambridge University Engineering Department, *Materials data book*. Cambridge, 2003.

[38] C. Yeni and M. Kocak, "Fracture toughness analysis of laser-beam-welded superalloys Inconel 718 and 625," *Fatigue Fract. Eng. Mater. Struct.*, vol. 29, no. 7, pp. 546–557, Jul. 2006, doi: 10.1111/j.1460-2695.2006.01025.x.

[39] E1820-18ae1, "Standard Test Method for Measurement of Fracture Toughness," *ASTM Stand.*, p. E 1820 – 01, 2019, doi: 10.1520/E1820-18AE01.

[40] P. Ganesh *et al.*, "Fatigue and fracture toughness characteristics of laser rapid manufactured Inconel 625 structures," *Mater. Sci. Eng. A*, vol. 527, no. 29–30, pp. 7490–7497, 2010, doi: 10.1016/j.msea.2010.08.034.

[41] A. B. Spierings, T. L. Starr, and K. Wegener, "Fatigue performance of additive manufactured metallic parts," *Rapid Prototyp. J.*, vol. 19, no. 2, pp. 88–94, Mar. 2013, doi: 10.1108/13552541311302932.

[42] V. Kratochvilova, F. Vlasic, P. Mazal, and D. Palousek, "Fatigue Behaviour Evaluation of Additively and Conventionally Produced Materials by Acoustic Emission Method," *Procedia Struct. Integr.*, vol. 5, pp. 393–400, Jan. 2017, doi: 10.1016/J.PROSTR.2017.07.187.

[43] ASTM E647−13, "Standard Test Method for Measurement of Fatigue Crack Growth Rates," *Am. Soc. Test. Mater.*, vol. i, pp. 1–50, 2014, doi: 10.1520/E0647-13A.2.

[44] K. Rege and H. Lemu, "A review of fatigue crack propagation modelling techniques using FEM and XFEM," *IOP Conf. Ser. Mater. Sci. Eng.*, vol. 276, p. 12027, 2017, doi: 10.1088/1757-899X/276/1/012027.

[45] BS 7910(1999) : 1999, "Guide on methods for assessing the acceptability of flaws in metallic structures," *Br. Stand. Inst.*, 1999.

[46] M. S. Dahar, S. M. Seifi, B. P. Bewlay, and J. J. Lewandowski, "Effects of test orientation on fracture and fatigue crack growth behavior of third generation as-cast Ti–48Al–2Nb–2Cr," *Intermetallics*, vol. 57, pp. 73–82, Feb. 2015, doi: 10.1016/j.intermet.2014.10.005.

[47] ASTM E8/E8M, "Standard Test Method for Tension Testing of Metallic Materials," *Am. Soc. Test. Mater.*, pp. 1–28, 2013.

[48] BS 7448: Part 1 (1991), "Fracture mechanics toughness tests, Part 1. Method for determination of K_{1C}, critical CTOD and critical J values of metallic materials, *Br. Stand. Inst.,* 1991.

[49] ASTM B311-17, “Standard Test Method for Density of Powder Metallurgy (PM) Materials Containing Less Than Two Percent Porosity,” *ASTM Int.*, pp. 1–5, 2017, doi: 10.1520/B0311-17.2.

[50] L. E. Murr *et al.*, “Fabrication of Metal and Alloy Components by Additive Manufacturing: Examples of 3D Materials Science 43 Fabrication of Metal and Alloy Components by Additive Manufacturing: Examples of 3D Materials Science,” *Journal of Materials Research and Technology,* vol. 1, pp. 43-54. 2012. doi 10.1016/S2238-7854(12)70009-1.

[51] K. Kumar *et al.*, “Use of miniature tensile specimen for measurement of mechanical properties,” *Procedia Eng.*, vol. 86, pp. 899–909, 2014, doi: 10.1016/j.proeng.2014.11.112.

[52] Y. Zhao, Q. Guo, Z. Ma, and L. Yu, “Comparative study on the microstructure evolution of selective laser melted and wrought IN718 superalloy during subsequent heat treatment process and its effect on mechanical properties,” *Mater. Sci. Eng. A*, vol. 791, no. June, p. 139735, 2020, doi: 10.1016/j.msea.2020.139735.

[53] E. Hosseini and V. A. Popovich, “A review of mechanical properties of additively manufactured Inconel 718,” *Addit. Manuf.*, vol. 30, no. August, p. 100877, 2019, doi: 10.1016/j.addma.2019.100877.

10. Bibliography

The bibliography below is comprised of various internet links and other sources that were used to obtain images and provide useful information on the various topics in this thesis. These sources were not reviewed and therefore, are not included in Section 9.

[a] "products | Cape Aerospace Technologies." [Online]. Available: http://www.capeaerospace.tech/products/. [Accessed: 25-Jan-2019].

[b] "The Future of Energy: New HL-Class Gas Turbine - Energy & Efficiency - Pictures of the Future - Innovation - Home - Siemens Global Website," 2018. [Online]. Available: https://www.siemens.com/innovation/en/home/pictures-of-the-future/energy-and-efficiency/the-future-of-energy-high-level-efficiency-gas-turbine.html. [Accessed: 15-Feb-2019].

[c] "Blisk-IBR - Leistritz Turbine Technology." [Online]. Available: https://turbines.leistritz.com/en/aviation/products/blisk-ibr.html. [Accessed: 15-Feb-2019].

[d] "Superalloys, High Performance Alloys, Corrosion-Resistant Superalloys - MEGA MEX." [Online]. Available: http://megamex.com/superalloys.htm. [Accessed: 25-Jan-2019].

[e] "Conceptual Physics: FACE CENTERED CUBIC STRUCTURE." [Online]. Available: http://www.conceptualphysicstoday.com/2015/09/face-centered-cubic-structure.html. [Accessed: 03-Sep-2019].

[f] "Nickel Alloy Inconel 718 - Properties and Applications by United Performance Metals." [Online]. Available: https://www.azom.com/article.aspx?ArticleID=4459. [Accessed: 11-Oct-2019].

[g] "High Level Processes: Directed Energy Deposition." [Online]. Available: https://www.bintoa.com/directed-energy-deposition/. [Accessed: 20-Sep-2019].

[h] "Direct Metal Deposition Fabrication Process for Metal 3D Prints." [Online]. Available: https://www.sculpteo.com/en/glossary/dmd-definition/. [Accessed: 20-Sep-2019].

[i] "What Is Directed Energy Deposition?: Modern Machine Shop." [Online]. Available: https://www.mmsonline.com/blog/post/what-is-directed-energy-deposition. [Accessed: 20-Sep-2019].

[j] "Empa - Coating Competence Center - Selective Laser Melting (SLM)." [Online]. Available: https://www.empa.ch/web/coating-competence-center/selective-laser-melting. [Accessed: 25-Jan-2019].

[k] Ben Redwood, "How does part orientation affect a 3D Print? | 3D Hubs." [Online]. Available: https://www.3dhubs.com/knowledge-base/how-does-part-orientation-affect-3d-print. [Accessed: 25-Jan-2019].

[l] "Residual Stress - Industrial Metallurgists." [Online]. Available: https://www.imetllc.com/training-article/residual-stress/. [Accessed: 03-Jun-2019].

[m] "Residual stress in additive manufacturing - Hill Engineering." [Online]. Available: http://hill-engineering.com/general-interest/residual-stress-additive-manufacturing/. [Accessed: 18-Nov-2019].

[n] L. Langnau, "What does part density mean in additive manufacturing? - Make Parts Fast." [Online]. Available: https://www.makepartsfast.com/part-density-mean-additive-manufacturing/. [Accessed: 25-Jan-2019].

[o] “Archimedes’ principle | Description & Facts | Britannica.com,” 2018. [Online]. Available: https://www.britannica.com/science/Archimedes-principle. [Accessed: 25-Jan-2019].

[p] “Nickel Alloys - SLM Solutions NA, Inc.” [Online]. Available: https://slm-solutions.us/product/nickel-superalloys/#material-composition. [Accessed: 06-Sep-2019].

[q] “Additive Manufacturing: 3D printed gas turbine blades - Industry & Automation - Pictures of the Future - Innovation - Home - Siemens Global Website,” 2017. [Online]. Available: https://www.siemens.com/innovation/en/home/pictures-of-the-future/industry-and-automation/additive-manufacturing-3d-printed-gas-turbine-blades.html. [Accessed: 15-Feb-2019].

[r] “Stress Intensity Factor.” [Online]. Available: https://www.fracturemechanics.org/sif.html. [Accessed: 07-Jun-2019].

[s] NDT Resource Center, “Fracture Toughness.” [Online]. Available: https://www.nde-ed.org/EducationResources/CommunityCollege/Materials/Mechanical/FractureToughness.htm. [Accessed: 03-Jun-2019].

[t] “Fracture Mechanics | MechaniCalc.” [Online]. Available: https://mechanicalc.com/reference/fracture-mechanics#fracture-toughness-vs-thickness. [Accessed: 06-Nov-2019].

[u] “Fracture Materials Database | MechaniCalc.” [Online]. Available: https://mechanicalc.com/calculators/fracture-materials/. [Accessed: 27-Dec-2019].

[v] “eFunda: Crack Tip Opening Displacement (CTOD).” [Online]. Available: https://www.efunda.com/formulae/solid_mechanics/fracture_mechanics/fm_epfm_CTOD.cfm. [Accessed: 13-Dec-2019].

[w] NDT Resource Center, “Fatigue Crack Initiation.” [Online]. Available: https://www.nde-ed.org/EducationResources/CommunityCollege/Materials/Structure/fatigue.htm. [Accessed: 07-Jun-2019].

[x] Channa Nageswaran, “Measuring the crack growth rate (da/dt) of a fatigue crack using phased array ultrasonics - TWI,” *TWI Member Publication*, 2013. [Online]. Available: https://www.twi-global.com/technical-knowledge/published-papers/measuring-the-crack-growth-rate-da-dt-of-a-fatigue-crack-using-phased-array-ultrasonics. [Accessed: 06-Feb-2019].

[y] “V-Slot Wheel Kit, Solid, Delrin.” [Online]. Available: http://www.3dprintingstore.co.za/aluminium-t-slot-extrusions/v-slot-wheels/v-slot-wheel-kit-solid-delrin/. [Accessed: 27-Sep-2019].

[z] “ASM Material Data Sheet.” [Online]. Available: http://asm.matweb.com/search/SpecificMaterial.asp?bassnum=MA6063T5. [Accessed: 27-Sep-2019].

[aa] “Wire Cut EDM (Electrical Discharge Machining).” [Online]. Available: https://www.thomasnet.com/articles/custom-manufacturing-fabricating/Wire-Cut-EDM. [Accessed: 11-Feb-2019].

[ab] “EDM Wire Cutting | Ian Brown Engineering T/A Supertech Engineering.” [Online]. Available: http://www.ianbrown.co.za/edm-wire-cutting/. [Accessed: 11-Feb-2019].

11. Appendices

11.1. Design iterations for microscope rig

The various design iterations that were developed throughout the design process are shown in this section.

11.1.1. Design 1

The initial design of the rig required a smooth combination of the various elements mentioned above such as the linear motion mechanism, the clamping mechanism and the microscope mounting mechanism. A Solidworks model of the design was generated and is shown in the figure below.

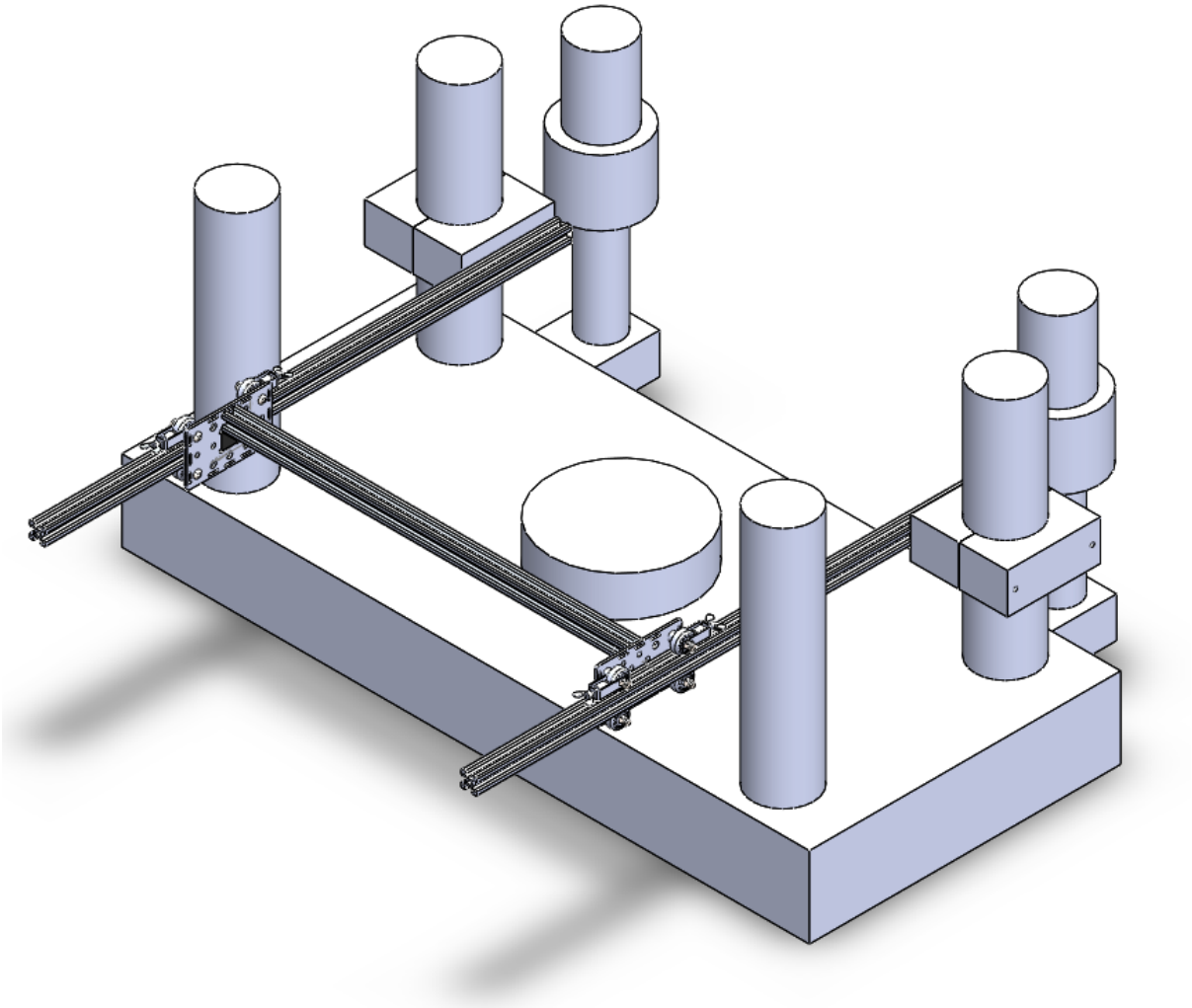

Figure 11.1: Isometric view of design 1

This design was developed during the preliminary stages of the rig development. As a result, a general understanding of where the individual components would fit was obtained and not much thought was devoted to developing the intricacies of each sub-system. The ESH base and supporting uprights are depicted in the model to gain an understanding of how the rig fits into the testing area and how it coincides with the existing structure. In the figure above, the clamping mechanism is attached to the rear upright supports of the ESH by means of a two-part block clamp. This clamp was not designed to be fully functional but used as a concept to develop further designs. The linear motion mechanism is

then attached to the clamp by means of a long bolt and a slide T-nut which will be positioned in the V-slot rail. This then allows for a clamping force to be induced and hence the rail will remain horizontal.

The rolling mechanism is then comprised of a gantry plate and 4 rollers on each rail. Which is depicted below.

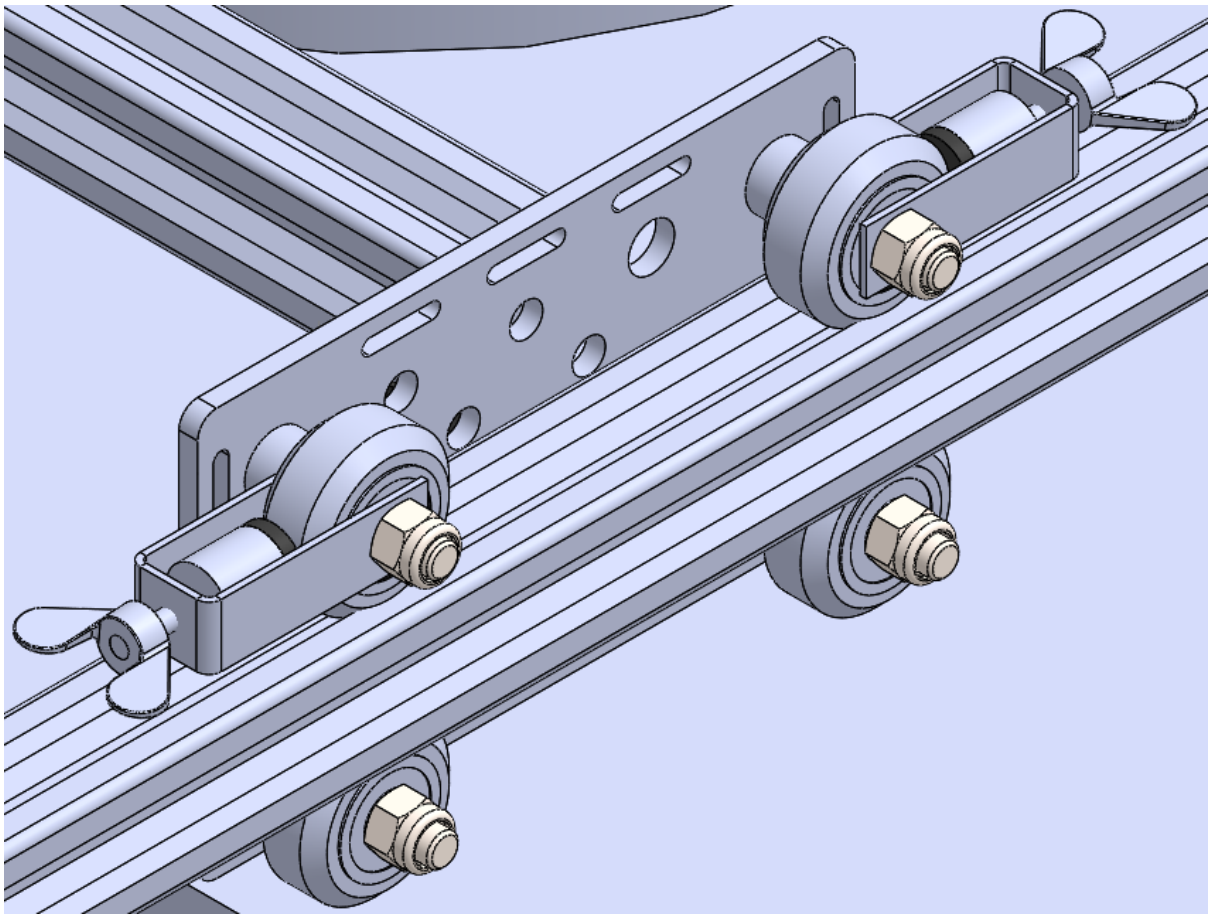

Figure 11.2: Isometric view of rolling mechanism

This design allows for smooth and stable linear translation of the microscope when movement is required. In order to lock the rig in place, a locking mechanism was required. This locking mechanism can be seen in the figure above on the top two rollers. It is a simple design comprising a wing nut, a threaded stud, a drilled disk and a polymer pad (shown in black). When locking is required, the wing nut will be turned until the polymer pad contacts the surface of the roller and tightened until motion is restricted completely.

The microscope mounting mechanism was preliminarily designed in order to provide a platform on which to place the microscope but was not designed fully in this initial draft. The figure below illustrates the connection of the mount to the rolling mechanism.

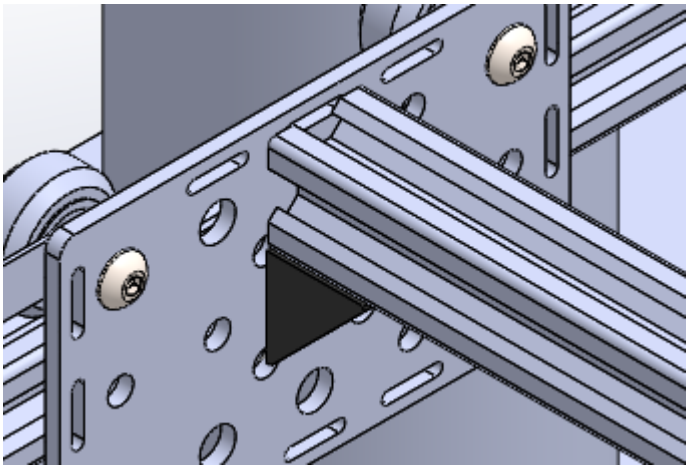

Figure 11.3: Isometric view of microscope mount attachment point

The microscope will be mounted on a cross member that connects each of the rolling assemblies via the two gantry plates. These will be connected to the plates with the use of the corner brackets and the slide T-nuts mentioned in Section 3.4.3.4.3.

The design shown in this section is the concept upon which the final design was based. The iterations following this design address the lack of detail in this design and respond to intricacies that required attention.

11.1.2. Design 2

The first iteration of the concept design extended the initial ideas of the concept and narrowed down on the working ability of the rig. The figure below illustrates this design.

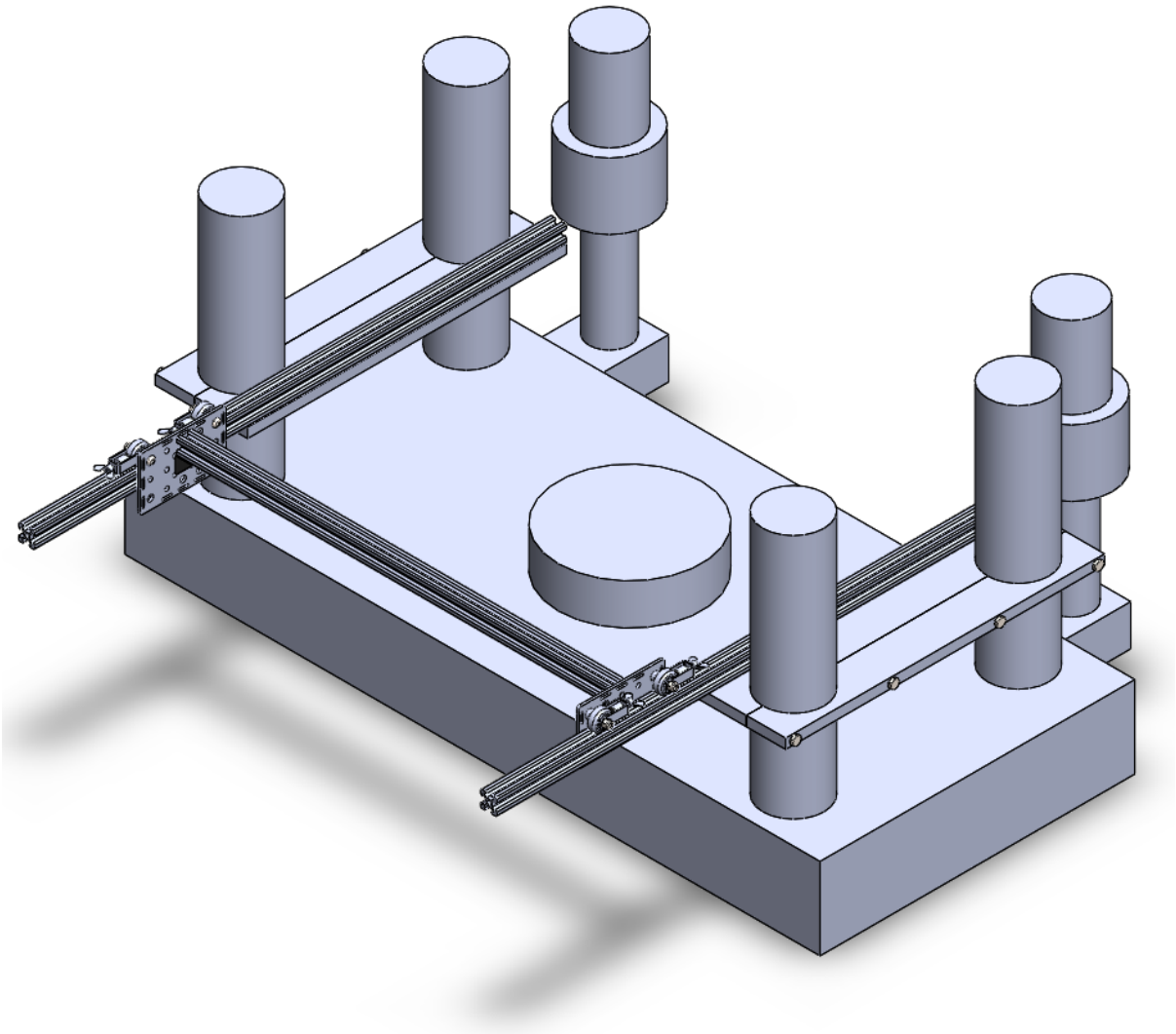

Figure 11.4: Isometric view of design 2

The figure above displays noticeable changes in the design, but the overall location of the sub-assemblies remains the same. Firstly, the clamping mechanism was changed from the initial two-part block clamp to a shelf clamp. This mechanism works by having two plates fastened together by a bolt to induce a clamping force on the upright supports of the ESH. These plates will then act as a shelf on which the V-slot rails will sit on. The V-slot rails will be fastened to the shelf by means of several slide T-nuts along the length of the shelf. This provides secure location and stability of the rails without having the cantilever effect which was seen in the concept design. The mass of the microscope was measured to be 2.2 kg. With the addition of other supporting components in the microscope mounting sub-assembly the total mass was conservatively assumed to be 5 kg. Calculations were performed to theoretically determine the bending stresses induced in each of the rails as well as the deflection at a distance away from the machine. These calculations were modified throughout the design process until the final design was obtained. Those calculations can be found in Appendix 10.2.

Since the rail sits on top of the shelf, the rolling mechanism needed to be modified. The previous design utilised 4 rollers on each gantry plate. This design made use of 2 rollers on the top section of the rail so that the microscope can roll as freely as possible without interfering with the shelf. This is shown in the figure below.

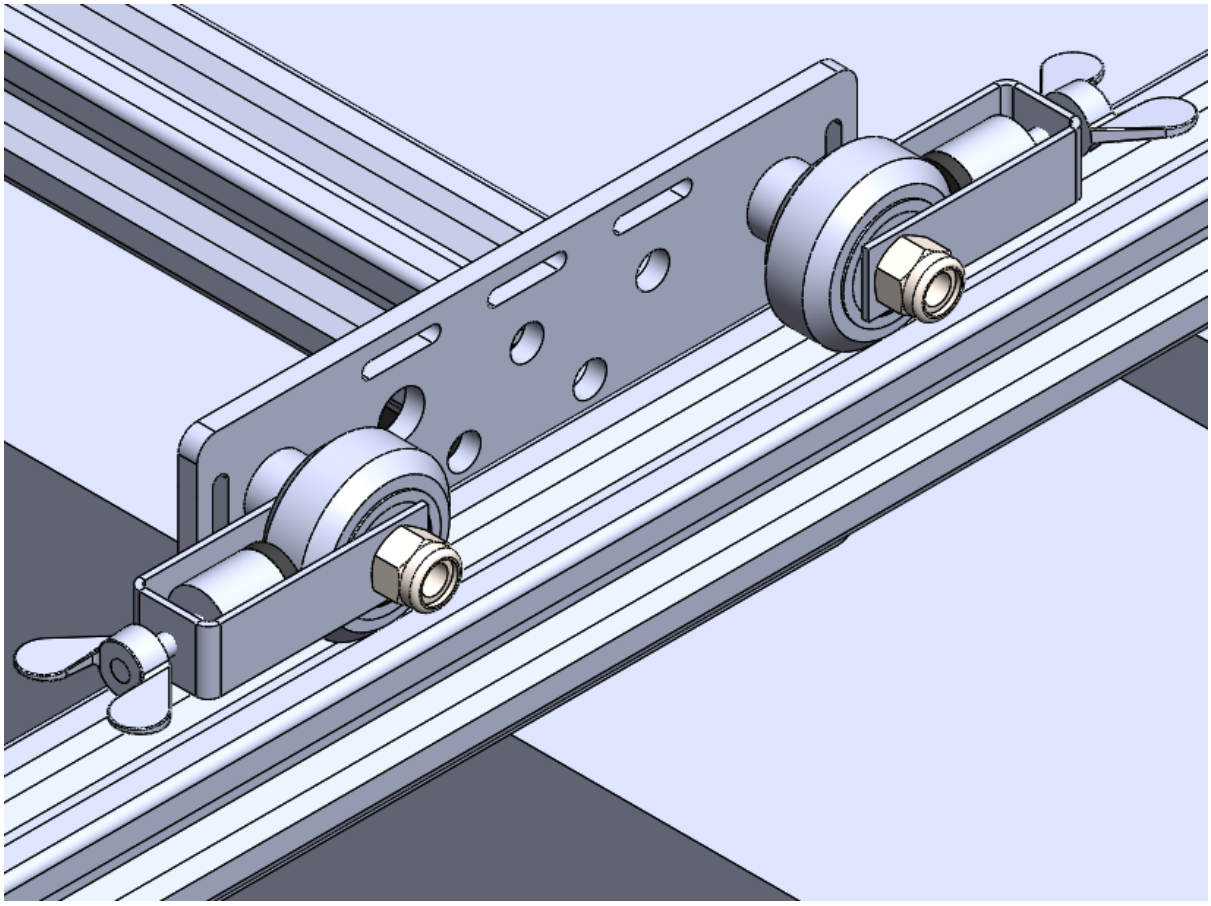

Figure 11.5: Rolling mechanism with top rollers only

At this stage of the design process, the microscope mounting mechanism was still not designed and hence no changes were made from the previous design. In this design, the major changes were seen on the clamping and rolling mechanism.

11.1.3. Design 3

The second iteration of the rig design picked up on certain flaws of the previous design and finalised the microscope mount aspect which was not developed in the previous two designs. The figure below illustrates the second iteration and includes the fatigue assembly with the compact tension specimen in red.

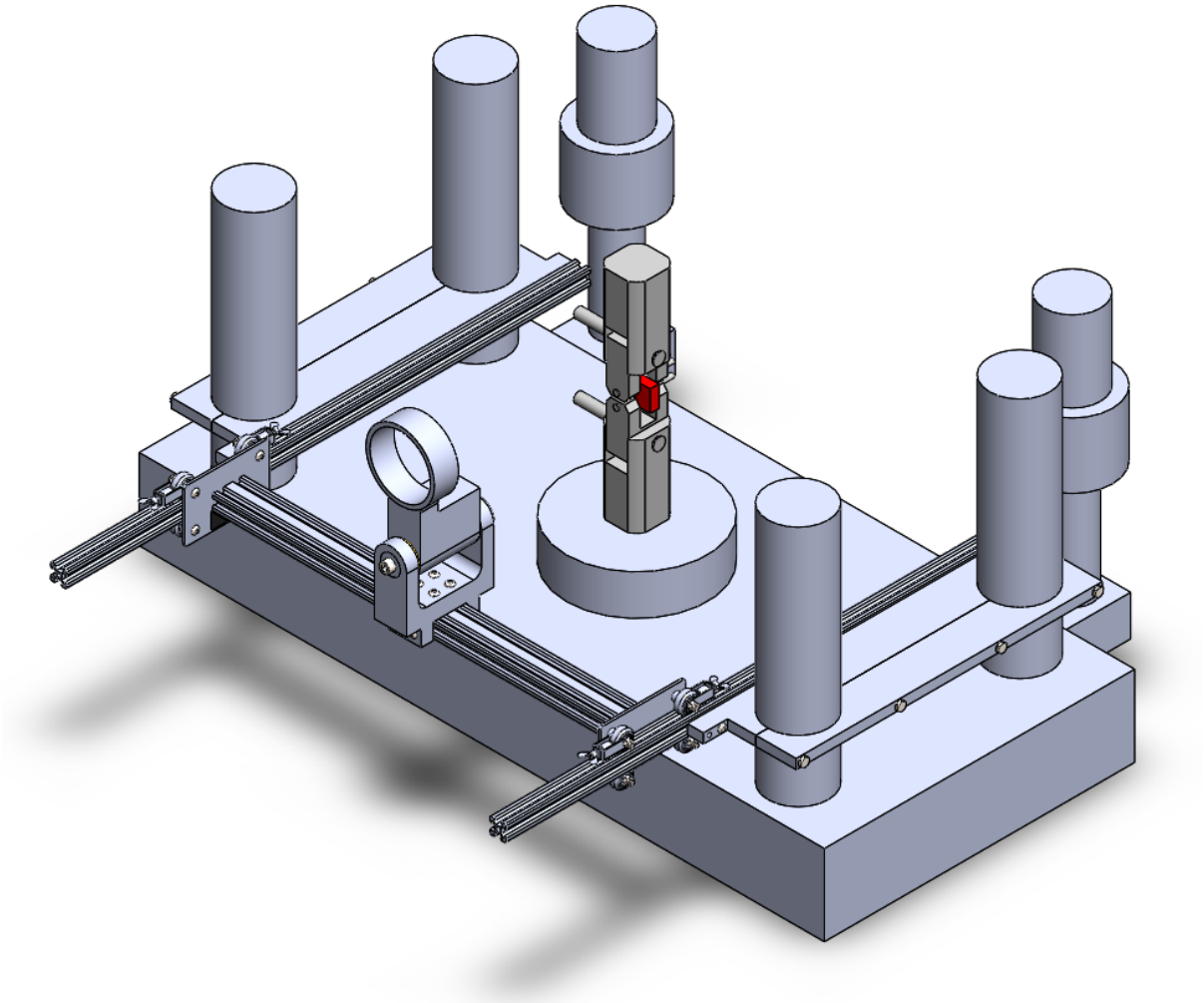

Figure 11.6: Isometric view of design 3

The figure above shows slight changes to that of design 2. In the previous iteration, the shelf clamp was introduced. This allowed for the rail to sit on top of the shelf and hence aid in supporting the rolling mechanism and furthermore, supporting the microscope during service. The number of rollers, however, was reduced to two on either gantry plate due to interference reasons. This was noticed to have potential complications during the practical application of the design as the centre of gravity of the microscope and its associated parts would unlikely be directly in the middle of the cross-member support. This centre of gravity offset could potentially result in the microscope support assembly to topple over if there is no support at the bottom of the rail as well. As a result, the rail was designed to be attached to the side of the inner shelf. The figure below illustrates this as well as the revised gantry plate with 4 rollers.

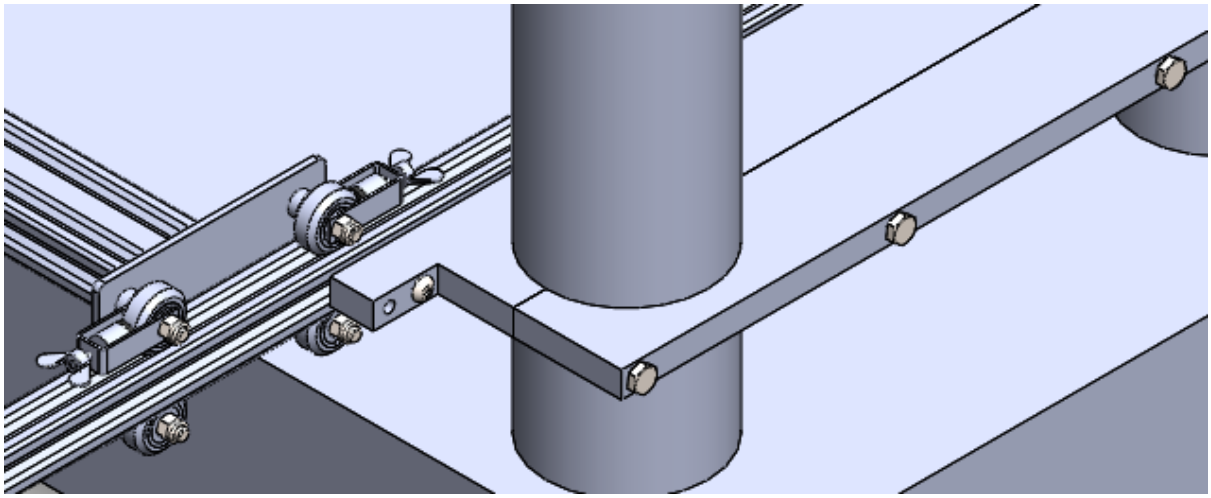

Figure 11.7: Attachment point of roller and shelf

In the figure above, the inner shelf can be seen, as well as the rolling mechanism sub-assembly. The rail is attached to the side of the shelf with the use of a slide T-nut and a bolt which will provide the necessary clamping force. There are provisions for multiple slide T-nuts to be used if a greater clamping force is required. The gantry plate is also shown with 4 rollers attached which will result in greater stability.

The microscope mounting mechanism was designed in this iteration and is shown more clearly in the figure below.

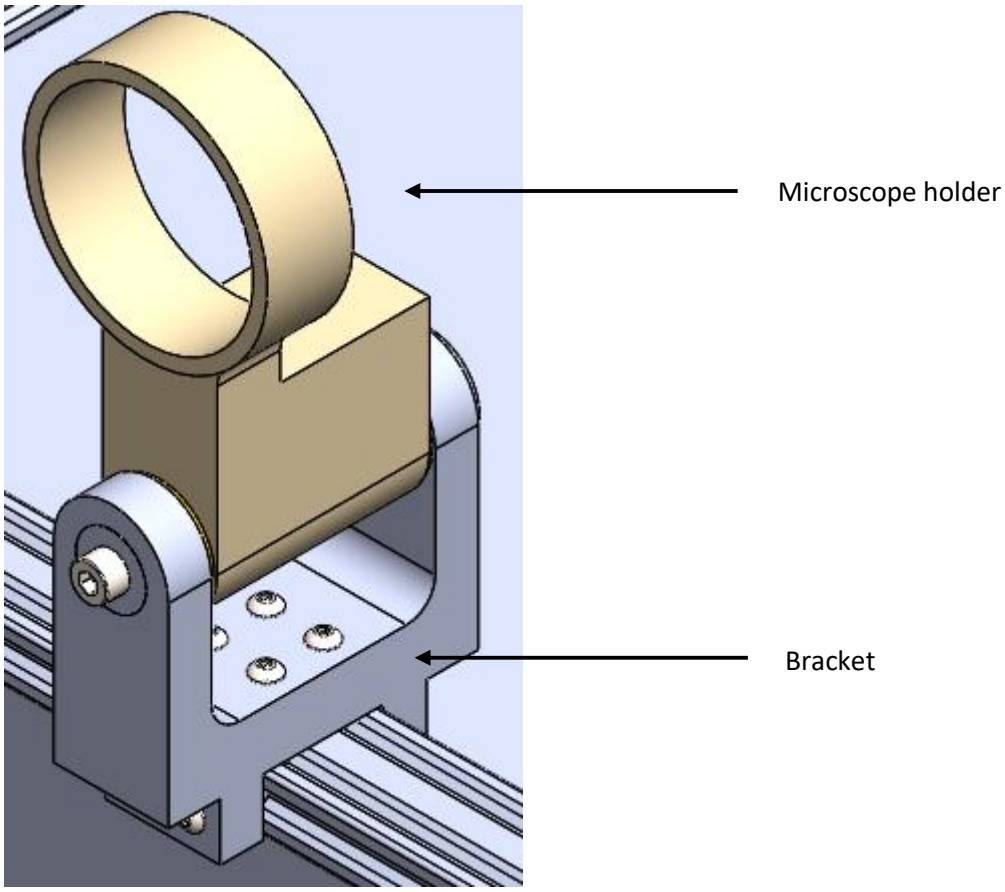

Figure 11.8: Microscope mount mechanism

The mounting rig for the microscope is mounted to the cross member that joins the two gantry plates. The original holder for the microscope is shown in brown in the figure above and is joined to the cross member using the bracket shown in the figure above. The bracket is fixed to the rail by means of several turn T-nuts and bolts in order to increase the stability of the microscope during operation. This bracket was designed based on the original stereomicroscope bracket but was modified in order to accommodate adaptation for this rig. The microscope will then fit through the circular portion of the holder as it was designed for and will allow for the lens to focus directly on the specimen during the fatigue test.

This design was iteration was eventually chosen to be manufactured as the first prototype to assess the functionality of the overall design. Upon assembly of this design iteration, it was seen that the shelves were not fitting around the upright supports as intended. This was due to the change in distance between the upright supports as the cross head of the machine moves up and down which was not taken into consideration. Therefore, alternate solutions were required. These solutions will be shown below.

11.1.4. Design 4

This iteration involved addressing the interference issue of the shelf plates with the upright supports of the ESH. The shelves were cut into four individual clamping systems on all four uprights rather than two clamps spanning the width of the machine. This is shown in the figure below.

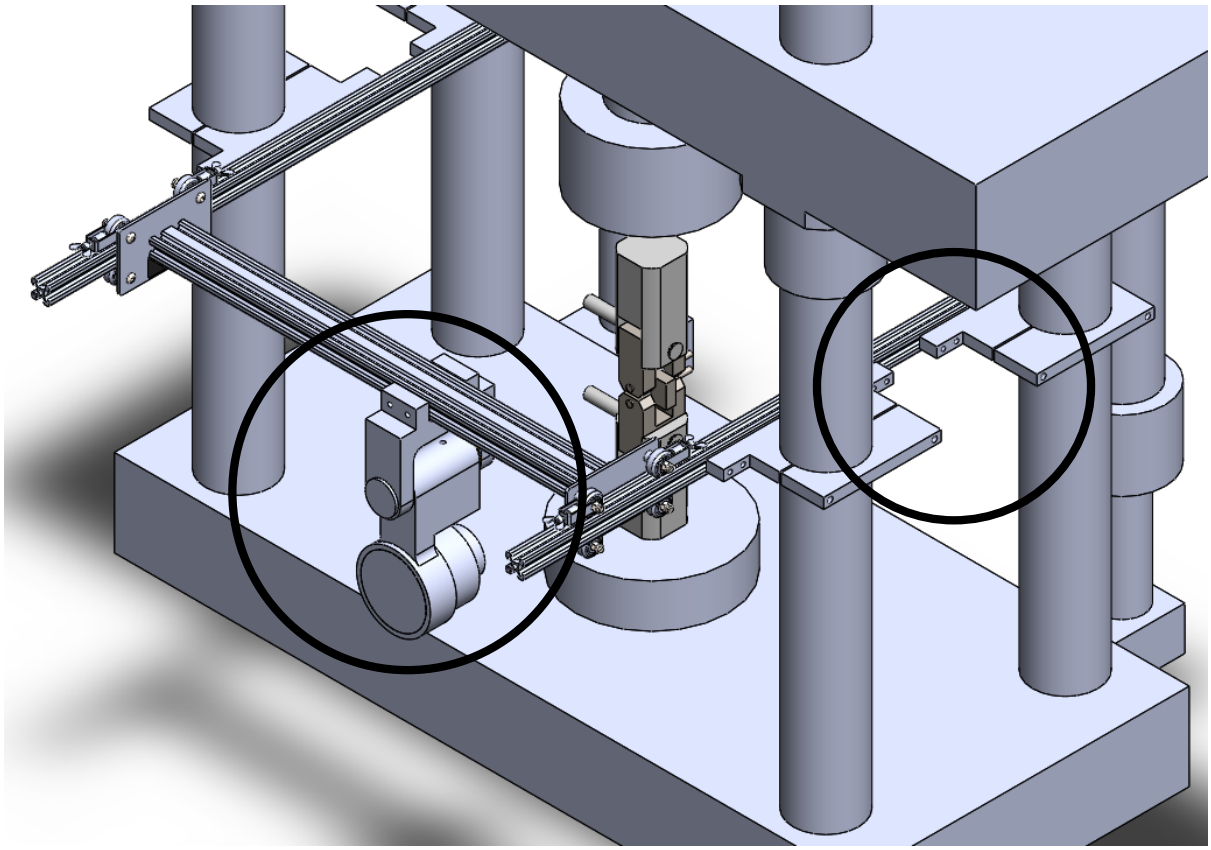

Figure 11.9: Isometric view of design 4

In this figure the middle portion of the shelves are removed which will eliminate the problem of interference as the cross head moves up and down. This solution also reduces the weight of the system since the middle piece is removed. The only issue with this method is that the number of parts will be increased so the assembly process will not be as easy. The microscope was also flipped to be upside-

down instead of on top of the cross member. This will reduce the toppling moment generated by the microscope and its supporting components by lowering the centre of gravity of the system. The changes in this iteration are circled in the figure above.

11.1.5. Design 5

An alternate perspective was looked at for the following design iterations. The microscope was to be mounted on the rear side of the specimen instead of the front. This was done to minimise the amount of clutter in the test area and to allow the rig to form more of an integral part of the machine. The figures below show the fourth iteration of the design.

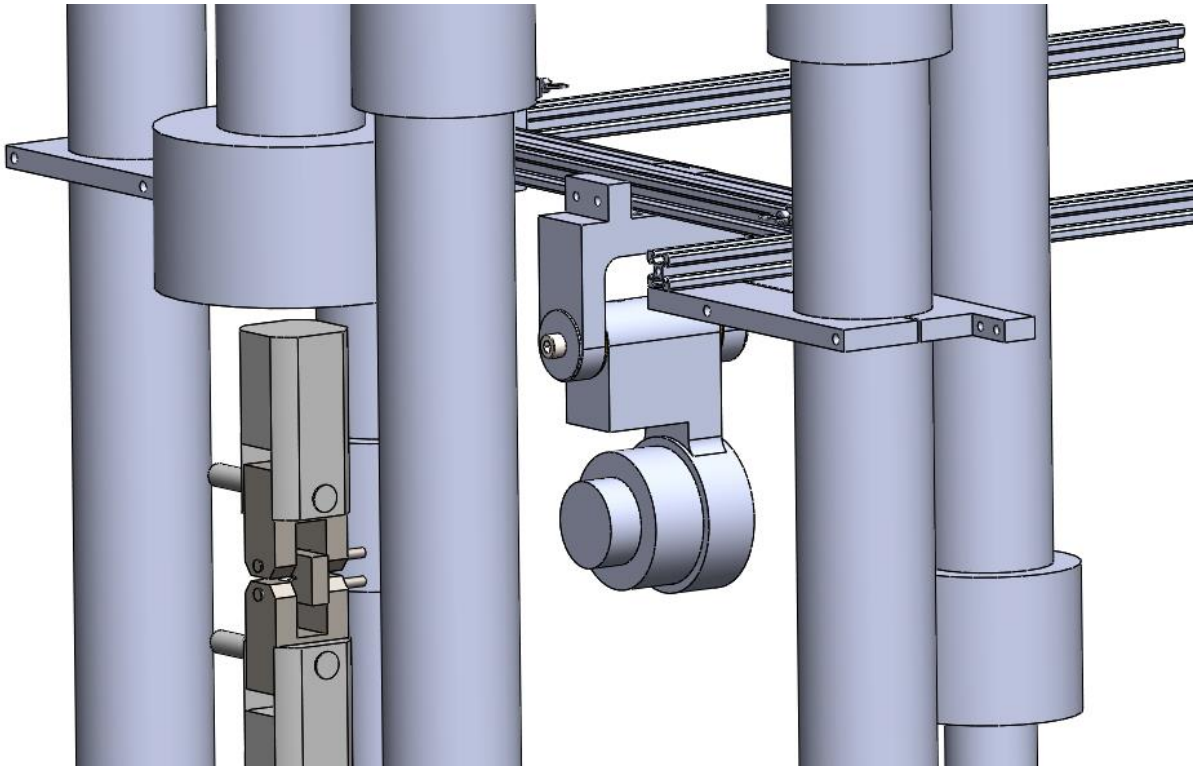

Figure 11.10: Isometric view of design 5

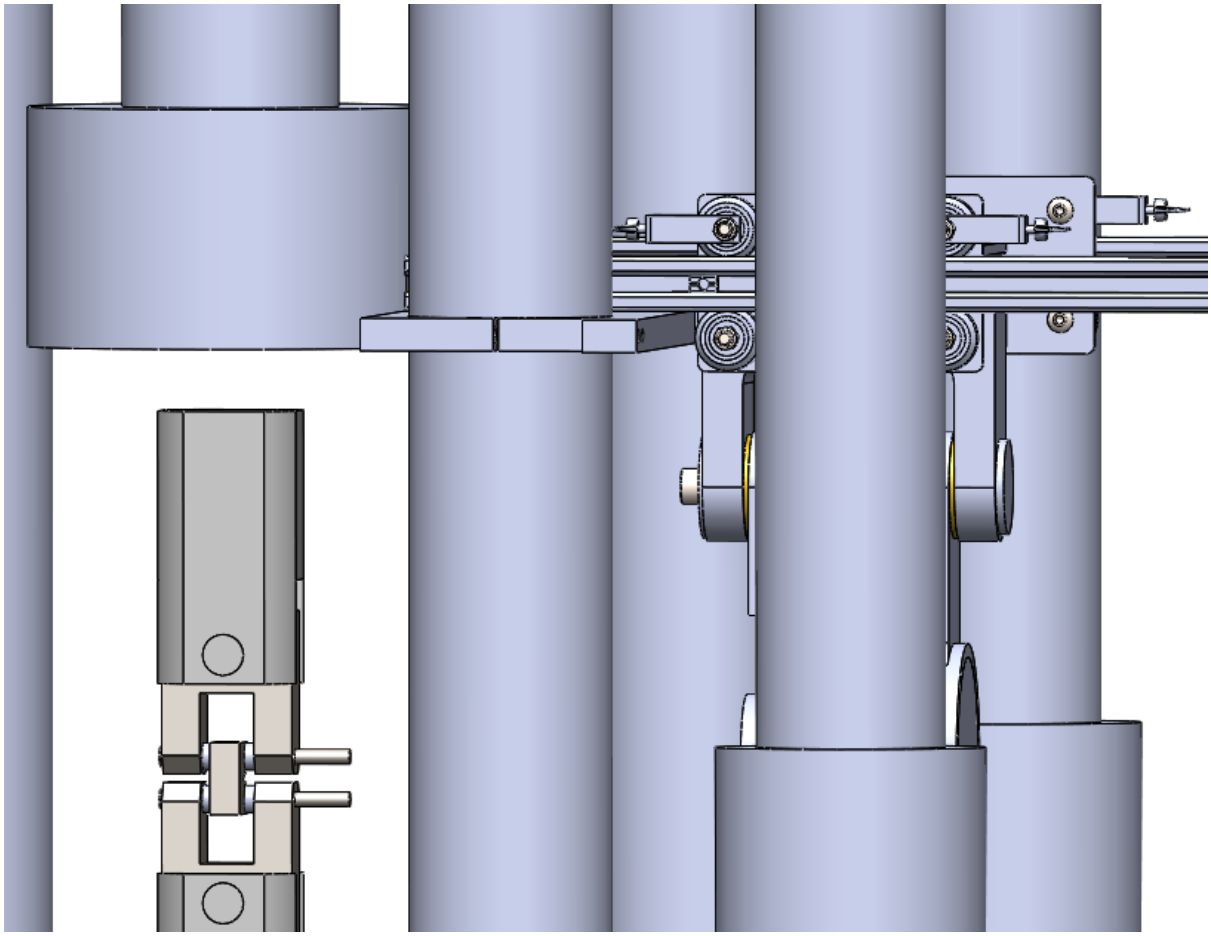

Figure 11.11: Rear mounted microscope

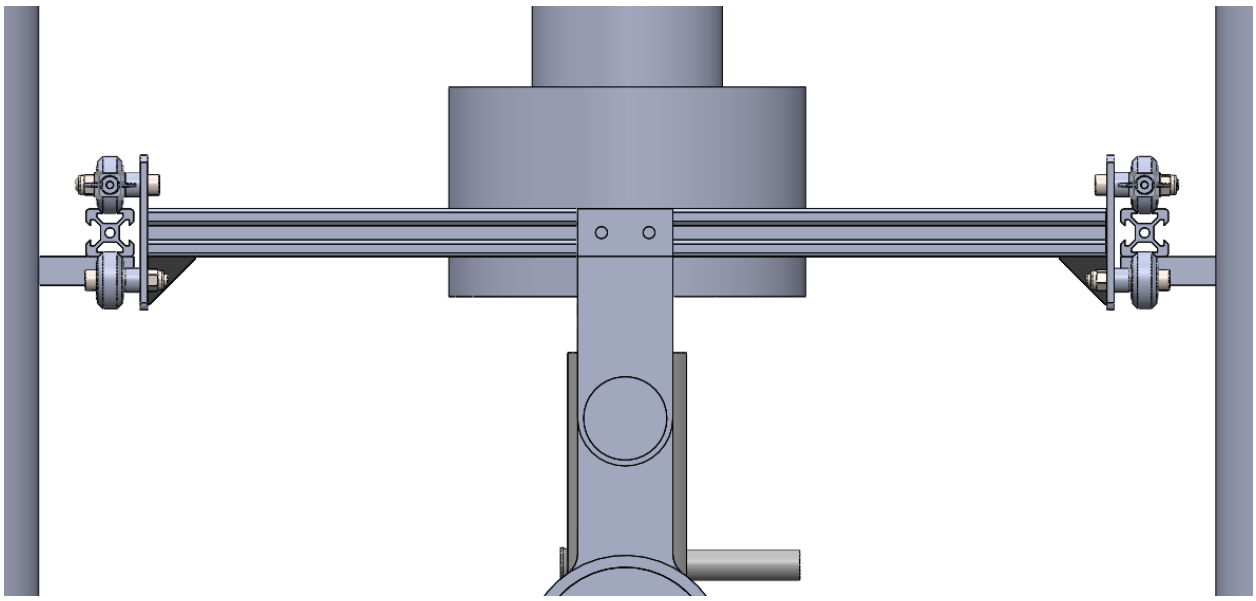

Figure 11.12: Rear view of design 5

In the figures above, it can be seen that the microscope is now mounted on the rear side of the machine. Furthermore, the shelf has been cut into a shorter piece and is only clamped on to one of the upright supports on each side of the machine which reduces the complexity of assembly. The shelf has also been rotated by 90° to allow for clearance of the runner and the furnace support. This

configuration allows for an open testing area in which samples can be inserted and removed easily without having any machinery in the way. The issue with this design is that the lower wheels on either gantry assembly interfere with the shelf as shown Figure 11.11. This will prevent the microscope from moving any closer than is shown in the figure above which way be problematic in terms of zoom and focus. This design provides a good foundation for further iterations which will be shown below.

11.1.6. Design 6

To address the issue generated by the previous design where the microscope movement was restricted, a revised design was created that solved this issue. The figure below details the design.

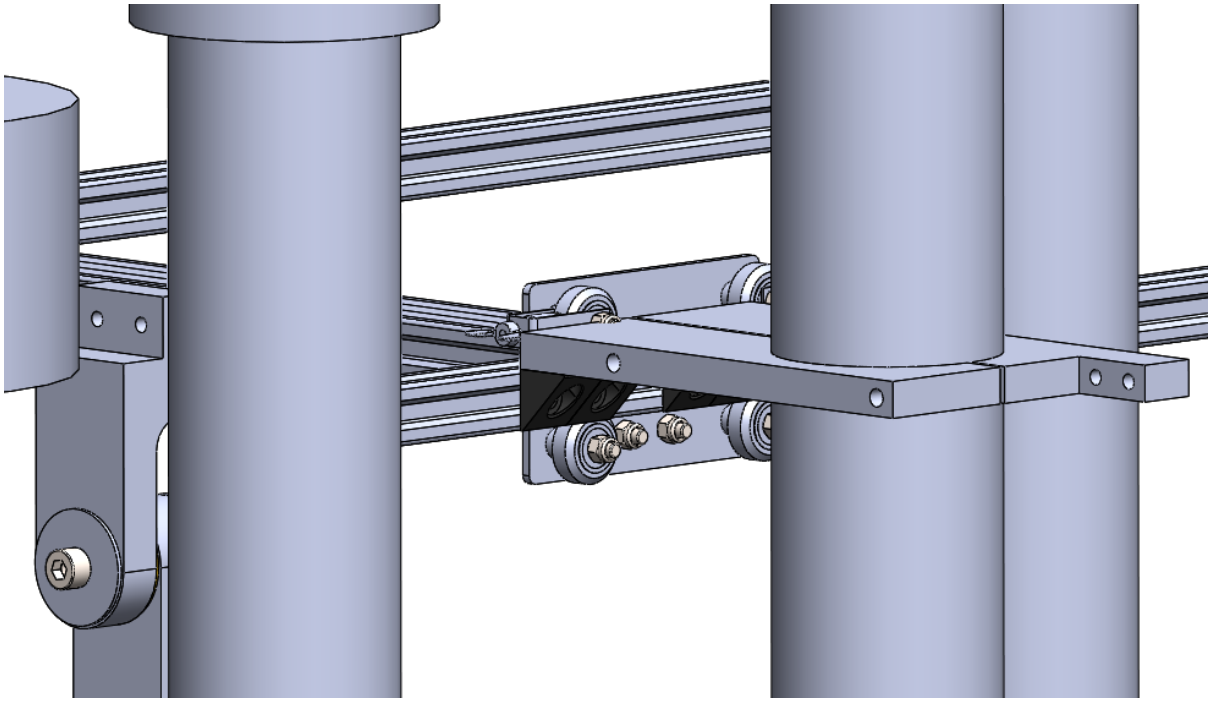

Figure 11.13: Mounting mechanism of design 6

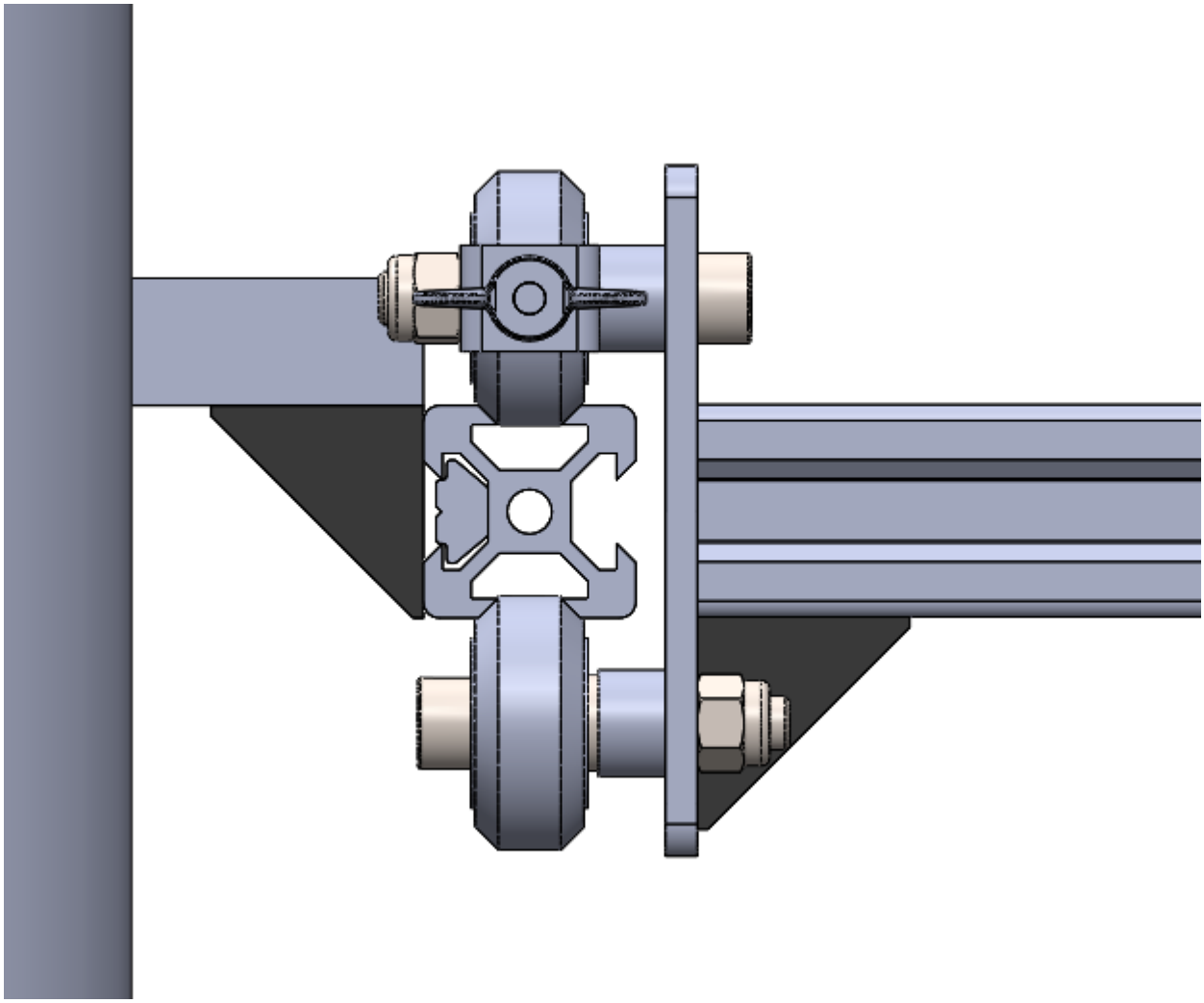

Figure 11.14: Front view of rail attachment point

In the figure above, it can be seen that the runner is now attached to the shelf using the corner brackets. This allows the runner to be further away from the shelf and in turn, allows the gantry system to roll as close to the test specimen as possible. The only issue with this design would be the stability of having so many corner brackets together since they are designed to have some play in them when fastening. Furthermore, the entire weight of the microscope system will be supported by these brackets and the slide T-nuts which might not be the most effective solution.

11.1.7. Design 7

This design iteration addressed the issue of stability in the corner brackets mentioned above. The figure below illustrates the design.

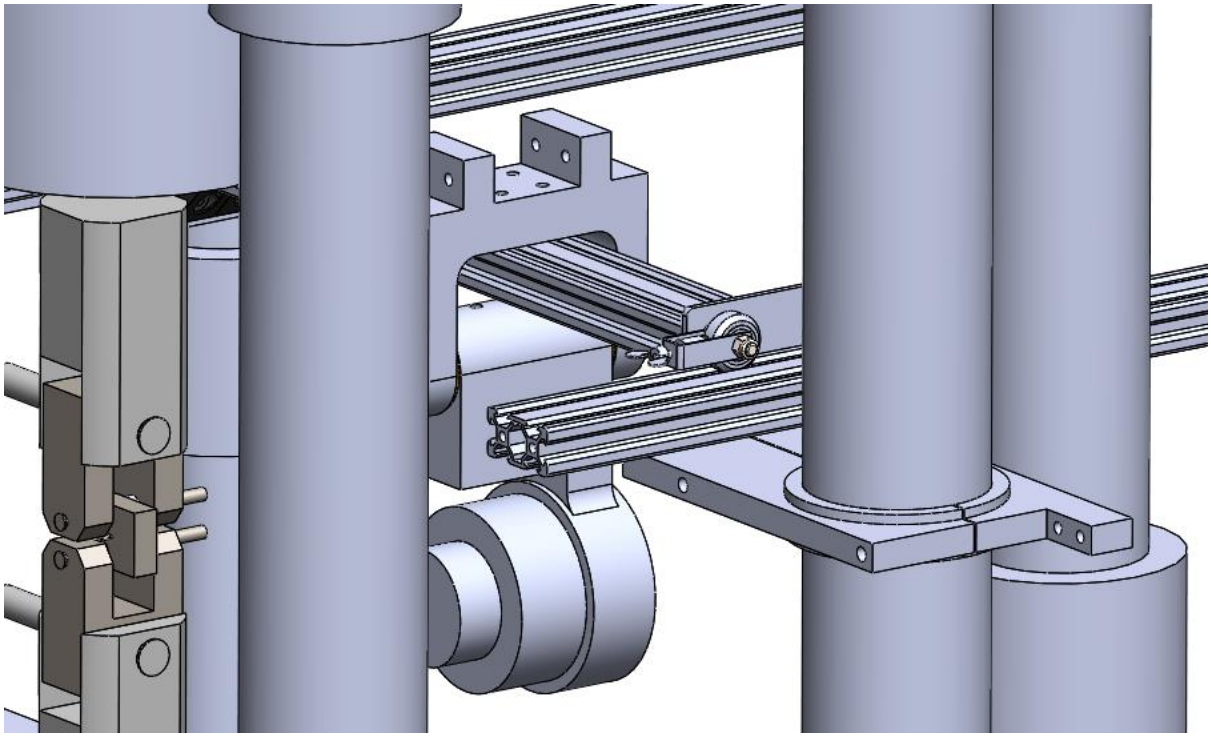

Figure 11.15: Isometric view of design 7

The figure above shows a revised runner system as well as a new configuration for mounting the microscope. A 20x40 V-slot rail will be used instead of a 20x20 rail which will allow the gantry to roll along the entire length of the runner without interfering with the shelf. This is also the most stable option as the runner is fully supported by the shelf under the weight of the microscope and cross runner assembly. The microscope is also mounted on the top side of the cross runner so that it can support its own weight instead of the T-nuts supporting the weight of the entire system. It also allows for the system to become more compact. The figure below shows the runner and gantry clearance from the shelf.

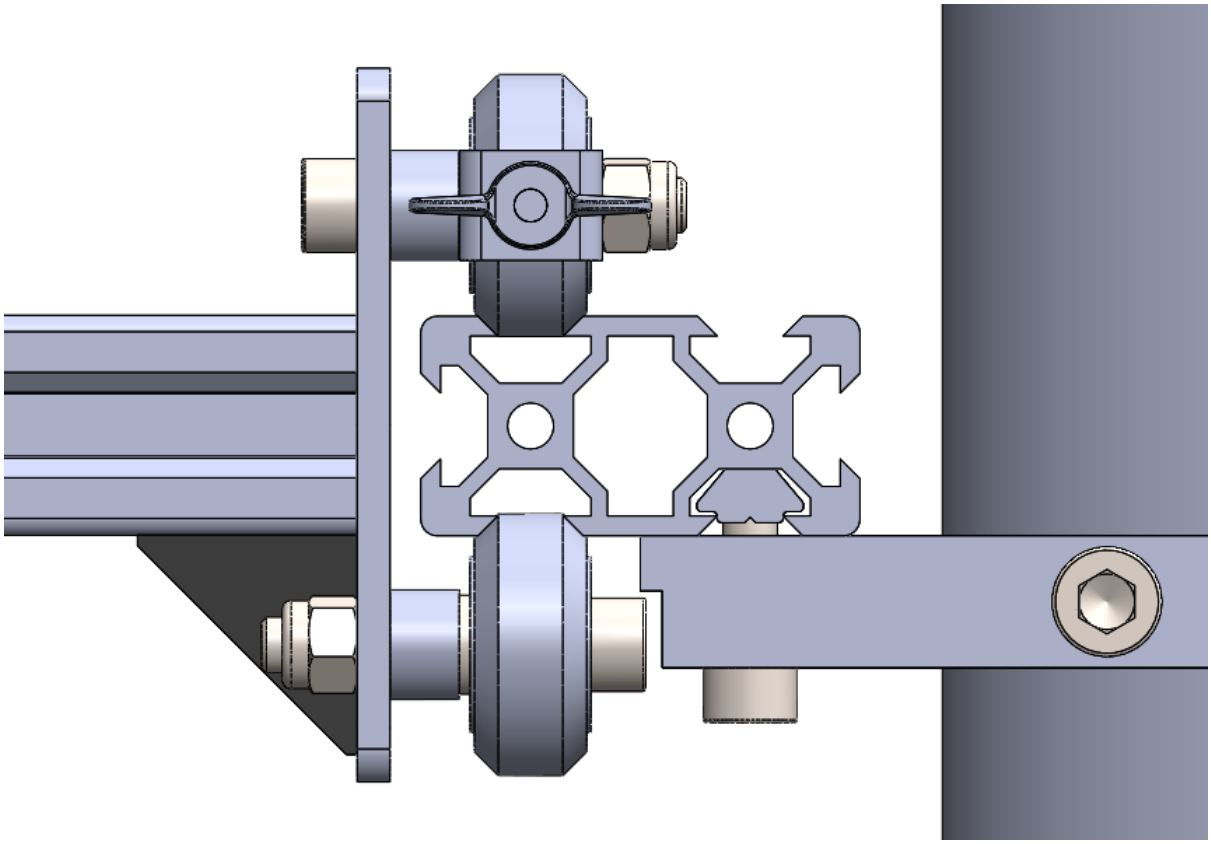

Figure 11.16: Revised mounting mechanism for design 7

It can be seen in the figure above that the runner overhangs off the shelf and the bottom roller is allowed to move past the shelf without any interference. The bolt head fastening the roller to the gantry does interfere with the shelf and therefore, a small recess has been cut out from the shelf to allow for enough clearance. This iteration was chosen to be built due to its superior stability and range of motion as compared to the other designs. The parts for this design were already manufactured for the second iteration therefore not much time and resources were required to make the necessary changes that this design required. Minor machining was required to size the shelves correctly and cut the recess for the bolt heads to travel past along with drilling holes for fastening the runners.

11.1.8. Design 8

Upon assembling the final rig and installing it on the ESH, it was seen that the rig was not as user friendly as intended. Since the magnification is so large, extremely fine adjustments are required in terms of position control of the microscope. The current design allowed for smooth movement to and from the testing area by means of the rollers however, the right to left motion of the microscope was significantly hindered since the microscope mount bracket was attached to the cross runner with the use of T-nuts. Therefore, incremental and smooth motion is not possible. An alternate design was developed which catered for this unforeseen problem that involved the use of rollers to allow smooth translational motion. The design is shown in the figure below.

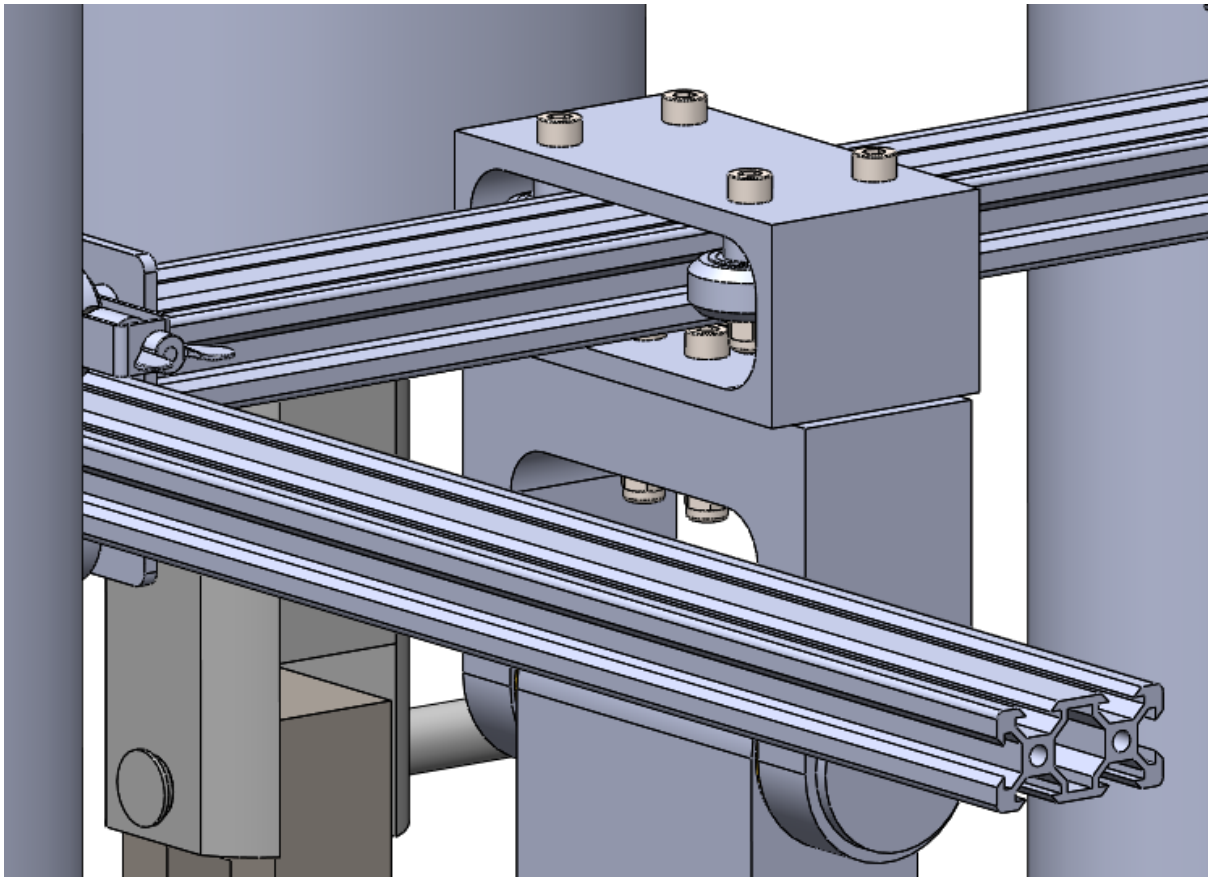

Figure 11.17: Cross member rolling mechanism

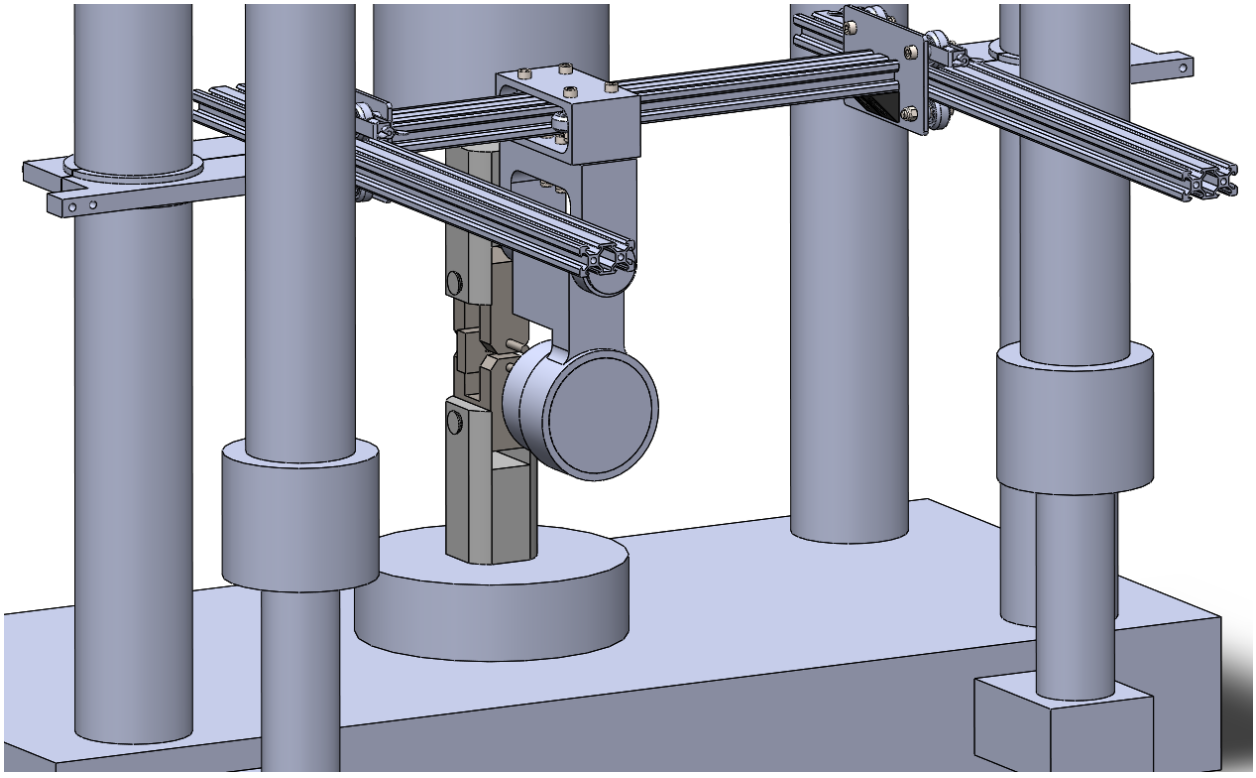

Figure 11.18: Rear isometric view of design 8

The new proposed design involves the use of rollers on the cross runner which is mounted to the microscope using the existing microscope bracket and a new mount housing the rollers. The rollers will be required to move on the sides of the runner which is different to the other rollers in the design which run on the top and bottom of the runner however, the V-slot rail geometry supports this type of loading. The bearings in the rollers are also able to support axial loads in conjunction with radial loads.

11.2. Stress calculations for microscope rig

This section outlines the calculations that were performed to assess the bending stresses and deflection in the V-slot rails and cross member as a result of the microscope load during service.

11.2.1. V-slot rail analysis

The mass of the microscope along with all supporting structures was weighed to be 4.81 kg. The load used during the calculations was rounded up to 5 kg to obtain more conservative bending stress and deflection result. A free body diagram for one of the rails can be seen below.

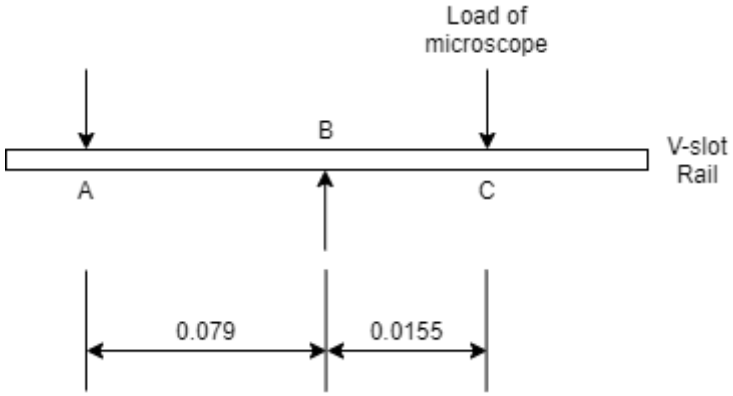

Figure 11.19: Free body diagram of rail

Points A and B represent the regions where the rail is bolted to the support plate with two M5 bolts and slide T-nuts. Point C is the exact location of the microscope load with all supporting structures such as the cross member and the gantry plates with rollers. This is the location during the FCGR test which is very close to the specimen. The load was converted to point load for simplicity of the calculation and also to simulate the worst case scenario from a bending stress point of view. Taking the reaction forces on each wheel would require the centre of gravity of the microscope to be found which would be a labour intensive process therefore, a point load was used. The reaction forces were firstly required at A and B therefore the sum of moments was taken at point A. This is shown below.

$$\sum M_A = 0$$

$$-F_B(0.079) + F_C(0.0945) = 0$$

$$F_B = \frac{F_C(0.0945)}{0.079}$$

Where $\boldsymbol{F_C = 24.525\ N}$ (total load divided by 2 for each of the V-slot rails)

$$\boldsymbol{F_B = 29.34\ N}$$

$$\sum F = 0$$

$$F_A + F_B + F_C = 0$$

$$F_A = -29.337 + 24.525$$

$$\boldsymbol{F_A = -4.815\ N}$$

The shear force and bending moment diagrams were developed from these reaction forces. This is shown below.

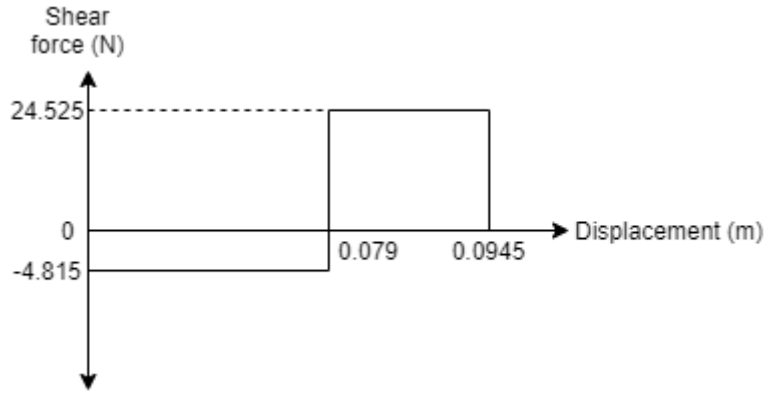

Figure 11.20: Shear force diagram for rail

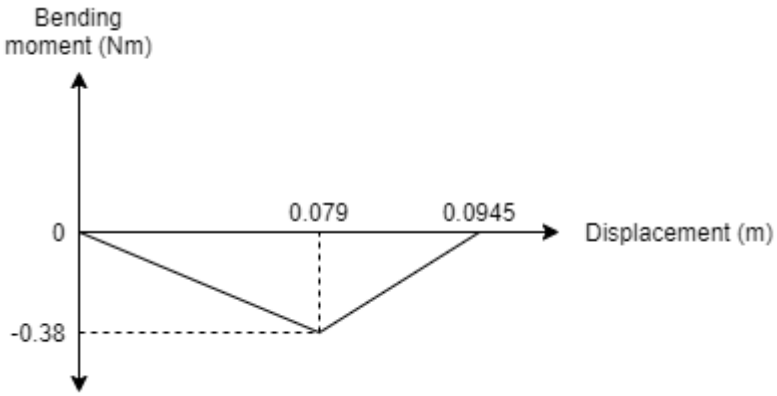

Figure 11.21: Bending moment diagram for rail

The maximum bending moment was seen to occur at point B with a magnitude of 0.38 Nm. The bending stress was then calculated and can be seen below. The neutral axis "y" was seen to be half the thickness of the rail (0.01 m) and the second moment of area "I' was obtained from the supplier to be 1.28 x 10^{-9} m^4.

$$\sigma_{bending} = \frac{My}{I}$$

$$\sigma_{bending} = \frac{0.38 \times 0.01}{1.28 \times 10^{-9}}$$

$$\boldsymbol{\sigma_{bending} = 2.969\ MPa}$$

This bending is far below the yield and shear strength of the material (6063-T5 Aluminium) which are 145 and 117 MPa respectively. This confirms that the rail will not yield under the operating conditions by a safety margin of almost 50. There were no direct stress components to this loading scenario hence, only bending stress was considered.

The deflection of the rail at the operating position of the rig was calculated using Macaulay's method. A diagram of the beam is shown below which precedes the deflection calculations.

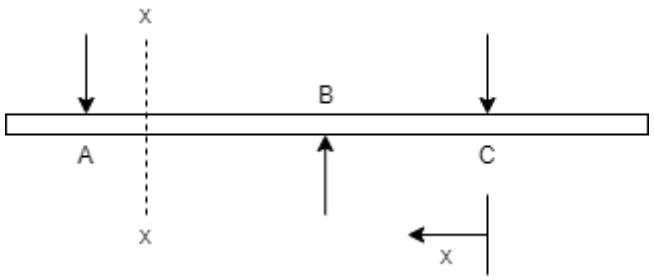

Figure 11.22: Macaulay's deflection analysis diagram for rail

$$EI\frac{d^2y}{dx^2} = -24.525x + 29.337(x - 0.0155)$$

$$EI\frac{dy}{dx} = -\frac{24.525x^2}{2} + \frac{29.337(x - 0.0155)^2}{2} + A$$

$$EIy = -\frac{24.525x^3}{6} + \frac{29.337(x - 0.0155)^3}{6} + Ax + B$$

Boundary conditions: $@\ x = 0.0155; y = 0$

$@\ x = 0.0945; y = 0$

$$(1) Sub\ x = 0.0155;\ EI(0) = -\frac{24.525(0.0155)^3}{6} + \frac{29.337(0.0155 - 0.0155)^3}{6} + A(0.0155) + B$$

$$(2) Sub\ x = 0.0945;\ EI(0) = -\frac{24.525(0.0945)^3}{6} + \frac{29.337(0.0945 - 0.0155)^3}{6} + A(0.0945) + B$$

Solve simultaneously; (1) – (2)

$$0 = 1.023 \times 10^{-3} - A(0.079)$$

$$A = 0.0129$$

Sub A = 0.0129 into (1);

$$B = -1.847 \times 10^{-4}$$

Therefore, at point C; $x = 0$

$$y = \frac{-\frac{24.525(0)^3}{6} + \frac{29.337(0 - 0.0155)^3}{6} + 0.0129(0) - 1.847 \times 10^{-4}}{EI}$$

$$Where\ E = 68.9\ GPa\ and\ I = 1.28 \times 10^{-9} m^4$$

$$y = \frac{0 + \frac{29.337(-0.0155)^3}{6} - 1.847 \times 10^{-4}}{(68.9 \times 10^9)(1.28 \times 10^{-9})}$$

$$y = -2.301 \times 10^{-6} m$$

$$y = -0.023\ mm$$

The total deflection per rail, y, was calculated to be 0.023 mm downwards which is an insignificant level of deflection and therefore, the rig would be stable enough during operation. A worst case scenario bending stress and deflection was determined at the maximum length of the rail which was

at 300 mm away from the supporting plates. The microscope would never need to be this far away from the testing area but the calculation was performed to assess the stresses and deflection induced at the worst case scenario in the unlikely event of the microscope being at this point. The calculation is exactly the same as the previous calculation and is therefore omitted from the report but a diagram of the scenario can be seen below along with the bending stress and deflection result.

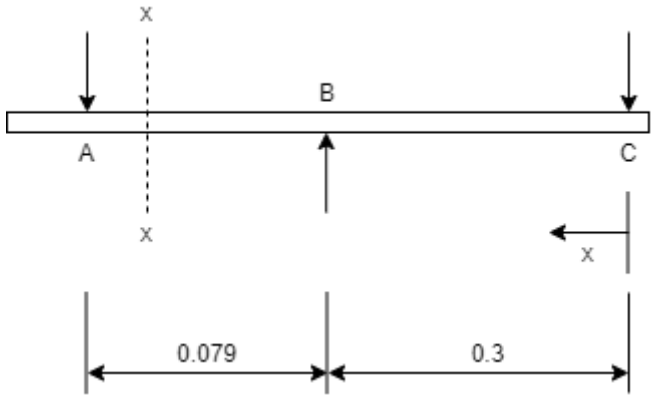

Figure 11.23: Worst case deflection scenario

$$\sigma_{bending} = 57.48\ MPa$$

$$y = 0.0559\ mm$$

11.2.2. Cross member

The bending stress and deflection of the cross member that the microscope is mounted to was determined. The cross member was a simply supported beam supporting the mass of the microscope and supporting structures. The mass on the cross beam was measured to be 4.15 kg. This mass was lower than the mass used for the calculations above as the above calculations included the mass of the gantry plates, rollers and the cross member itself. For calculation purposes however, a mass of 4.5 kg was used to be conservative. The free body diagram is shown below.

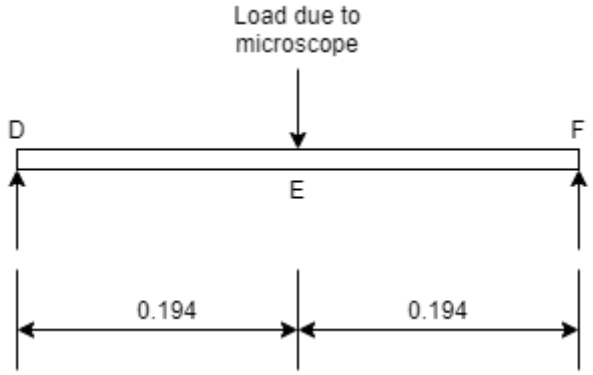

Figure 11.24: Free body diagram of cross member

The magnitude of the reaction forces at D and F were required and therefore, moments were taken at point D.

$$\sum M_D = 0$$

$$-F_E(0.194) + F_F(0.388) = 0$$

$$F_F = \frac{F_E(0.194)}{0.388}$$

Where $\boldsymbol{F_E = 44.145\ N}$ (represents 4.5 kg mass)

$$\boldsymbol{F_F = 22.0725\ N}$$

$$\sum F = 0$$

$$F_D - F_E + F_F = 0$$

$$F_D = 44.145 - 22.073$$

$$\boldsymbol{F_D = 22.0725\ N}$$

The shear force and bending moment diagrams were developed from these results and are shown below.

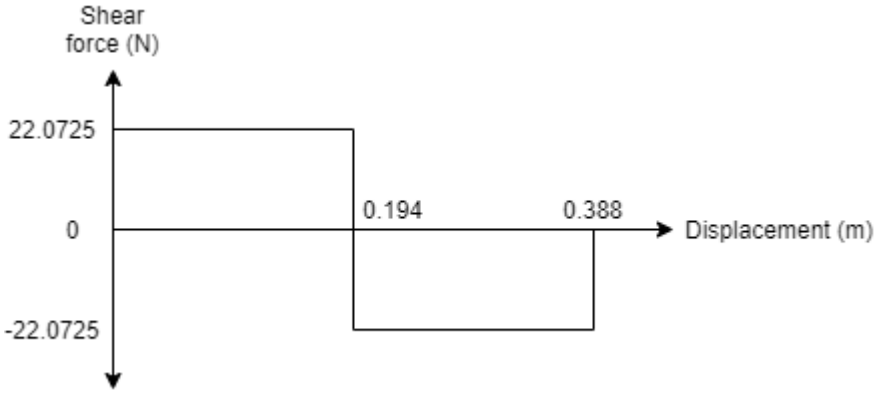

Figure 11.25: Shear force diagram for cross member

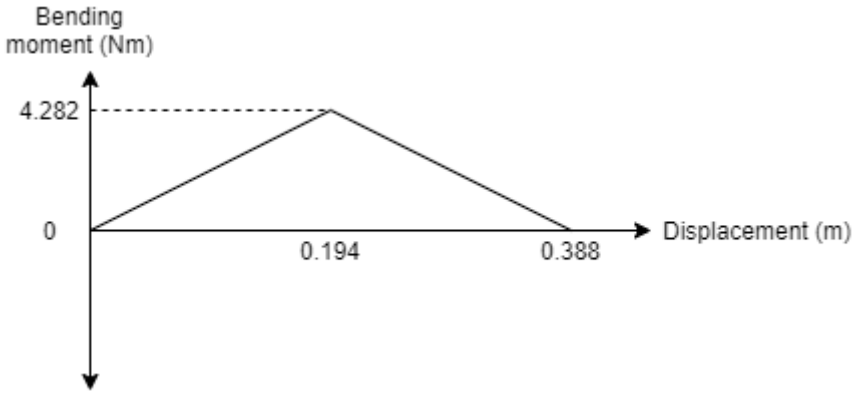

Figure 11.26: Bending moment diagram for cross member

The maximum bending moment was seen to occur at point E with a magnitude of 4.282 Nm. The bending stress was calculated and can be seen below. Since the same 20x40 V-slot rail was used for the cross member, the neutral axis "y" and second moment of area "I" were 0.01 m and 1.28 x 10^{-9} m^4 respectively.

$$\sigma_{bending} = \frac{My}{I}$$

$$\sigma_{bending} = \frac{4.282 \times 0.01}{1.28 \times 10^{-9}}$$

$$\boldsymbol{\sigma_{bending} = 33.45\ MPa}$$

The bending stress for the cross member is significantly higher than for the individual runners because the load is located much further from the supports. Nevertheless, the bending stress is still much lower than the yield stress of the T5 Aluminium.

The deflection of the cross member was also determined, and the calculations are shown below.

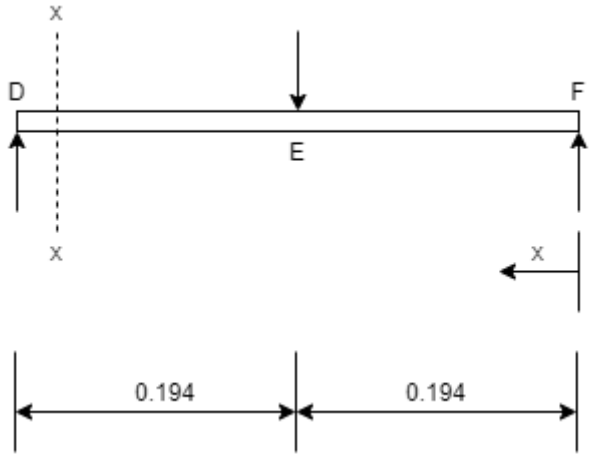

Figure 11.27: Macaulay's deflection analysis for cross member

The deflection at the centre of a simply supported beam can be determined using the following equation.

$$y = \frac{Pl^3}{48EI}$$

The load "P" corresponds to the load of the microscope which was measured to be 44.415 N and the length of the beam was 0.388 m. The Young's modulus "E" and second moment of area "I" were 68.9 GPa and 1.28 x 10^{-9} m^4. The deflection result is shown below.

$$y = \frac{-44.145(0.388)^3}{48(68.9 \times 10^9)(1.28 \times 10^{-9})}$$

$$y = 6.091 \times 10^{-4}\ m$$

$$y = 0.6091\ mm$$

The deflection of the cross member was calculated to be 0.6091 mm which is acceptable for the function of the rig.

11.3. Part drawings for rig components

In this section, the manufacturing drawings for the microscope rig will be shown. This includes all manufactured parts.

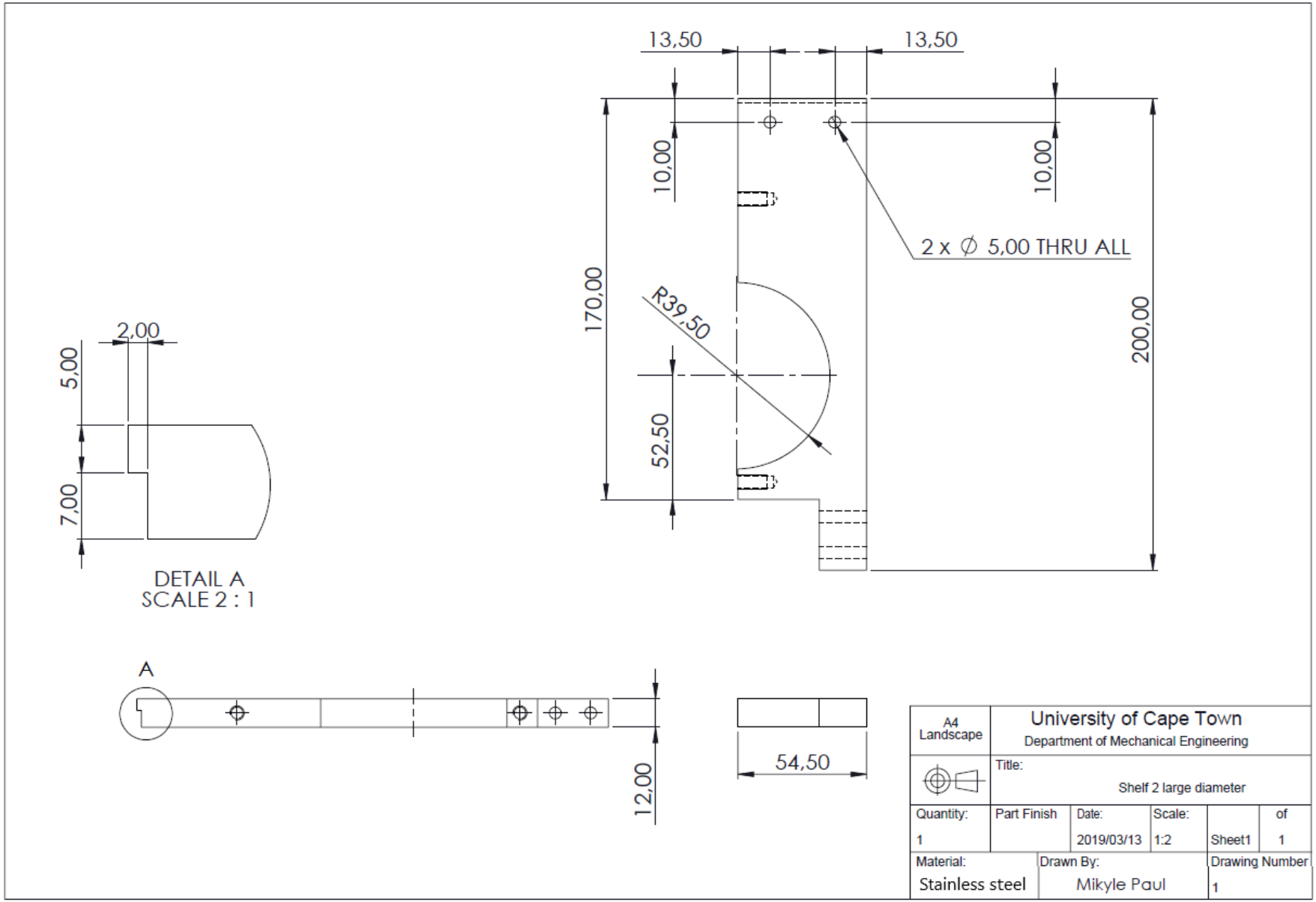
13,50
13,50
10,00
10,00
2 x ∅ 5,00 THRU ALL
170,00
R39,50
200,00
52,50
2,00
5,00
7,00
DETAIL A
SCALE 2 : 1
A
12,00
54,50
A4 Landscape
University of Cape Town
Department of Mechanical Engineering
Title:
Shelf 2 large diameter
Quantity:
1
Part Finish
Date:
2019/03/13
Scale:
1:2
Sheet1
of
1
Material:
Stainless steel
Drawn By:
Mikyle Paul
Drawing Number
1

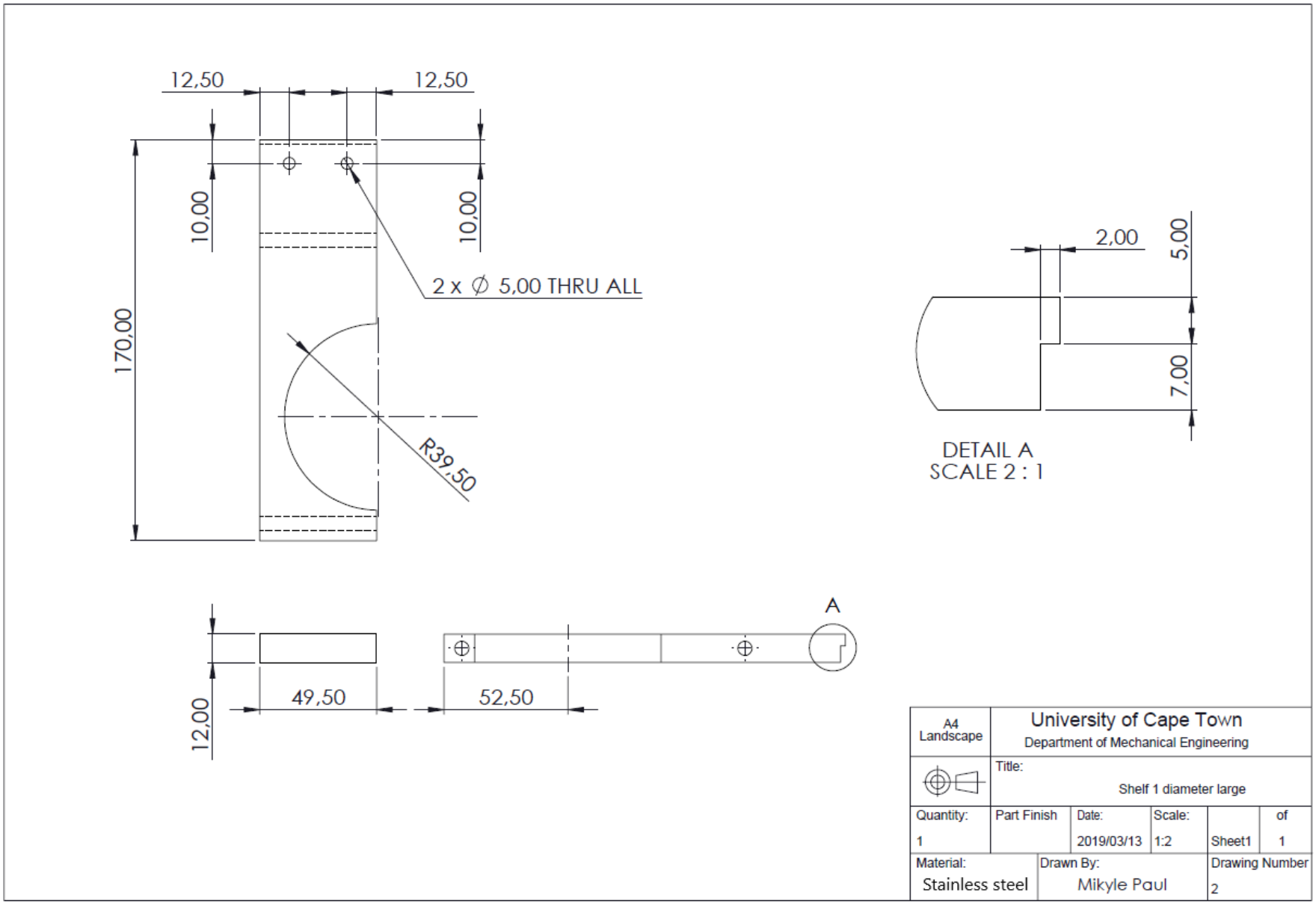
12,50
12,50
10,00
10,00
2 x ∅ 5,00 THRU ALL
170,00
R39,50
2,00
5,00
7,00
DETAIL A
SCALE 2 : 1
A
12,00
49,50
52,50
A4 Landscape
University of Cape Town
Department of Mechanical Engineering
Title:
Shelf 1 diameter large
Quantity: 1
Part Finish
Date: 2019/03/13
Scale: 1:2
Sheet1
of 1
Material: Stainless steel
Drawn By: Mikyle Paul
Drawing Number 2

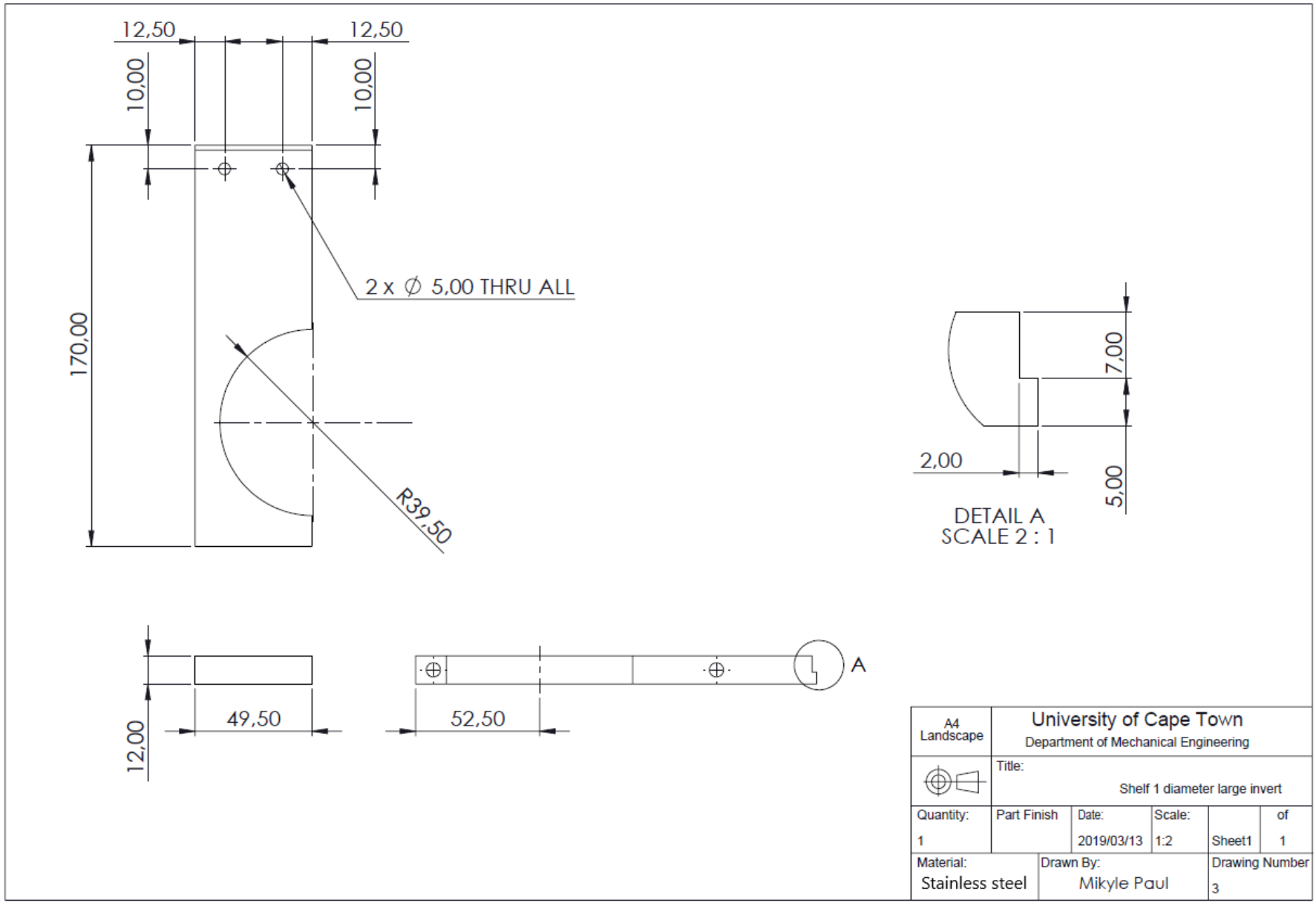
12,50
12,50
10,00
10,00
2 x ∅ 5,00 THRU ALL
170,00
R39,50
7,00
2,00
5,00
DETAIL A
SCALE 2 : 1
12,00
49,50
52,50
A
A4 Landscape
University of Cape Town
Department of Mechanical Engineering
Title:
Shelf 1 diameter large invert
Quantity:
1
Part Finish
Date:
2019/03/13
Scale:
1:2
Sheet1
of
1
Material:
Stainless steel
Drawn By:
Mikyle Paul
Drawing Number
3

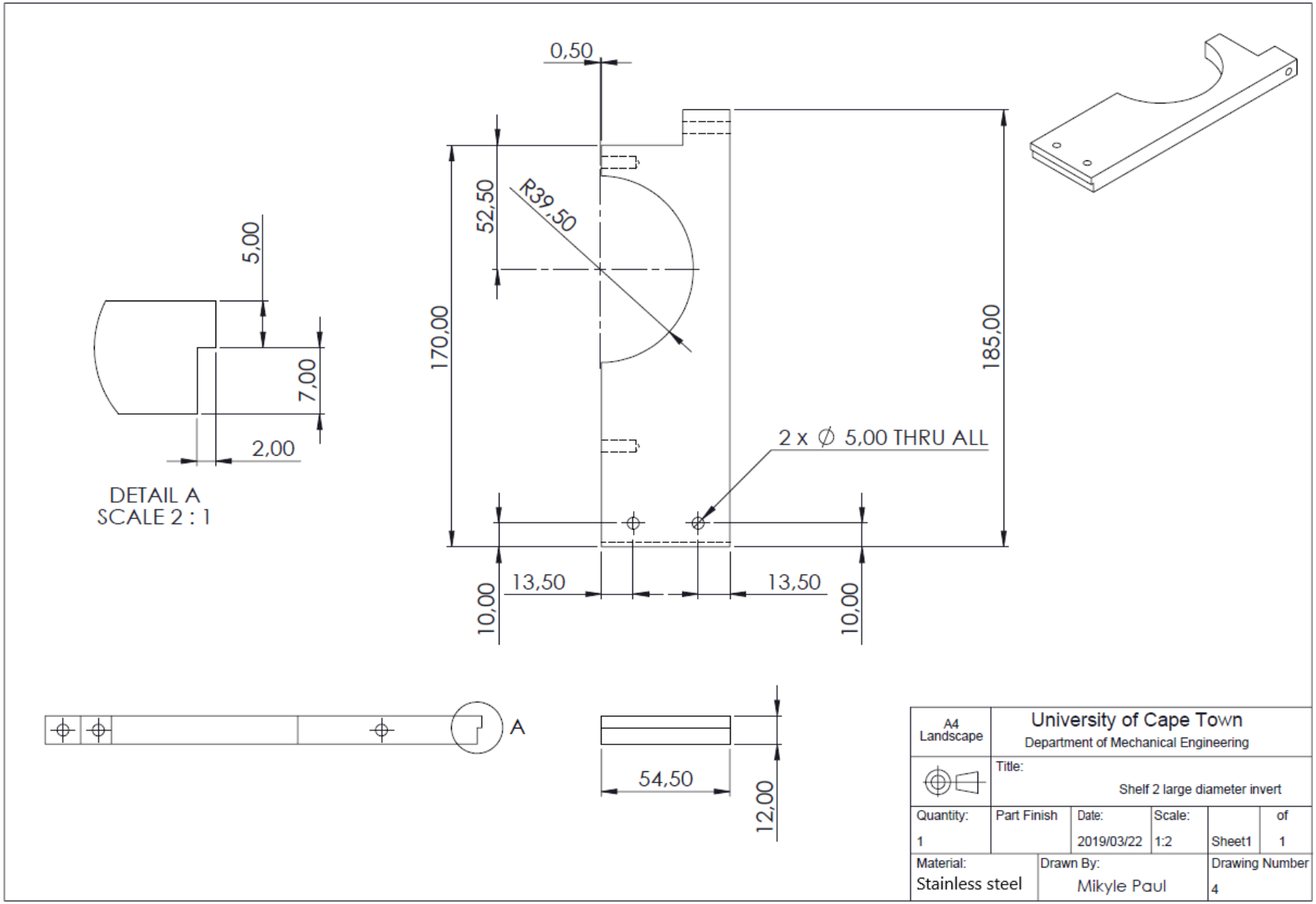
0,50
52,50
R39,50
170,00
185,00
2 x ∅ 5,00 THRU ALL
13,50
13,50
10,00
10,00
5,00
7,00
2,00
DETAIL A
SCALE 2 : 1
A
54,50
12,00
A4 Landscape
University of Cape Town
Department of Mechanical Engineering
Title:
Shelf 2 large diameter invert
Quantity: 1
Part Finish
Date: 2019/03/22
Scale: 1:2
Sheet1
of 1
Material: Stainless steel
Drawn By: Mikyle Paul
Drawing Number 4

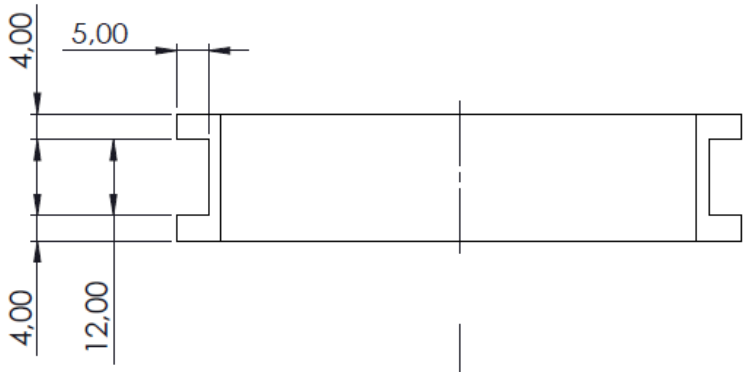

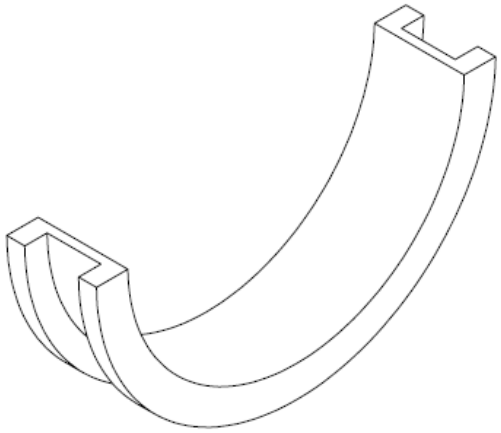

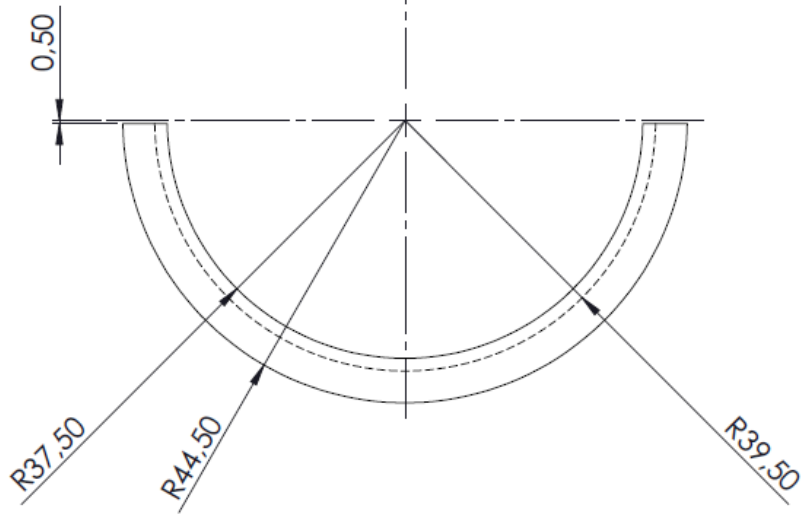

A4 Landscape	University of Cape Town Department of Mechanical Engineering				
	Title: Nylon half bushing				
Quantity: 4	Part Finish	Date: 2019/03/13	Scale: 1:1	Sheet1	of 1
Material: Nylon	Drawn By: Mikyle Paul			Drawing Number 5	

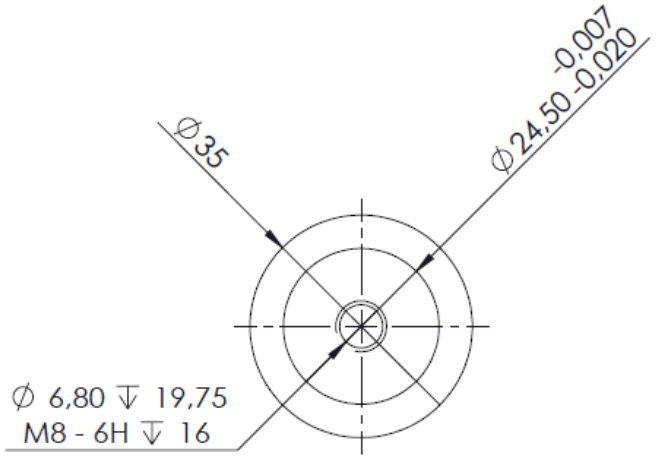

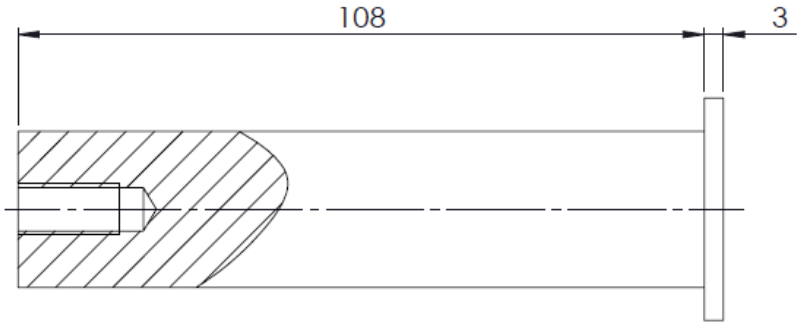

A4 Landscape	University of Cape Town Department of Mechanical Engineering				
	Title: Shaft				
Quantity: 1	Part Finish	Date: 2020/01/31	Scale: 1:1	Sheet1	of 1
Material: Stainless steel	Drawn By: Mikyle Paul			Drawing Number 6	

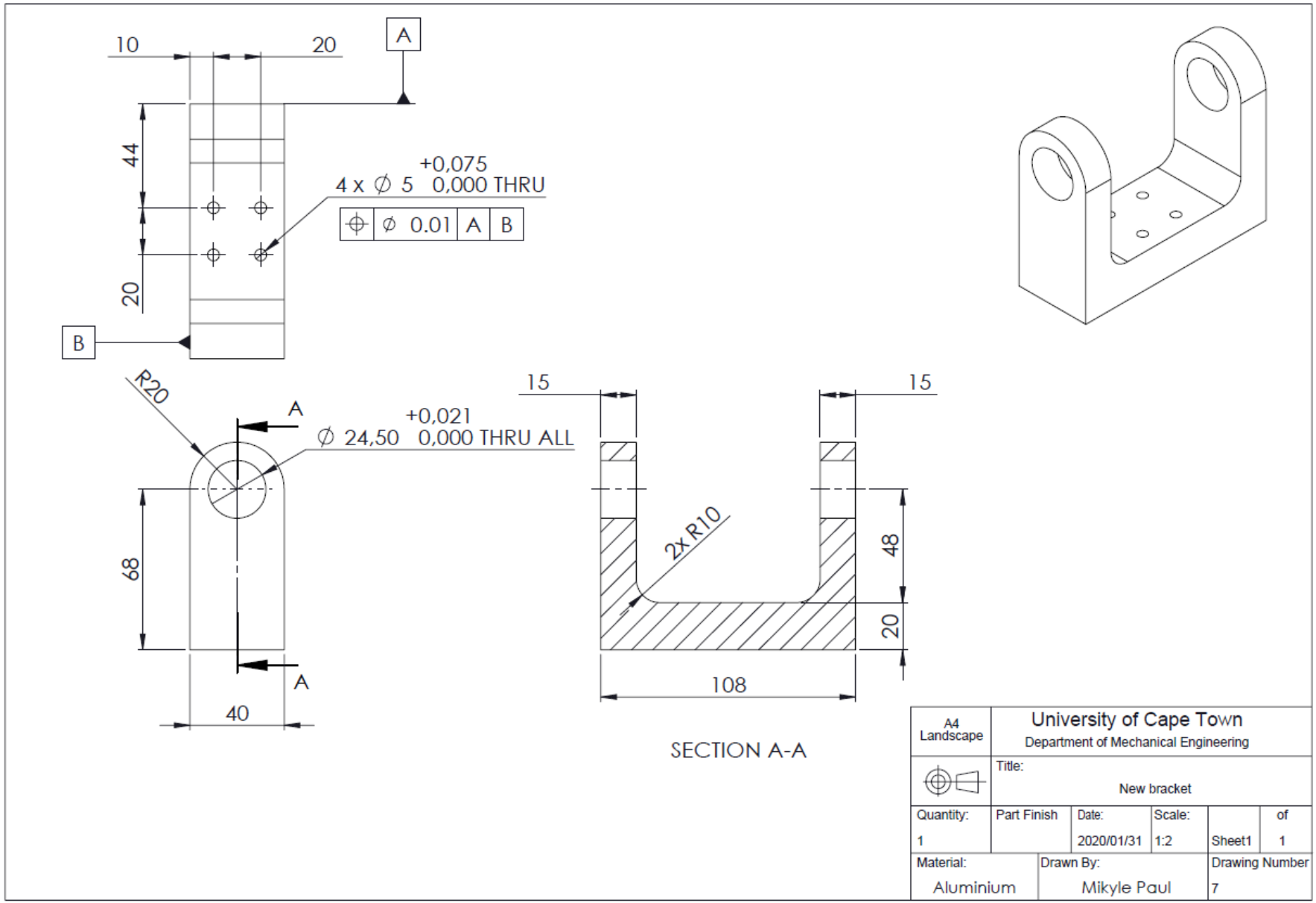
10
20
A
44
20
B
+0,075
4 x ∅ 5 0,000 THRU
⌖ ∅ 0.01 A B
R20
A
+0,021
∅ 24,50 0,000 THRU ALL
68
A
40
15
15
2x R10
48
20
108
SECTION A-A
A4 Landscape
University of Cape Town
Department of Mechanical Engineering
Title:
New bracket
Quantity:
1
Part Finish
Date:
2020/01/31
Scale:
1:2
Sheet1
of
1
Material:
Aluminium
Drawn By:
Mikyle Paul
Drawing Number
7

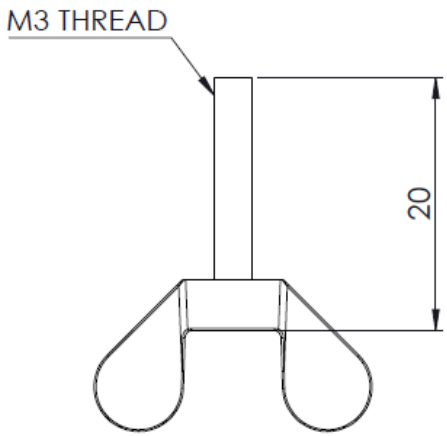

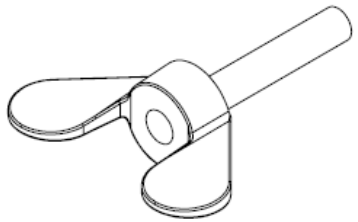

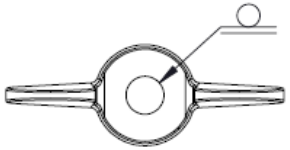

NOTE:
SPOT WELD TO JOIN WING NUT TO M3 THREAD
THREAD WILL FIT INTO DISK, REFER TO DRAWING 5 (DISK)

A4 Landscape	University of Cape Town Department of Mechanical Engineering				
	Title: Wing nut assembly				
Quantity: 4	Part Finish	Date: 2020/01/31	Scale: 2:1	Sheet1	of 1
Material: Stainless steel	Drawn By: Mikyle Paul			Drawing Number 8	

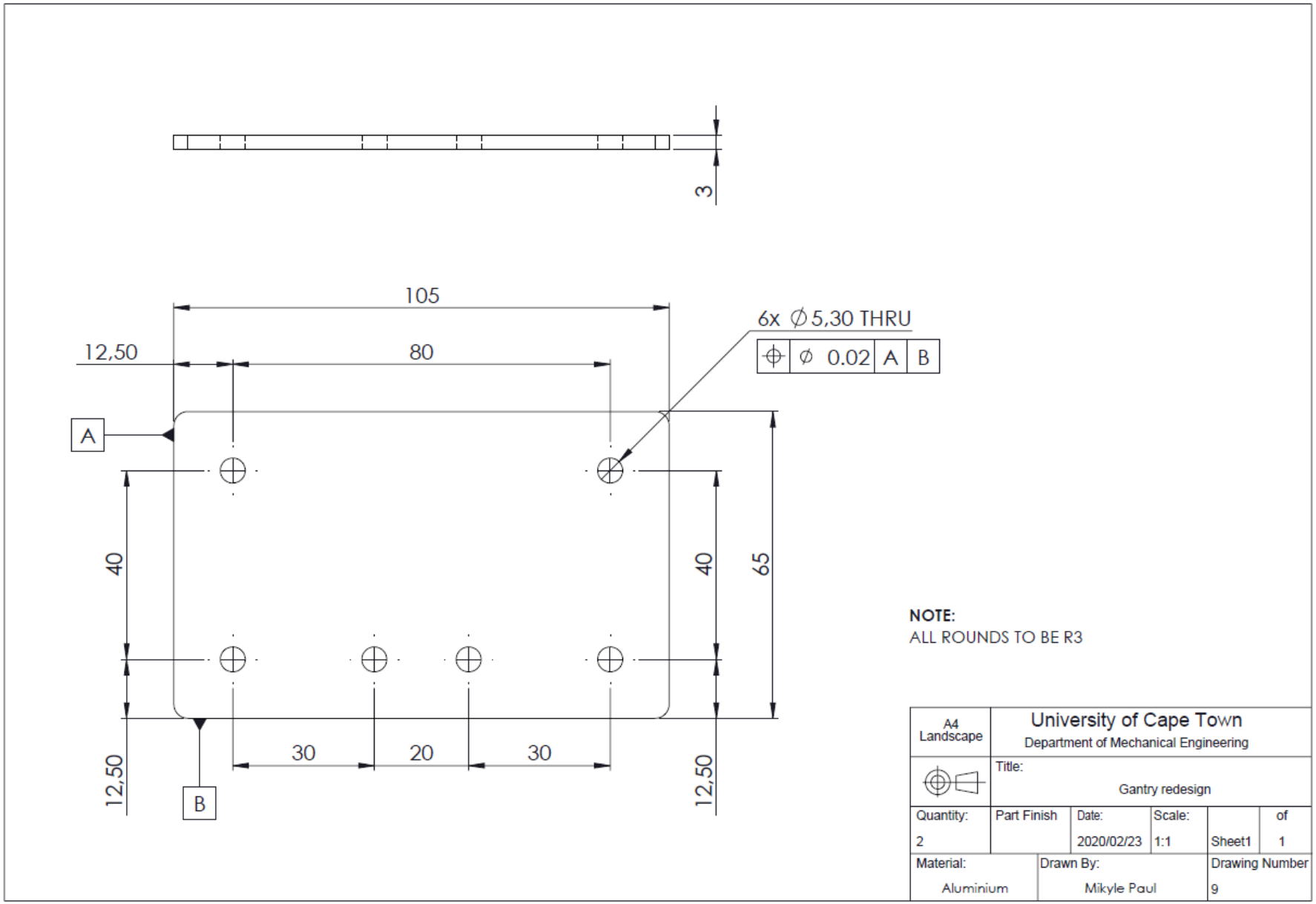

NOTE:
ALL ROUNDS TO BE R3

A4 Landscape	University of Cape Town Department of Mechanical Engineering				
	Title: Gantry redesign				
Quantity: 2	Part Finish	Date: 2020/02/23	Scale: 1:1	Sheet1	of 1
Material: Aluminium	Drawn By: Mikyle Paul			Drawing Number 9	

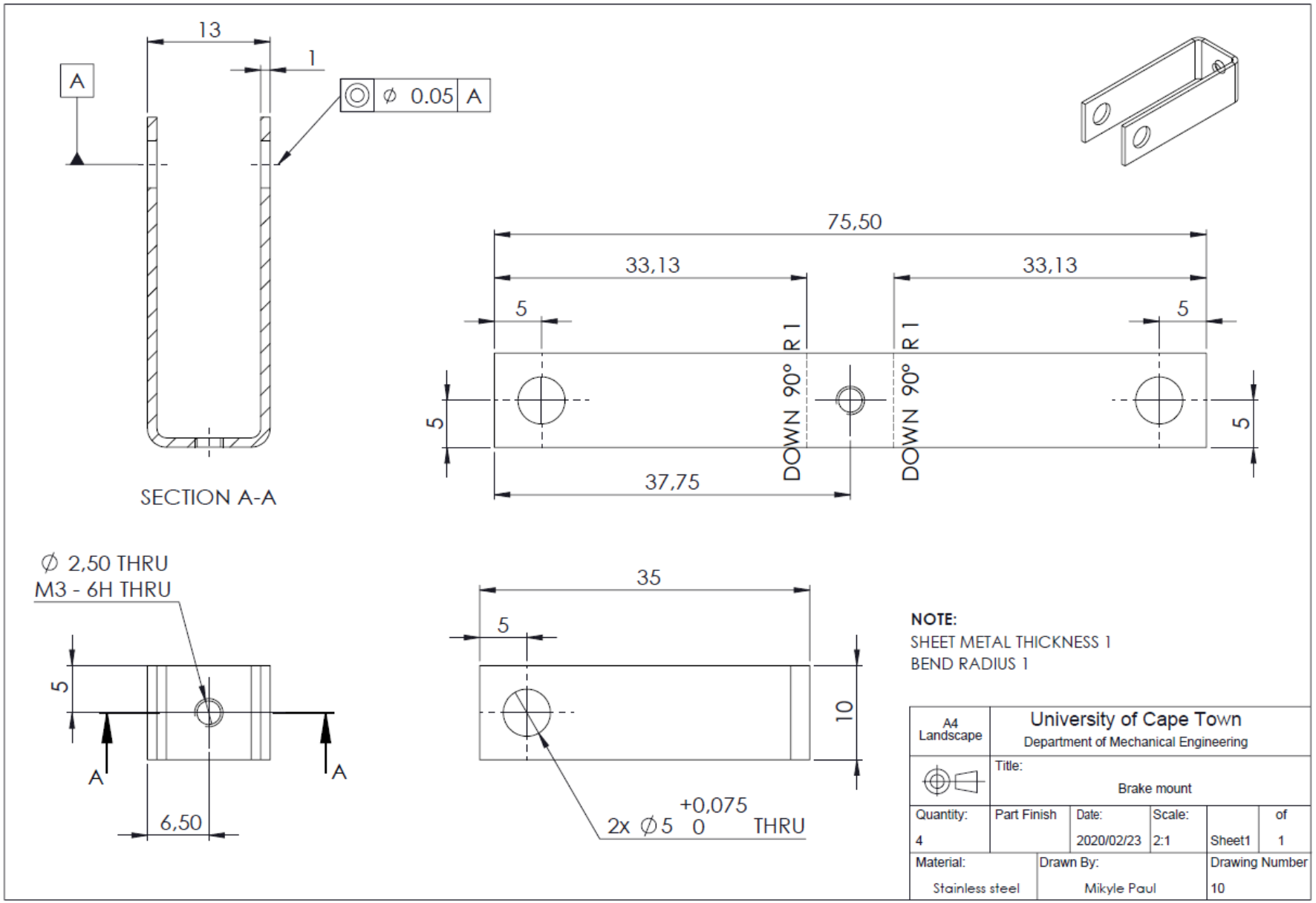
13
1
A
⌀ 0.05 A
SECTION A-A
75,50
33,13
33,13
5
5
R 1
R 1
DOWN 90°
DOWN 90°
5
5
37,75
⌀ 2,50 THRU
M3 - 6H THRU
5
A
A
6,50
35
5
10
+0,075
2x ⌀5 0 THRU
NOTE:
SHEET METAL THICKNESS 1
BEND RADIUS 1
A4 Landscape
University of Cape Town
Department of Mechanical Engineering
Title:
Brake mount
Quantity: 4
Part Finish
Date: 2020/02/23
Scale: 2:1
Sheet1
of 1
Material: Stainless steel
Drawn By: Mikyle Paul
Drawing Number 10

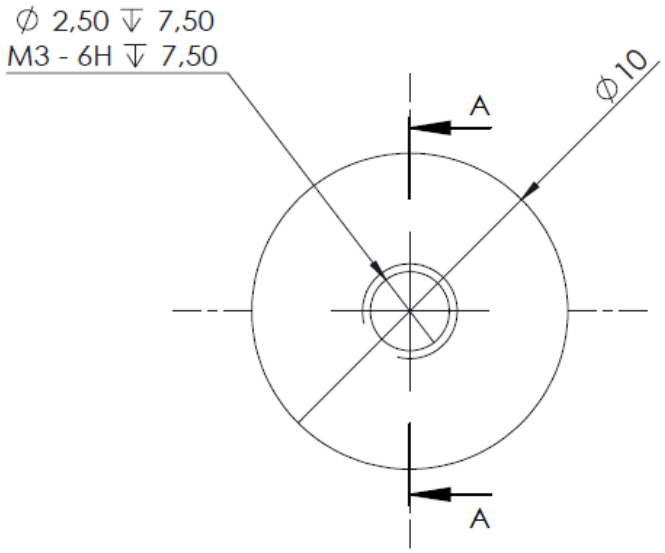

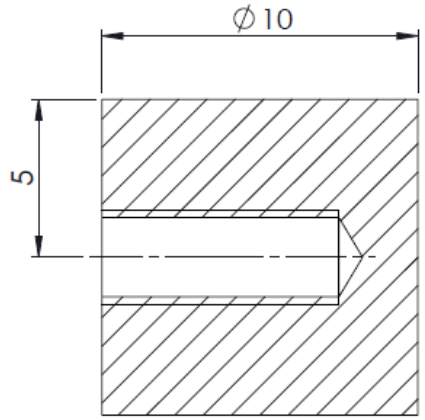

SECTION A-A

A4 Landscape	University of Cape Town Department of Mechanical Engineering				
	Title: Disk				
Quantity: 4	Part Finish	Date: 2020/02/23	Scale: 5:1	Sheet1	of 1
Material: Stainless steel	Drawn By: Mikyle Paul			Drawing Number 11	

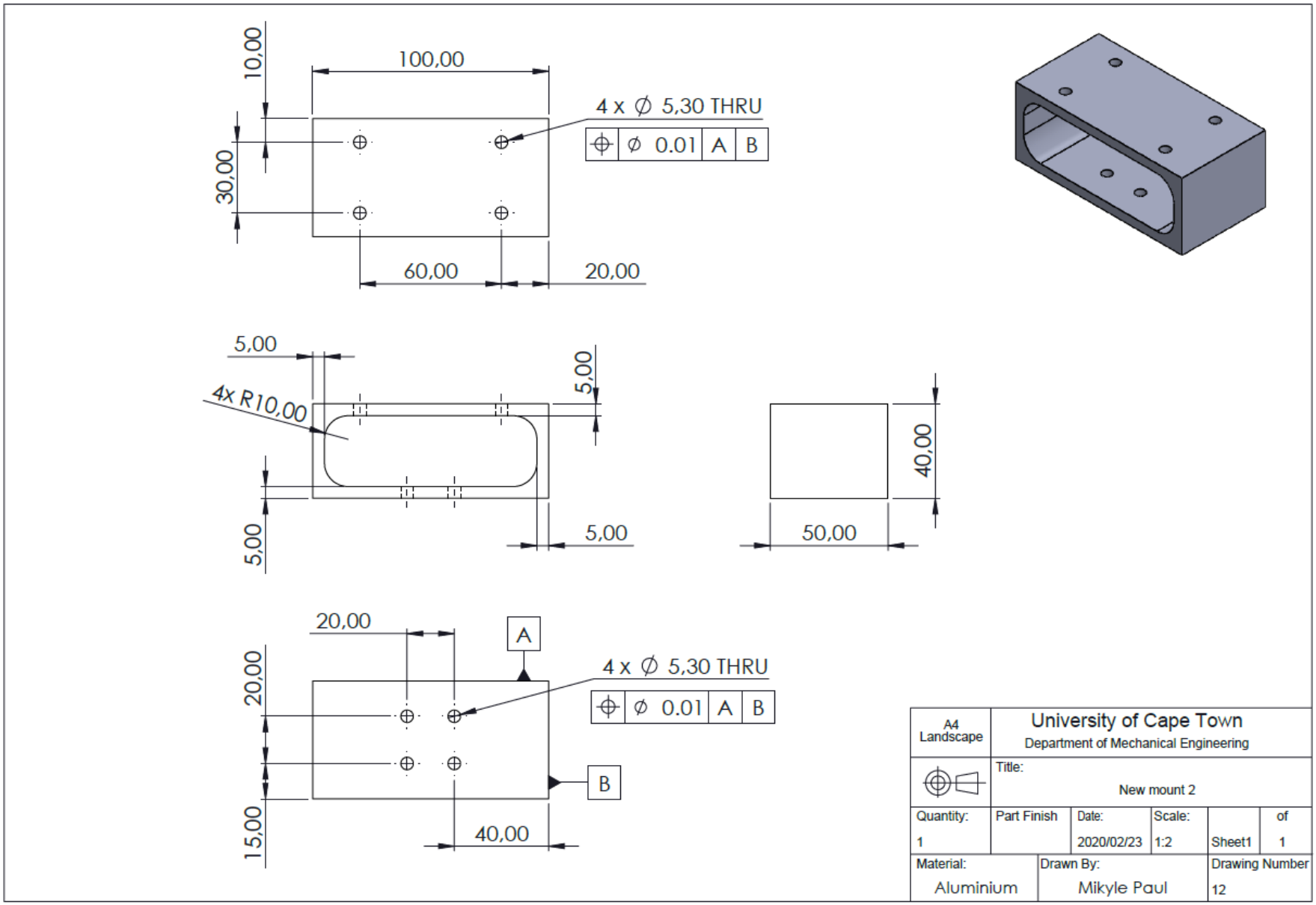
10,00
100,00
4 x ∅ 5,30 THRU
⌖ ∅ 0.01 A B
30,00
60,00
20,00
5,00
4x R10,00
5,00
5,00
5,00
40,00
50,00
20,00
A
4 x ∅ 5,30 THRU
⌖ ∅ 0.01 A B
20,00
B
15,00
40,00
A4 Landscape
University of Cape Town
Department of Mechanical Engineering
Title:
New mount 2
Quantity: 1
Part Finish
Date: 2020/02/23
Scale: 1:2
Sheet1
of 1
Material: Aluminium
Drawn By: Mikyle Paul
Drawing Number 12

11.4. Fatigue crack growth rate test parameters

This section contains the specimen parameters for each fatigue crack growth rate test which include the critical measurements such as *"W", "B"* and *"a_n"*, the load range *ΔP* used for each test, and the starting and ending stress intensity factor ranges *ΔK*. The stress ratio used for each test was 0.1 and is therefore omitted from the table. Specimens XY3, XY6, XY9 and XY10 were tested to failure and hence, the ending stress intensity factor range is significantly higher than the other test specimens.

Table 11.1: Fatigue crack growth rate test parameters

Specimen	W (mm)	B (mm)	a_n (mm)	ΔP (kN)	Starting ΔK (MPa√m)	Ending ΔK (MPa√m)
XY1	21.954	10.860	7.463	6.300	24.386	40.605
XY2	21.966	10.840	7.430	5.400	20.818	34.824
XY3	21.918	10.860	7.435	5.850	22.549	63.010
XY4	21.918	10.840	7.340	5.850	22.492	36.256
XY5	21.876	10.840	7.220	7.200	27.272	46.291
XY6	21.774	10.860	7.272	7.200	27.561	73.639
XY7	22.925	11.200	7.618	7.200	29.175	52.422
XY8	21.900	10.620	7.530	7.200	29.933	48.936
XY9	21.921	10.700	7.467	7.200	28.359	82.329
XY10	21.921	10.640	7.463	7.200	28.505	79.295
XY11	21.921	10.700	7.347	7.200	27.964	47.767
XY12	21.978	10.740	7.558	9.000	40.910	60.269
XY13	22.366	11.280	7.597	7.200	29.009	47.870
XY14	22.499	11.050	7.369	7.200	29.467	47.527
XZ1	22.260	11.080	6.255	7.200	25.798	50.582
XZ2	22.187	11.220	7.314	7.200	29.283	47.992
XZ3	22.089	11.010	7.756	7.200	30.016	49.173
XZ4	21.463	11.100	7.629	7.200	30.309	53.707
XZ5	21.672	11.020	8.020	7.200	32.094	52.056
XZ6	22.065	10.940	7.096	7.200	28.278	49.324
ZX1	22.146	11.200	7.302	7.200	29.302	50.034
ZX2	22.497	11.200	7.561	7.200	29.393	48.642
ZX3	22.400	11.200	7.230	7.200	28.007	47.258
ZX4	22.264	11.300	7.464	7.200	27.789	48.506
ZX5	22.167	11.180	7.386	7.200	28.808	48.837
ZX6	22.324	11.180	7.151	7.200	28.155	48.000

11.5. Final fatigue crack images

This section contains the final fatigue crack lengths for each CT test specimen that was tested.

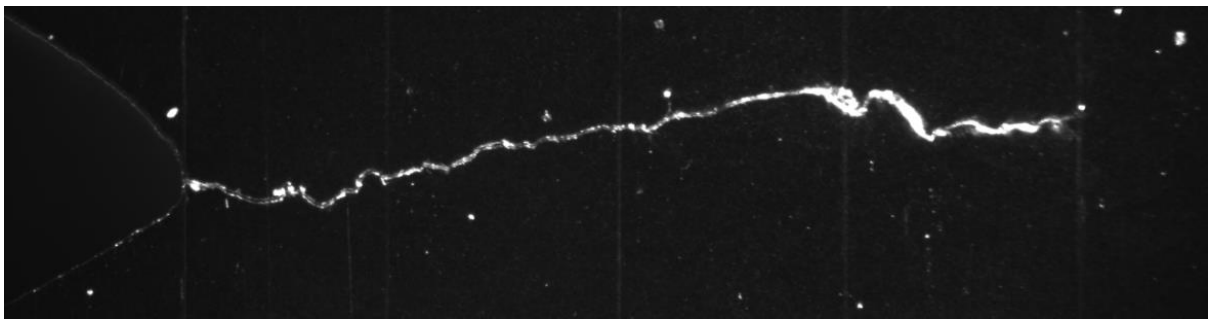

Figure 11.28: XY1 fatigue crack

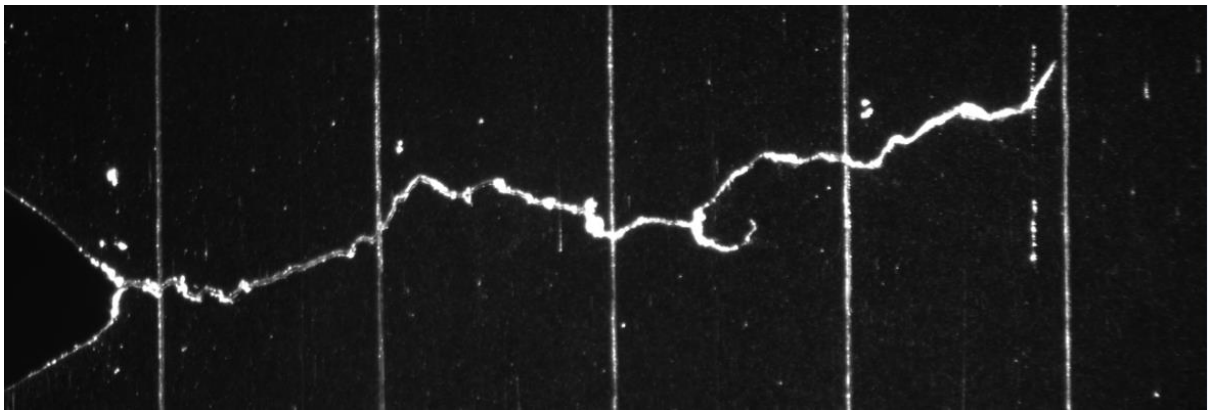

Figure 11.29: XY2 fatigue crack

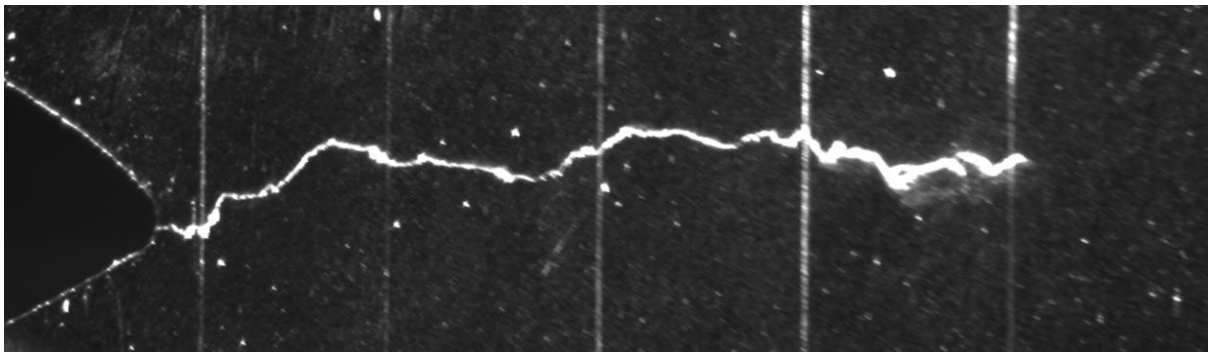

Figure 11.30: XY3 fatigue crack (initial)

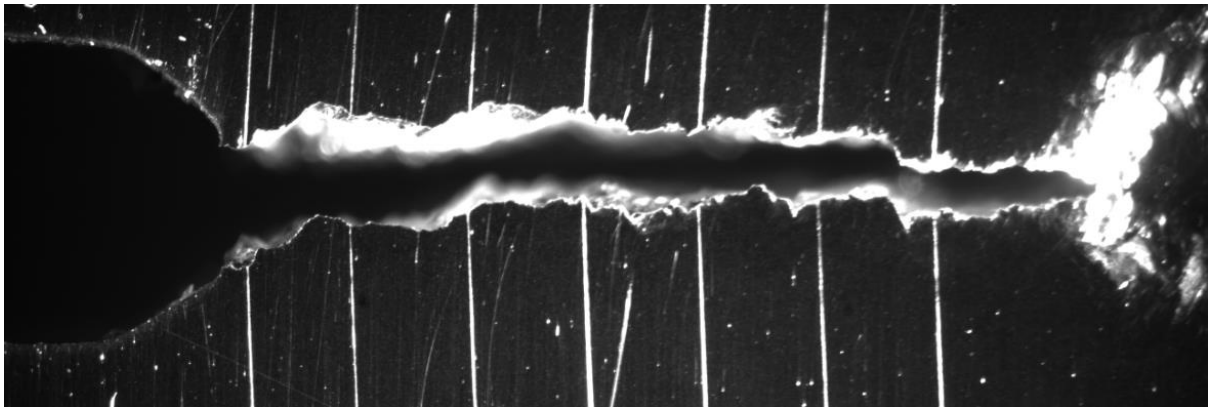

Figure 11.31: XY3 fatigue crack (to failure)

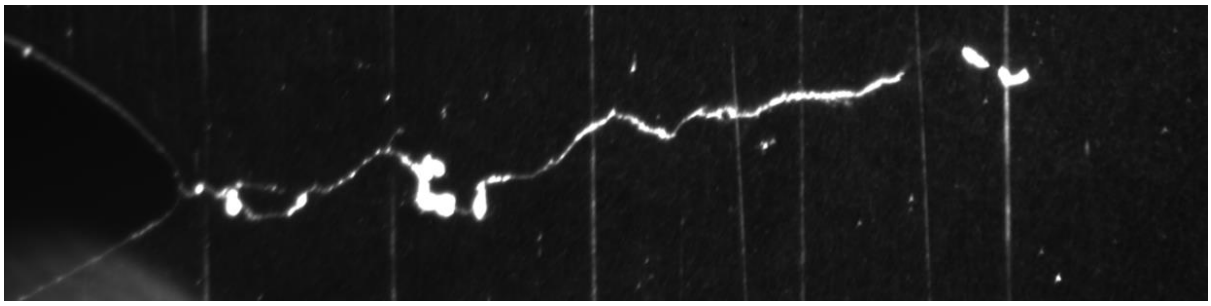

Figure 11.32: XY4 fatigue crack

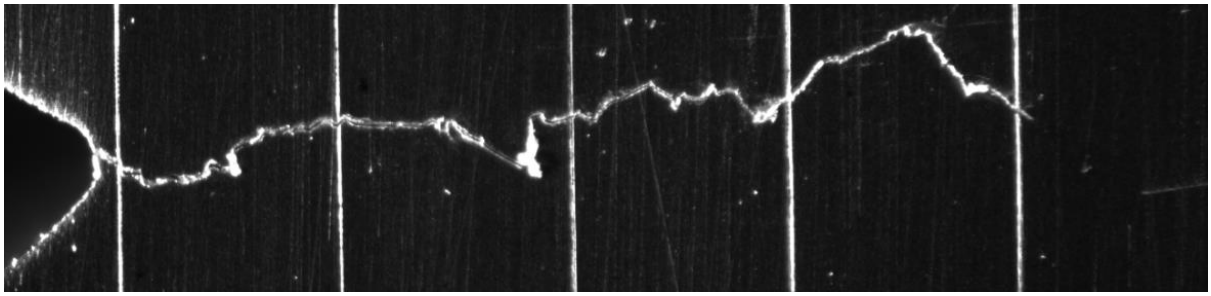

Figure 11.33: XY5 fatigue crack

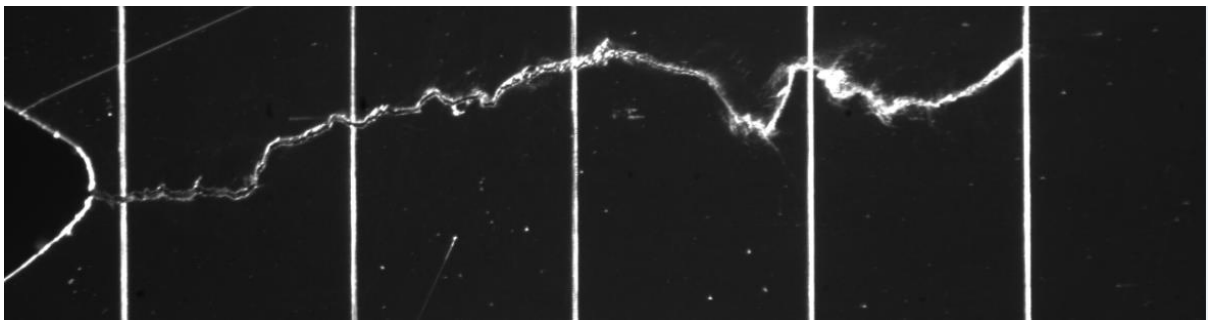

Figure 11.34: XY6 fatigue crack (initial)

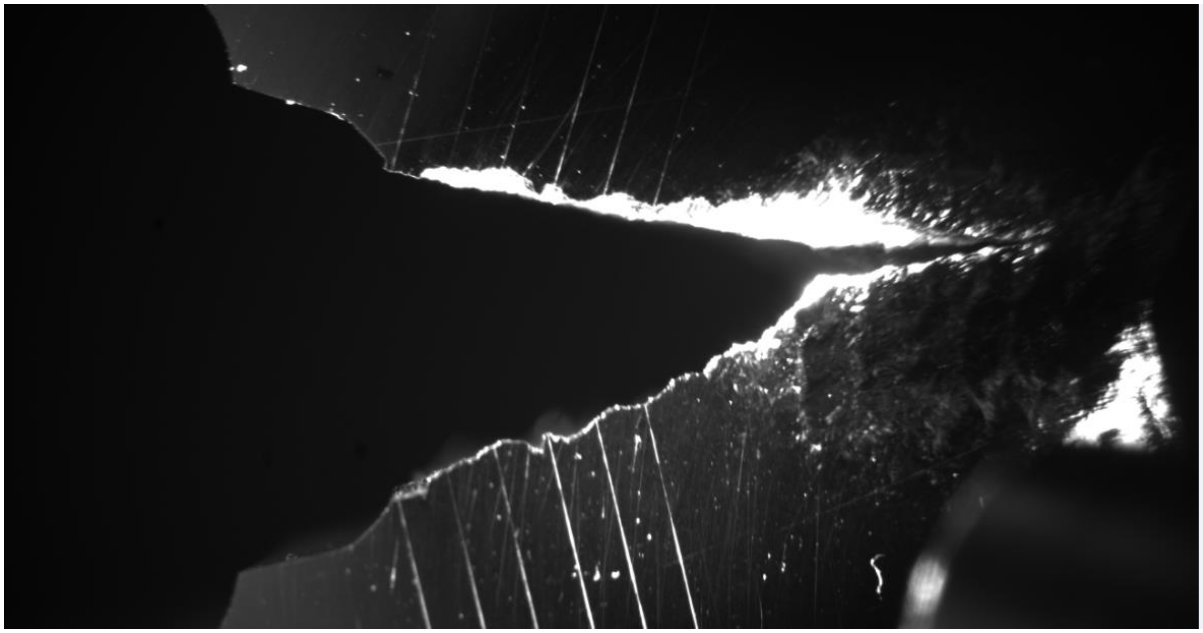

Figure 11.35: XY6 fatigue crack (to failure)

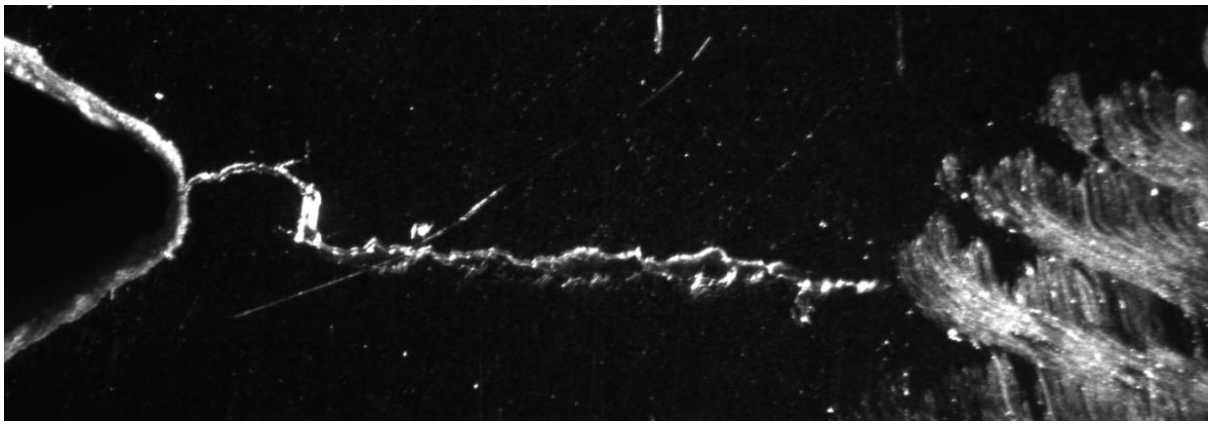

Figure 11.36: XY7 fatigue crack

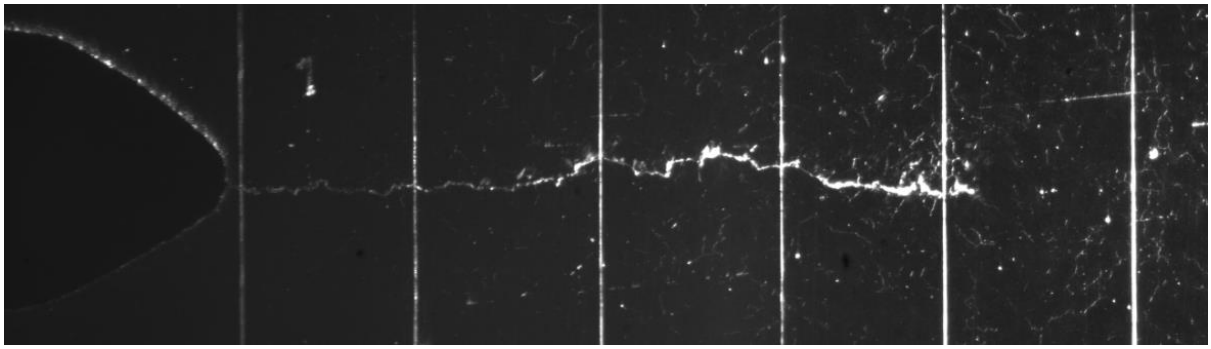

Figure 11.37: XY8 fatigue crack

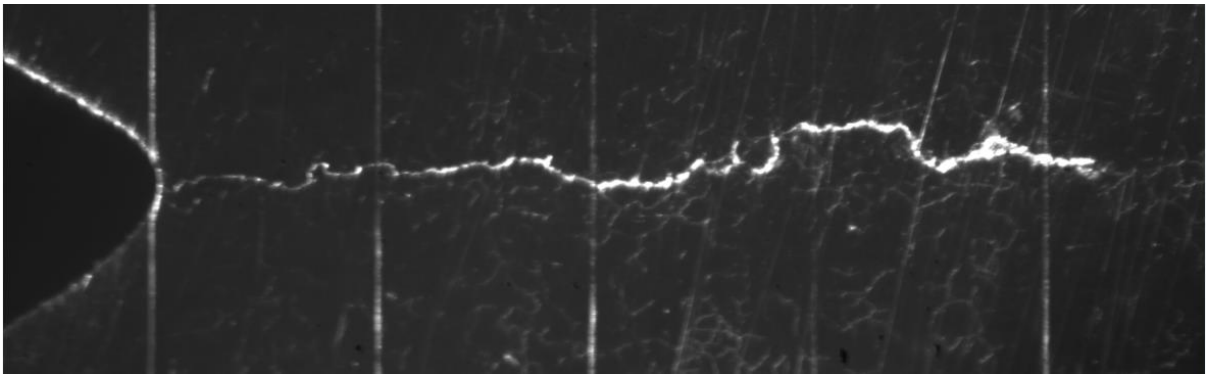

Figure 11.38: XY9 fatigue crack (initial)

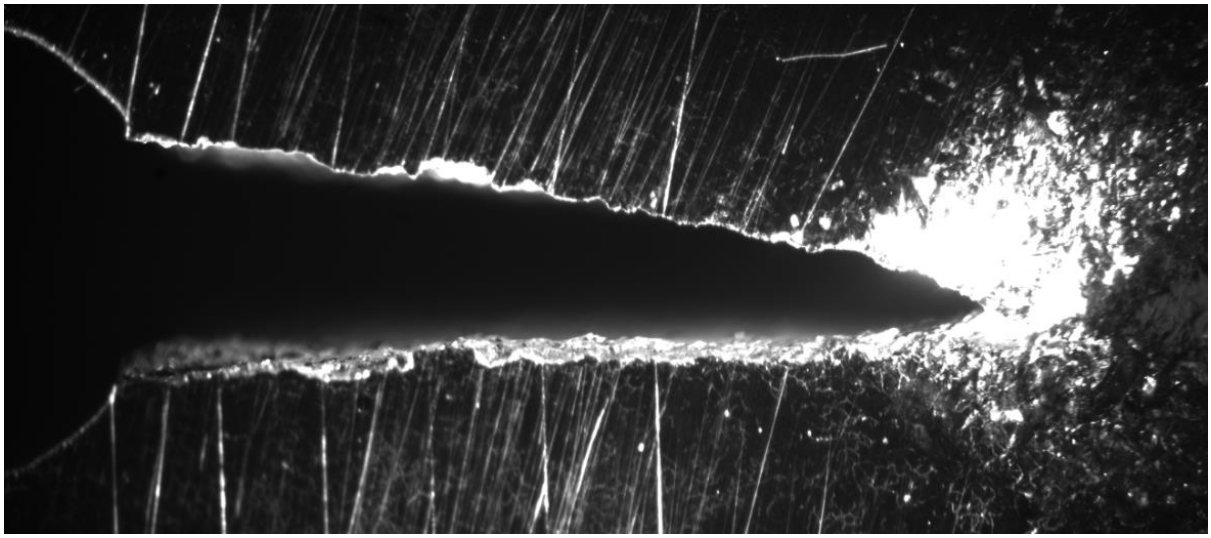

Figure 11.39: XY9 fatigue crack (to failure)

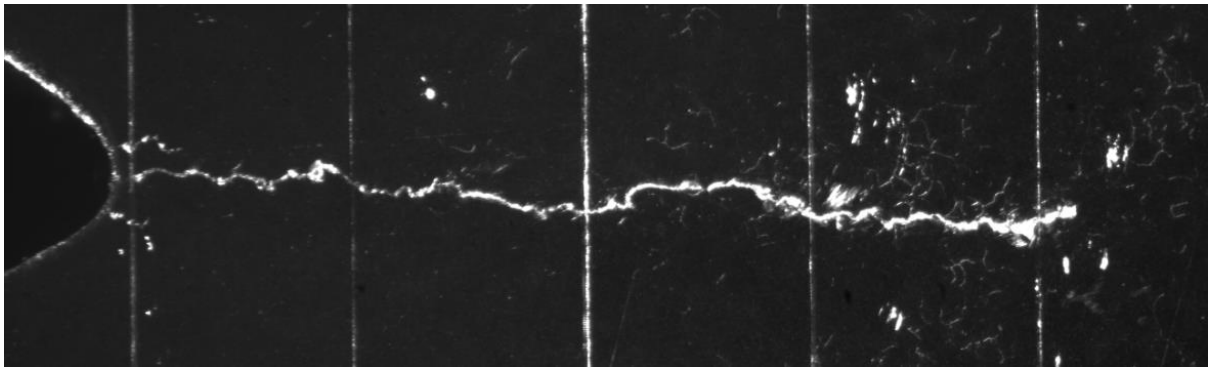

Figure 11.40: XY10 fatigue crack (initial)

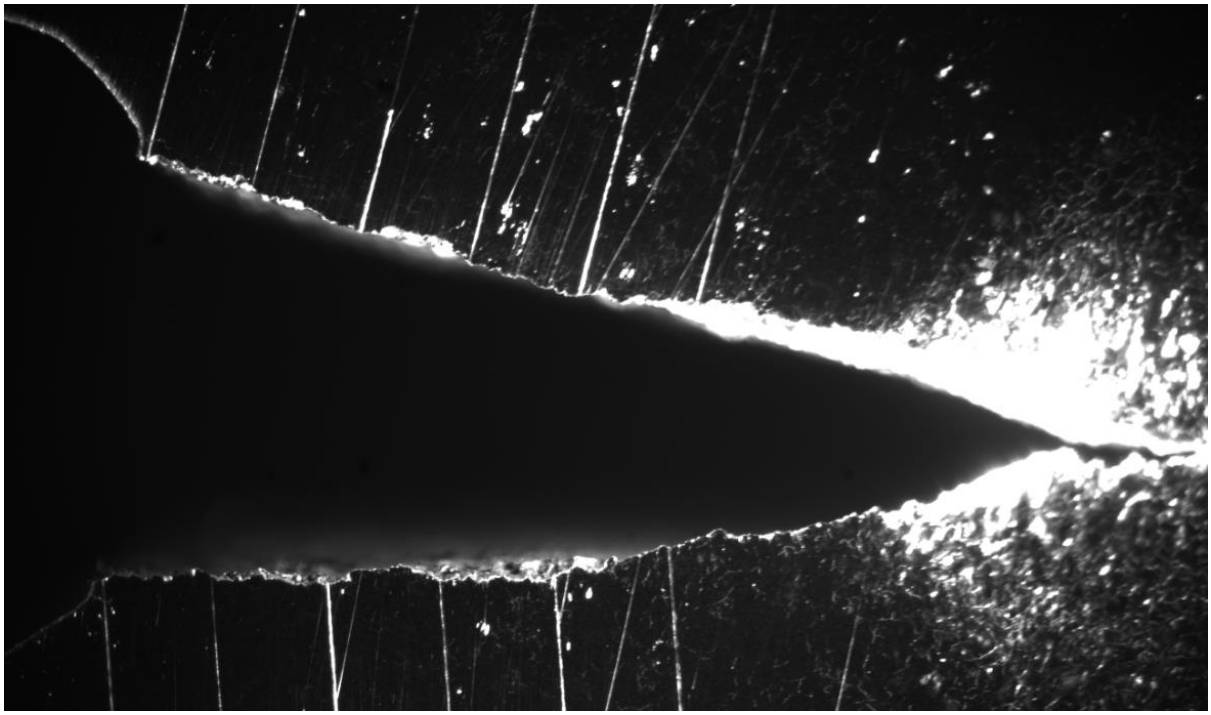

Figure 11.41: XY10 fatigue crack (to failure)

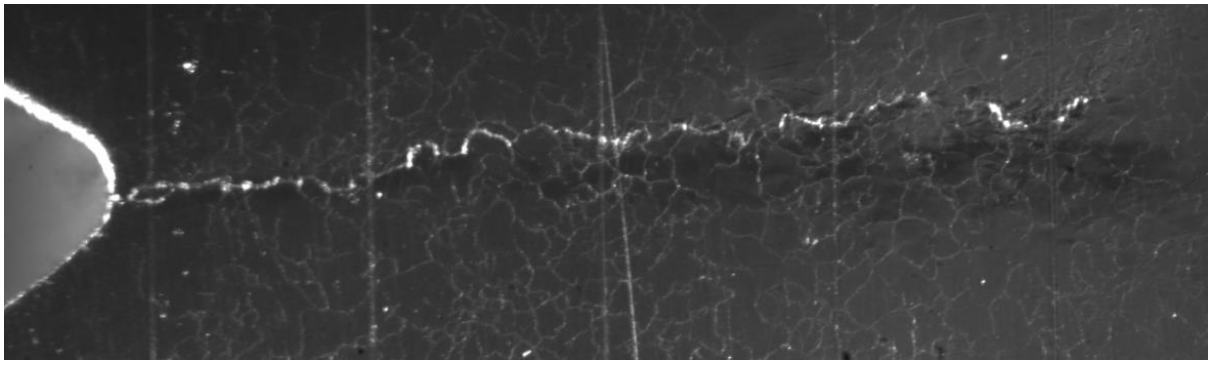

Figure 11.42: XY11 fatigue crack

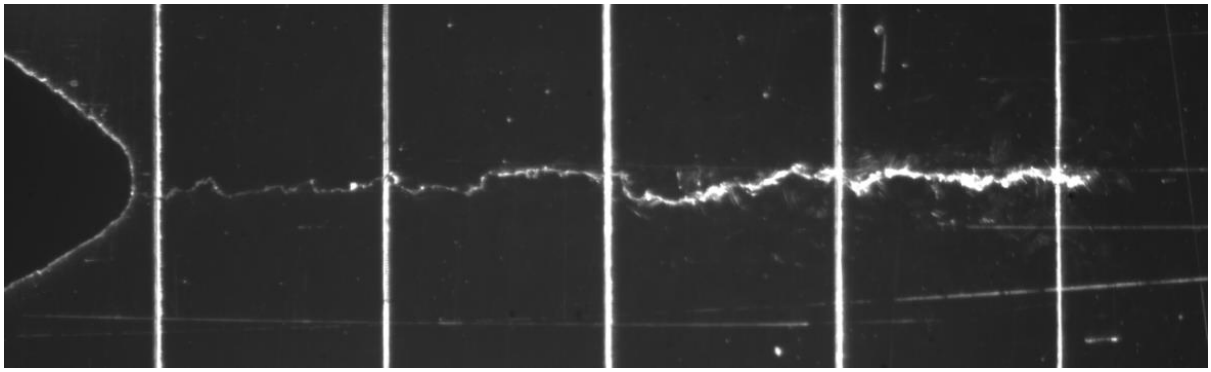

Figure 11.43: XY12 fatigue crack

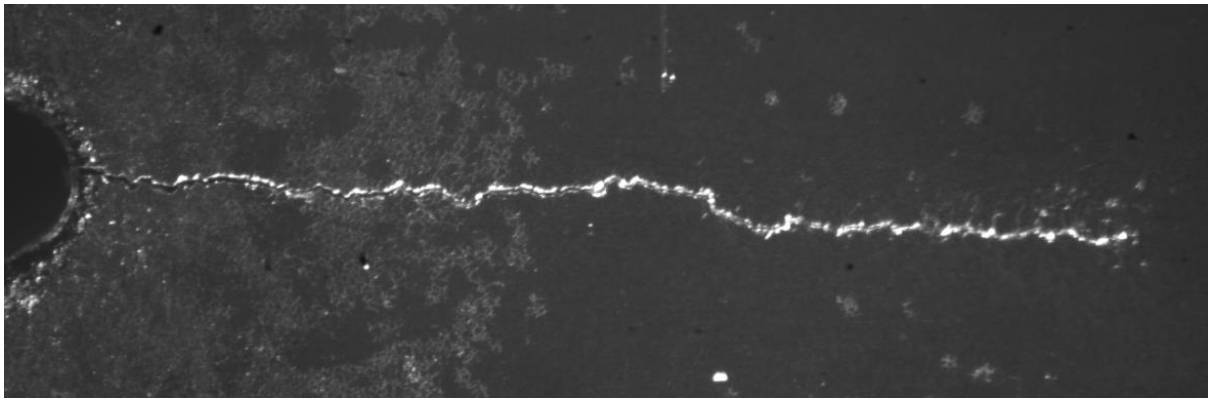

Figure 11.44: XY13 fatigue crack

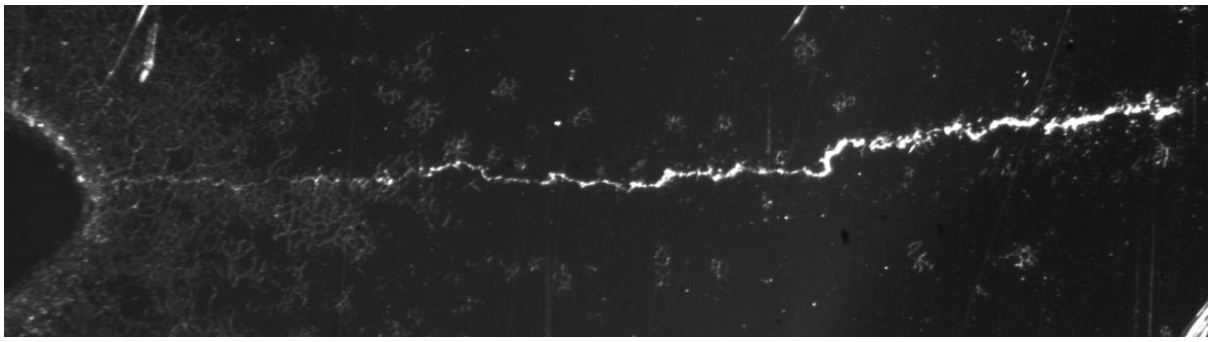

Figure 11.45: XY14 fatigue crack

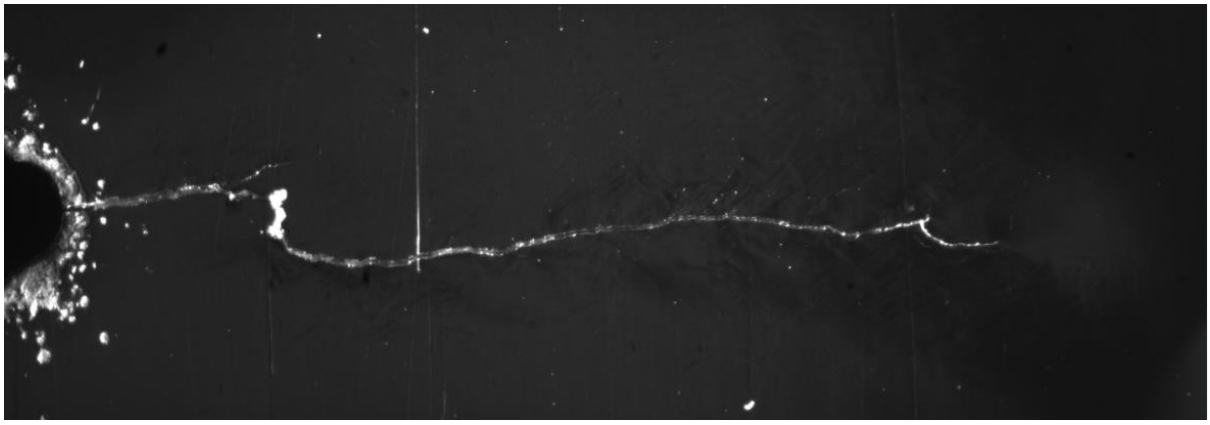

Figure 11.46: XZ1 fatigue crack

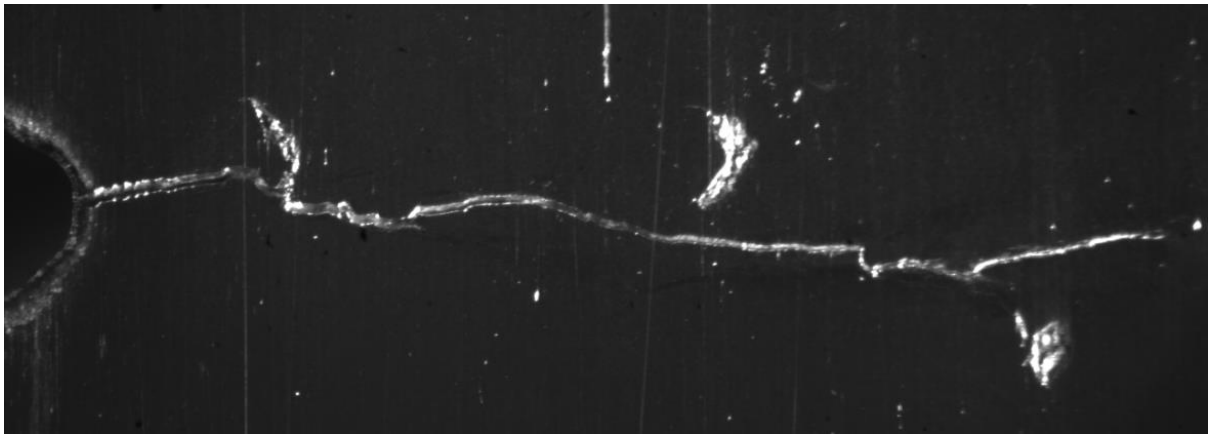

Figure 11.47: XZ2 fatigue crack

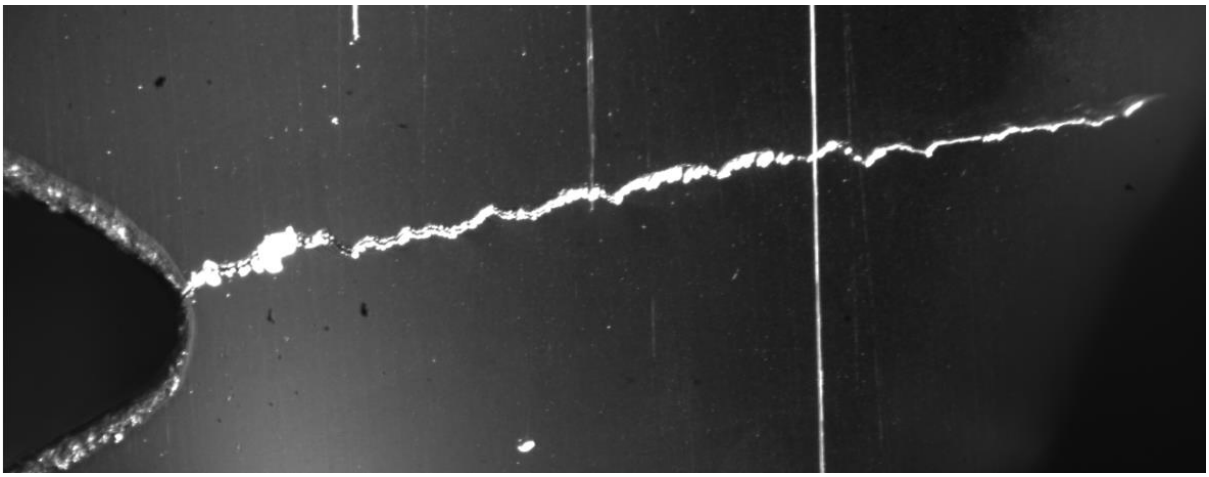

Figure 11.48: XZ3 fatigue crack

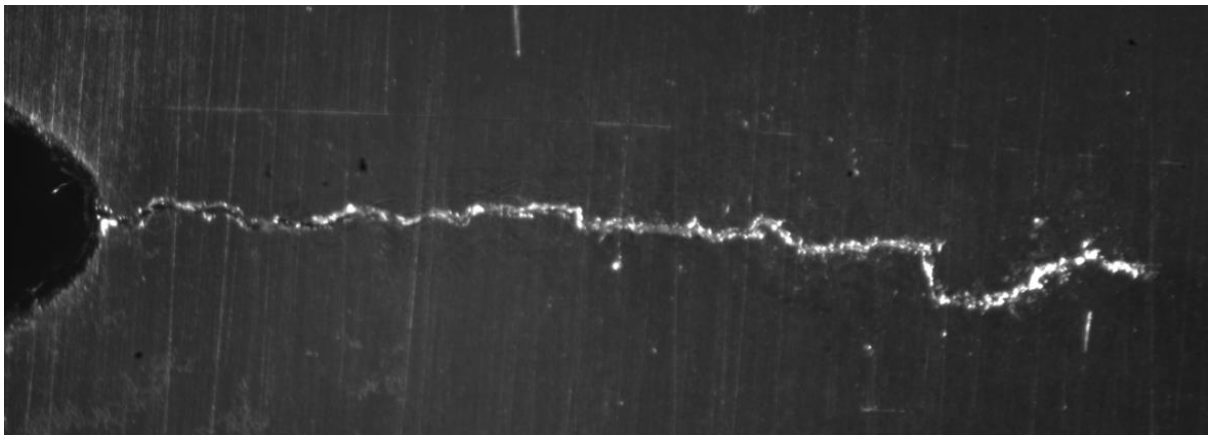

Figure 11.49: XZ4 fatigue crack

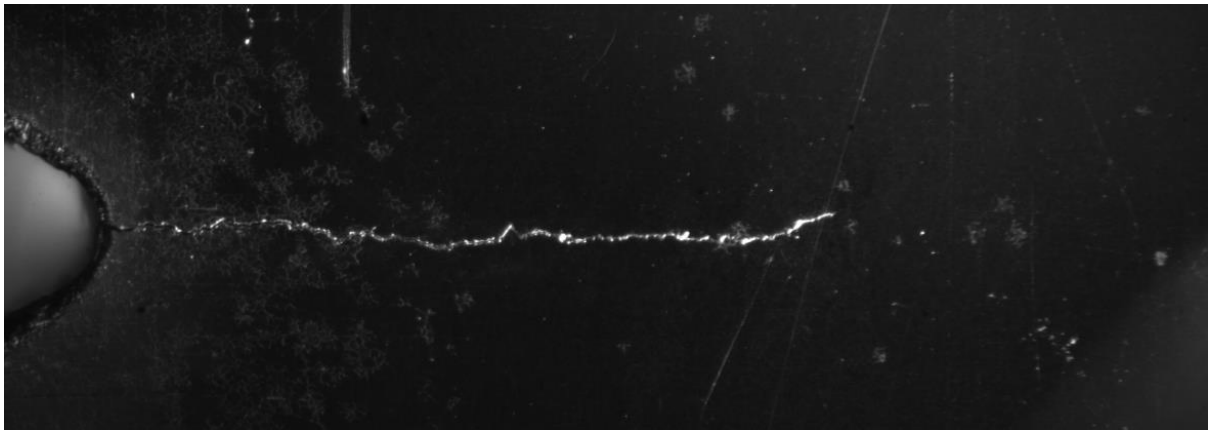

Figure 11.50: XZ5 fatigue crack

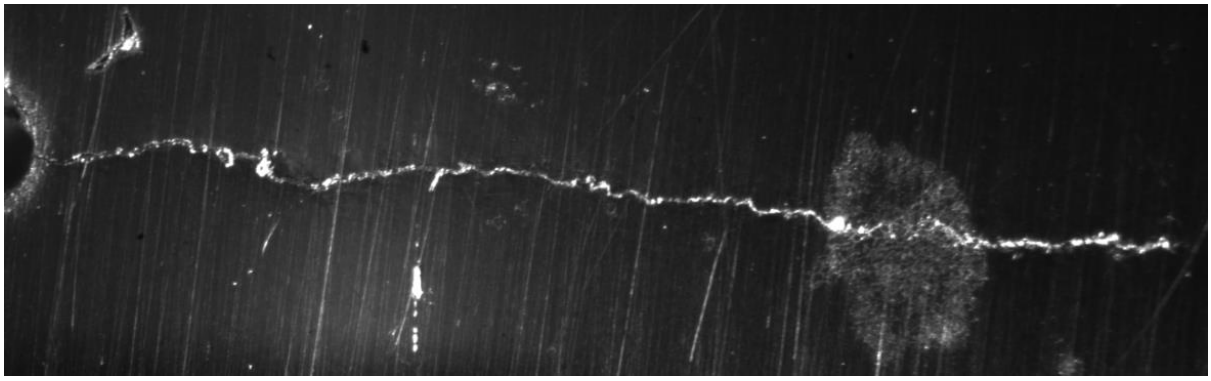

Figure 11.51: XZ6 fatigue crack

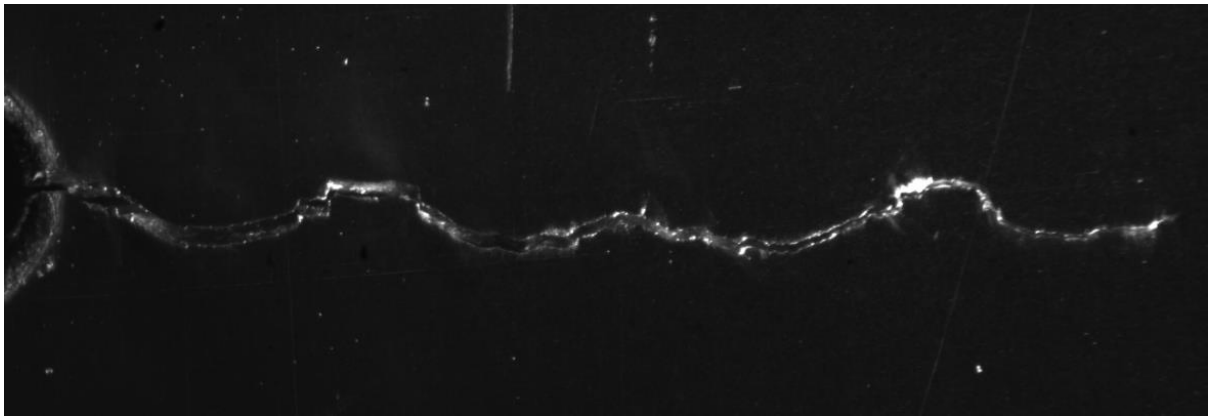

Figure 11.52: ZX1 fatigue crack

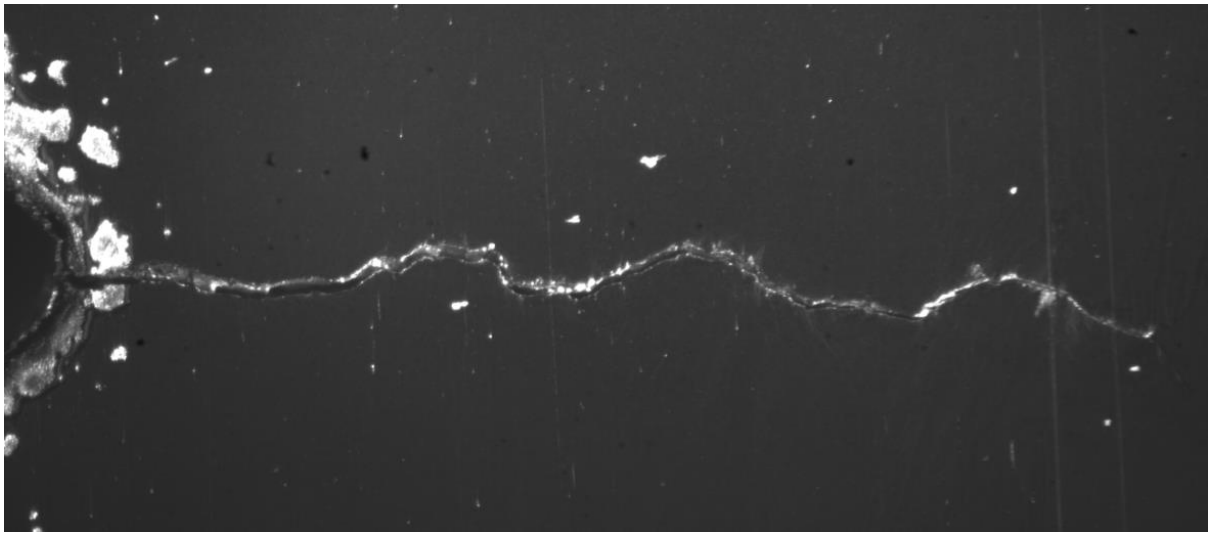

Figure 11.53: ZX2 fatigue crack

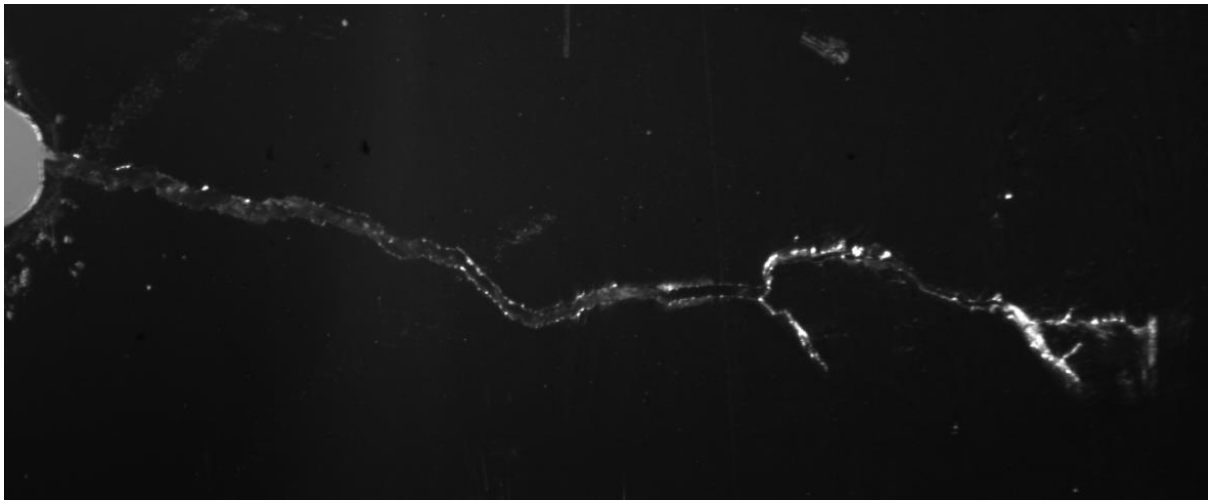

Figure 11.54: ZX3 fatigue crack

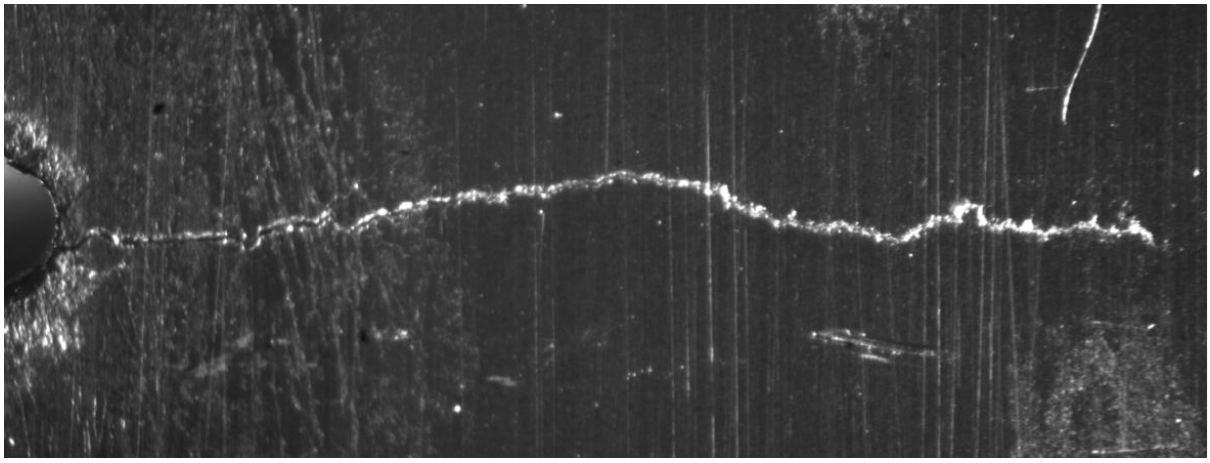

Figure 11.55: ZX4 fatigue crack

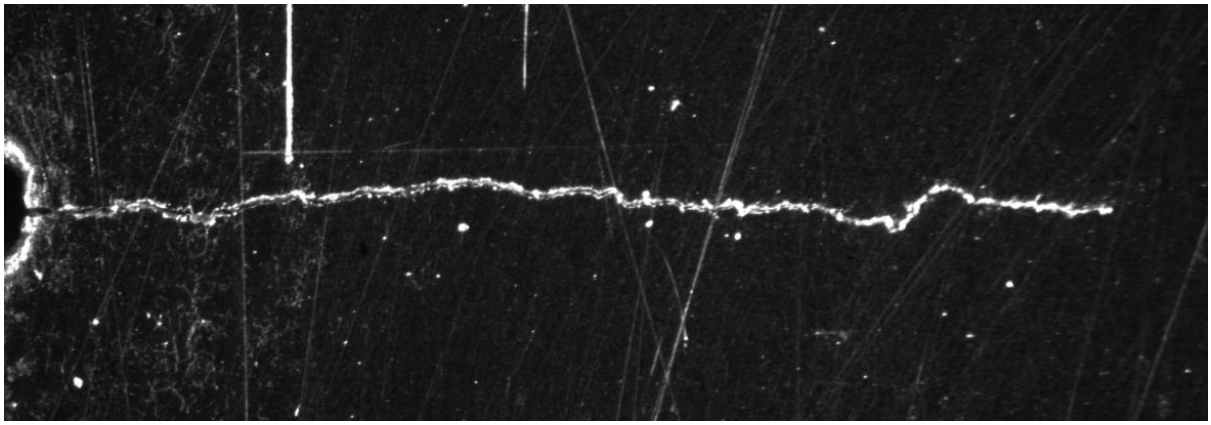

Figure 11.56: ZX5 fatigue crack

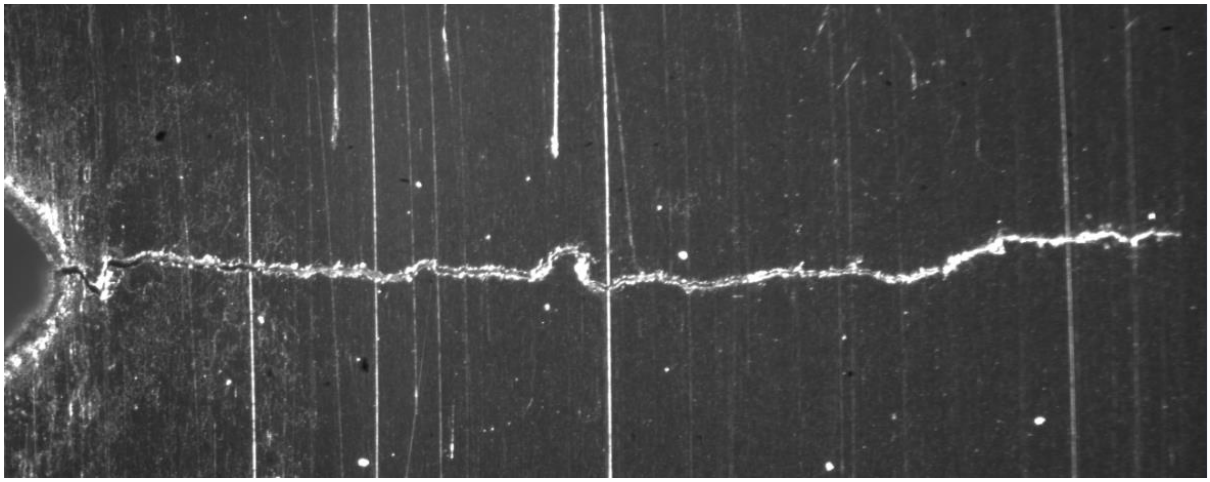

Figure 11.57: ZX6 fatigue crack

11.6. Load vs load line displacement graphs for fracture toughness tests

The load versus load line displacement curves that were developed from the fracture toughness test data can be seen in this appendix for each specimen that was tested. Load line displacement readings were recorded using an Instron 2670-116 displacement gauge. Each curve was generated using Octave.

11.6.1. XY orientation

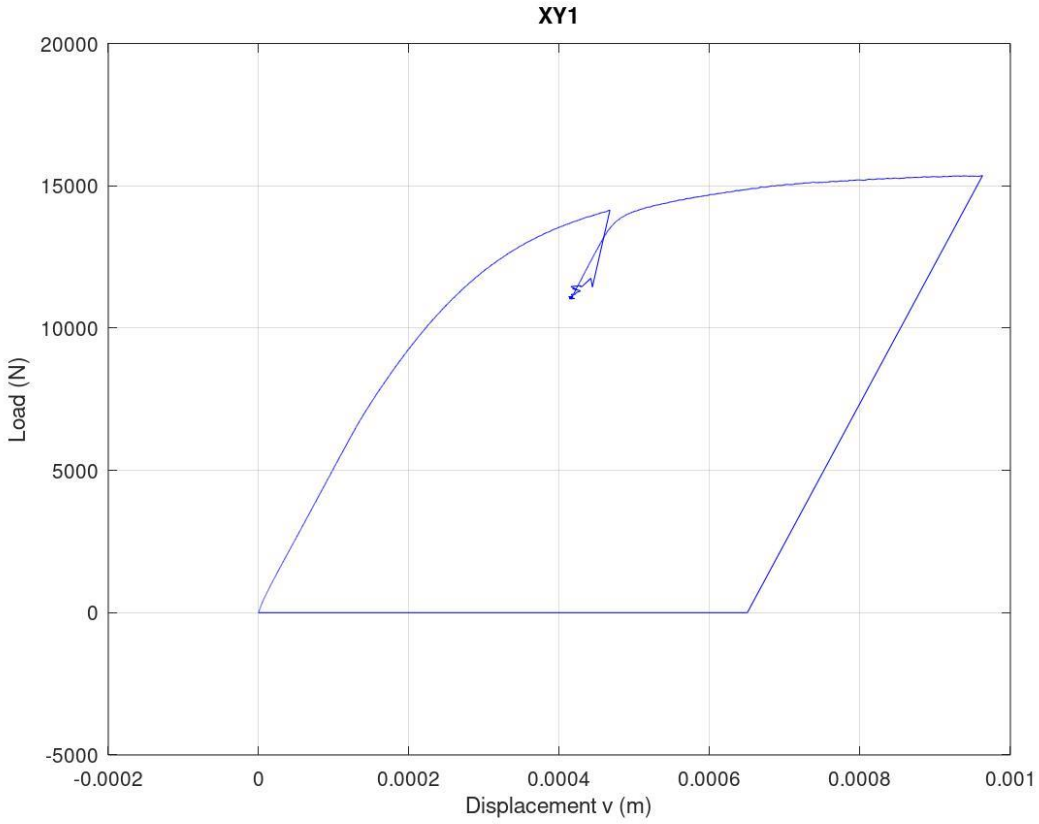

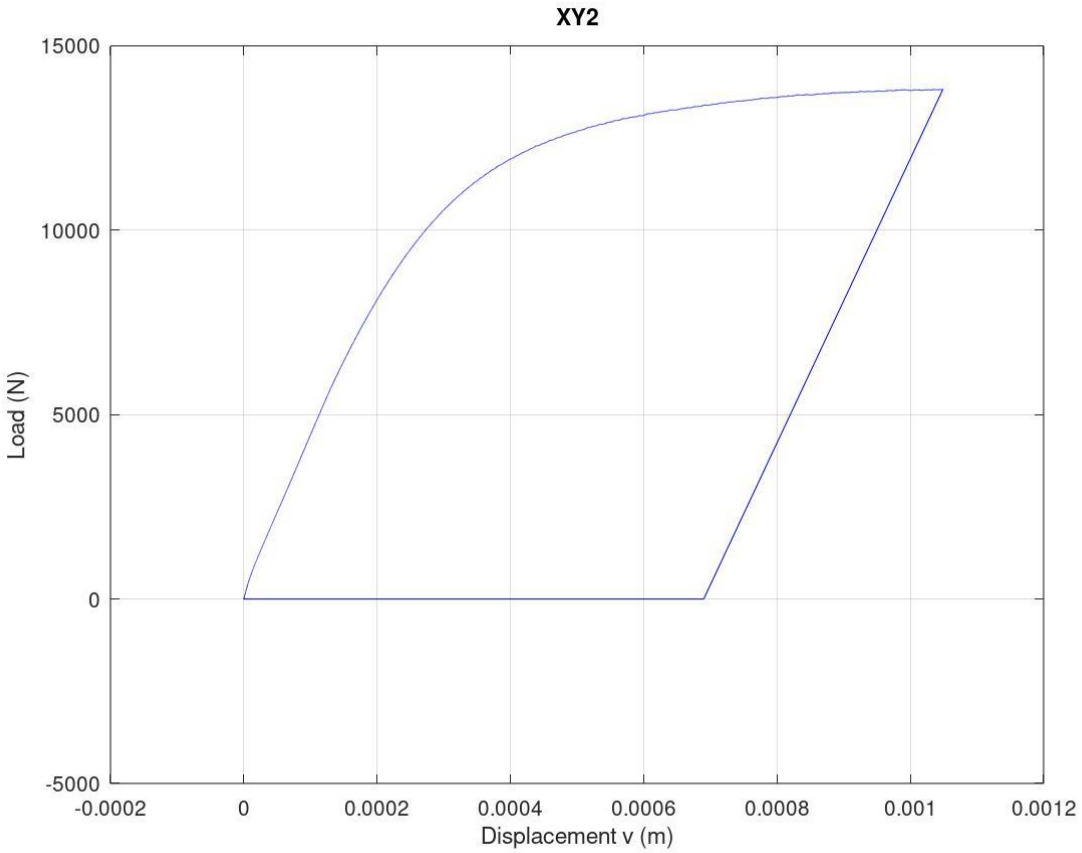

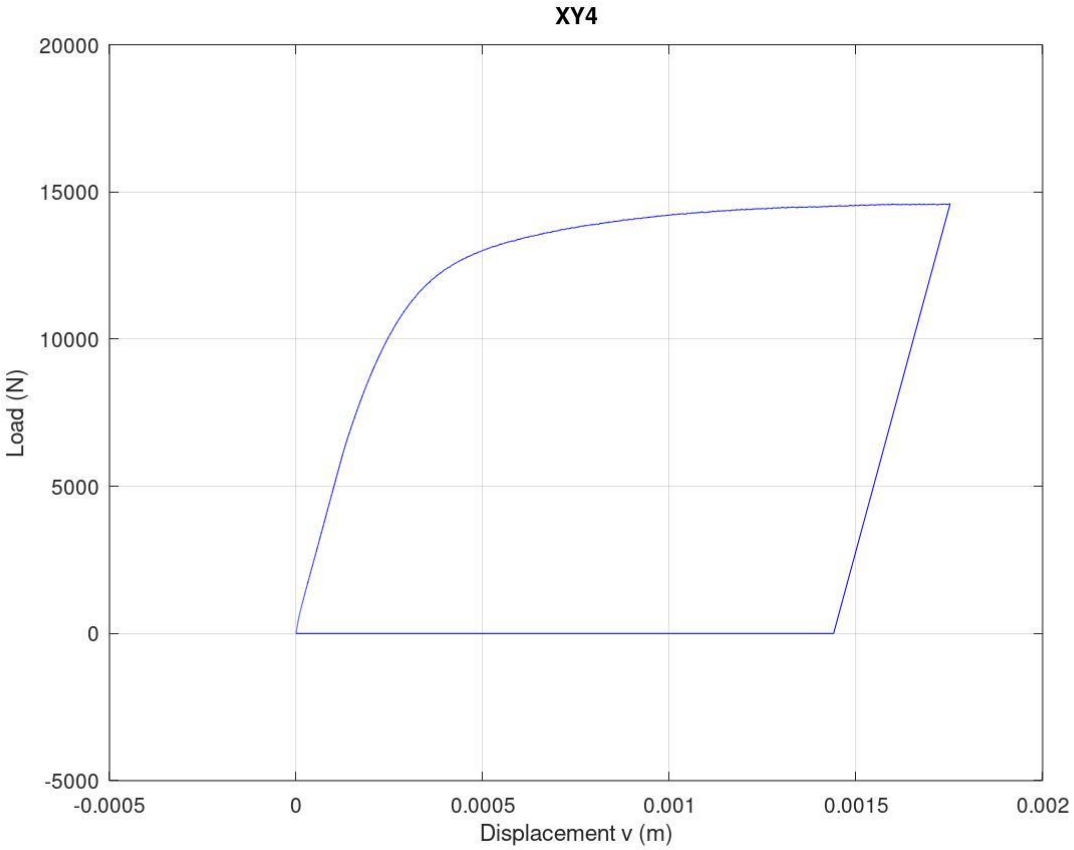
XY4
20000
15000
10000
5000
0
-5000
Load (N)
-0.0005
0
0.0005
0.001
0.0015
0.002
Displacement v (m)

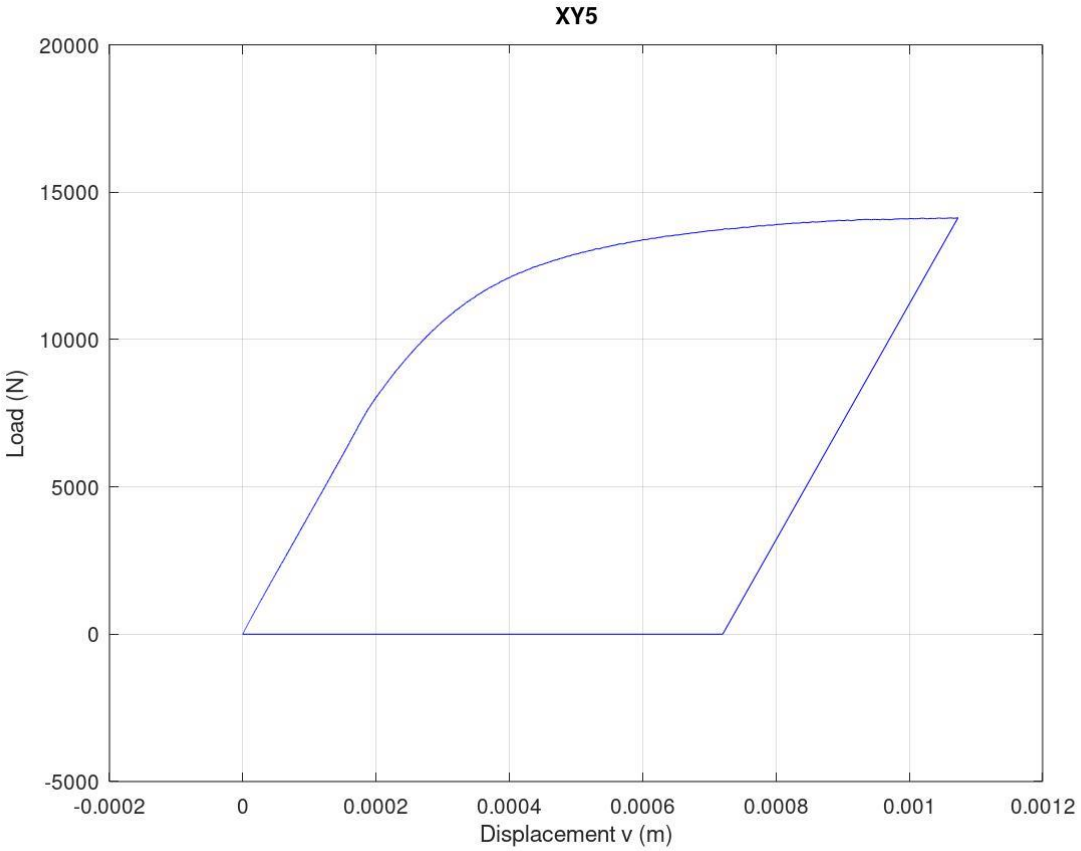
XY5
20000
15000
10000
5000
0
-5000
Load (N)
-0.0002
0
0.0002
0.0004
0.0006
0.0008
0.001
0.0012
Displacement v (m)

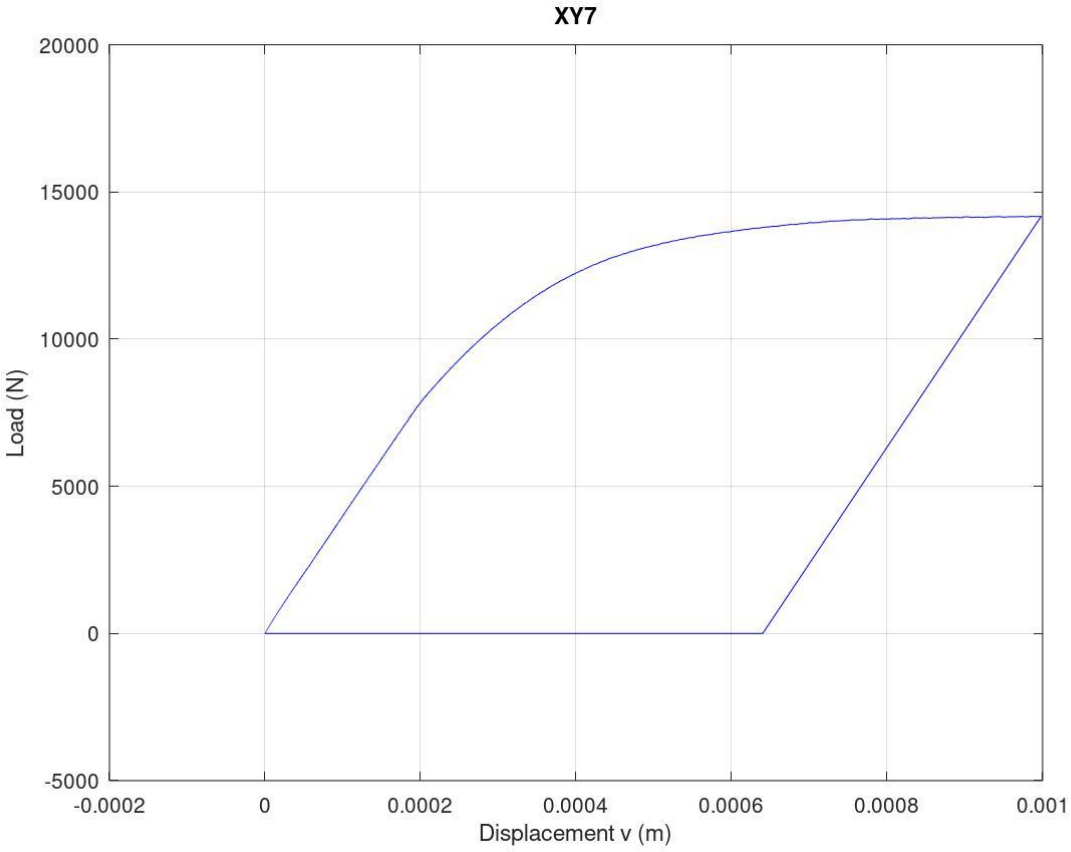
XY7
20000
15000
10000
5000
0
-5000
Load (N)
-0.0002
0
0.0002
0.0004
0.0006
0.0008
0.001
Displacement v (m)

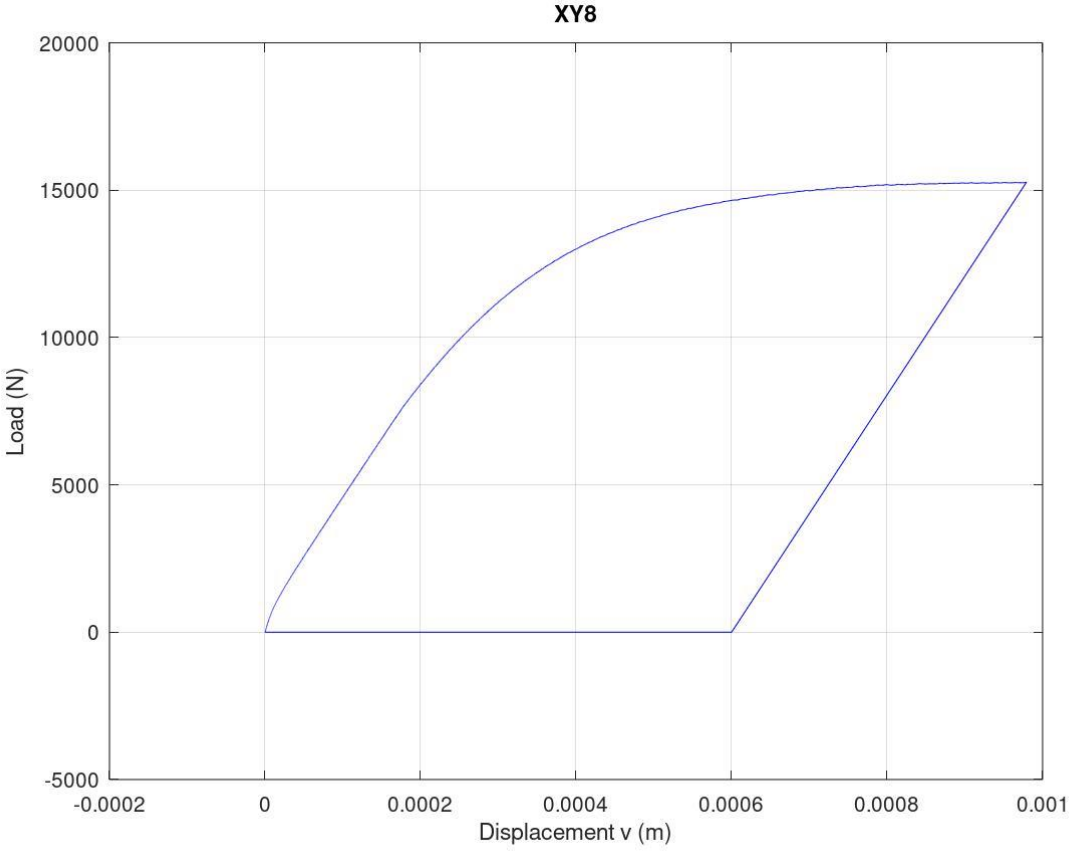
XY8
20000
15000
10000
5000
0
-5000
Load (N)
-0.0002
0
0.0002
0.0004
0.0006
0.0008
0.001
Displacement v (m)

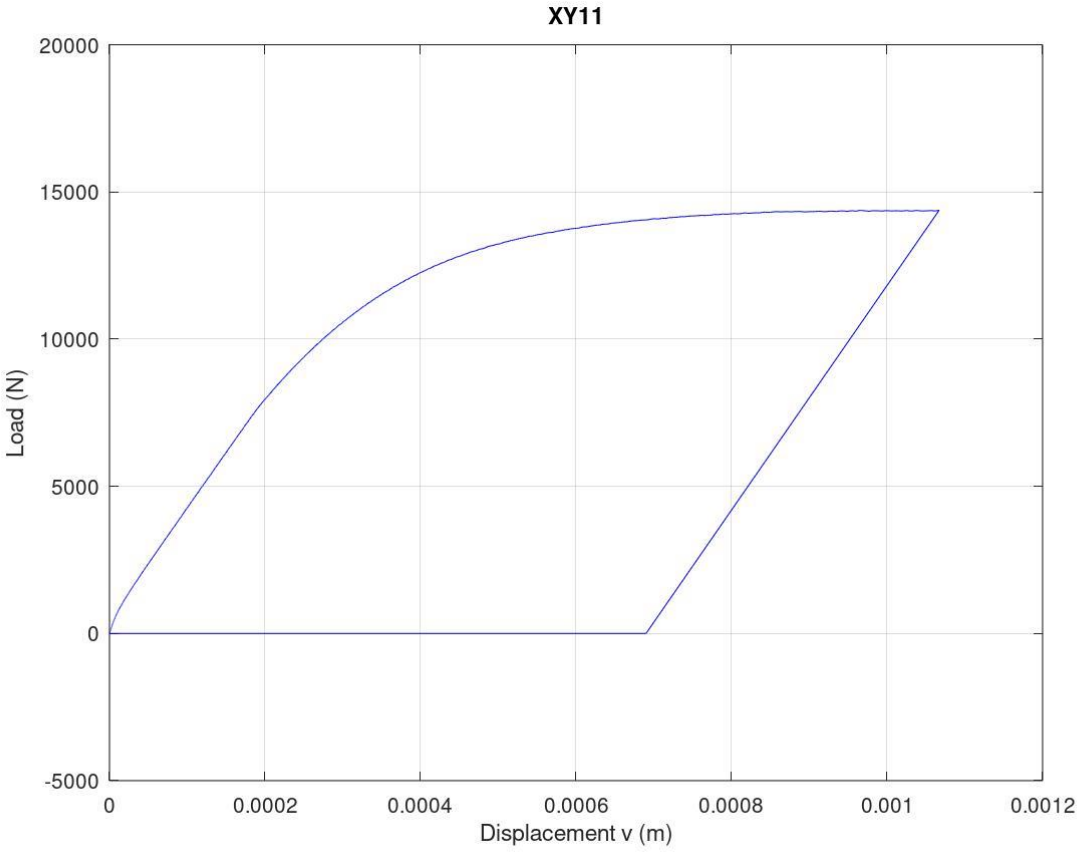
XY11
20000
15000
10000
5000
0
-5000
Load (N)
0
0.0002
0.0004
0.0006
0.0008
0.001
0.0012
Displacement v (m)

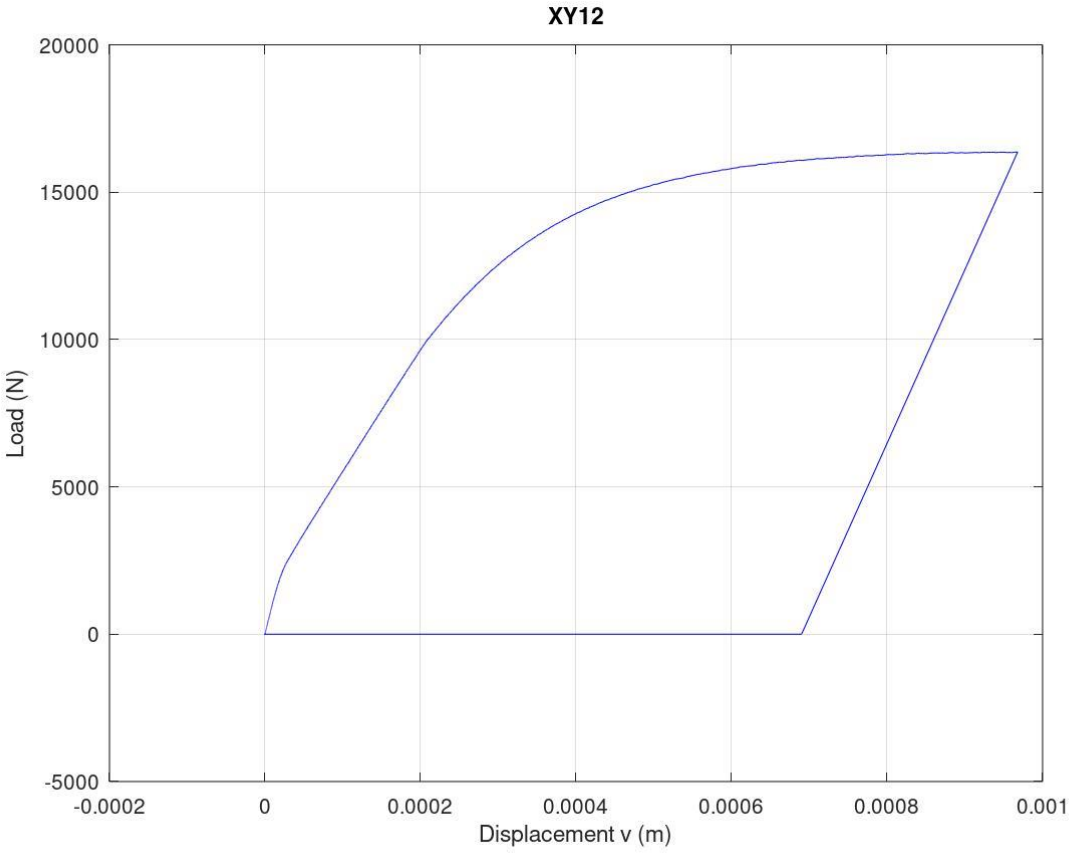
XY12
20000
15000
10000
5000
0
-5000
Load (N)
-0.0002
0
0.0002
0.0004
0.0006
0.0008
0.001
Displacement v (m)

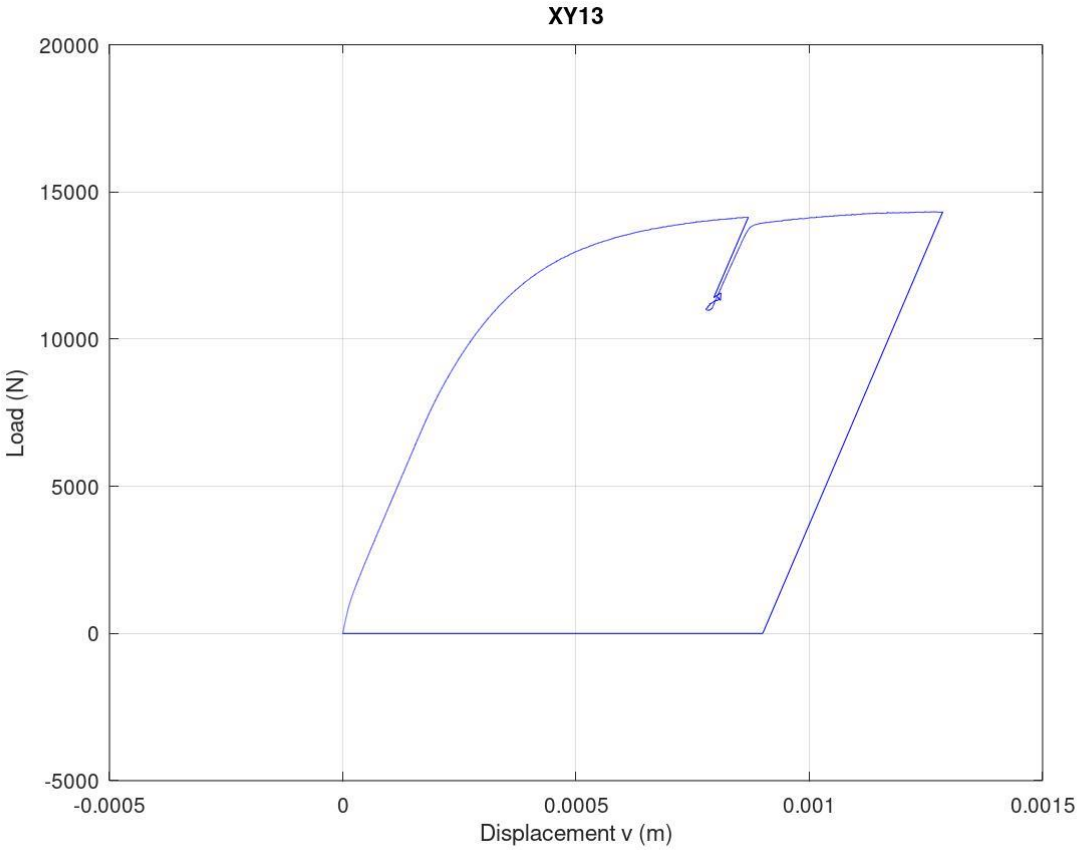
XY13
20000
15000
10000
5000
0
-5000
Load (N)
-0.0005
0
0.0005
0.001
0.0015
Displacement v (m)

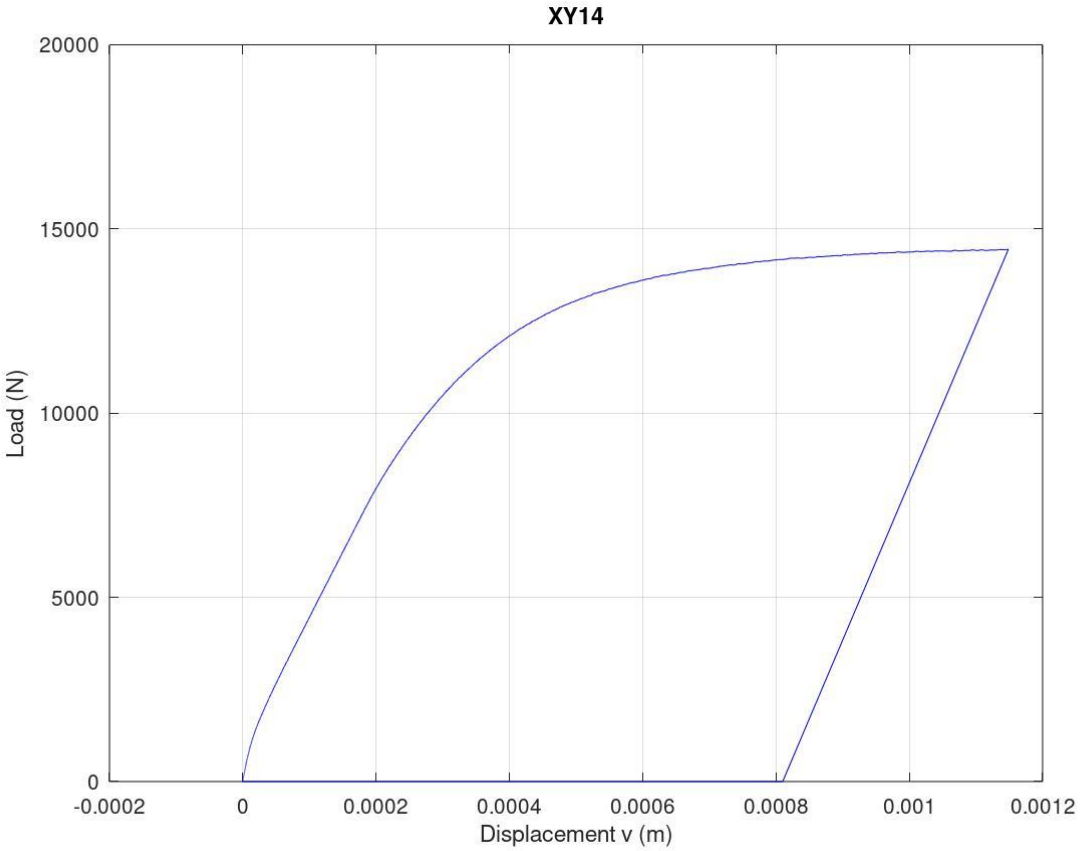
XY14
20000
15000
10000
5000
0
Load (N)
-0.0002
0
0.0002
0.0004
0.0006
0.0008
0.001
0.0012
Displacement v (m)

11.6.2. XZ orientation

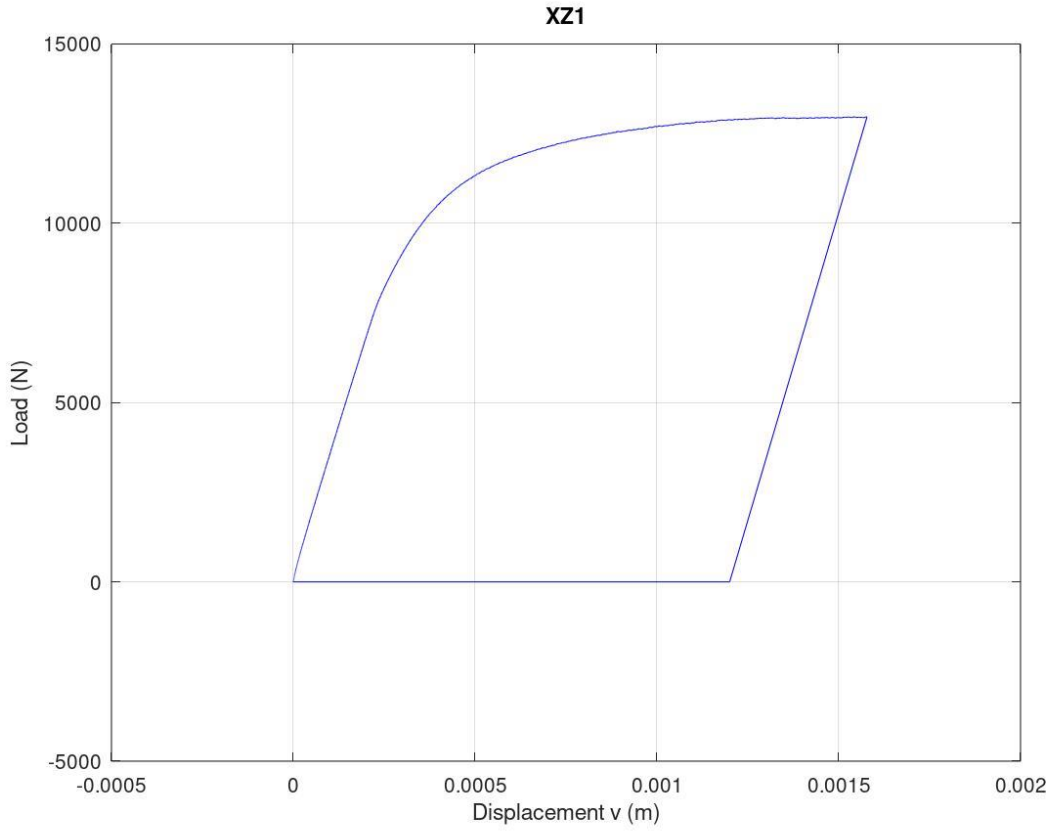

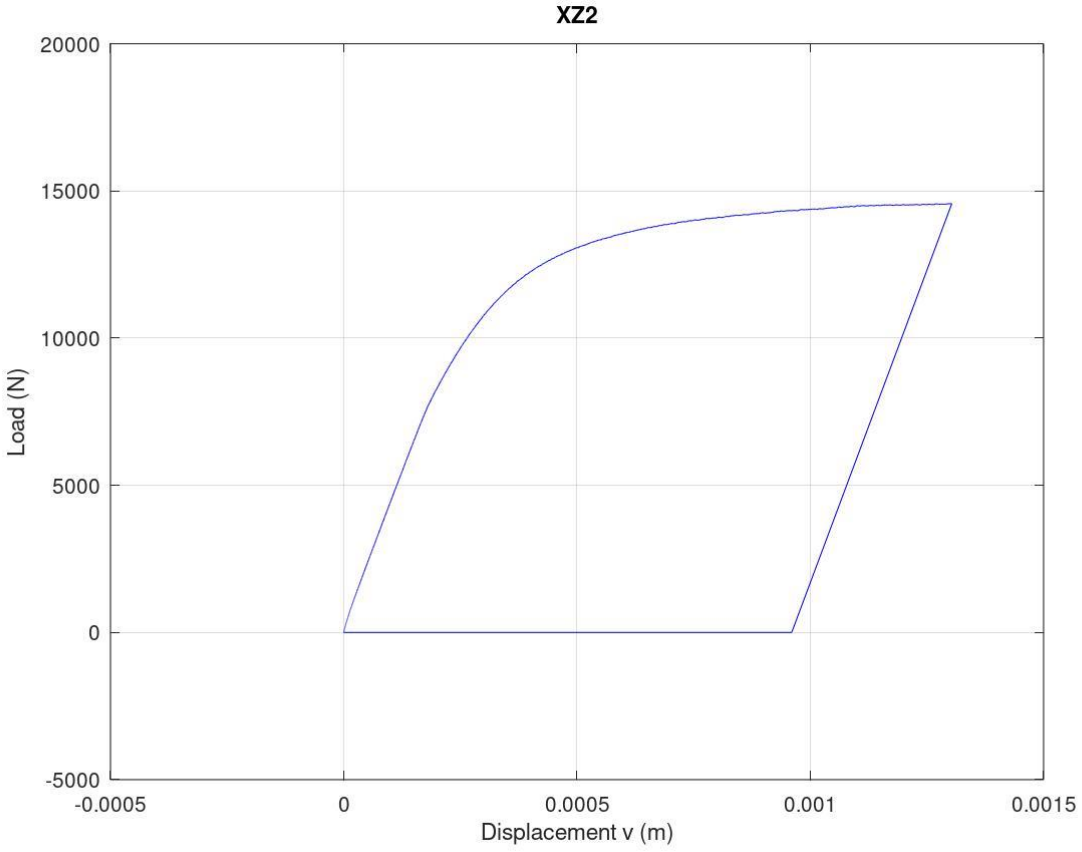

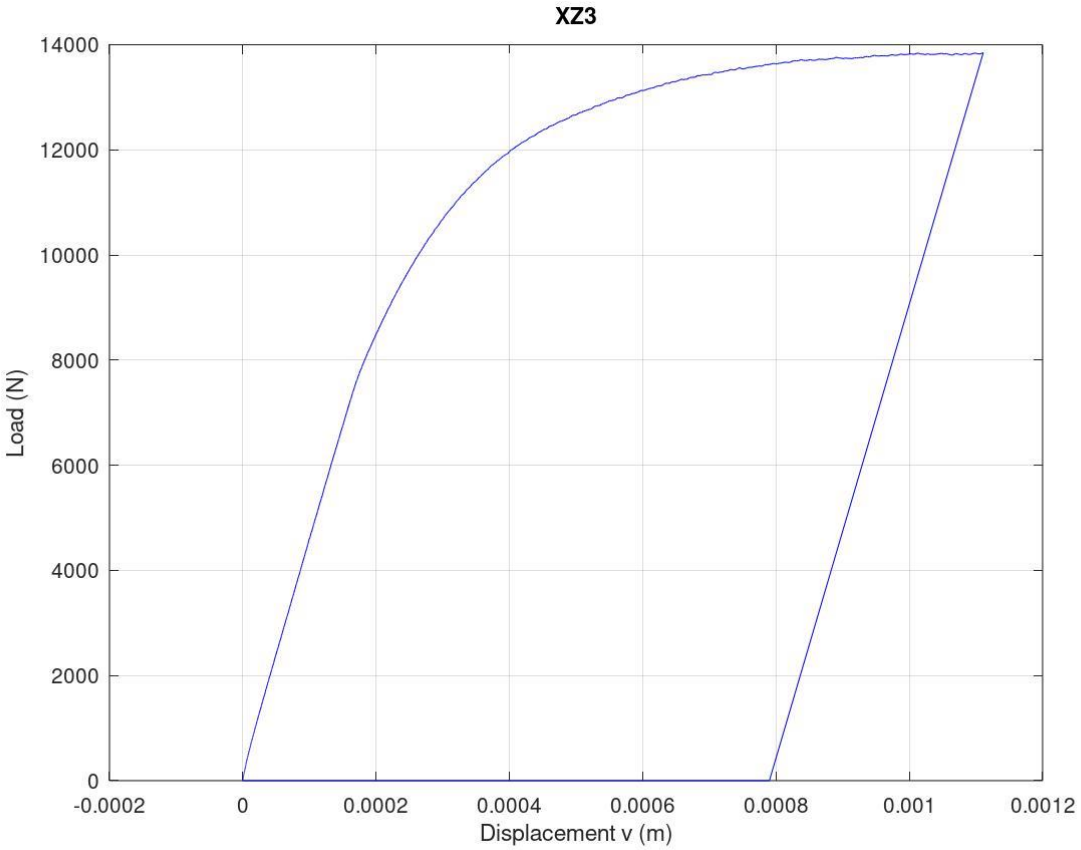
XZ3
14000
12000
10000
8000
6000
4000
2000
0
Load (N)
-0.0002
0
0.0002
0.0004
0.0006
0.0008
0.001
0.0012
Displacement v (m)

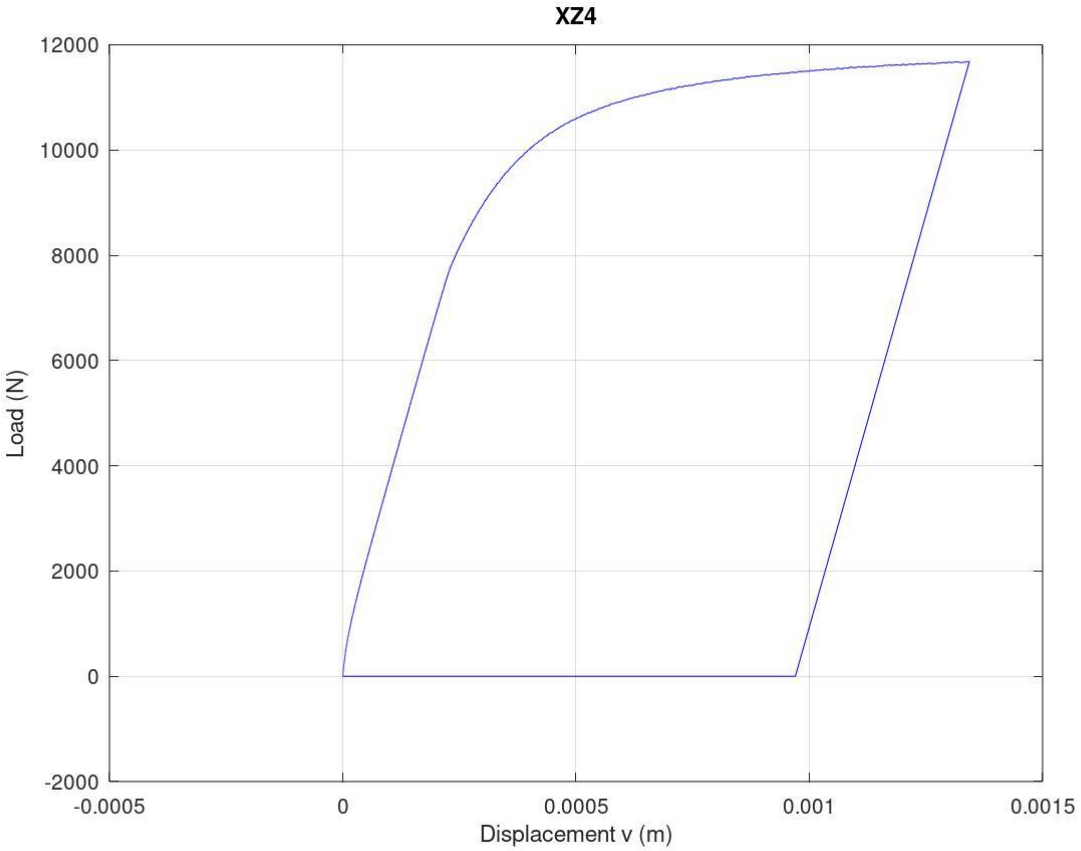
XZ4
12000
10000
8000
6000
4000
2000
0
-2000
Load (N)
-0.0005
0
0.0005
0.001
0.0015
Displacement v (m)

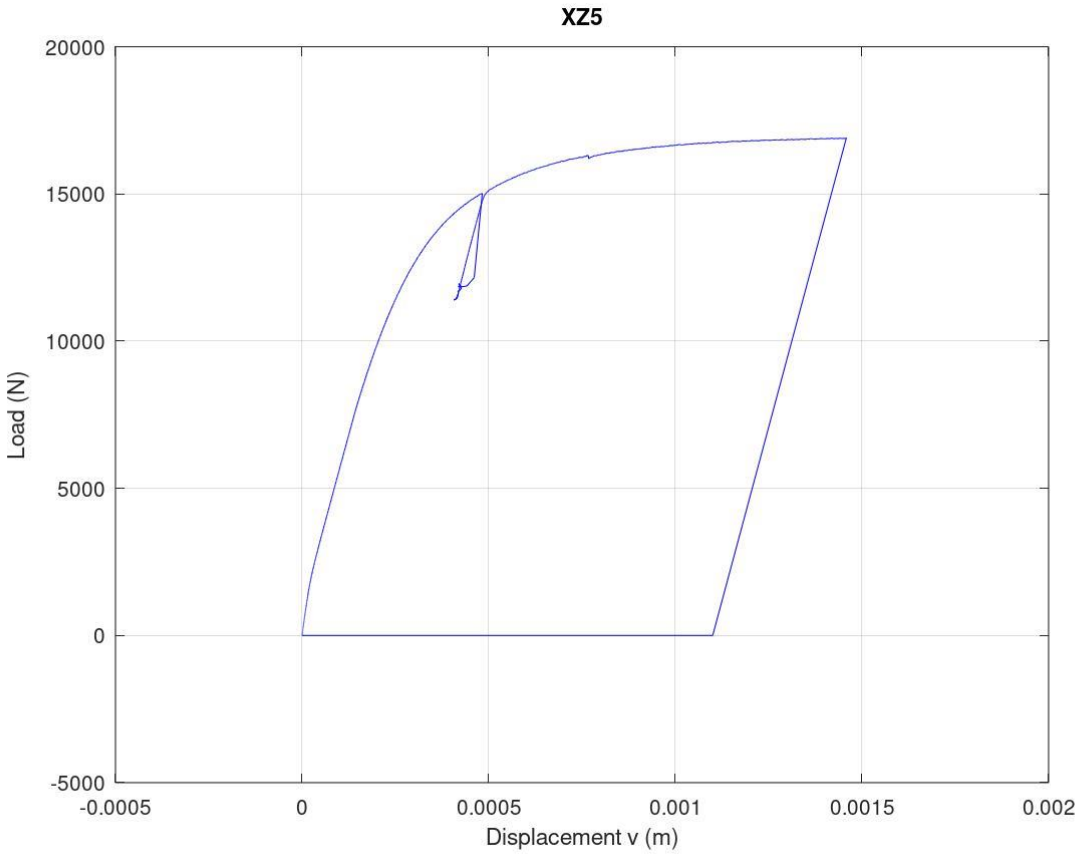
XZ5
20000
15000
10000
5000
0
-5000
Load (N)
-0.0005
0
0.0005
0.001
0.0015
0.002
Displacement v (m)

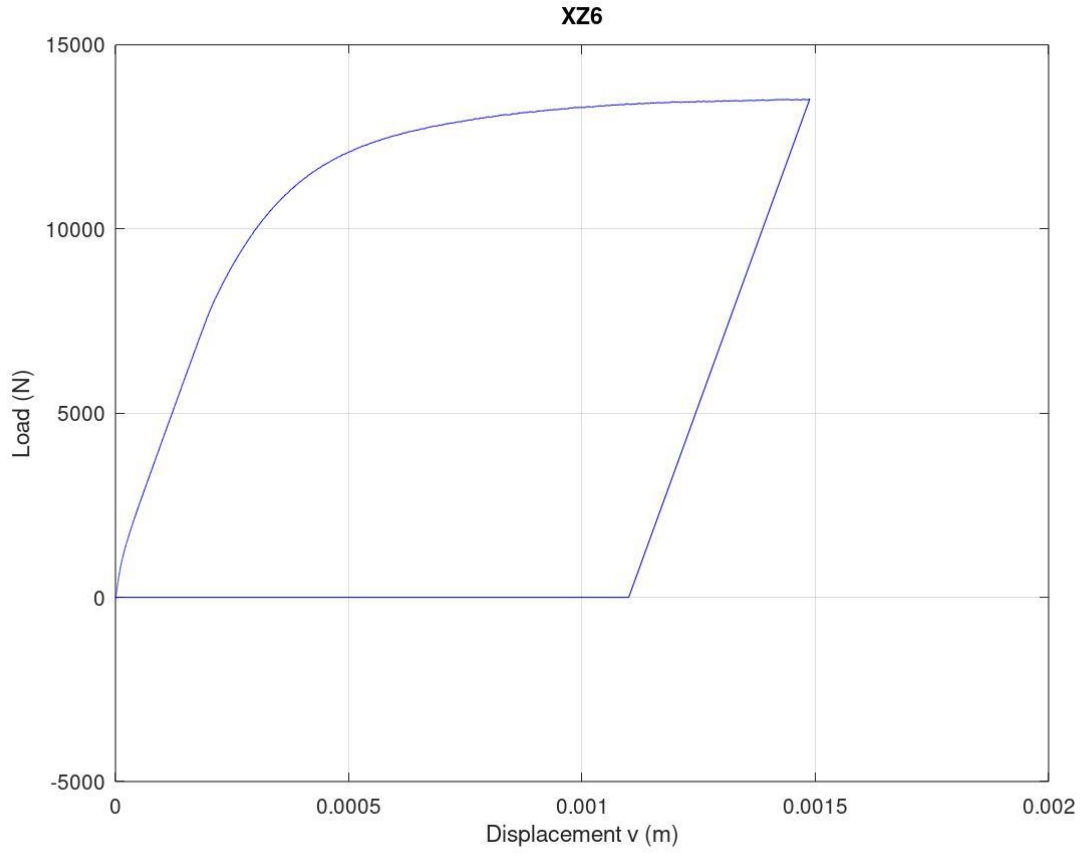
XZ6
15000
10000
5000
0
-5000
Load (N)
0
0.0005
0.001
0.0015
0.002
Displacement v (m)

11.6.3. ZX orientation

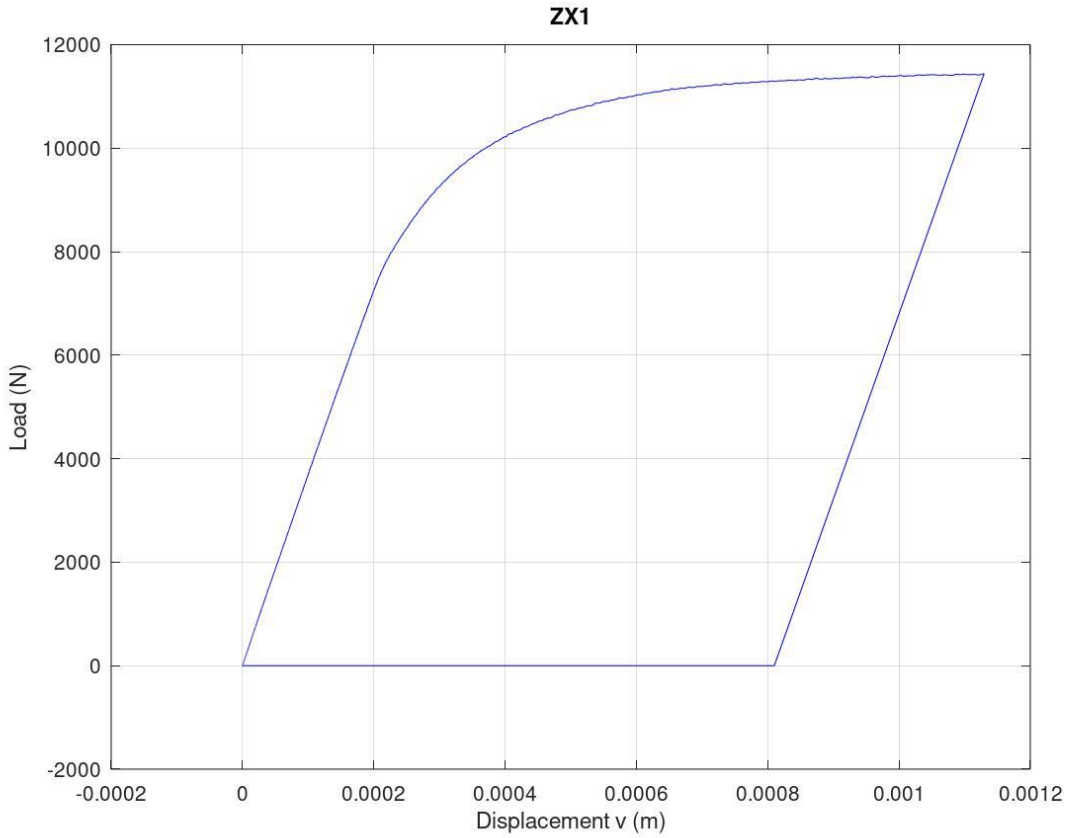

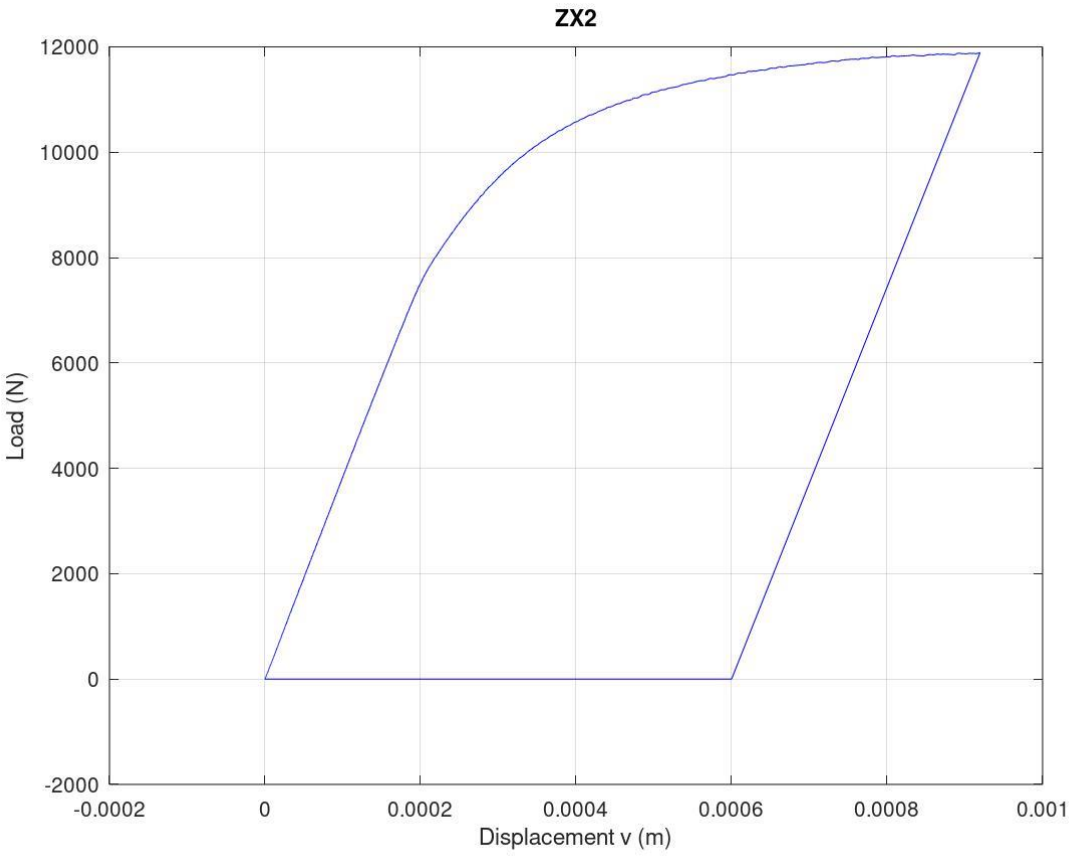

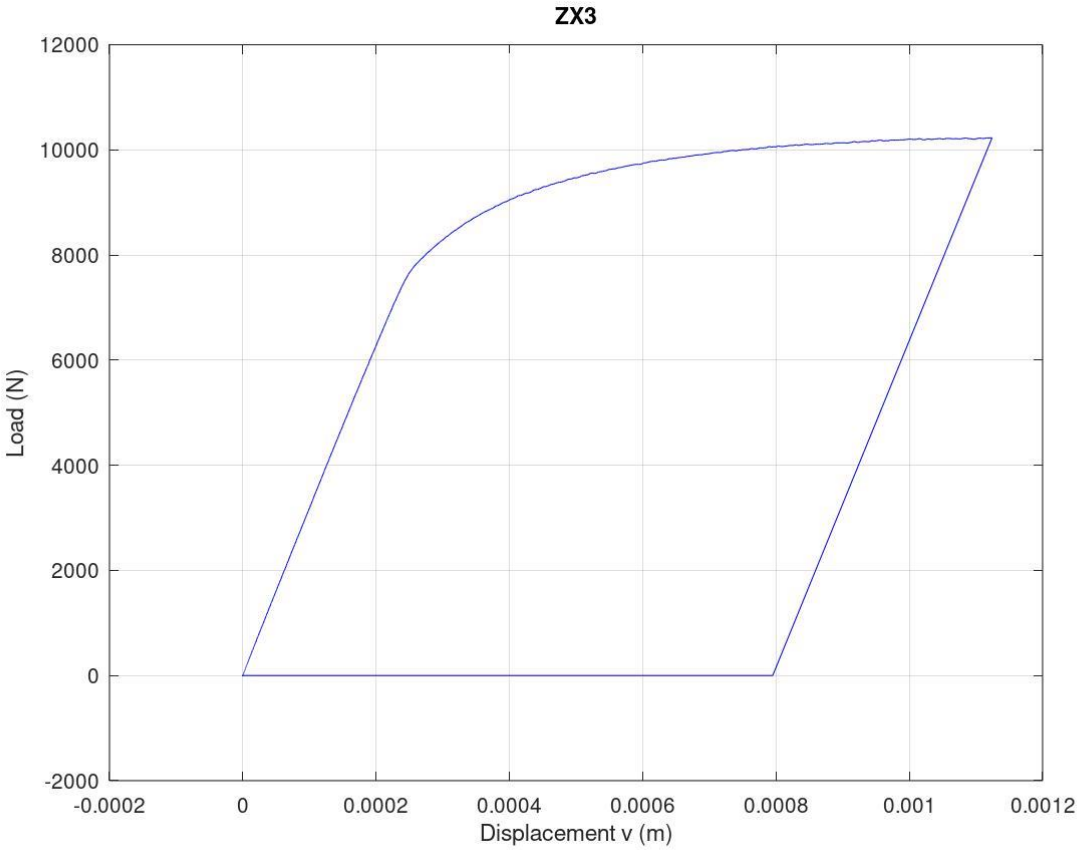
ZX3
12000
10000
8000
6000
4000
2000
0
-2000
Load (N)
-0.0002
0
0.0002
0.0004
0.0006
0.0008
0.001
0.0012
Displacement v (m)

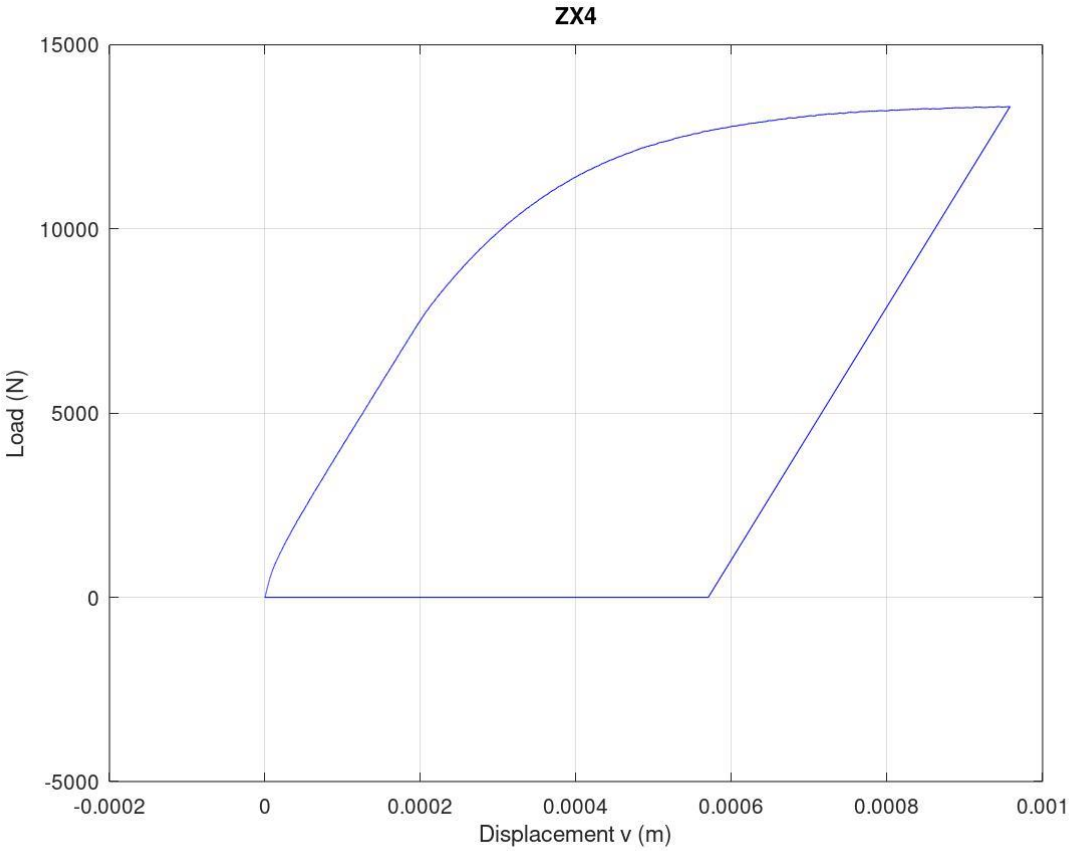
ZX4
15000
10000
5000
0
-5000
Load (N)
-0.0002
0
0.0002
0.0004
0.0006
0.0008
0.001
Displacement v (m)

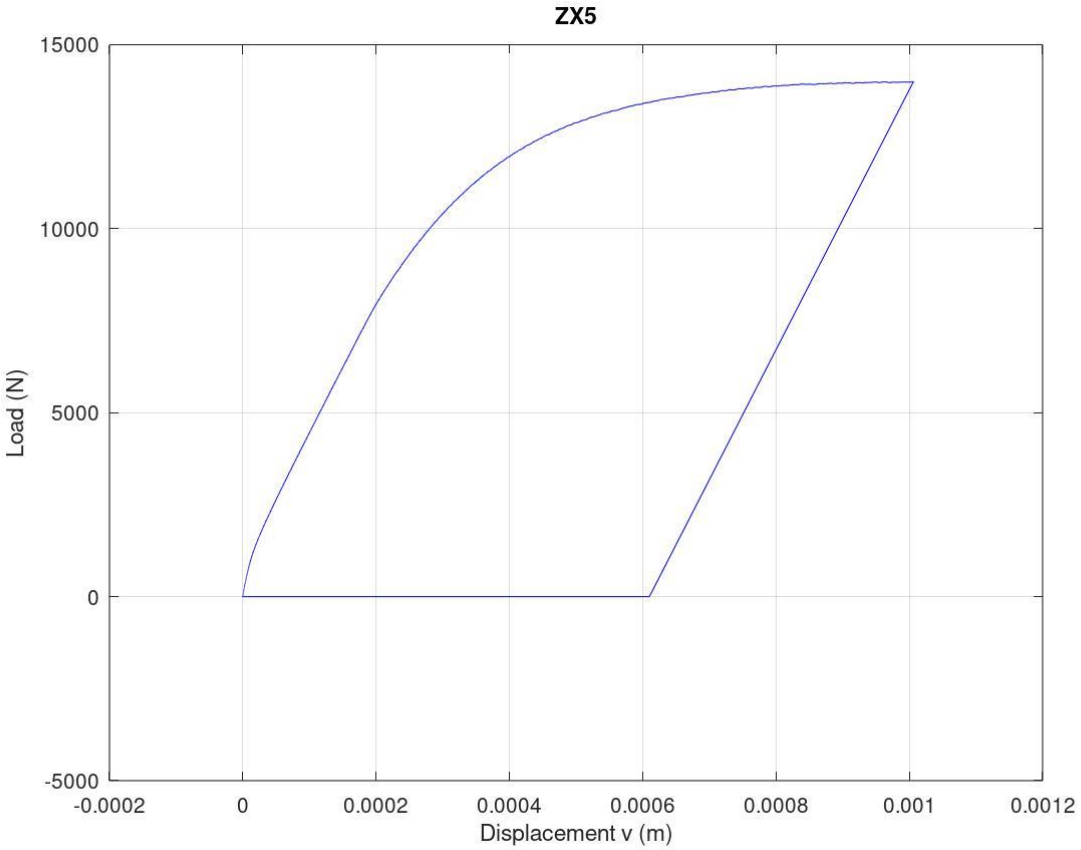
ZX5
15000
10000
5000
0
-5000
Load (N)
-0.0002
0
0.0002
0.0004
0.0006
0.0008
0.001
0.0012
Displacement v (m)

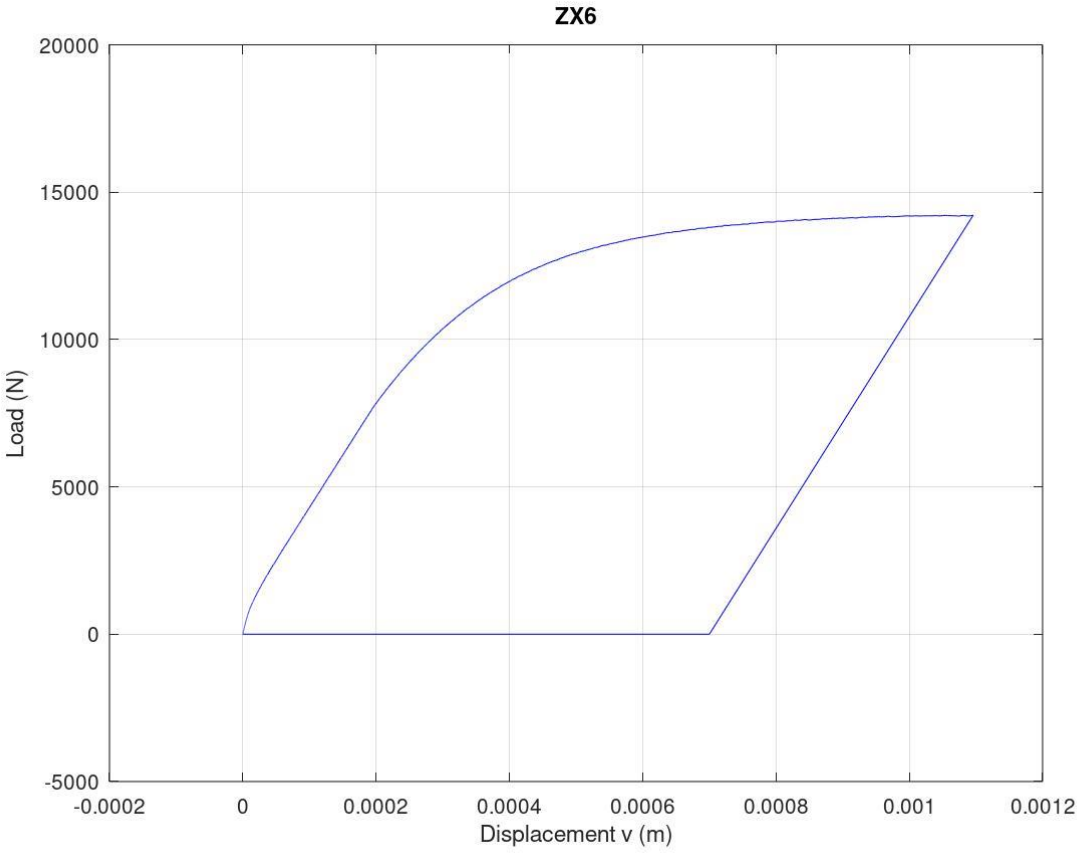
ZX6
20000
15000
10000
5000
0
-5000
Load (N)
-0.0002
0
0.0002
0.0004
0.0006
0.0008
0.001
0.0012
Displacement v (m)

11.7. Specimen measurements for fracture toughness tests

Each of the pictures taken after fracture toughness testing for crack length measurement are shown in this section.

11.7.1. XY orientation

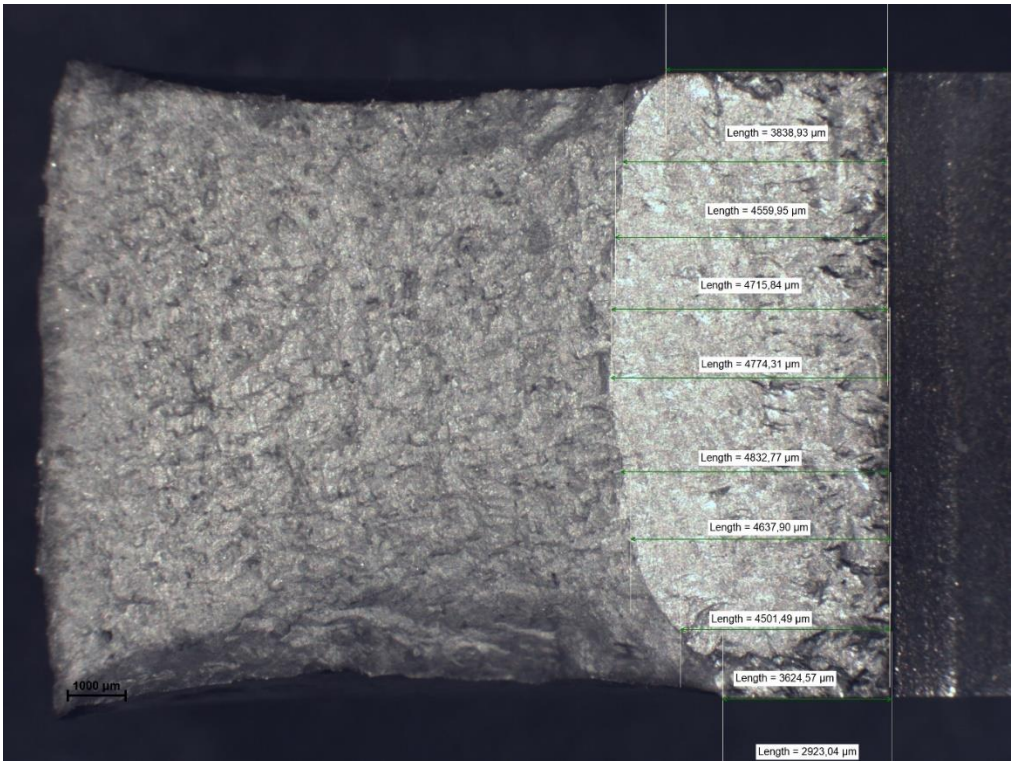

Figure 11.58: XY1 crack measurements

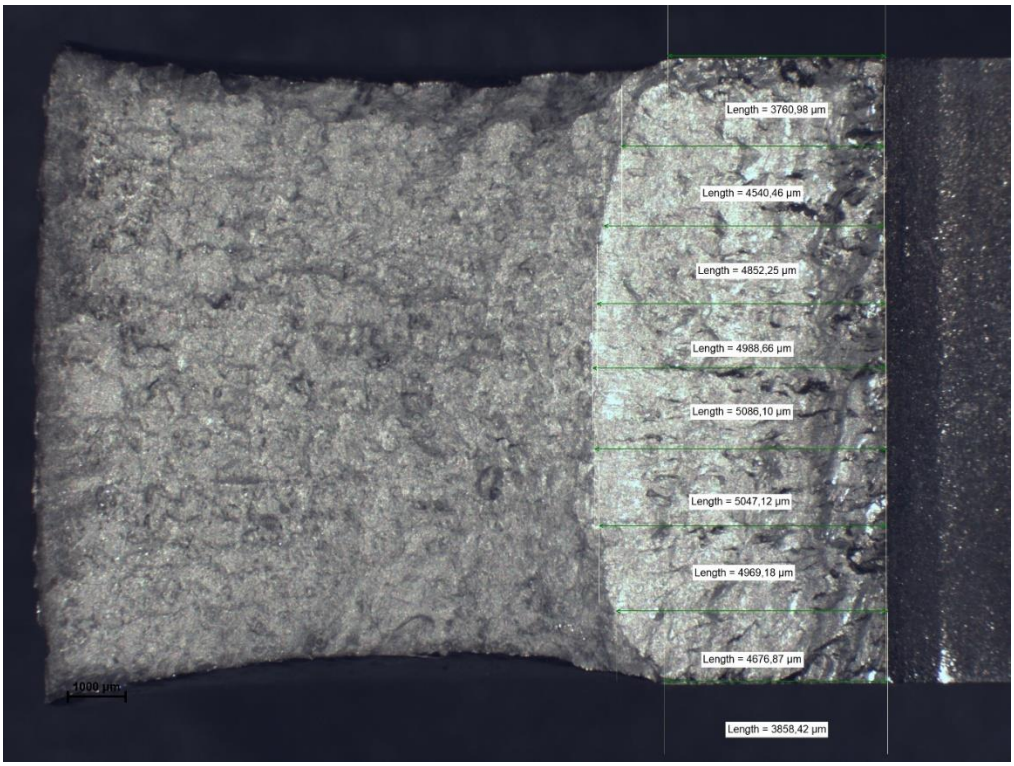

Figure 11.59: XY2 crack measurements

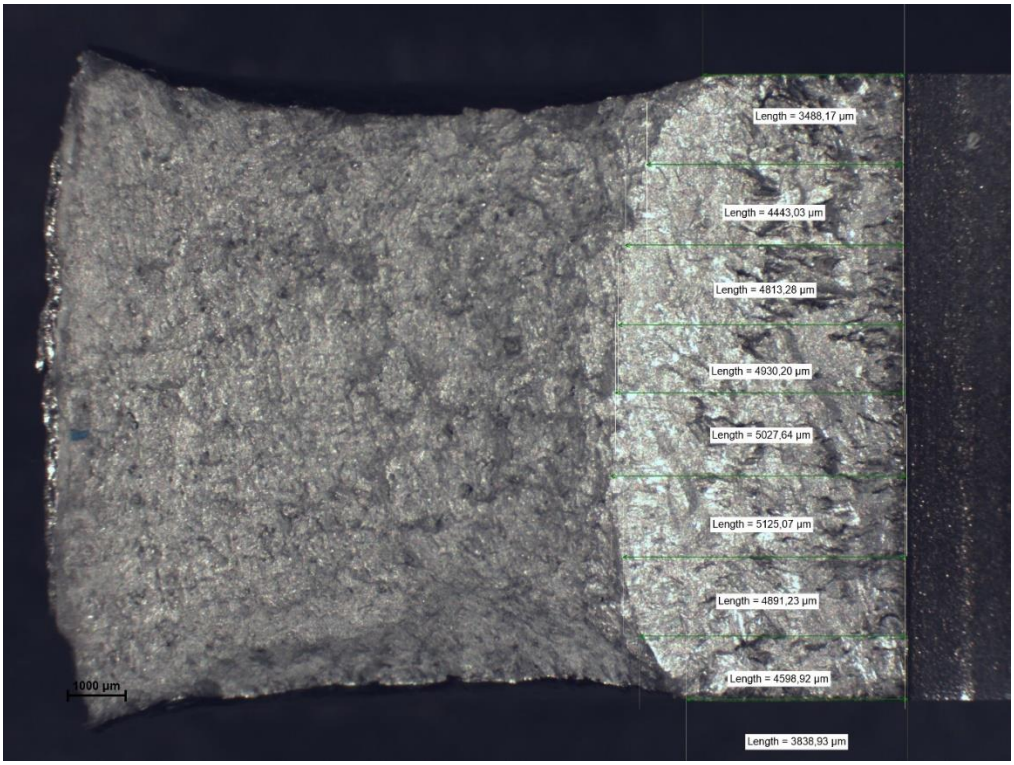

Figure 11.60: XY4 crack measurements

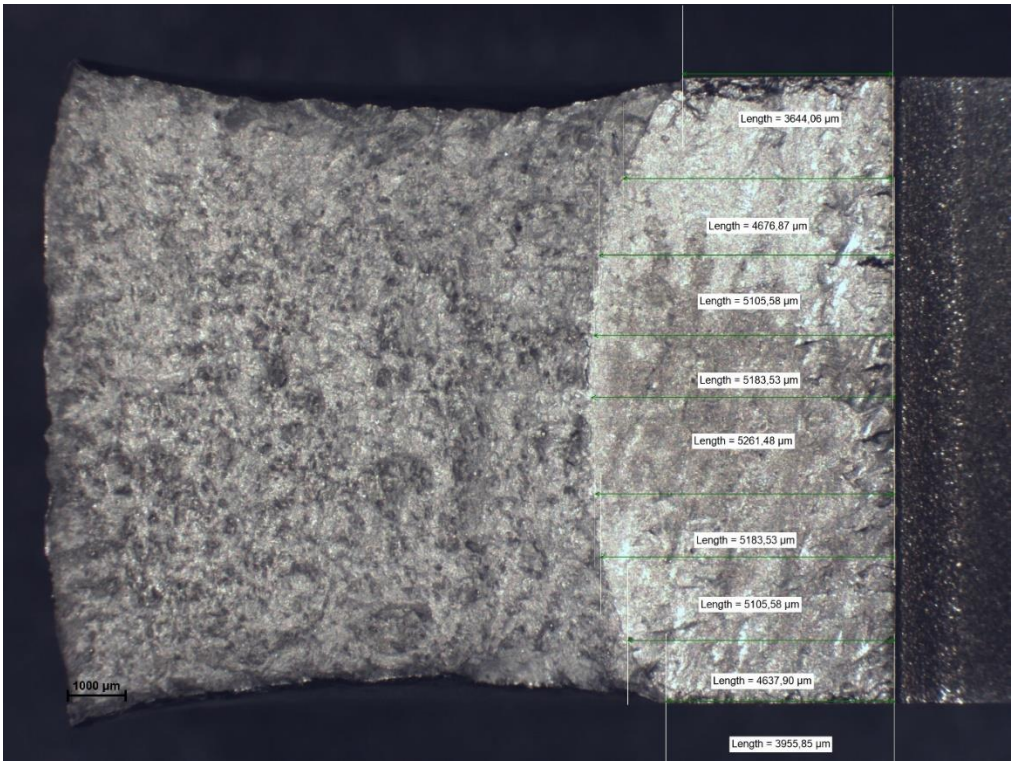

Figure 11.61: XY5 crack measurements

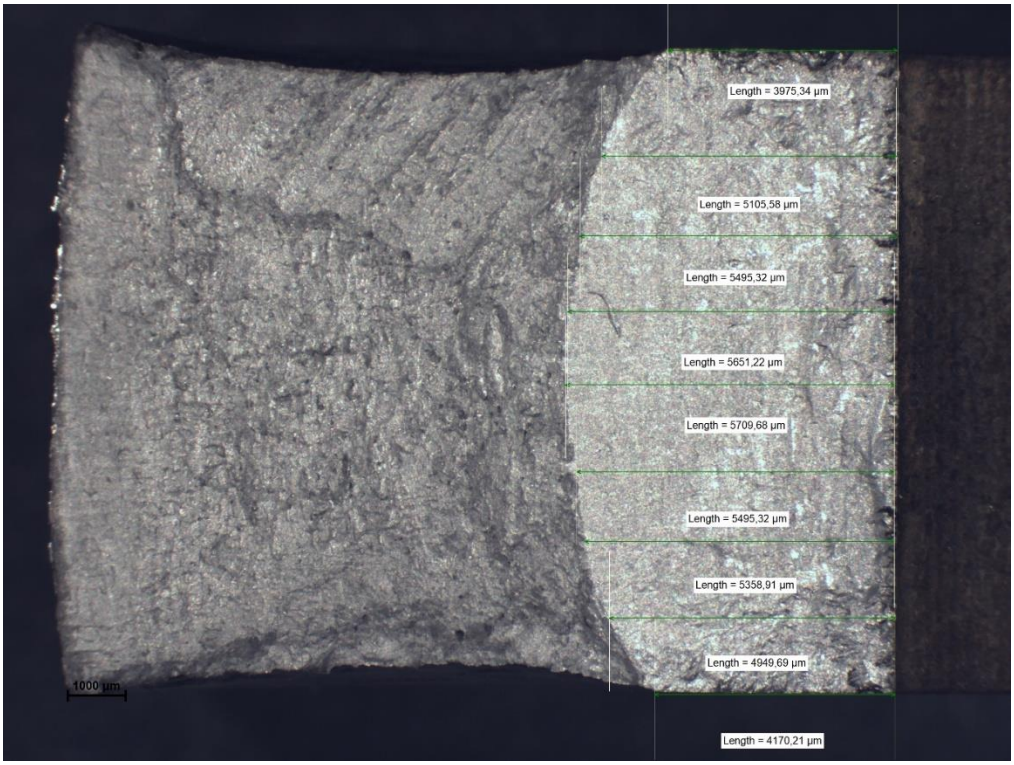

Figure 11.62: XY7 crack measurements

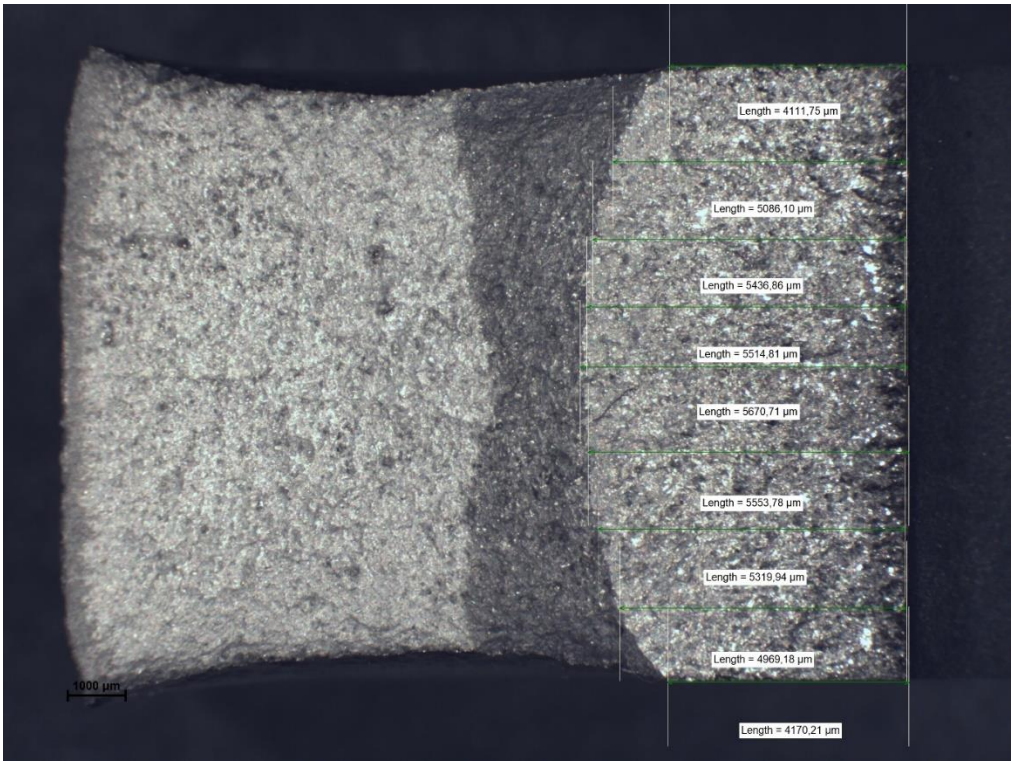

Figure 11.63: XY8 crack measurements

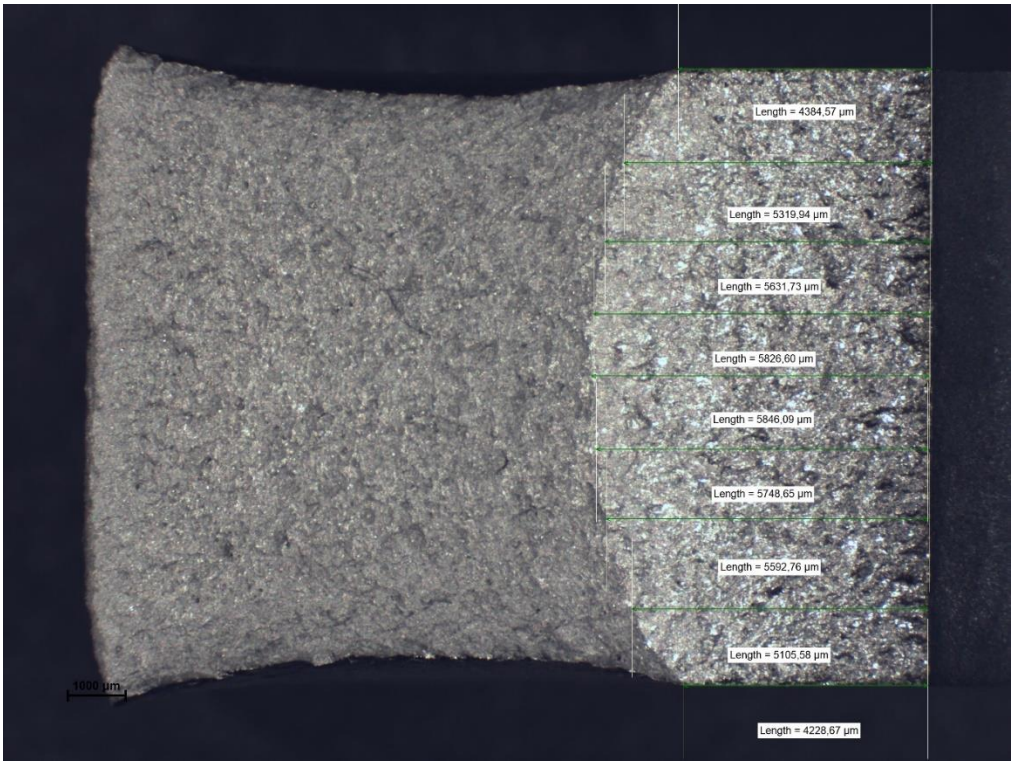

Figure 11.64: XY11 crack measurements

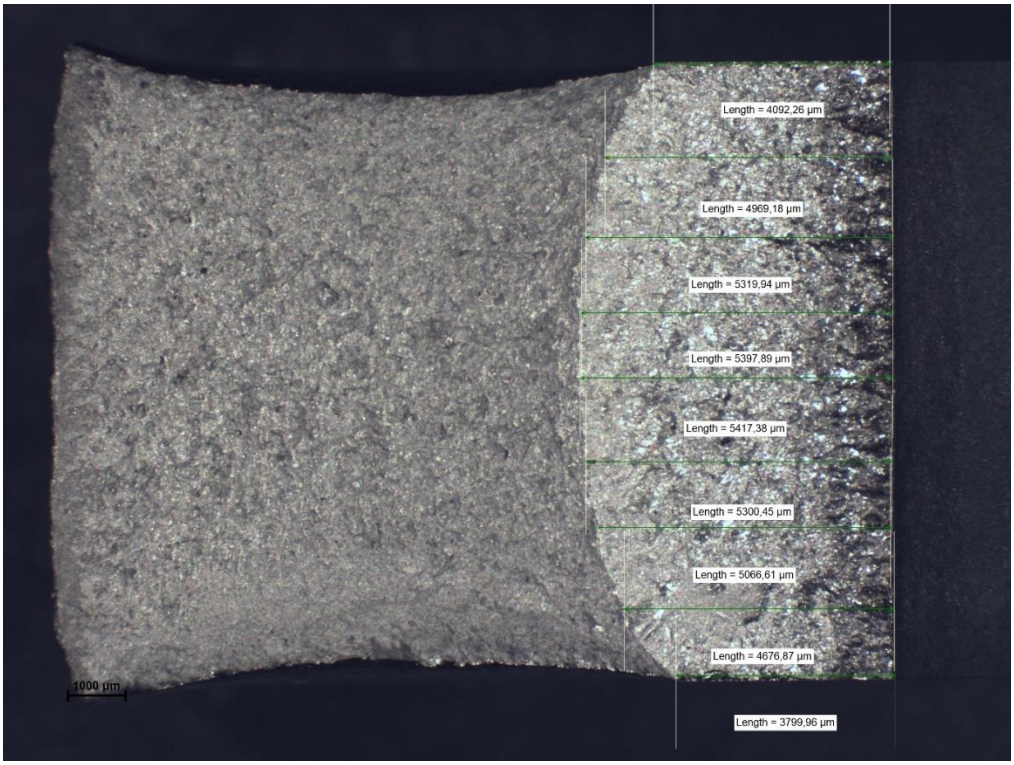

Figure 11.65: XY12 crack measurements

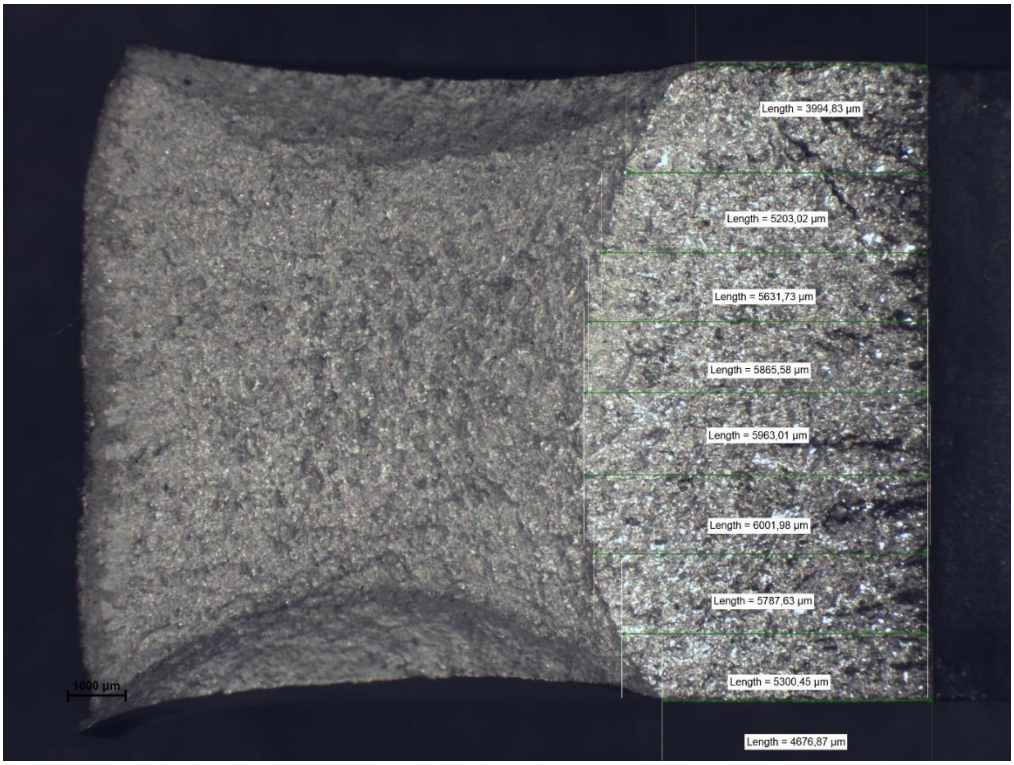

Figure 11.66: XY13 crack measurements

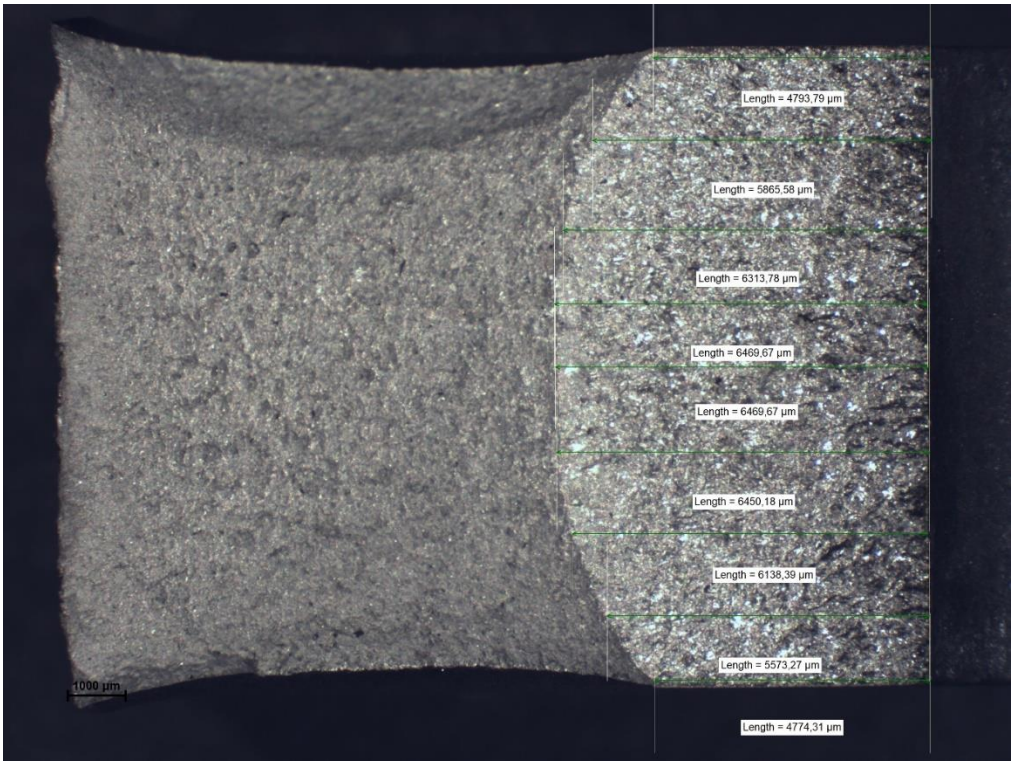

Figure 11.67: XY14 crack measurements

11.7.2. XZ orientation

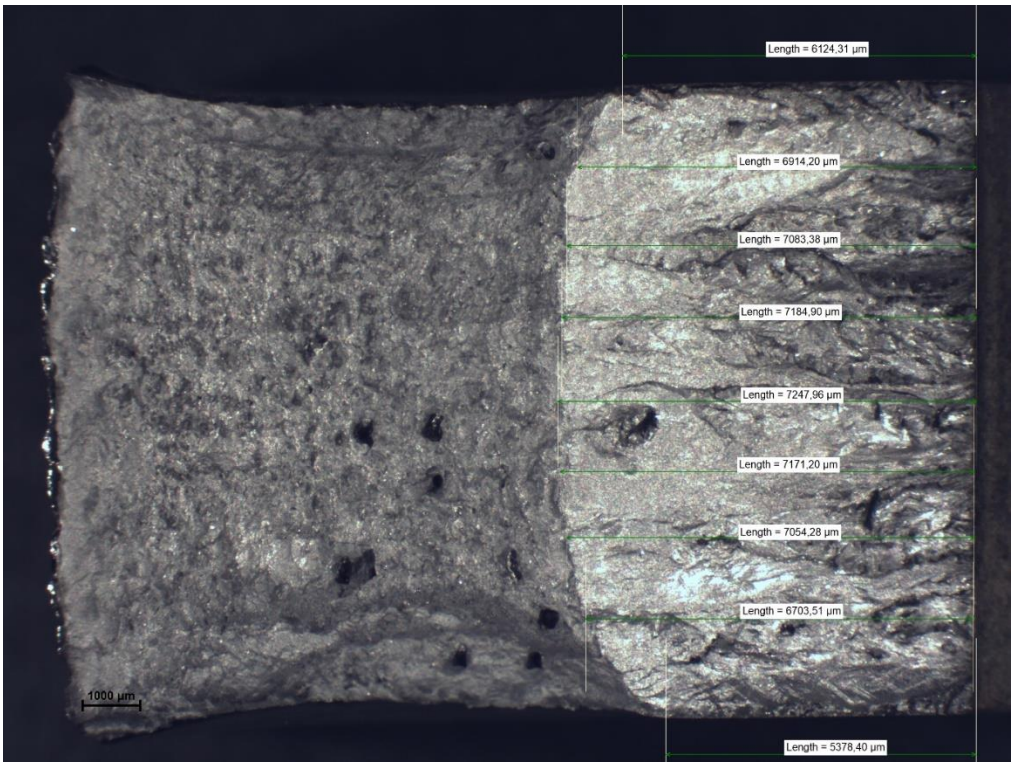

Figure 11.68: XZ1 crack measurements

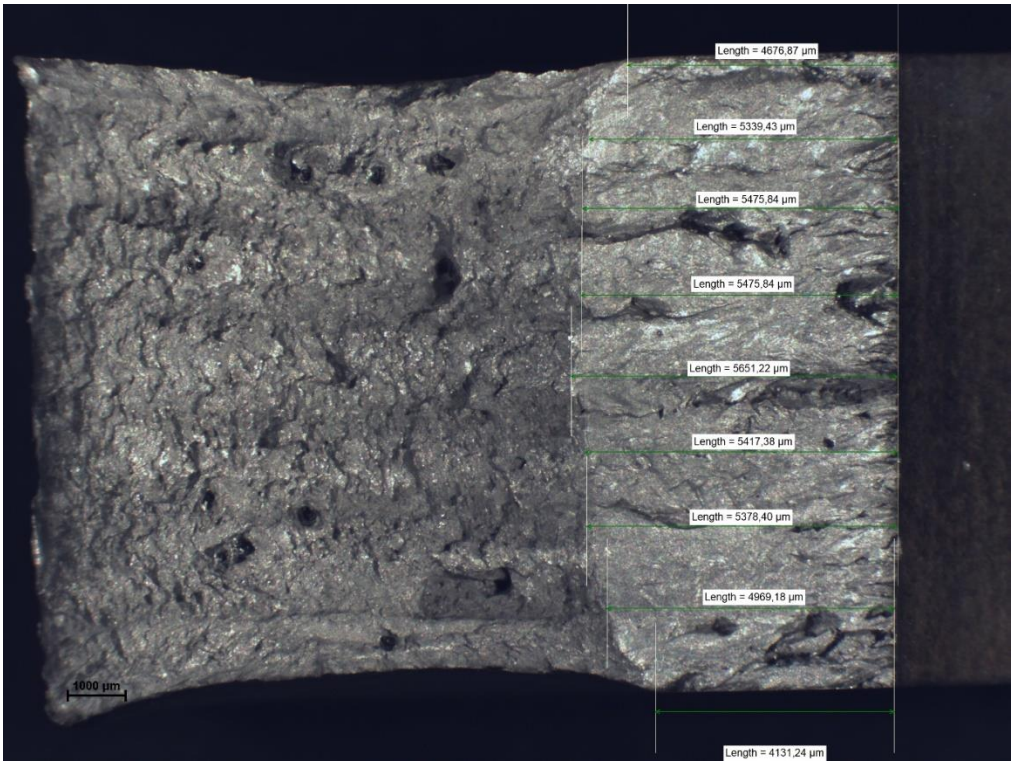

Figure 11.69: XZ2 crack measurements

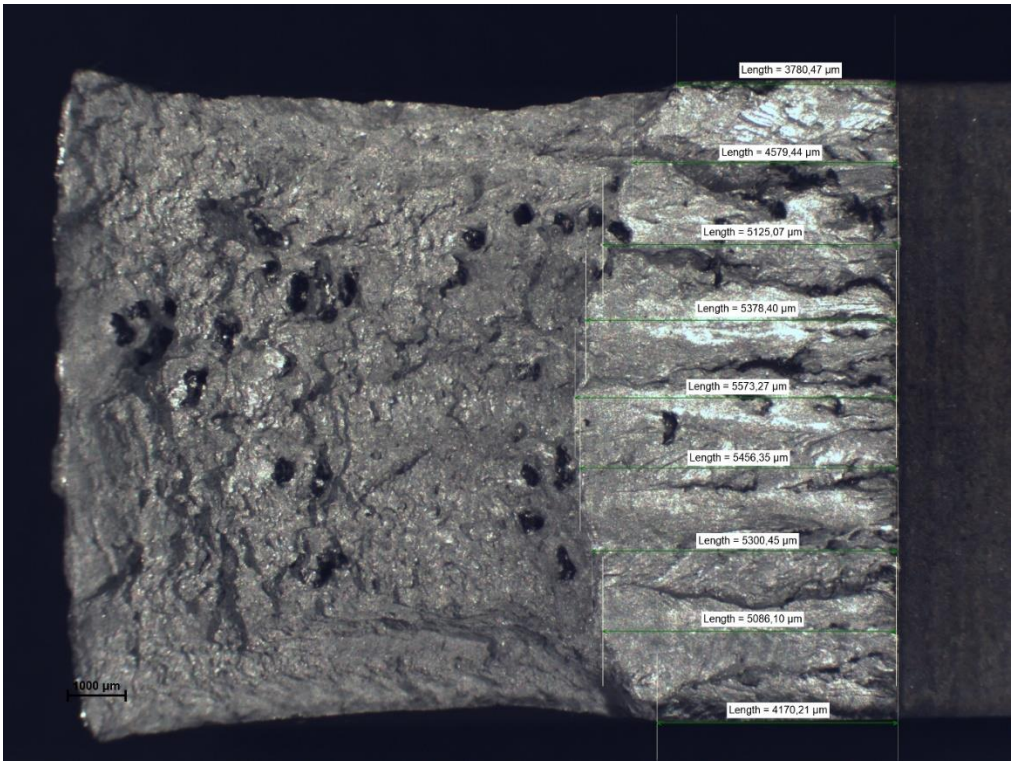

Figure 11.70: XZ3 crack measurements

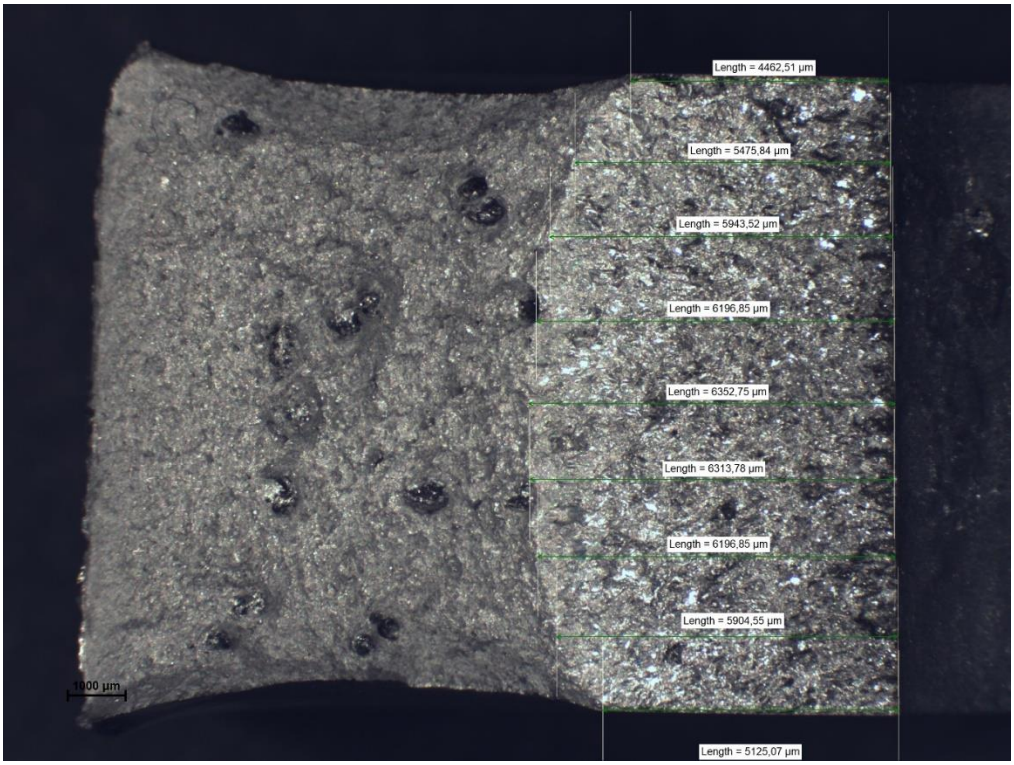

Figure 11.71: XZ4 crack measurements

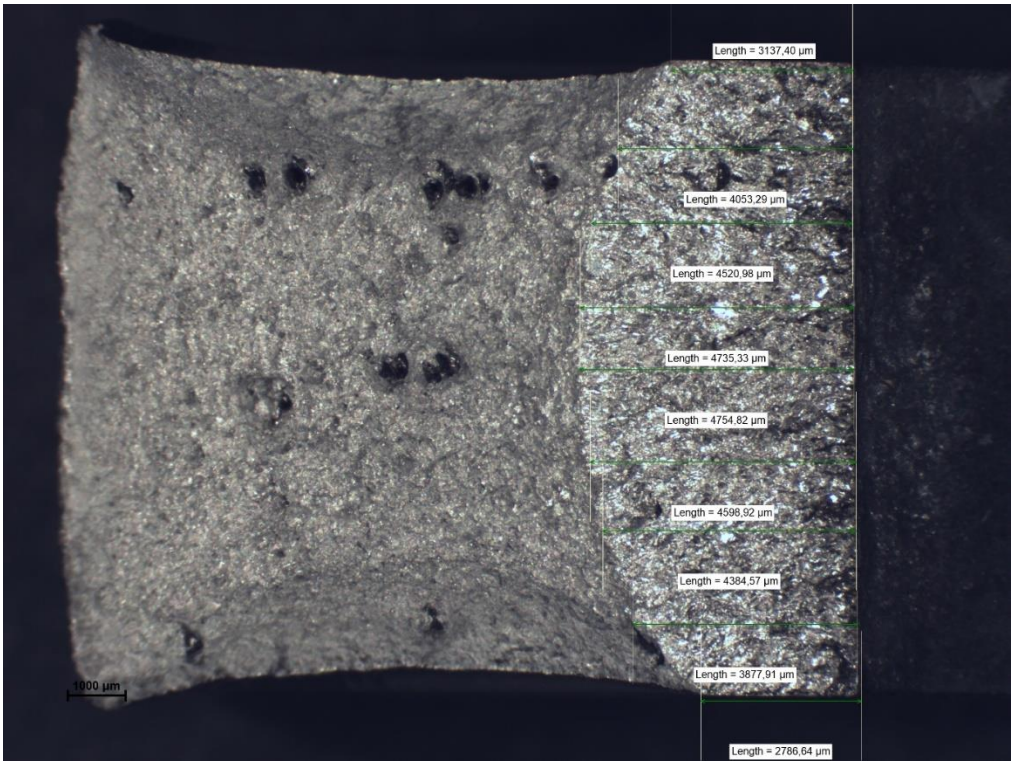

Figure 11.72: XZ5 crack measurements

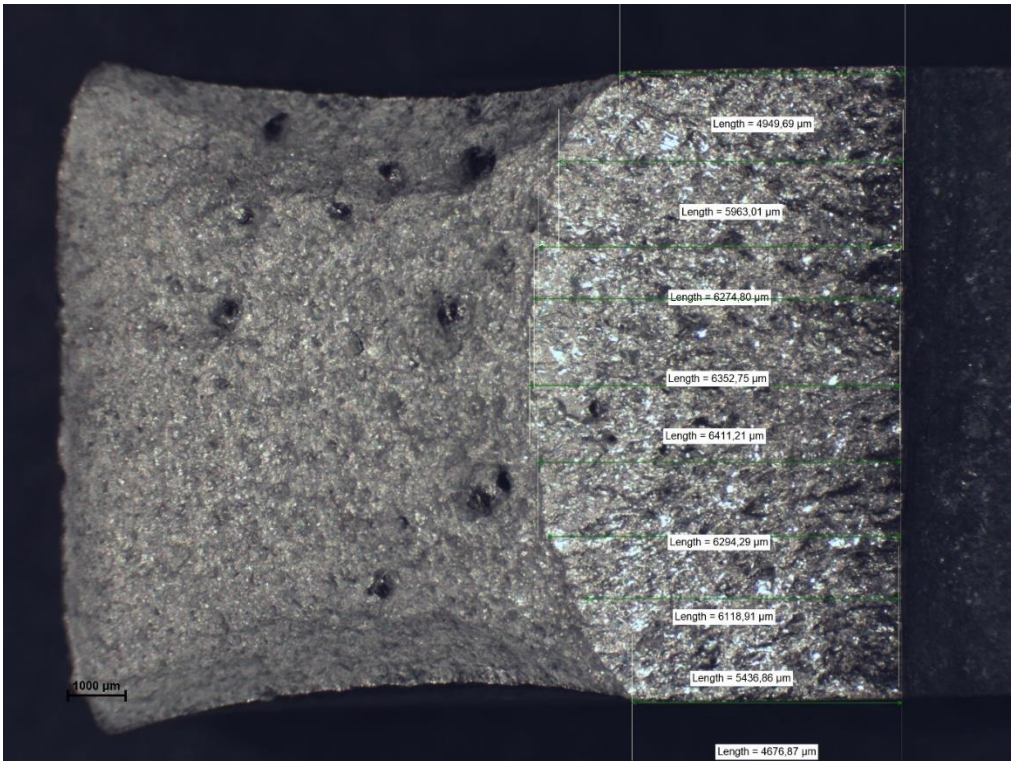

Figure 11.73: XZ6 crack measurements

11.7.3. ZX orientation measurements

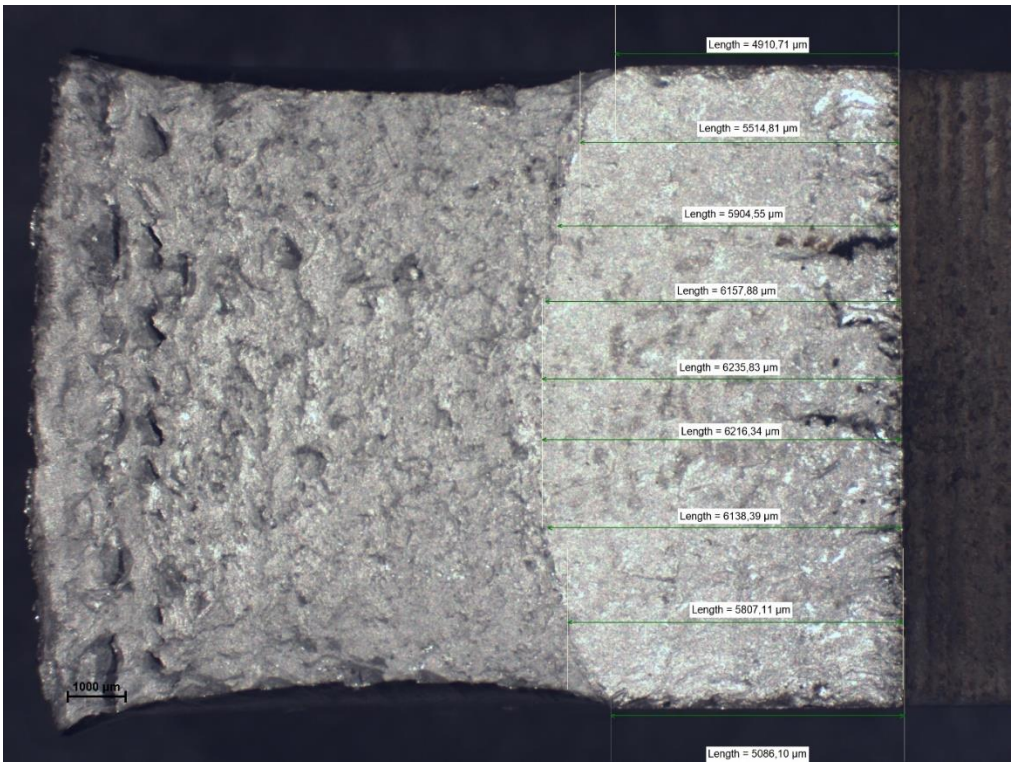

Figure 11.74: ZX1 crack measurements

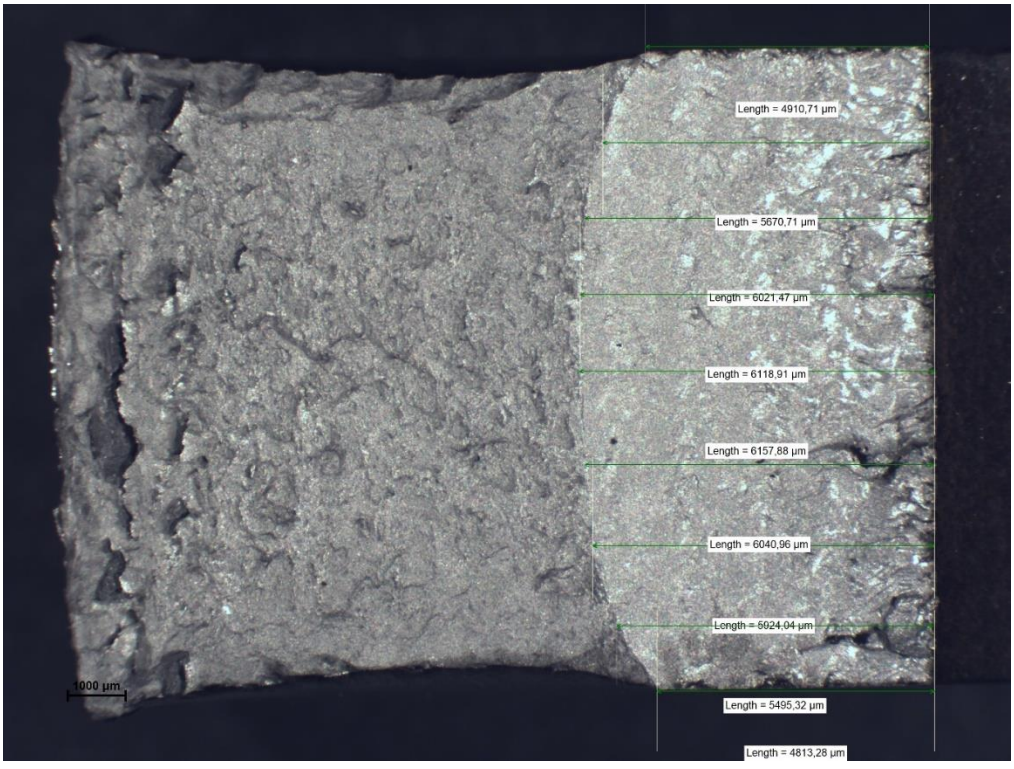

Figure 11.75: ZX2 crack measurements

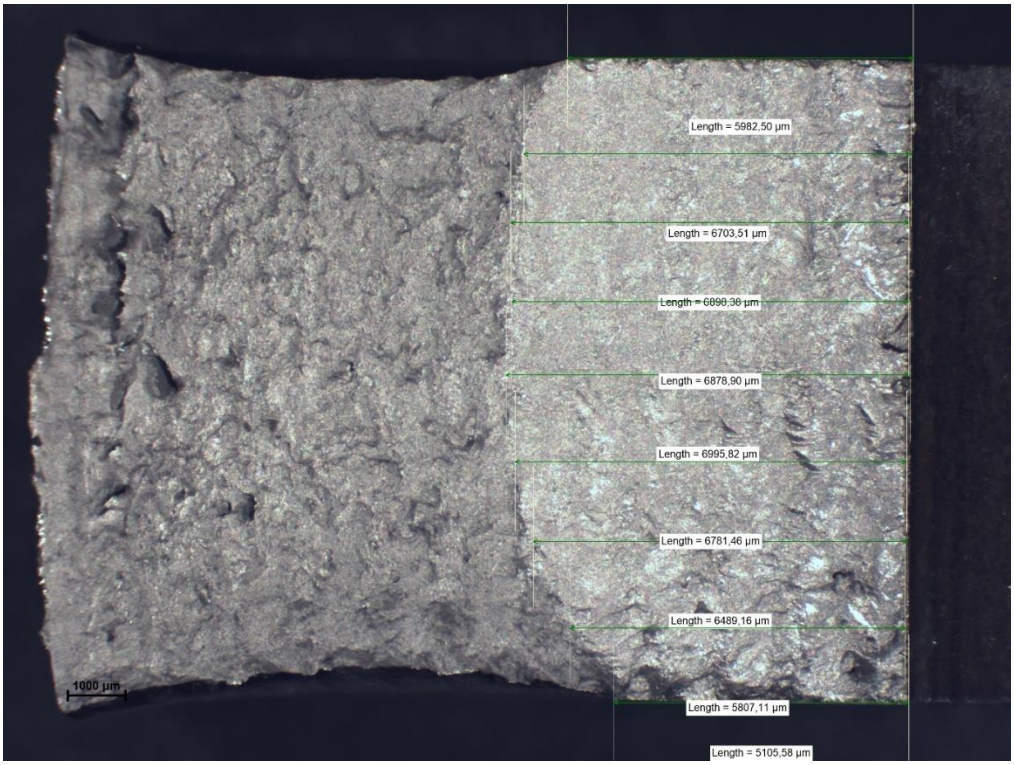

Figure 11.76: ZX3 crack measurements

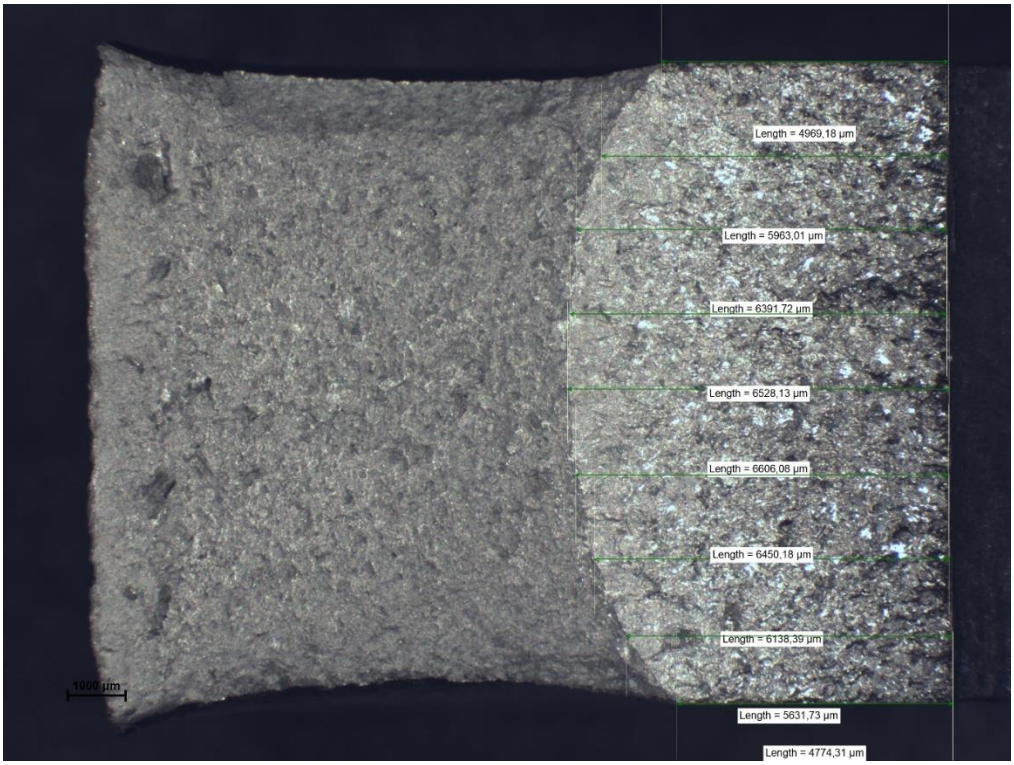

Figure 11.77: ZX4 crack measurements

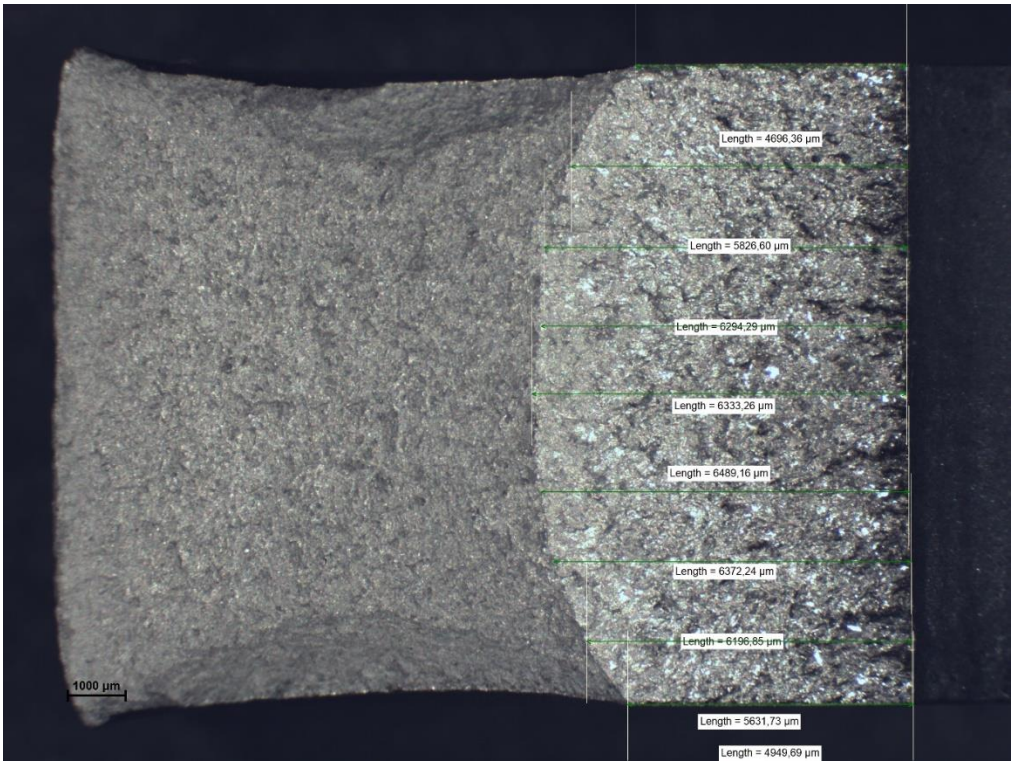

Figure 11.78: ZX5 crack measurements

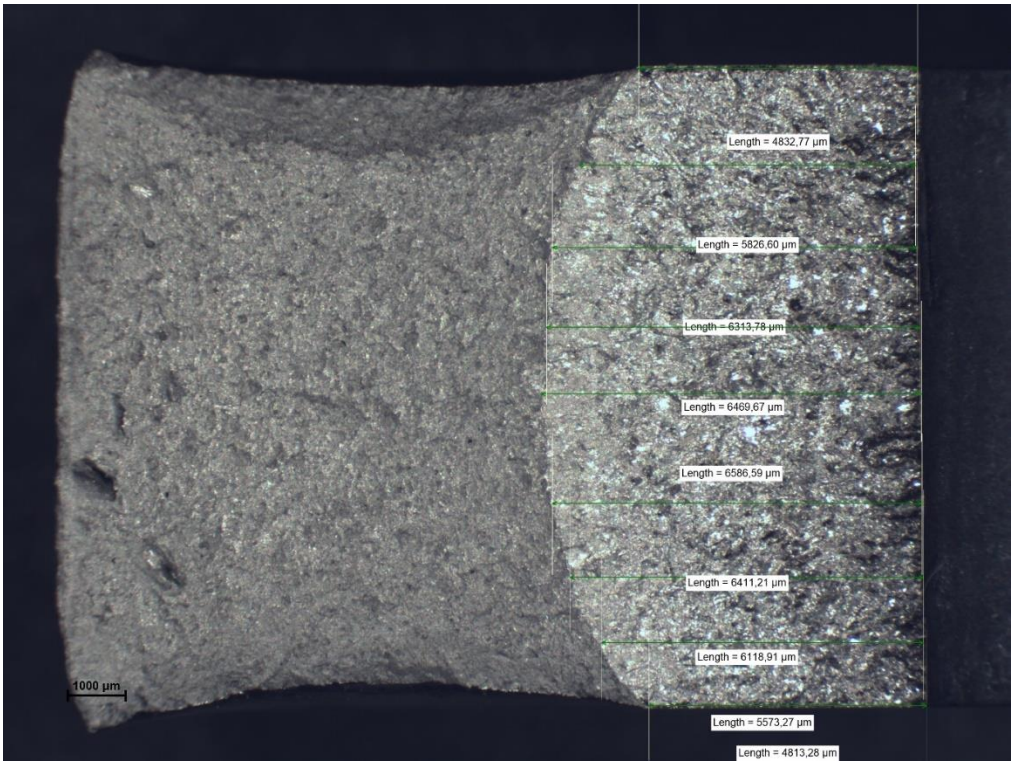

Figure 11.79: ZX6 crack measurements

11.8. Octave script for calculation of J_{max}

The Octave script developed for the fracture toughness analysis of the material is shown below.

J_int_general.m

```
%J integral

name=input('Enter the sample name: ', 's');   %enetering sample measurements
vp=input('Enter vp in m: ');
an=input('Enter an in m: ');              %machined notch length
B=input('Enter B in m: ');
W=input('Enter W in m: ');
a=input('Enter a in m: ');              %actual pre-crack length


%Plotting area enclosed by the curve
x1=[vp max(x)];                         %x coordinates for line OA
y1=[0 max(y)];                          %y coordinates for line OA
x2=[0 vp];                              %x cooridnates for base line
y2=[0 0];                               %y coordinates for base line
plot(x,y,'b',x1,y1,'b',x2,y2,'b')     %plotting data on grpah
grid on
xlabel('Displacement v (m)');
ylabel('Load (N)');
title(name);

totalarea=trapz(x,y)       %trapz function to calculate total area under graph

%Calculating area of triangle to subtract from total area
height=max(y)
base=max(x)-vp
triangle=0.5*base*height    %area of triangle to subtract from trapz area

%Plastic area
A_pl=trapz(x,y)-triangle    %U_p determination

%Calculating K for elastic component of J
P=max(y);
a0=(an+a);             %original crack length is the machined notch + pre-crack

f=((2+a0/W)*(0.886+4.64*a0/W-13.32*(a0/W)^2+14.72*(a0/W)^3-5.6*(a0/W)^4))/(1-a0/W)^1.5

K=((P/((B)*(W)^0.5))*f)
K_mpa=K/1e6                %K in mpa.m^0.5

%Elastic component of J
v=0.294;                   %poisson's ratio
E=200e9;                   %young's modulus

J_el=((K^2)*(1-v^2))/E    %elastic component

%Plastic component of J
b0=W-a0;
n_pl=2+(0.522*(b0))/W;

J_pl=(n_pl*A_pl)/(B*b0)

%Total J
J=(J_el+J_pl)/1000      %J in kJ/m^2
```

11.9. Density tables

The density test results for each build direction are shown in the tables below.

Table 11.2: Density test results for XY orientation

Specimen	Mass in air (g)	Mass in water (g)	Mass of support (g)	Density (g/cm³)	Average density for as-built (g/cm³)	Average density for build orientation (g/cm³)
XY1	24,756	19,625	-2,131	8,234		
XY2	26,167	20,863	-2,131	8,229		
XY4	26,694	21,369	-2,141	8,365	8.254	
XY5	24,635	19,514	-2,131	8,221		
XY7	25,366	20,155	-2,132	8,220		
					Average density for heat-treated (g/m³)	8.250
XY8	25,320	20,093	-2,157	8,229		
XY11	26,071	20,753	-2,159	8,235		
XY12	26,394	21,042	-2,156	8,240	8.246	
XY13	25,040	19,832	-2,175	8,238		
XY14	26,584	21,194	-2,190	8,289		

Table 11.3: Density test results for XZ orientation

Specimen	Mass in air (g)	Mass in water (g)	Mass of support (g)	Density (g/cm³)	Average density for as-built (g/cm³)	Average density for build orientation (g/cm³)
XZ1	26,903	21,480	-2,158	8,222		
XZ2	26,220	20,881	-2,156	8,219	8.217	
XZ3	25,412	20,168	-2,156	8,211		8.232
					Average density for	

					heat-treated (g/m^3)	
XZ4	26,339	21,001	-2,154	8,254	8.247	
XZ5	25,205	20,005	-2,153	8,254		
XZ6	24,045	18,979	-2,152	8,233		

Table 11.4: Density test results for ZX orientation

Specimen	**Mass in air (g)**	**Mass in water (g)**	**Mass of support (g)**	**Density (g/cm^3)**	**Average density for as-built (g/cm^3)**	**Average density for build orientation (g/cm^3)**
ZX1	26,979	21,541	-2,173	8,245	8.243	8.247
ZX2	27,236	21,770	-2,169	8,243		
ZX3	27,061	21,618	-2,167	8,242		
					Average density for heat-treated (g/m^3)	
ZX4	27,411	21,929	-2,166	8,248	8.250	
ZX5	27,788	22,264	-2,165	8,255		
ZX6	27,537	22,046	-2,160	8,249		

11.10. Hardness tables

The Vickers hardness test results for each build orientation will be shown in the tables below.

Table 11.5: Vickers hardness test results for XY orientation

Specimen	**Vickers hardness readings XY orientation**							
	1	2	3	4	5	Average	Average as-built hardness	Average hardness gained
XY1	358	362	341	329	342	346	355 ±5.45	106
XY2	362	348	358	358	379	361		
XY4	355	340	352	355	352	351		
XY5	375	342	335	327	330	342		

XY7	381	381	348	386	384	376		
							Average heat-treated hardness	
XY8	453	471	450	484	450	462	461 ±13.27	
XY11	441	429	445	471	448	447		
XY12	443	436	479	474	445	455		
XY13	458	424	427	413	409	426		
XY14	529	555	490	510	493	515		

Table 11.6: Vickers hardness test results for XZ orientation

Specimen	**Vickers hardness readings XZ orientation**							
	1	2	3	4	5	Average	Average as-built hardness	Hardness gained
XZ1	438	450	441	450	455	447	461 ±6.11	94
XZ2	460	473	468	482	448	466		
XZ3	476	471	473	450	487	471		
							Average heat-treated hardness	
XZ4	538	545	510	551	561	541	555 ±8.70	
XZ5	545	561	579	522	538	549		
XZ6	548	541	747	538	507	576		

Table 11.7: Vickers hardness test results for ZX orientation

Specimen	**Vickers hardness readings ZX orientation**							
	1	2	3	4	5	Average	Average as-built hardness	Hardness gained
ZX1	364	379	352	355	364	363	366 ±4.26	105
ZX2	355	371	364	360	345	359		

ZX3	364	379	381	384	373	376		
							Average heat-treated hardness	
ZX4	473	490	450	453	487	471	471 ±7.40	
ZX5	490	496	468	487	493	487		
ZX6	476	463	438	455	445	455		

11.11. Error calculation for microscope rig camera system

The error of the microscope rig camera system was compared to the NIS elements measurement system to quantify any error in measurements, if any. This is shown in the table below.

Table 11.8: Error calculation table for test specimens

	NIS (mm)	**Image J (mm)**	**Error %**
XY1	3,849	4,010	4,19
XY3	4,078	4,123	1,09
XY4	3,806	4,072	6,99
XY5	4,105	4,170	1,59
XY6	4,106	4,140	0,83
XY13	4,549	4,611	1,37
XY14	4,831	4,753	-1,61
XZ3	4,368	4,285	-1,89
XZ1	6,191	6,127	-1,04
XZ4	4,618	4,573	-0,99
XZ6	5,025	4,907	-2,35
ZX1	4,990	4,999	0,19
ZX2	4,717	4,804	1,83
ZX3	4,818	4,877	1,23
ZX4	4,883	4,778	-2,15
ZX6	4,909	4,995	1,75

From the table above, it can be seen that the results from both measurement systems correlate quite closely and therefore, Image J is a suitable tool for fatigue crack measurement in conjunction with the supporting rig designed in this project.